

## REPORT DOCUMENTATION PAGE

Form Approved  
OMB No. 0704-0188

Public reporting burden for this collection of information is estimated to average 1 hour per response, including the time for reviewing instructions, searching existing data sources, gathering and maintaining the data needed, and completing and reviewing this collection of information. Send comments regarding this burden estimate or any other aspect of this collection of information, including suggestions for reducing this burden, to Department of Defense, Washington Headquarters Services, Directorate for Information Operations and Reports (0704-0188), 1215 Jefferson Davis Highway, Suite 1204, Arlington, VA 22202-4302. Respondents should be aware that notwithstanding any other provision of law, no person shall be subject to any penalty for failing to comply with a collection of information if it does not display a currently valid OMB control number. PLEASE DO NOT RETURN YOUR FORM TO THE ABOVE ADDRESS.

1. REPORT DATE (DD-MM-YYYY) 12-08-2007.	2. REPORT TYPE Final	3. DATES COVERED (From - To) 01-01-2004 - 31-12-2006		
4. TITLE AND SUBTITLE (U) Turbulent mixing and combustion for high-speed, air-breathing propulsion applications			5a. CONTRACT NUMBER  5b. GRANT NUMBER FA9550-04-1-0020  5c. PROGRAM ELEMENT NUMBER 61102F	
6. AUTHOR(S)  Paul E. Dimotakis			5d. PROJECT NUMBER 2308  5e. TASK NUMBER BX  5f. WORK UNIT NUMBER	
7. PERFORMING ORGANIZATION NAME(S) AND ADDRESS(ES)  Aeronautics, MC 301-46 California Institute of Technology Pasadena, CA 91125			8. PERFORMING ORGANIZATION REPORT NUMBER	
9. SPONSORING / MONITORING AGENCY NAME(S) AND ADDRESS(ES) AFOSR/NA 875 North Randolph Street Suite 325, Room 3112 Arlington VA 22203-1768			10. SPONSOR/MONITOR'S ACRONYM(S)	
12. DISTRIBUTION / AVAILABILITY STATEMENT  Approved for public release; distribution is unlimited			11. SPONSOR/MONITOR'S REPORT NUMBER(S)  AFRL-SR-AR-TR-07-0298	
13. SUPPLEMENTARY NOTES				
14. ABSTRACT  Work was completed on mixing, chemical-reaction, and combustion processes in turbulent, subsonic, and supersonic flows. Research included high-speed internal flows of interest to scramjet mixing and combustion, aimed at flow-control and flameholding issues. The control authority and mixing in subsonic and transonic flows affected by mass injection and heat release was quantified. In parallel, Large Eddy Simulation (LES) with Sub-Grid Scale (SGS) modeling of these flows was conducted with codes verified against predictions of Linear Stability Analysis (LSA) theory. Research on hydrocarbon combustion was conducted on premixed methane-air, ethane-air, and (diluted) ethylene-air flames. Detailed measurements of flame extinction strain-rate and flame speed were obtained at different compositions at atmospheric pressure. Direct Numerical Simulations (DNS) of axisymmetric unsteady flows in both cold and chemically reacting impinging jets with full chemistry were also performed. Experimental investigations of the three-dimensional full-field structure of scalar dispersion fields in grid turbulence were initiated.				
15. SUBJECT TERMS  Combustion, turbulence, mixing, subsonic, supersonic, hydrocarbon flames				
16. SECURITY CLASSIFICATION OF:  a. REPORT Unclassified		17. LIMITATION OF ABSTRACT UL	18. NUMBER OF PAGES 126	19a. NAME OF RESPONSIBLE PERSON Julian M. Tishkoff  19b. TELEPHONE NUMBER (include area code) (703) 696-8478

**GRADUATE AERONAUTICAL LABORATORIES  
CALIFORNIA INSTITUTE OF TECHNOLOGY**

Pasadena, California 91125

**TURBULENT MIXING AND COMBUSTION FOR HIGH-SPEED,  
AIR-BREATHING PROPULSION APPLICATIONS**

P. E. Dimotakis, Principal Investigator

*John K. Northrop Professor of Aeronautics and  
Professor of Applied Physics  
California Institute of Technology*

Air Force Office of Scientific Research  
AFOSR Grant FA9550-04-1-0020

Final Progress Report for the period  
1 January 2004 – 31 December 2006

31 March 2007  
Revised: 12 August 2007

**Best Available Copy**

**20070815505**

## Summary

This is the final scientific report on research and work undertaken under the sponsorship of AFOSR Grant FA9550-04-01-0020, on "Turbulent Mixing and Combustion for High-Speed, Air-Breathing Propulsion Applications." The research focused on fundamental investigations of mixing and combustion, in turbulent, subsonic, and supersonic flows, and was motivated by applications in high-speed air-breathing propulsion. The work was a closely coordinated effort between experiments and numerical simulation, and exploited recent advances and developments in diagnostics and instrumentation, some undertaken as part of this effort. In large measure, the experimental and diagnostics-development part of the work described below was enhanced and made possible by support under the DURIP Grant FA9550-04-1-0253. The numerical-simulation work also benefited from the close collaboration with the Caltech DOE ASC Center (D. Meiron, PI).

## 1. Mixing and Combustion in Complex High-Speed Flows

### 1.1. Experiments

Over the length of this project, an extensive, systematic and methodical investigation of the control and mixing produced by the expansion-ramp geometry has been undertaken. In this geometry, a high-speed upper "air" stream is expanded over a ramp inclined at  $30^\circ$  to the flow. A low-speed "fuel" stream is injected through perforations in the ramp and generates a turbulent mixing layer between the two streams. As fluid from the two streams is entrained into the mixing layer, the lower stream eventually is exhausted, causing the mixing layer to attach to the lower guidewall. Reattachment establishes a key flow feature: a recirculation zone with upstream transports of hot products toward the fuel-injection location and provides a low strain-rate flameholding region. A schematic of the facility and the key flow features is presented in Fig. 1.

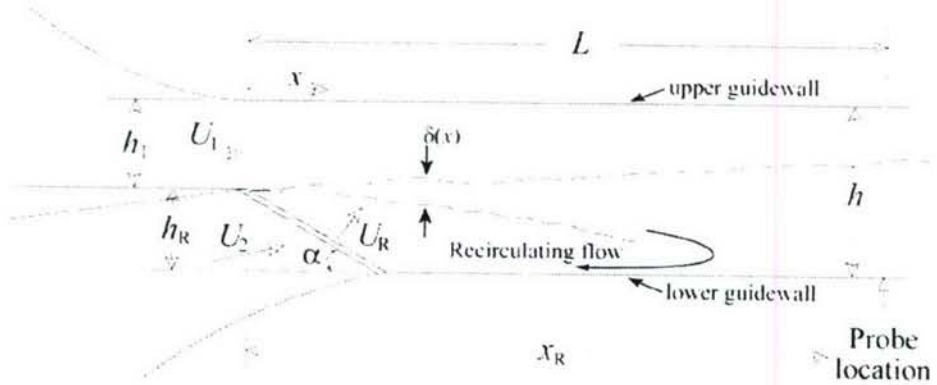


Fig. 1 Schematic of the expansion-ramp geometry.

Johnson (2005) and Bergthorson *et al.* (2007) characterized the flow for subsonic and transonic injection velocities in the top stream. A measure of the aerodynamic performance of the device is the overall pressure coefficient,  $C_p = 2(p_e - p_i)/(\rho U_1^2)$ , where  $p_e$  and  $p_i$  are the exit and inlet pressures, respectively. In Fig. 2, the pressure coefficient is plotted versus the injection velocity ratio,  $r \equiv U_2/U_1$ , for several values of the upper and lower stream speeds,  $U_1$  and  $U_2$ , respectively. The plotted curve-fit derives from a control-volume analysis of the geometry and is given by:

$$C_p = \left[ 2\left(\frac{h_1}{h}\right) - \frac{8}{3}\left(\frac{h_1}{h}\right)^2 \right] - \frac{16}{3}\left(\frac{h_1 l_R}{h^2}\right)\frac{U_R}{U_1} + \left[ 2\sin\alpha\left(\frac{l_R}{h}\right) - \frac{8}{3}\left(\frac{l_R}{h}\right)^2 \right]\left(\frac{U_R}{U_1}\right)^2,$$

where  $h_1$  is the top stream height,  $h$  is the test section height,  $l_R$  is the length of the ramp,  $U_1$  is the top stream speed and  $U_R$  is the ramp injection velocity, as defined in Fig. 1. The pressure coefficient decreases from a positive value, typical of a diffuser, to zero, typical of a free shear layer, with the injection of only 20% of the upper-stream flow. At higher inlet velocities the control authority improves, i.e., the amount of mass injection required to achieve the same overall pressure coefficient decreases.

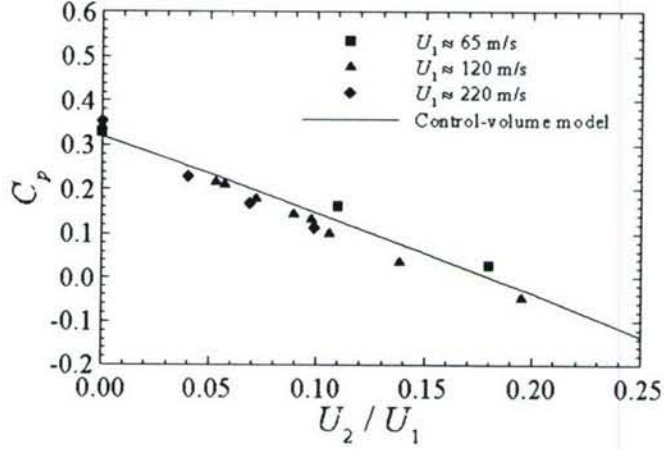


Fig. 2 Pressure coefficient versus velocity ratio for subsonic upper-stream velocities.

When the top stream is seeded with a mixture of hydrogen [ $H_2$ ] and nitric oxide [ $NO$ ], and the lower stream with fluorine [ $F_2$ ], the two streams react hyperbolically on contact and the molecular mixing can be measured through the use of the flip experiment technique (Mungal & Dimotakis 1984). Two measures of mixing can be computed, the mixed fluid in the duct,  $\delta_m/h$ , and the mixed fluid within the mixing layer,  $\delta_m/\delta_t$ . Measurements focused on a velocity injection ratio of  $r = 0.1$ , corresponding to an equivalent mass-flux ratio close to the stoichiometric ratio for hydrocarbon fuels. Both measures of mixing were found to decrease with increasing upper-stream injection velocity, as seen in Fig. 3.

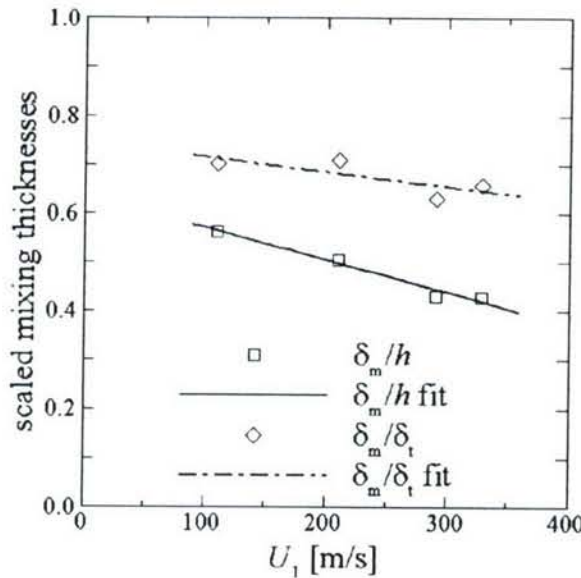


Fig. 3 Scaled mixing thicknesses as a function of the top-stream velocity for an injection ratio of  $r = 0.1$ . Straight lines are fit to the data and included for reference

Recent work has focused on supersonic top stream speeds:  $M_1 = 1.5$  and  $2.5$ . Composite schlieren images of the flow-field for the above Mach numbers are reproduced in Fig. 4.

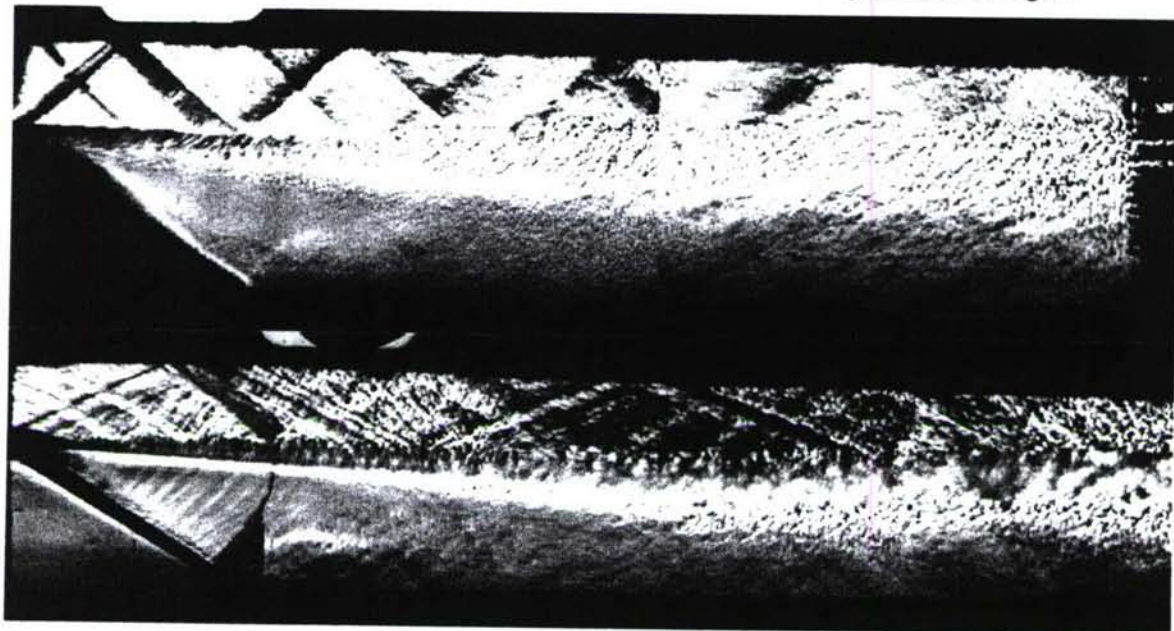


Fig. 4 Composite schlieren images for  $M_1 = 1.5$  (top) and  $2.5$  (bottom),  $r = 0.1$ . Both streams are pure  $[N_2]$ .

For supersonic velocities, the trend of the pressure coefficient is reversed, namely the pressure coefficient increases, from a negative value, typical of a supersonic flow in a duct with losses, to zero, typical of the free shear layer value. Data are presented in Fig. 5. Interestingly, 20% of the upper stream velocity suffices to change the pressure coefficient from a negative to a positive value.

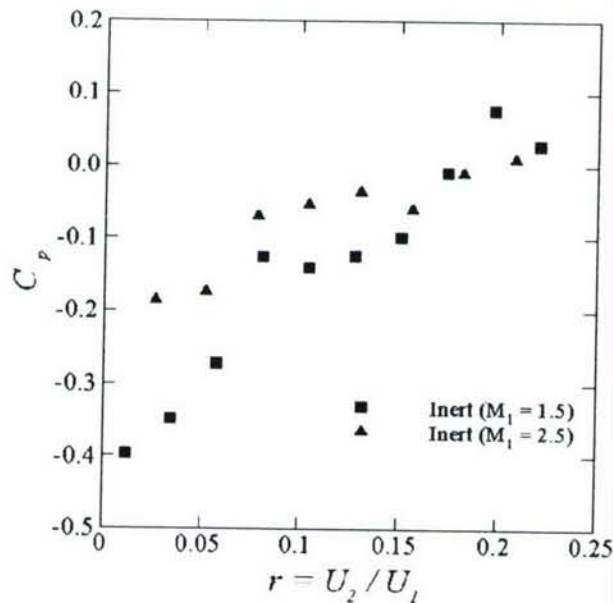


Fig. 5 Pressure coefficient versus velocity ratio for supersonic top-stream velocities.

Measurements of molecular mixing using the flip experiment were also made for supersonic shear-layer conditions. The trend of reduction in mixing with increasing top-stream velocity

persists in the supersonic regime. However, the amount of mixing of the expansion-ramp geometry is still greater than that for a free-shear layer. The research described above was performed by J. Bergthorson, A. Bonanos, and M. Johnson.

### 1.2. Simulations

An accompanying computational effort has concentrated on verification of the complex code and simulations in complicated geometries. The compressible LES fluid dynamics solver of the Virtual Test Facility developed under the DOE-sponsored Caltech ASC program is used for the simulations. The solver has Adaptive Mesh Refinement (AMR) capabilities and is implemented in a fully parallel manner with dynamic load balancing and data redistribution (Pantano *et al.* 2007).

A new code verification technique that utilizes solutions from Linear Stability Analysis (LSA) was developed and used to verify the inviscid part of Caltech's solver. The method can be used for time-dependent problems with non-trivial boundary conditions and is essentially a verification of the boundary closure. Simple exact solutions cannot be used to verify the correctness of the boundary closure that is of paramount importance in air-breathing propulsion applications. A spatially developing shear layer was used in this verification study. The real and imaginary parts of the most unstable mode from LSA and computation were compared for an incompressible and a compressible shear layer. The work is novel, with no prior examples. The effort and results were responsible for several improvements in computational technology.

Three-dimensional simulations with Large Eddy Simulation (LES) and Sub-Grid Scale (SGS) modeling were completed for compressible flows with ramp injection. The simulations model experiments conducted at Caltech and are part of the effort to develop and validate computational methods for compressible turbulent mixing. The simulations are in good qualitative agreement with the experiment, with quantitative comparisons presently in progress. Fig. 6 shows the instantaneous passive scalar isosurfaces resulting from low-speed injection through the inclined ramp into a high-speed top stream at  $M_1 = 0.5$ . The pressure coefficient on the top and bottom guide walls is shown in Fig. 7. This work is part of the Ph.D. research of G. Matheou and performed in close collaboration with the experimental work documented above.

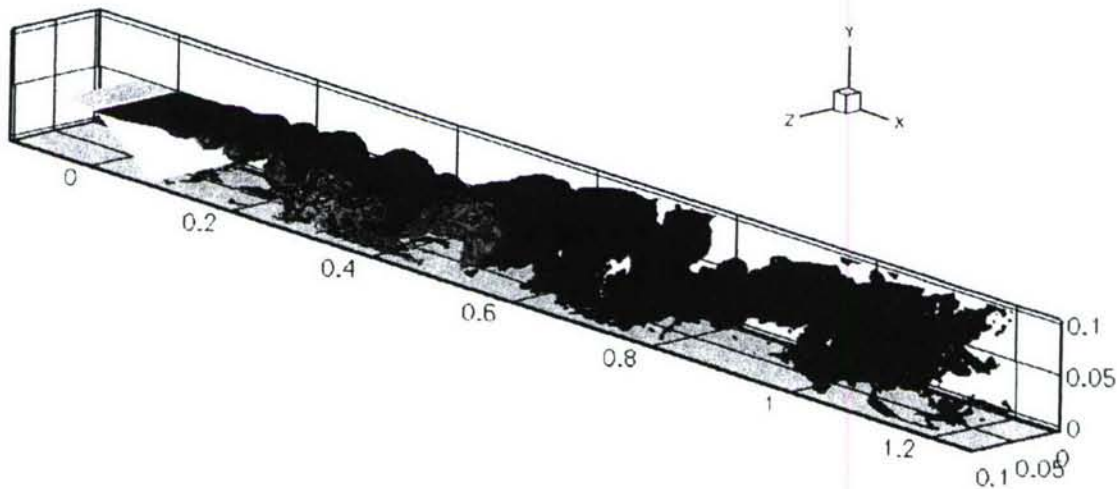


Fig. 6 Instantaneous passive scalar isosurfaces for a  $M_1 = 0.5$  top stream.

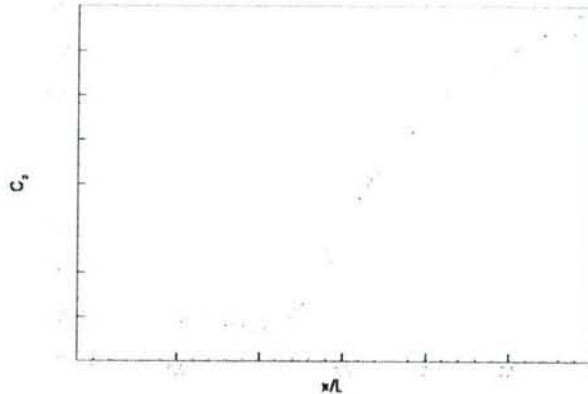


Fig. 7 Computed pressure coefficient on the top (solid line) and bottom (dashed line) guidewall.

## 2. Hydrocarbon flames and combustion

### 2.1. Experiments

This part of the research effort focused on flame stability and chemical kinetics issues that represent crucial components of both fundamental hydrocarbon combustion as well as applications in high-speed flow propulsion, such as scramjets.

Predictions of flame phenomena using detailed descriptions of molecular transport and chemical kinetics, and their comparison with experiment have been central to recent advances in hydrocarbon flame research. In particular, comparisons of such predictions with the results of experiments in simple and well-characterized configurations that can be modeled accurately have been responsible for significant progress in the performance of kinetics models by allowing the validity of chemical-kinetic mechanisms to be tested (e.g., Bergthorson & Dimotakis 2006b). An increasing number of chemical-kinetic mechanisms are proposed in the literature, each predicting different flame behavior in various regimes. The variance in the predictions is traceable to differences in the modeled reactions – not all rely on the same reaction set – and rate parameters chosen in each model. Although methane ( $\text{CH}_4$ ) combustion is claimed to be well understood, our experiments have revealed discrepancies between accepted models and experiments, with higher discrepancies for ethylene ( $\text{C}_2\text{H}_4$ ), for example, that has only one more carbon atom than methane and is potentially an important fuel in scramjet applications. To make progress towards a universal model of flame kinetics, our research on hydrocarbon flames provides a way to compare and validate these mechanisms. The research also extends the existing experimental database with high-accuracy simultaneous measurements of flow velocity through the flame, as well as CH-radical profiles in a jet-wall-stagnation flow. This targets the mitigation of the imbalance among the hundreds of constants required in each model and the small number of data sets available to validate the mechanisms that leads to indeterminacies and non-uniqueness in the various kinetics models. Experiments are currently in progress at  $p = 1$  atm. Work is in progress to develop the capability for elevated-pressure measurements ( $1 \text{ atm} < p < 12\text{-}15 \text{ atm}$ ).

Detailed measurements of the velocity and CH-radical profiles have been performed, which are then predicted by numerical simulations based on detailed chemical-kinetic models. The CH-radical profiles, in particular, are predicted directly and provide an accurate marker of the reaction zone. Axial velocity profiles through the flames were performed using Particle Streak Velocimetry (PSV) and Planar Laser Induced Fluorescence (PLIF) with excitation by UV laser

illumination and detection in the visible, respectively. Sample images for each of these techniques are reproduced in Fig. 8.

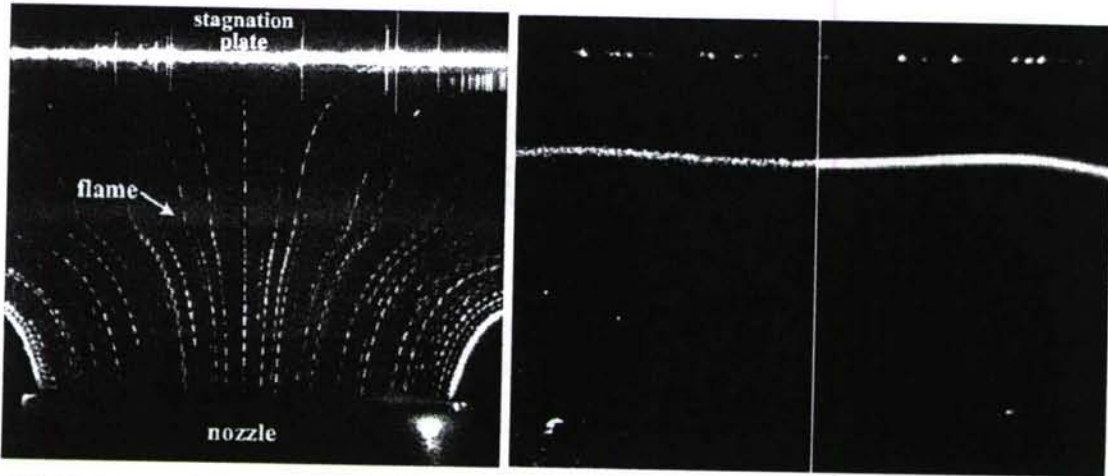


Fig. 8 Left: PSV image in a methane-air flame ( $\Phi = 0.8$ ). Stagnation plate and short vertical streaks from CCD pixel charge overflow are visible. Right: Sample CH PLIF images in a  $\Phi = 1.0$  methane-air flame, (a) single image, (b) average of 1000 exposures.

A sample comparison of the experimental data and the predicted profiles using GRI-Mech 3.0 (Smith *et al.*) that was performed is reproduced in Fig. 9. To account for the systematic uncertainties in measuring flow velocities with a particle velocimetry technique, the particle motion through the flame was solved using a Lagrangian technique that accounts for the combined particle inertia and thermophoretic effects (Bergthorson & Dimotakis 2006a).

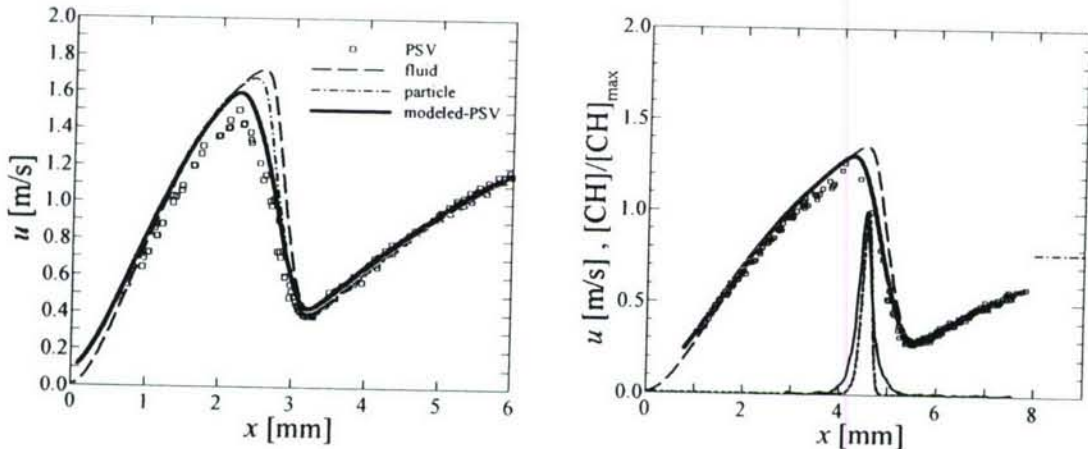


Fig. 9 Left: Comparison of PSV data in a  $\Phi = 0.9$  methane-air flame with the predictions of GRI-Mech 3.0. The simulated fluid velocity profile, the modeled particle profile through the flame, and the estimated profile that would be measured using the PSV implementation are compared to the data. Right: Comparison of PSV and CH PLIF data in a  $\Phi = 1.3$  methane-air flame

The PSV analysis technique was applied to the modeled particle location in time to account for finite particle-track interval effects. Improved agreement between simulation and experiment was found when the systematic uncertainties in the experiment were included and explicitly accounted for in the models. However, the predicted velocity profiles are still above the experimental data in the region of the velocity minimum and maximum, indicating that predicted flame speeds by GRI-Mech 3.0 are higher than in the experiments for lean methane-air flames. For rich methane-air flames, good agreement was found between the predicted velocity and CH

radical profiles, indicating that the predicted flame speed is close to that measured experimentally. These comparisons are consistent with results published on the GRI-Mech website for laminar flame speeds (Smith *et al.*).

Similar measurements and comparisons to simulations were completed for ethane and ethylene flames. The approach in this part of the work was to test and evaluate multiple published mechanisms from the literature, rather than restrict the study to a particular model. A comparison of the data for a lean and rich ethylene flame is given in Fig. 10, with comparisons using model predictions based on GRI-Mech 3.0, a mechanism by Davis *et al.* (DLW99: 1999), and two versions of the San Diego mechanism (SD2003, SD2005). The best overall agreement between simulation and experiment for C<sub>1</sub>-C<sub>2</sub> fuels occurred for the 2005 version of the San Diego mechanism.

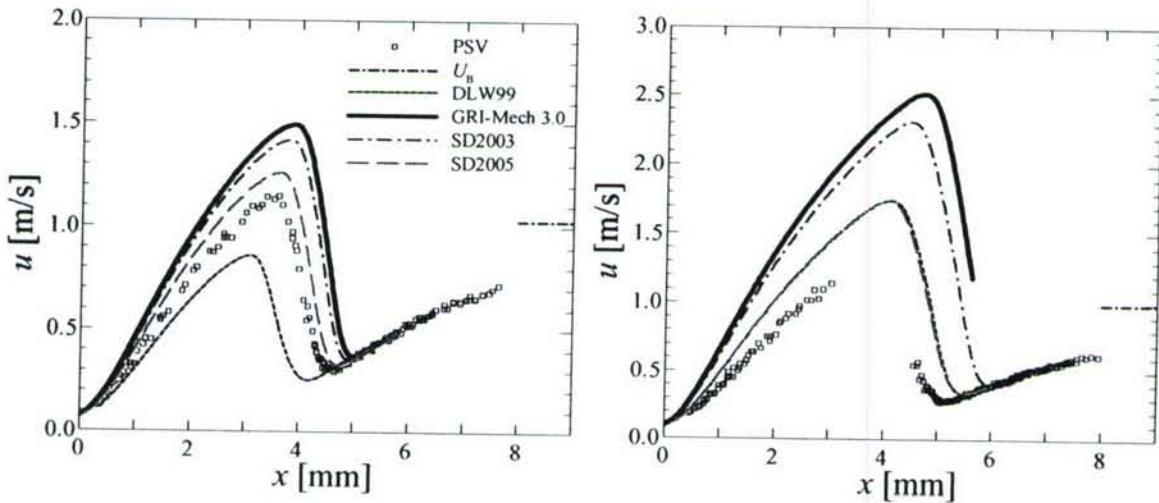


Fig. 10 Comparison of measured and predicted velocity profiles based on with several published combustion chemistry models. Left: Comparison for a  $\Phi = 0.6$  ethylene-air flame. Right: Comparison for a  $\Phi = 1.8$  ethylene-air flame.

Fuel blends of interest to scramjet propulsion are desirable for their flame-holding properties that are related closely to flame speed. Measurements in high-flame speed mixtures, however, present experimental challenges of their own. In particular, fuel blends such as ethylene-hydrogen have much higher peak velocities (6 m/s for ethylene and 22 m/s for hydrogen, versus 3 m/s for methane). High-pressure environments are also troublesome because flame thickness decreases with increasing pressure, with higher gradients and curvatures encountered in high-pressure flames. Such flames present challenges that placed them beyond the capabilities of the originally employed Particle Streak Velocimetry (PSV) techniques that were applied successfully to measure flow velocities in methane-air, ethane-air, and diluted ethylene-air flames so far.

A new Particle Tracking Velocimetry (PTV) technique was developed that retains the low-particle-loading advantage of PSV (relative to PIV and LDV), but characterized by higher spatio-temporal resolution, thanks to a new pulsed-lser illumination source (Coherent Evolution-75, high repetition-rate (up to 20 kHz) Nd:YLF 527 nm, diode-pumped Q-switched laser with double-pulse option) and a new imaging system (high-resolution: 4008×2672 pix<sup>2</sup>, low-noise (cooled) Cooke PCO-4000 CCD camera). The superiority of the new PTV technique was demonstrated in cold impinging jets, where the range of velocities that can be measured was increased by a factor 6 compared with PSV, while the scatter in the measurements was reduced by a factor 2 at the same time. CH PLIF metrology was upgraded as well, with a 60 % increase in collected light that proved significant in such light-starved diagnostics. The simultaneous use

of the new PTV and CH PLIF measurement techniques was also enhanced by state-of-the-art spectrally selective optical filters. Thanks to the capabilities of the new PTV technique, relevant combustion chemistry models now can be tested in pure ethylene flames, blends of hydrocarbon fuels, higher ( $C_3$ ) hydrocarbons, and hydrogen flames at atmospheric, as well as moderately high pressures.

One-dimensional (1D) models can provide reasonable approximations to the hydrodynamics of both cold and reacting stagnation flows, subject to some caveats, however, that will be discussed below. The 1D hydrodynamic model was validated against cold impinging jet data, where the velocity and velocity gradient of the simulation are specified from a fit of the experimental data in the range  $x < 0.8 d$  (Bergthorson *et al.* 2005b). Here,  $x$  is the axial coordinate measured from the wall, and  $d = 0.995$  cm is the nozzle diameter. For stagnation-flame simulations, values of the velocity and its gradient are applied as boundary conditions at  $x = 0.6 d$  from estimates derived from parabolic fits to the cold-flow velocity data for each experimental case (Bergthorson *et al.* 2005a). A parabolic profile is an exact solution of the cold-flow equations and parabolic fits provide an excellent match to the actual measurements. This has mitigated a long-standing difficulty, with the appropriate specification of the velocity boundary conditions in stagnation flow simulations previously identified as critical in properly predicting flame behavior, such as extinction strain rates (Kee *et al.* 1988). The improvements described above allowed the detailed direct comparison between experiment and numerical simulations.

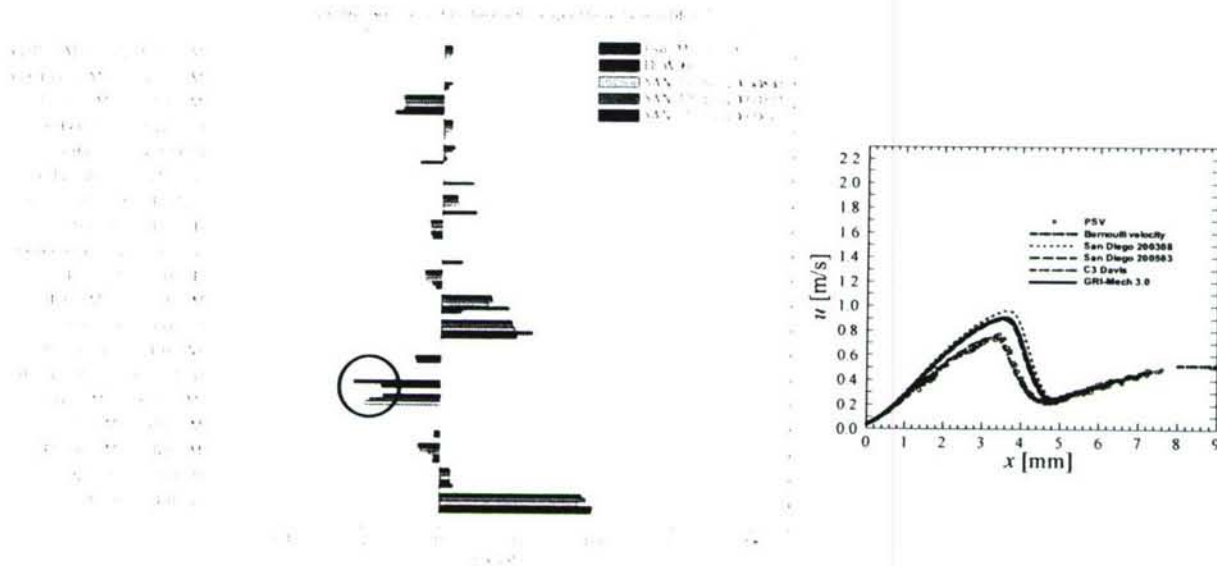


Fig. 11 Left: Logarithmic sensitivity of the laminar flame speed of a  $p = 1$  atm,  $\Phi = 0.7$  methane-air flame for multiple mechanisms. Right: Comparison of stagnation flame velocity profiles in a  $p = 1$  atm,  $\Phi = 0.7$  methane-air flame with multiple mechanisms.

The number of reactions in hydrocarbon chemical-kinetic mechanisms is large. A new approach combining sensitivity analysis in the comparison with experimental data to each reaction, with reaction-pathway analysis is under development that will automatically identify the dominant causes of variances between experiment and different models based on predictions from multiple mechanisms. Sensitivity analysis alone already provides some answers, such as in the systematic overprediction of flame speeds by all mechanisms except DLW99 in an atmospheric-pressure, lean methane-air flame, as shown on Fig. 11. First, sensitivity analysis identifies the reactions that most affect the solution. After identifying these reaction rates, they can be compared among the mechanisms considered. In particular, the larger kinetic rate of the  $H + O_2 + H_2O \rightarrow HO_2 + H_2O$

reaction (cf. Fig. 11) was found to be likely responsible for the improved agreement. The experiments and analysis described above were initiated in the course of the Ph.D. research of J. Bergthorson and are continuing as part of the Ph.D. research by L. Benezech.

## 2.2. Simulations

A new code was developed to perform Direct Numerical Simulations (DNS) of the laboratory setup in a 2D axisymmetric domain with a full hydrocarbon chemistry model. All relevant length scales were resolved and differential-diffusion effects also were taken into account. The code integrates the unsteady low-Mach-number Navier-Stokes equations. Various techniques were applied to verify the code, such as the method of manufactured solutions, which demonstrated the expected rate of convergence.

The uniform-pressure-eigenvalue assumption in 1D models and the inappropriateness of plug-flow boundary conditions were shown to cause erroneous results for cold flow (e.g., Bergthorson *et al.* 2005). The behavior of the same one-dimensional model when the chemical reactions are present was now investigated numerically. One-dimensional numerical solutions for the same separation distance at the same flow condition were obtained *a priori* for each two-dimensional simulation, and the solution is extrapolated in the radial direction to obtain an initial condition to the two-dimensional model. The inflow velocity condition and the entrainment flux are specified at the nozzle exit. The wall is isothermal and was maintained at  $T_w = 300$  K throughout the study. Outflow boundary conditions are applied at the outermost radial boundary in the computational domain, at  $r = 2.0$  cm.

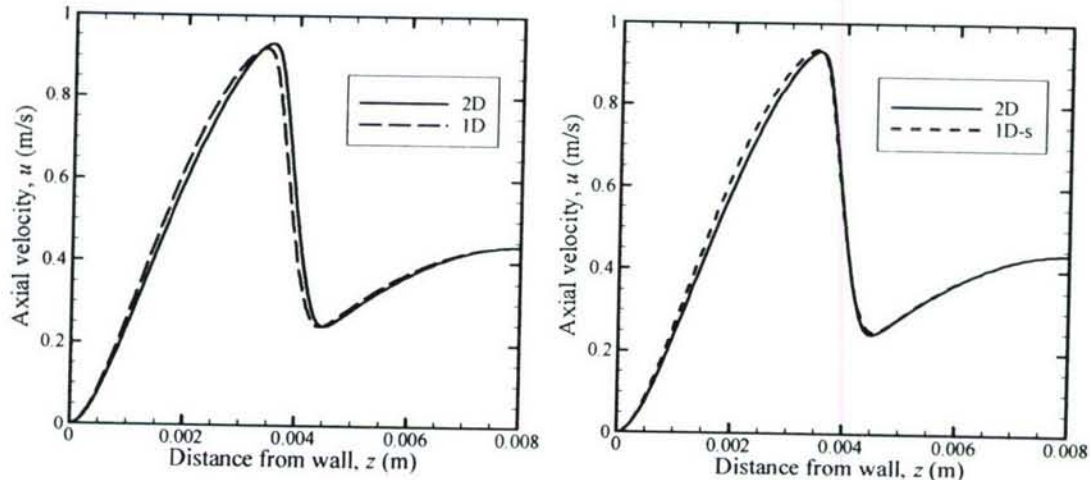


Fig. 12 Axial velocity profile along the axis in a methane-air flame ( $\Phi = 0.7$ ). Left: Comparison of 2D model and 1D model with plug-flow boundary conditions. 1D model is unable to predict flame location correctly. Right: Comparison of 2D model and 1D model with the boundary conditions obtained from a 2D numerical solution. X marks the location where the boundary condition is specified in the 1D model.

Shown in Fig. 12 is an axial velocity profile comparison between the two-dimensional and one-dimensional model (Cantera), at an equivalence ratio of  $\Phi = 0.70$ . The velocity profiles are seen to differ from each other as the flame is approached, when plug-flow boundary conditions are used. This is also responsible for a difference in the prediction of flame location between two-dimensional and one-dimensional simulations. This difference is attributable to the incorrect pressure-eigenvalue assumption in the one-dimensional formulation. However, it was found that the 1D model is more successful when the boundary condition is specified in the middle of the nozzle-flame region, with velocity boundary condition values taken directly from the corresponding two-dimensional simulation. Hereafter, this short domain case with a finite

spreading rate boundary condition is denoted as '1D-s'. Generally, plug-flow boundary conditions were found to be unreliable for any detailed comparison to experimental data, or in multi-dimensional simulations, even when there is no velocity gradient at the nozzle exit. This is consistent with previous findings in the case of non-reacting flow (Bergthorson *et al.*, 2005b).

Figure 13 illustrates the discrepancy between two- and one-dimensional models in terms of the pressure-eigenvalue data. In 1D models, the pressure eigenvalue is assumed constant, as indicated in Fig. 13 (dashed line). The pressure eigenvalue has a large spike near the flame front. This is in contrast to earlier hydrogen flame simulations reported by Frouzakis *et al.* (1998) and provides another reason that renders hydrocarbon flame simulations challenging. This spike is attributable mainly to the thinness (high dilatation) in the flame region, as well as the (slight) curvature of the flame front.

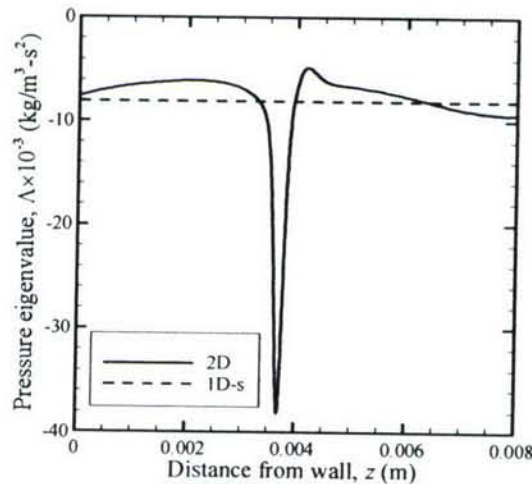


Fig. 13 The pressure-eigenvalue profile along the axis in a methane-air flame ( $\Phi = 0.7$ ). Note the sharp spike at the flame front when the correct pressure field is obtained, in contrast to a uniform value (dashed line) assumed in the one-dimensional model.

The magnitude of the pressure eigenvalue affects the prediction of the spreading rate,  $\sigma_t$ , in the 1D model and can be responsible for either an overprediction or underprediction of the spreading rate in the near- and post-flame region, as shown in Fig. 14. On the other hand, the location and the size of the spike have no discernible effect on the prediction of flame location in the 1D model, as seen in Fig. 12. This implies that the pressure-eigenvalue profile between nozzle and the flame is an important factor in determining flame location and somehow must be accounted for in 1D formulations and simulations, if high fidelity and accuracy are important.

The main purpose of this research is to study the capability and limitation of current methane combustion model such as GRI-Mech 3.0. Simulation software that allows such direct comparisons has not been available previously but was made possible through the development of an efficient algorithm as part of this effort, using spectral-element methods.

The computational domain used for this study is shown in Fig. 15. The domain includes the interior and exterior of the nozzle-plate assembly at the dimensions specified in the corresponding laboratory setup (Bergthorson 2005b). The combustible mixture is introduced at the bottom of the nozzle whereas a moderate amount of air is introduced at the bottom of the exterior between nozzle and the enclosure (the bottom-right end) to accommodate the entrainment requirements of the jet flow. To stabilize the flame in both experiments and simulations, a small amount of nitrogen is introduced from an outer nozzle, for which an exit

velocity profile is specified. All fluids entering the computational domain exit from the side of the stagnation plate, which can be seen at the upper-right end in the figure.

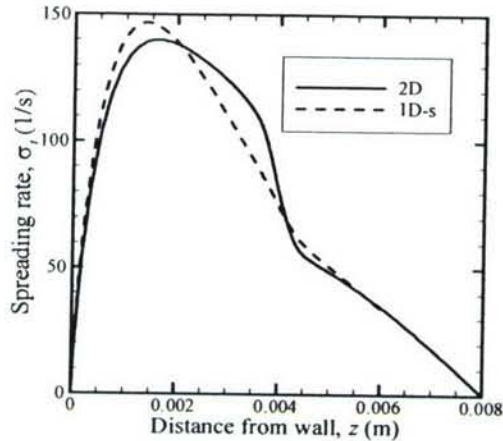


Fig. 14 The spreading rate profile along the axis in a methane-air flame ( $\Phi = 0.7$ ). Within the reaction zone, the spreading rate changes. This effect cannot be accommodated in one-dimensional models as a consequence of the uniform pressure eigenvalue assumption.

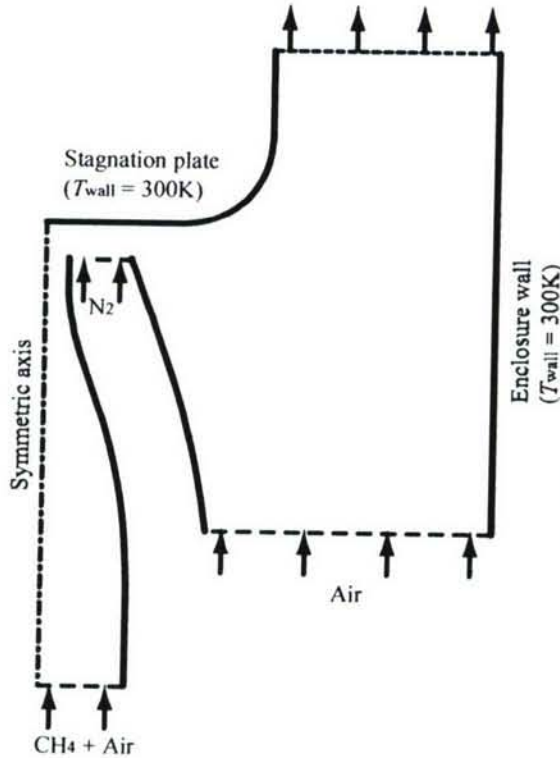


Fig. 15 The computational domain used for simulation of the laboratory stagnation flames. Solid lines indicate solid isothermal walls, held at 300 K. Inflow/outflow boundaries are identified by the direction of the flow arrows. Their length is for illustration purposes and does not indicate the velocity magnitude.

Fig. 16 shows contours of the CH radical mass fraction superimposed on computed streamlines. Compared to the earlier case, in which the velocity boundary condition is specified at the nozzle exit, the flame observed in this setting exhibits a dip in the flame shape, which is attributable to nozzle-flame proximity effects that, in turn, modify the velocity profile at the nozzle exit. Such flame shapes have been observed in experiments.

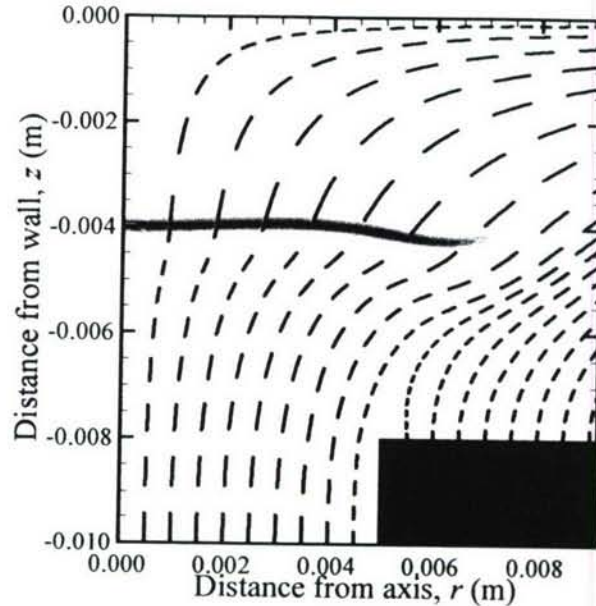


Fig. 16 CH mass fraction (pink) on top of streamlines (dashed lines) at  $\Phi = 0.70$ . Note the slight dip in flame front because of nozzle-flame proximity effect. This is also discernible in experiments.

This work is part of the Ph.D. research of K. Sone, is performed in collaboration with D. Meiron, and is co-funded by Caltech's DOE ASC Center.

### 3. Scalar Dispersion

#### 3.1. Introduction

Scalar dispersion is the dispersion of a (passive) scalar marker in a turbulent flow (e.g. the dispersion of a pollutant or biological agent in the wind). The first experiment addresses the dispersion of the scalar marker from a continuous (steady) point release behind a grid (well defined turbulent flow).

#### 3.2. Experimental setup

The experiment was performed in the Free Surface Water Tunnel (FSWT) of the GALCIT (Graduate Aeronautical Laboratories, California Institute of Technology). The FSWT has a cross sectional area of  $20'' \times 20''$  and can produce flow velocities from 1.0 mm/s to 8 m/s. A stainless steel grid with a wire size of  $\frac{1}{4}''$  and spacing between the wires of  $1''$  (64% open area) is placed in the test section to produce uniform grid turbulence. With a flow velocity of 5.22 cm/s measured at the beginning of the test section, the Reynolds number based on the mesh size is  $Re_M = 1650$  and the initial Taylor Reynolds number is  $Re_T \approx 41$ . The scalar marker (disodium fluorescein in these experiments) is released into the water at the center of a cell in the stainless steel grid. The dispersion of the marker is viewed using laser-induced fluorescence induced by a spatially scanned argon-ion laser (Fig. 17).

A high-speed 2-axis galvanometric scanner from GSI Lumonics (VM500C with a 0.8 ms step time for a  $50^\circ$  step size) is used to sweep the argon-ion laser beam across the measurement volume in a serpentine pattern (Fig. 18).

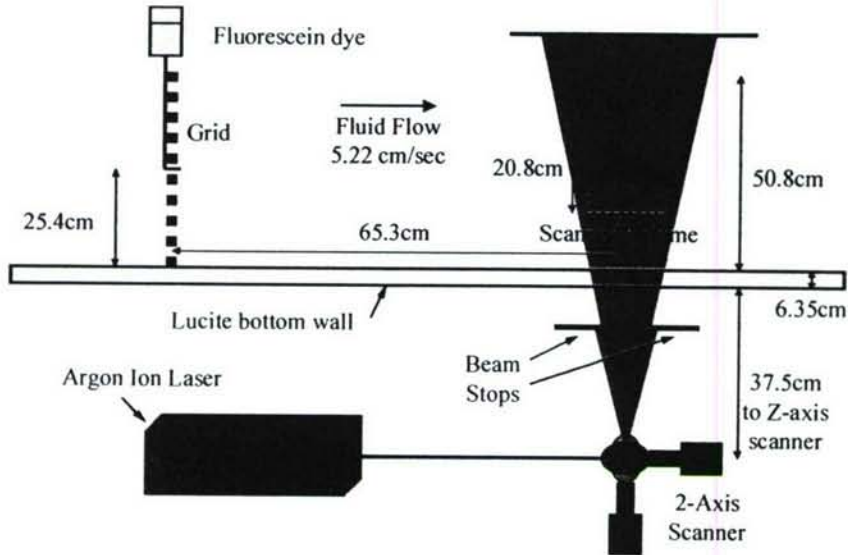


Fig. 17 Side view of experimental setup in the Free Surface Water Tunnel (FSWT).

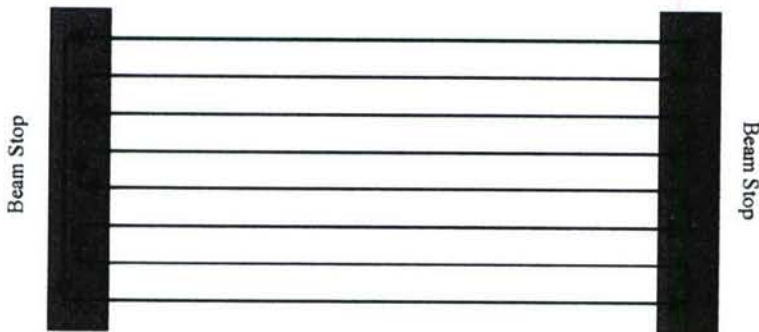


Fig. 18 X-Z laser scan pattern (only 8 sweeps/volume shown).

The scanner takes 5.2 ms to sweep across the field of view and 5.2 ms to step to the next Z-axis (depth) position. During the time the beam is moving to the next Z-axis position, the beam is blocked by the beam stop, and the previously exposed image is read out of the camera. The scanner makes 32 sweeps across the field of view before returning to the start of the volume. The total time to sweep the volume is 333 ms (3 volume sweeps/s).

### 3.3. KFS CCD camera system

The KFS CCD camera system was designed in-house for high-speed low-noise image acquisition. The KFS CCD image sensor was designed by Mark Wadsworth of JPL and has a resolution of  $1024 \times 1024$  pix<sup>2</sup>,  $12 \times 12$   $\mu\text{m}$  pixel size, 32 output channels, and a noise figure of  $\sim 26$  e<sup>-</sup>/pix at 200 fps (frames per second) at room temperature. The readout noise of a CCD is proportional to the square root of the readout rate, so a CCD with 32 output channels improves the noise figure by a factor of 4, compared with a CCD, for example, with 2 output channels.

The camera head data acquisition is performed by eight 4-channel A/D converter boards housed in a VXI enclosure along with camera head power and timing/control boards (Fig. 19). Each A/D converter board has 4 input signal-conditioning stages, 4 12-bit 40 MHz A/D converters, and 512 MB (megabytes) of RAM. The input signal-conditioning stages incorporate

programmable high- and low-pass filters, Correlated Double Sampling (CDS), and programmable gain and offset to optimize dynamic range and signal-to-noise ratio. The outputs of the A/D converters are compressed in real-time using a lossless compression algorithm and stored in the local (on-board) RAM. The A/D converter boards also provide a high-speed S-Link fiber-optic output. The S-Link is a low-overhead fiber-optic link developed by CERN with a maximum transfer rate of 160 MB/s, or a total of 1.28 GB/s ( $1.28 \times 10^9$  bytes/s), for 8 channels.

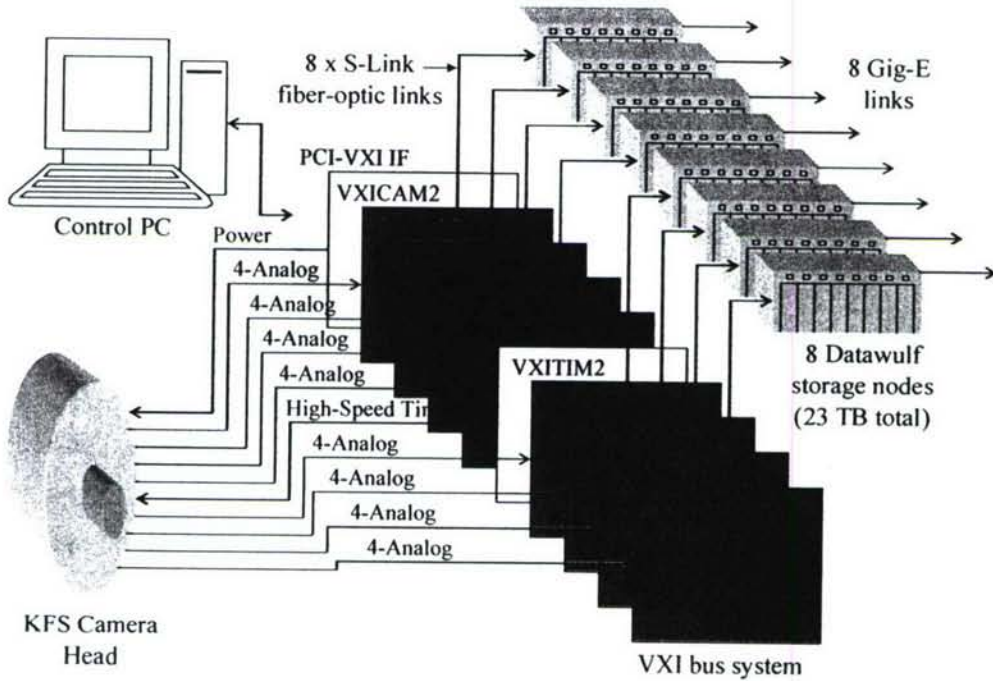


Fig. 19 KFS camera head, VXI bus system, control PC, and Datawulf storage nodes.

In order to increase the maximum number of contiguous frames beyond the 4000 to 8000 frame limit of the A/D converter board memories, a high-speed Datawulf disk array storage subsystem was developed. The Datawulf subsystem contains 8 storage nodes with 2.9 TB/node (terabytes/node) for a total of 23 TB of high-speed data storage. The incoming data are double-buffered in the local memory on the A/D converter boards before being sent over the S-Links to the Datawulf storage nodes. A sustained lossless, error-free, transfer rate of 200 fps (frames per second), corresponding to 328 MB/s, was achieved for a total of  $3 \times 10^5$  frames.

### 3.4. 3-D geometry changes

It is necessary to correct for the geometric distortions caused by the divergence of the scanned beam and camera image cone and for the mean fluid flow between sweeps and within a sweep. Snell's law and the small-angle approximation are used to calculate the virtual origins of the camera image acquisition cone and the cone swept by the scanner (in the water) with an error of less than 0.5%. Once the two virtual origins are known, the intersection of the scanned beam with the image cone is computed to obtain the actual field of view (Fig. 20).

For the data displayed below (Run 003), the calculated virtual origins are:

- X-axis scanner virtual origin,  $L_{sx} = 82.0$  cm,
- Z-axis scanner virtual origin,  $L_{sz} = 80.9$  cm, and

- Image cone virtual origin,  $L_{im} = 118.0$  cm.

At  $Y = 0$ , the scanned beam sweeps a total of 24 cm along the  $x$ -axis and 11.5 cm along the  $z$ -axis (span). Note that the  $x$ -axis scanner virtual origin and sweep size has no direct bearing on the image field of view as this is defined by the camera image cone. The field of view calculated from the CCD size and lens focal length is 21.87 cm, in good agreement with the measured field of view using a ruler placed in the water of 21.9 cm.

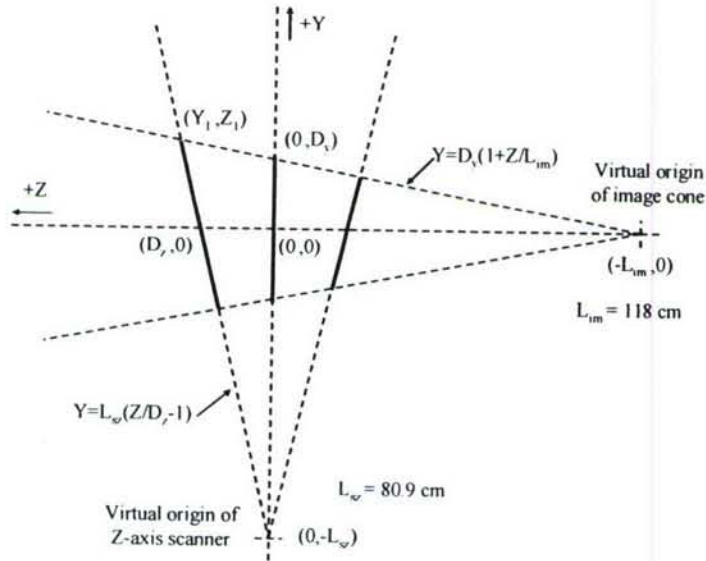


Fig. 20 Calculation of scanned volume (individual sweeps shown with solid lines).

### 3.5. 3-D rendering

After the geometric corrections indicated above, the data were visualized interactively using standard volume-rendering hardware. The camera head control computer, as well six nodes of a volume-rendering cluster, was equipped with TeraRecon's 1 GB VolumePro 1000 volume-rendering cards. The VolumePro cards can process  $1024 \times 1024 \times 1024$  volumetric data sets efficiently, at over 8 fps. The camera head control computer was used for dynamic inspection of individual frames, while the cluster was used as a rendering farm to create movies of stored experiments. The farm can render 1000 frames of a  $1024 \times 1024 \times 1024$  8-bit volume set, with subsets of the data stored at each node, in less than 30 min.

The scans produced a sequence of  $1024 \times 1024 \times 32$  volumes, with 16-bit values per voxel. Each frame was calibrated to reduce the fixed pattern noise and normalize per-pixel intensity values. Multiple dark frames were acquired at the beginning and end of each run, and averaged to obtain  $\langle F_{dark} \rangle$ . Full-field frames were acquired using a LED calibrator that illuminates the CCD image sensor (nearly uniformly) and then averaged to obtain  $\langle F_{full} \rangle$ . A pixel-by-pixel image correction was performed using  $F_{cal} = (F_{uncal} - \langle F_{dark} \rangle) / (\langle F_{full} \rangle - \langle F_{dark} \rangle)$ . Geometrical corrections were applied next, as described above.

Applying the geometrical corrections to the voxel coordinates to obtain the spatial coordinates produces a skewed frustum. For visualization purposes, however, it is best to have a uniformly spaced rectangular grid. This can be achieved by resampling the geometrically corrected data on a uniform rectangular grid.

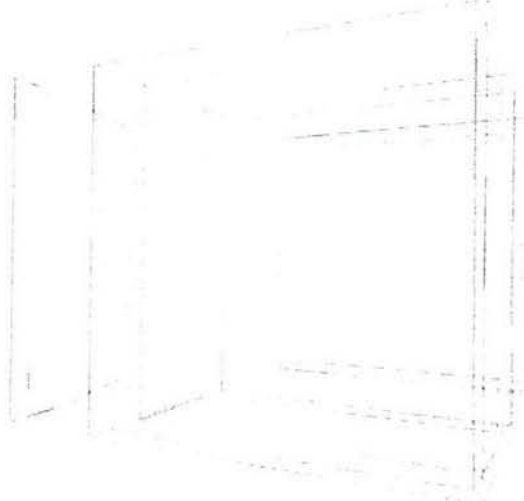


Fig. 21 Inscribed (orange) and enveloped (blue) rectangular grids.

The green outline in Fig. 21 marks the scanned volume after applying the geometrical corrections. To obtain a uniformly spaced rectangular grid, one can re-sample either the inscribed volume (orange outline) or the enveloped volume (blue outline). Since the choice of the sampling volume placed the part of the scalar field of interest in the center region, the inscribed volume was chosen. The computed inscribed volume is  $\Delta x = 20.0$  cm,  $\Delta y = 20.8$  cm, and  $\Delta z = 9.9$  cm.

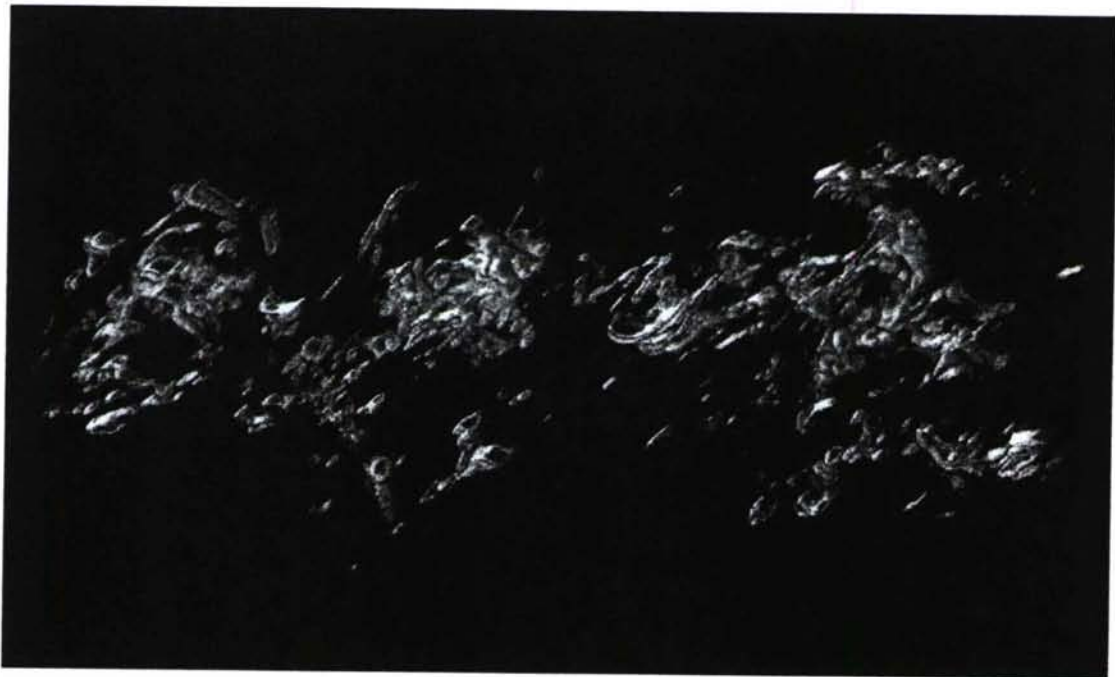


Fig. 22 Reconstructed and shaded 3-D image for Run 003.  $U = 5.22$  cm/s. The center of the field of view is located 65.3 cm downstream of the turbulence-generating grid where the dye filament is released.

Rather than translating the original volume and then re-sampling it to produce uniformly sampled data in the inscribed volume, the desired vertex was calculated for the voxels of the

inscribed volume. A reverse transform of the coordinate system into the distorted volume space was then performed, with a linear interpolation of the resulting values. Better sampling for movie generation was made possible by re-sampling the volume on a  $512 \times 512 \times 128$  rectangular grid. A reconstructed and shaded 3-D image of the three-dimensional scalar field is shown in Fig. 22.

### 3.6. Future work

Work is underway to document these results and develop a new facility that will allow the study of dispersion for a longer time period and at higher Reynolds numbers. The frame rate will be increased from 100 fps to 200 fps, allowing a doubling in z-axis resolution and, perhaps, more, depending on the flow. Finally, a rectangular swept volume will be employed that will greatly simplify geometrical corrections.

## 4. Conclusions

Research performed during the three-year period of this grant has relied on experimental work, augmented and sometimes led by numerical simulation work, as well as significant instrumentation and data-acquisition developments. The research was responsible for significant progress in the understanding of (molecular) mixing in high-speed flows in complicated geometries relevant to scramjet combustors and propulsion. A series of publications are in progress. Hydrocarbon combustion and flameholding requirements for such flows have led to investigations to improve predictions of hydrocarbon flames as part of this work through close comparisons of detailed experiments and detailed predictions in stagnation-flame environments that replicate the fundamental effects influencing flame stability and extinction. Finally, an investigation that probes the three-dimensional structure of scalar dispersion has begun, with a focus on grid turbulence that already has yielded new information with relevance to non-premixed combustion and other applications of turbulent mixing, such as the dispersion of pollutants.

## References

BERGTHORSON, J.M. and P.E. DIMOTAKIS 2006a Particle velocimetry in high-gradient/-curvature flows. *Exp. Fluids* 41:255-263

BERGTHORSON, J.M. and P.E. DIMOTAKIS 2006b Premixed laminar C1-C2 stagnation flames: experiments and simulations with detailed thermochemistry models. *Proc. Combustion Institute* 31:1139-1147

BERGTHORSON, J.M., D.G GOODWIN, and P.E. DIMOTAKIS 2005a Particle streak velocimetry and CH laser induced fluorescence diagnostics in strained, premixed, methane-air flames. *Proc. Combustion Institute* 30:1637-1644

BERGTHORSON J.M., M.B. JOHNSON, A.M. BONANOS, AND P.E. DIMOTAKIS 2007 Measurements of molecular mixing in an expansion-ramp combustor. 21<sup>st</sup> ICDERS Conference (Poitiers, France).

BERGTHORSON, J.M., K. SONE, T.W. MATTNER, P.E. DIMOTAKIS, D.G GOODWIN, and D.I. MEIRON 2005b Impinging laminar jets at moderate Reynolds numbers and separation distances. *Phys. Rev. E* 72:066307

DIMOTAKIS, P.E. 2001 Laboratory and computer experiments on turbulent mixing. 14<sup>th</sup> Australasian Fluid Mechanics Conference.

JOHNSON, M.B. 2005 *Aerodynamic control and mixing with ramp injection*. Aeronautical Engineer's thesis, California Institute of Technology.

KERN, B., P.E. DIMOTAKIS, D.B LANG, C. MARTIN, R. THESSIN 2003 Aberrating Medium Characterization and Image Reconstruction with a Quadrature-Phase Interferometer. *AIAA 34<sup>th</sup> Plasmadynamics and Lasers Conference*, AIAA Paper 2001-2797.

KERN, B., D.B. LANG, C. MARTIN, P.E. DIMOTAKIS, AND M. WADSWORTH 2001 A high-speed quadrature-phase rotation-shearing interferometer for imaging through turbulence. AIAA Paper 2001-2797.

LANG, D.B., S. LOMBEYDA, J. LINDHEIM, P.E. DIMOTAKIS 2006 Laser Scanning of Three-Dimensional Time-Varying Fluid Phenomena. *ACM Siggraph 2006*. Sketch Submission #0325.

MUNGAL, M.G., P.E. DIMOTAKIS 1984 Mixing and combustion with low heat release in a turbulent shear layer. *J. Fluid Mech.* 148:349-382

PANTANO, C., R. DEITERDING, D.J. HILL, D.I. PULLIN 2007 A low-numerical dissipation patch-based adaptive mesh refinement method for large-eddy simulation of compressible flows. *J. Comp. Phys.* (submitted).

SMITH, G.P., D.M. GOLDEN, M. FRENKLACH, N.W. MORIARTY, B. EITENEER, M. GOLDENBERG, C.T. BOWMAN, R.K. HANSON, S. SONG, W.C. GARDINER, V.V. LISSIANSKI, Z. QIN GRI-Mech 3.0. Available from [http://www.me.berkeley.edu/gri\\_mech/](http://www.me.berkeley.edu/gri_mech/)

## Personnel

### 4.1. Personnel supported by this grant

- Benezech, Laurent, Graduate Research Assistant, Aeronautics.
- Bergthorson, Jeffrey, Graduate Research Assistant, Aeronautics.<sup>1</sup>
- Bonanos, Aristides, Postdoctoral Scholar, Aeronautics.<sup>2</sup>
- Dahl, Earl, (retired) Member of the Technical Staff, Aeronautics (part-time consultant).
- Dimotakis, Paul, John K. Northrop Professor of Aeronautics and Professor of Applied Physics (PI), and (since January 2006) Chief Technologist, Jet Propulsion Laboratory.
- Johnson, Michael, Graduate Research Assistant, Aeronautics.<sup>3</sup>
- Katzenstein, Garrett, Research Engineer, Aeronautics.<sup>4</sup>
- Lang, Daniel, Research Engineer, Aeronautics.
- Matheou, George, Graduate Research Assistant.
- Mojahedi, Christina, Administrative Assistant, Aeronautics.
- Pantano, Carlos, Senior Research Scientist, Aeronautics.<sup>5</sup>
- Sone, Kazuo, Graduate Research Assistant, Aeronautics.
- Valiherdowski, Bahram, Member of the Technical Staff, Aeronautics.

Support for all personnel from this grant is part time.

### 4.2. Other collaborators

- Goodwin, D. G., Professor Mechanical Engineering and Applied Physics, collaborator on direct-numerical simulations of hydrocarbon flames.
- Lombeyda, S., Member of the Technical Staff, Center for Advanced Computing Research, Caltech. Collaborator on 3-D computer visualization.
- Meiron, D. I., Fletcher Jones Professor of Applied and Computational Mathematics, and Computer Science, Caltech. Collaborator, on direct-numerical simulations of 3-D, variable-density flows.
- Shan, J. W., Rutgers U. Continuing collaborator.

### 4.3. Air Force contacts and discussions

Meetings and discussions with people listed below from the Air Force Research Laboratories at Wright Patterson Air Force Base on SCRAMJET technology. Some of these took place in the annual Contractors' Meeting (20-22 June 2005, Indianapolis, IN) and others as part of a hypersonic technology review (15 June – 15 August 2004) led by P. E. Dimotakis.

- Campbell Carter: Discussions on SCRAMJET mixing and the application of Image Correlation Velocimetry to Hydroxyl Tagging Velocimetry (HTV).
- J. Tim Edwards: Discussion on choices for scramjet fuels.

---

<sup>1</sup> Through June 2005, Postdoctoral Scholar; June 2005 – June 2006. Presently, Assistant Professor, McGill University.

<sup>2</sup> Beginning September 2006.

<sup>3</sup> Through May 2004.

<sup>4</sup> Through May 2005.

<sup>5</sup> Through October 2006.

[This page intentionally left blank.]

**Appendix: Principal Investigator Annual Data Collection (PIADC) Survey Form****PI DATA**

Name (Last, First, MI):\_ Dimotakis, Dr. Paul E.  
 Institution California Institute of Technology

**Co-PI DATA**

Name (Last, First, MI):\_ Not applicable  
 Institution --

**NUMBER OF CONTRACT/GRANT CO-INVESTIGATORS**

Faculty 1 Post Doctorates 1 Graduate Students 6 Other 2

**PUBLICATIONS RELATED TO AFOREMENTIONED CONTRACT/GRANT***Physical Review E*

Impinging laminar jets at moderate Reynolds numbers and separation distances.  
 Bergthorson, J.M., Sone, K., Mattner, T.W., Dimotakis, P.E., Goodwin, D.G. and Meiron, D.I.  
 Volume: 72 Pages: 0663071-12 Month: December Year: 2005

*Proceedings of the Combustion Institute* 30

Particle streak velocimetry and CH laser-induced fluorescence diagnostics in strained, premixed, methane-air flames

Bergthorson, J.M., Goodwin, D.G. and Dimotakis, P.E.

Volume: 30 Pages: 1637-1644 Month: January Year: 2005

*IEEE Transactions on Electron Devices*

Charge injection noise in CCDs

Kern, B.

Volume: \_\_\_\_\_ Pages: \_\_\_\_\_ Month: June Year: 2005

*Experiments in Fluids*

Particle velocimetry in high-gradient/-curvature flows

Bergthorson, J.M. and Dimotakis, P. E.

Volume: 41 Pages: 255-263 Month: August Year: 2006

*Physics of Fluids*

Planar shock cylindrical focusing by a perfect-gas lens

Dimotakis, P.E. and Samtaney, R.

Volume: 18 Pages: \_\_\_\_\_ Month: March Year: 2006

*ACM Siggraph*

Laser scanning of three-dimensional time-varying fluid phenomena

Lang, D.B., Lombeyda, S., Lindheim, J. and Dimotakis, P.E.,

Volume: \_\_\_\_ Pages: \_\_\_\_ Month: \_\_\_\_ Year: 2006

*Journal of Fluid Mechanics*

Reynolds-number effects and anisotropy in transverse-jet mixing  
Shan, J.W. and P.E. Dimotakis

Volume: 566 Pages: 47-96 Month: November Year: 2006

*Proceedings of the Combustion Institute* 31

Premixed laminar C1-C2 stagnation flames: experiments and simulations with detailed thermochemistry models

Bergthorson, J. M. and Dimotakis, P. E.

Volume: 31 Pages: 1139-1147 Month: January Year: 2007

In preparation:

*Journal of Computational Physics*

On numerical and physical boundary conditions for high Reynolds number large-eddy simulation of wall bounded turbulent flows

Pantano, C., Pullin, D.I., and Dimotakis, P. E.

Volume: \_\_\_\_ Pages: \_\_\_\_ Month: \_\_\_\_ Year: \_\_\_\_

*AIAA Journal*

Aerodynamic control and mixing with expansion-ramp injectin: Subsonic and transonic flow

Bergthorson, J.M., Johnson, M.B., Bonanos, A.M., Slessor, M., Su, W.J., and Dimotakis, P. E.

Volume: \_\_\_\_ Pages: \_\_\_\_ Month: \_\_\_\_ Year: \_\_\_\_

*Journal of Computational Physics*

Verification of fluid dynamics solvers using correlations with linear stability results

Matheou, G., Pantano, C., and Dimotakis, P. E.

Volume: \_\_\_\_ Pages: \_\_\_\_ Month: \_\_\_\_ Year: \_\_\_\_

Other:

*California Institute of Technology – Engineer's Thesis*

Johnson, M.B. (2005)

Aerodynamic control and mixing with ramp injection

<http://resolver.caltech.edu/CaltechETD:etd-05262005-112117>

*California Institute of Technology – Ph.D. Thesis*

Bergthorson, J.M. (2005)

Experiments and modeling of impinging jets and premixed hydrocarbon stagnation flames

<http://resolver.caltech.edu/CaltechETD:etd-05242005-165713>

**HONORS/AWARDS/APPOINTMENTS DURING CONTRACT/GRANT LIFETIME**

Includes, "all honors and awards received during the lifetime of the contract or grant, and any life achievement honors such as (Nobel prize, honorary doctorates, and society fellowships) prior to this contract or grant."

Honor/Award: William F. Ballhaus Prize \_\_\_\_\_ Year received: 2005

Honor/Award Recipient(s): Bergthorson, Jeffrey M.

Awarding Organization: Graduate Aeronautical Laboratories, California Institute of Technology

Honor/Award: Michelson Fellowship \_\_\_\_\_ Year received: 2002

Honor/Award Recipient(s): Kern, Brian

Awarding Organization: Jet Propulsion Laboratory, California Institute of Technology

Honor/Award: John K. Northrop Chair in Aeronautics \_\_\_\_\_ Year received: 1995

Honor/Award Recipient(s): Dimotakis, Paul E.

Awarding Organization: California Institute of Technology

Honor/Award: Associate Fellow \_\_\_\_\_ Year received: 1989

Honor/Award Recipient(s): Dimotakis, Paul E.

Awarding Organization: American Institute of Aeronautics & Astronautics

Honor/Award: Fellow \_\_\_\_\_ Year received: 1980

Honor/Award Recipient(s): Dimotakis, Paul E.

Awarding Organization: American Physical Society

**Published papers documenting the work performed.**

# Impinging laminar jets at moderate Reynolds numbers and separation distances

Jeffrey M. Bergthorson,\* Kazuo Sone, Trent W. Mattner, Paul E. Dimotakis, David G. Goodwin, and Dan I. Meiron  
*California Institute of Technology, Pasadena, California 91125, USA*  
 (Received 7 June 2005; published 14 December 2005)

An experimental and numerical study of impinging, incompressible, axisymmetric, laminar jets is described, where the jet axis of symmetry is aligned normal to the wall. Particle streak velocimetry (PSV) is used to measure axial velocities along the centerline of the flow field. The jet-nozzle pressure drop is measured simultaneously and determines the Bernoulli velocity. The flow field is simulated numerically by an axisymmetric Navier-Stokes spectral-element code, an axisymmetric potential-flow model, and an axisymmetric one-dimensional stream-function approximation. The axisymmetric viscous and potential-flow simulations include the nozzle in the solution domain, allowing nozzle-wall proximity effects to be investigated. Scaling the centerline axial velocity by the Bernoulli velocity collapses the experimental velocity profiles onto a single curve that is independent of the nozzle-to-plate separation distance. Axisymmetric direct numerical simulations yield good agreement with experiment and confirm the velocity profile scaling. Potential-flow simulations reproduce the collapse of the data; however, viscous effects result in disagreement with experiment. Axisymmetric one-dimensional stream-function simulations can predict the flow in the stagnation region if the boundary conditions are correctly specified. The scaled axial velocity profiles are well characterized by an error function with one Reynolds-number-dependent parameter. Rescaling the wall-normal distance by the boundary-layer displacement-thickness-corrected diameter yields a collapse of the data onto a single curve that is independent of the Reynolds number. These scalings allow the specification of an analytical expression for the velocity profile of an impinging laminar jet over the Reynolds number range investigated of  $200 \leq Re \leq 1400$ .

DOI: 10.1103/PhysRevE.72.066307

PACS number(s): 47.15.-x

## I. INTRODUCTION

Axisymmetric jets impinging perpendicularly on a wall are encountered in a variety of contexts, from large-scale applications of fully developed turbulent jets impinging on the ground, as in VTOL aircraft [1], to the small-scale use of laminar jets to determine the shear strength of vascular tissue in the study of atherosclerosis [2]. Impinging jets are also used in chemical vapor deposition (CVD) processes [3,4] and in the study of laminar flames [5–9]. Work has also been done on opposed-jet stagnation flow, a configuration widely used in combustion experiments [10–13]. Definitive experimental data for laminar impinging jets in the nozzle-to-plate separation distance  $L$  to nozzle diameter  $d$  ratio (see Fig. 1) range of  $0.5 \leq L/d \leq 1.5$  are not widely available. This range of  $L/d$  is useful in the study of strain-stabilized flames in combustion research. Available data in this range do not include detailed axial velocity profile measurements along the flow centerline, except for the study of Mendes-Lopes [7]. Such measurements are important in assessing one-dimensional flame models. This work focuses on the hydrodynamics of nonreacting impinging-jet flow, as a basis for related studies of strained flames [8,9].

Flow velocities in impinging jets have been measured by various means, such as laser-Doppler velocimetry (LDV) [12] or particle image velocimetry (PIV) [14]. In this study, particle streak velocimetry (PSV) [8,9,15], a technique similar to particle tracking velocimetry (PTV) [16], is used to

obtain instantaneous flow-field measurements and, in particular, axial velocities along the flow centerline. A new PSV methodology has been implemented in this work that includes digital imaging, image processing, and new analysis techniques [8,9]. These improvements allow quantitative velocity data to be obtained throughout the flow field with PSV, without excessive post-processing. This allows PSV to achieve accuracies that compete favorably with LDV or PIV, while providing advantages such as low-particle-mass loading, easy discrimination against agglomerated particles that may not track the flow, short-run-time experiments, and re-

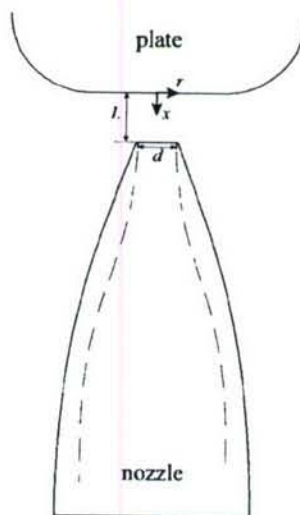


FIG. 1. Experimental geometry.

\*Electronic address: jeffb@tyrvos.caltech.edu

liable velocity measurement from Lagrangian particle trajectories. The static (Bernoulli) pressure drop across the nozzle contraction is measured concurrently, providing measurement redundancy and a valuable independent parameter, as will be discussed below.

Impinging-jet flows have been described analytically, or simulated numerically, using different formulations and techniques. Schlichting [17] presents a one-dimensional axisymmetric model for an infinite-diameter jet impinging on a plate, which has been used in flame studies [5,7]. This model was extended to allow both the velocity and velocity gradient to be specified at some distance from the stagnation plate [10,18], providing a flexible boundary condition for finite-nozzle-diameter impinging-jet flows. Two-dimensional, steady, axisymmetric calculations of viscous [2] and inviscid [1,19–21] impinging-jet flow have also been performed. Except for the work of Strand [21], these calculations do not include nozzle-to-wall proximity effects.

In this work, the flow is modeled with varying levels of complexity: by means of an axisymmetric unsteady Navier-Stokes simulation, an axisymmetric potential-flow formulation, and a one-dimensional stream-function model. The first method is a spectral-element scheme [22,23] that solves the incompressible axisymmetric Navier-Stokes equations. The unsteady spectral-element method is robust and time and space accurate. The second method is a finite-difference potential-flow solution based on the classical ideal-jet approach [24,25]. The potential- and viscous-flow calculations presented here capture wall-proximity effects by including parts of the nozzle and plenum assembly in the computational domain. The one-dimensional model relies on a stream-function formulation that is used in CVD studies [3,4] and by the combustion community [5–10,18].

The experimental results are used to evaluate the accuracy of the different simulation methodologies. Additionally, new scaling parameters and empirical properties of the centerline axial velocity field are discussed. The new scaling allows the identification of an analytical expression for the axial velocity profile of a laminar impinging jet for Reynolds numbers in the range investigated of  $200 \leq Re \leq 1400$ .

## II. EXPERIMENTS

In the experiments documented here, a room-temperature jet was generated in atmospheric pressure air from a contoured nozzle with an internal (nozzle-exit) diameter of  $d = 9.9$  mm. The nozzle interior was designed by optimizing the inner radius profile  $r(x)$  through the contraction section, expressed in terms of a seventh-degree polynomial, to minimize the exit boundary-layer displacement thickness and avoid the formation of Taylor-Görtler vortices in the concave section (see Fig. 1 and [9]). The nozzle exterior was designed with attention to the upstream entrainment-induced flow and to avoid flow separation and unsteadiness (see Fig. 1 and [9]). The air mass flux was controlled using a sonic metering valve. The flow was seeded with particles, using a seeder developed in-house, before entering the jet plenum, where screen and honeycomb sections were used for flow uniformity and turbulence management. The nozzle-plenum sys-

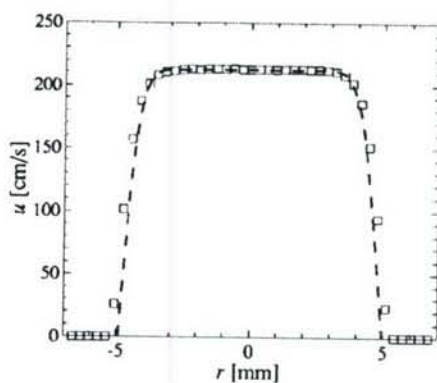


FIG. 2. Nozzle-exit velocity profile ( $d=9.9$  mm,  $Re_j=1400$ ): (□) experimental data, (dashed line) viscous-simulation results. Pitot-probe internal opening is  $d_{\text{pitot}} \approx 0.4$  mm.

tem produced a uniform velocity profile in a free-jet configuration. The jet-exit velocity profile was measured with a flattened pitot probe ( $d_{\text{pitot}} \approx 0.4$  mm in the radial direction) and an electronic-capacitance manometer (BOC Edwards W57401100) with a temperature-stabilized 1-torr differential-pressure transducer (BOC Edwards W57011419). Figure 2 compares the nozzle-exit velocity profile with the profile obtained from the two-dimensional viscous simulation, at a Reynolds number  $Re_j = \rho d U_j / \mu \approx 1400$ , where  $U_j$  is the centerline velocity at the jet exit,  $\rho$  is the density, and  $\mu$  is the viscosity. The profile is uniform, with less than 1% variation outside the wall boundary layers ( $r/R \leq 0.6$ ,  $R=d/2$ ). The slight disagreement between simulation and experiment in the wall boundary layer region is attributable to the finite pitot-probe extent in the radial direction  $d_{\text{pitot}}$ , for which no corrections were applied.

The jet was aligned normal to a solid wall (stagnation plate assembly), at separation-distance to nozzle-diameter ratios of  $L/d=0.7$ , 1.0, and 1.4. Significant changes in flow characteristics are observed over this  $L/d$  range. The stagnation plate was a circular, copper block, 7.62 cm (3 in.) in diameter and 5.08 cm (2 in.) thick, with a 2.03-cm (0.8-in.) bottom-edge radius. A bottom-edge radius was introduced to mitigate upstream effects of flow-separation and edge-flow unsteadiness in the stagnation-flow region (see Fig. 1).

PSV is well suited as a velocity-field diagnostic for this flow. In this axisymmetric, steady flow, the axial velocity component can be reliably measured on the centerline. Particle paths do not cross or overlap, and out-of-plane particle displacements are small and easily discernible when they occur (in-focus and out-of-focus streaks). The high sensitivity of the scattering cross section to particle size, in the size range employed, allows easy identification of agglomerates that may not track the high-spatial-gradient regions in the flow. Streaks used for PSV processing were from in-plane, nonagglomerated particles. A single image frame can capture the entire velocity field, allowing PSV to be implemented in short-run-time experiments. A sample image of a cold-jet flow with particle streaks is reproduced in Fig. 3, for a nozzle-to-plate separation distance to nozzle-diameter ratio of  $L/d=1.0$ . In this flow, the jet-nozzle centerline velocity is  $U_j=106$  cm/s, yielding a Reynolds number  $Re_j \approx 700$ . The

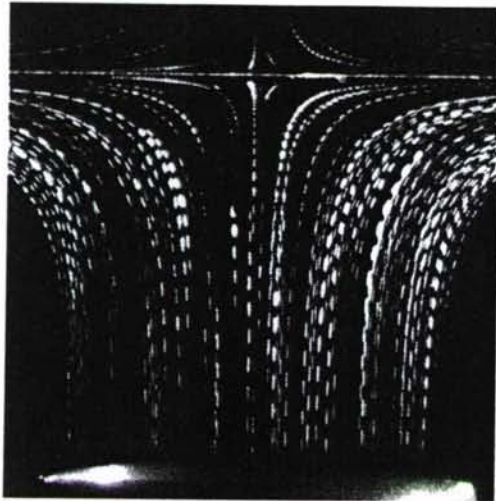


FIG. 3. Impinging-jet flow ( $Re_j=700$ ,  $U_j=106$  cm/s,  $L/d=1.0$ ). Stagnation plate and nozzle exit are visible. The nozzle-exit diameter is  $d=0.99$  cm. The image width corresponds to  $\approx 1.2$  cm.

top and bottom portions of the laser sheet are masked to minimize scattering from the solid plate and nozzle surfaces.

In a variable-velocity field, particles will follow the flow if the dimensionless product of the local strain rate  $\sigma = d\mathbf{u}/d\mathbf{x}$  and the Stokes time  $\tau_S$  is small—i.e., if,

$$\sigma\tau_S \equiv \sigma \frac{\rho_p d_p^2}{18\mu} \ll 1. \quad (1)$$

Measurements relied on alumina particles ( $\text{Al}_2\text{O}_3$ ; median size,  $d_p \approx 0.8$   $\mu\text{m}$ ,  $\rho_p \approx 3830$  kg/m $^3$ ; Baikowski Malakoff, RC-SPT DBM). At the maximum strain rates encountered in these experiments,  $\sigma\tau_S \approx 3 \times 10^{-3}$ .

A Coherent I-90 Ar-ion (CW) laser, operated at 2–3 W, was the illumination source. Two cylindrical lenses generated a thin laser sheet ( $\approx 500$   $\mu\text{m}$ ) in the field of view. An Oriel chopper system (model 75155), with a 50% duty-cycle wheel, modulated the laser beam. The chopper was placed at a horizontal waist in the laser beam to minimize chopping (on-off and off-on transition) times. Chopping frequencies were in the range  $0.5$  kHz  $\leq \nu_c \leq 2.4$  kHz, with  $\nu_c$  optimized depending on flow velocity, in each case.

Image data were recorded with the in-house-developed “Cassini” and “KFS” digital-imaging systems (see [9]). They are based on low-noise,  $1024^2$ -pixel charge-coupled devices (CCDs), on a  $12\text{-}\mu\text{m}$  pitch. The Cassini camera is based on a CCD developed for the NASA Cassini mission. The KFS CCD was designed by M. Wadsworth and S. A. Collins of JPL. The camera heads and data-acquisition systems were designed and built by D. Lang at Caltech. Output for both is digitized to 12 bits/pixel. Magnification ratios were in the range of 1:1–1:1.5, using a Nikon 105-mm,  $f/2.8$  macro lens. Exposure times were varied for optimum particle-streak density in the images, with framing rates for these experiments in the range of 8–10 fps.

Small-particle streaks approximate Lagrangian trajectories of the flow (see Fig. 3). Local velocities  $u(x)$  are esti-

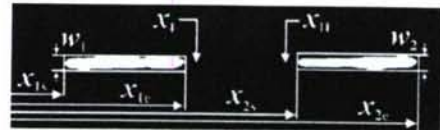


FIG. 4. PSV measurement implementation. The image width corresponds to  $\approx 1$  mm.

mated from streak pairs as  $u(x) \equiv \Delta X(x)/\Delta t$ , yielding  $u_1 = L_1/\tau_c$  and  $u_{11} = L_{11}/\tau_c$ , where  $\tau_c = 1/\nu_c$  (reciprocal of chopper frequency) and  $L_1 = x_{2s} - x_{1s}$  and  $L_{11} = x_{2e} - x_{1e}$  are the distances from the start or end of one streak to the start or end of the next, respectively (see Fig. 4). The velocity estimate  $u_1$  is located at  $x_1 = (x_{1s} + x_{2s})/2 + (w_1 + w_2)/4$ , where  $x_{is}$  is the spatial location of the start of the  $i$ th streak and  $w_i$  is the width of the  $i$ th streak (see Fig. 4). Similarly,  $u_{11}$  is located at  $x_{11} = (x_{1e} + x_{2e})/2 - (w_1 + w_2)/4$ , where  $x_{ie}$  is the location of the end of the  $i$ th streak. Using the same intensity threshold on a streak pair removes systematic errors in applying the Lagrangian time interval  $\tau_c$ . This methodology produces good agreement between velocity values derived from each streak pair. Streak lengths are estimated using bicubic fits on the two-dimensional streak-intensity image data, sampled to a 0.1-pixel resolution in both dimensions. An intensity threshold of approximately 0.4 of the maximum intensity of each streak is used to determine streak dimensions to this sampling resolution. The results are not sensitive to this choice and yield an overall PSV error of  $<0.01U_B$ .

The (Bernoulli) pressure difference between the jet plenum interior, at the straight section upstream of any contraction-section curvature, and the static pressure close to, but outside the jet-core flow region, was measured with an electronic-capacitance manometer (BOC Edwards W57401100) and a temperature-stabilized, 1-torr full-scale, differential-pressure transducer (BOC Edwards W57011419). Bernoulli and mass-flow data were acquired using the National Instruments LabView hardware-software environment, synchronized to the digital-image acquisition to provide independent concurrent estimates of jet-exit velocity for every image. The Bernoulli velocity

$$U_B = \sqrt{\frac{2\Delta p/\rho}{1 - (d/d_p)^4}} \quad (2)$$

was then calculated, where  $\Delta p$  is the static pressure drop across the nozzle,  $\rho$  is the density of the jet fluid (air),  $d$  is the diameter of the nozzle exit, and  $d_p$  is the plenum diameter. At the flow velocities in this study, Bernoulli pressure differences were in the range of 0.1–3 Pa. At the lowest speeds investigated, an error of  $<0.01U_B$  required an absolute measurement accuracy for the Bernoulli pressure drop of  $\delta(\Delta p) \leq 2 \times 10^{-3}$  Pa =  $2 \times 10^{-8}$  bar. This accuracy is achievable with the differential-pressure transducer employed if instrumental drifts and offsets are monitored. The Bernoulli pressure drop cannot be used to determine the jet-exit velocity for  $L/d \leq 1$  because streamline curvature in the nozzle-exit plane produces a velocity deficit at the centerline [11]. However, the Bernoulli pressure drop is an important parameter for this flow, as discussed below. Mass flow rate was

also measured concurrently (Omega FMA872-V-Air), providing an independent velocity estimate.

### III. NUMERICAL SIMULATIONS

In this study, three different numerical simulations were performed at varying levels of complexity. The first is an axisymmetric viscous Navier-Stokes simulation, the second is a potential-flow calculation, and the third is a one-dimensional stream-function formulation.

#### A. Axisymmetric Navier-Stokes formulation

The first numerical study relies on a spectral-element method [26] in an axisymmetric domain. The simulation code was developed by the authors and integrates the axisymmetric Navier-Stokes equations, with boundary conditions specified to capture this flow. Only a limited number of studies have employed the spectral-element method to study this type of flow. Frouzakis *et al.* [13] utilized the spectral-element method to study the flow field of opposed jets and flames, similar to the impinging-jet flows studied here. In that work, velocity boundary conditions were prescribed at the nozzle-exit locations. In this study, the inclusion of the nozzle interior and exterior allows nozzle-to-wall proximity effects, as well as entrainment, to be investigated.

The spectral-element method is a class of finite-element methods that can handle complex geometries. Additionally, this technique can achieve spectral accuracy by approximating the solution on Gauss-Lobatto-Legendre collocation points within each element. For elements adjacent to the axis, special Gauss-Radau-Legendre collocation points with a quadratic argument are utilized to achieve the appropriate parity for each field [27]. The code integrates a nondimensional form of the unsteady, incompressible, Navier-Stokes equations

$$\nabla \cdot \mathbf{u} = 0. \quad (3a)$$

$$\frac{\partial \mathbf{u}}{\partial t} = \mathbf{N}(\mathbf{u}) + \frac{1}{Re} \mathbf{L}(\mathbf{u}) - \nabla p, \quad (3b)$$

where the nonlinear term  $\mathbf{N}(\mathbf{u}) = -1/2[\mathbf{u} \cdot \nabla \mathbf{u} + \nabla \cdot (\mathbf{u} \mathbf{u})]$  is cast into the skew-symmetric form to reduce aliasing errors. The linear diffusion term is  $\mathbf{L}(\mathbf{u}) = \nabla^2 \mathbf{u}$ .

Figure 5 shows the elements and boundary conditions used for  $L/d = 1.424$ . In the current simulations, 9th- to 15th-order polynomials are used in each element. These choices provide a balance between desired solution accuracy and reasonable computational time. These boundary conditions reasonably model the experimental apparatus used in this study. The unsteady Navier-Stokes equations are integrated in time until the solution attains a steady-state condition, starting with the flow at rest in the domain interior.

A study of the effects of boundary conditions on the flow field was undertaken to ascertain that the near-field solution was insensitive to the particular choices. A nearly flat velocity profile is introduced at the nozzle inlet (Fig. 5),  $u_1(r)/U_p = -\tanh[c_1(1-r/r_p)]$ , where  $r_p = d_p/2$  is the radius of the plenum.  $U_p$  is the centerline velocity at the plenum,

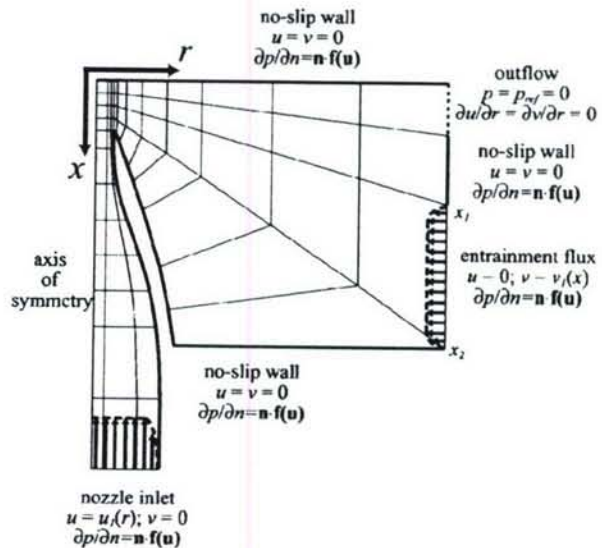


FIG. 5. Axisymmetric Navier-Stokes simulation domain and boundary conditions.  $\mathbf{f}(\mathbf{u}) = \nabla p - \mathbf{N}(\mathbf{u}) + \mathbf{L}(\mathbf{u})/Re$ .  $u_1(r)$  and  $v_1(x)$  are the nozzle and entrainment inlet velocity profiles, respectively.

and  $c_1$  was set to 50. This profile mimics the outflow from the turbulence-management section in the experiments. As expected, the jet profile at the nozzle exit is insensitive to the choice of inlet profile, owing to the high contraction ratio in the nozzle design (see Fig. 1).

To simulate the entrained flow, an entrainment flux  $Q_e$  is introduced through the lower portion of the outer boundary. Over the range  $1/4 \leq Q_e/Q \leq 4$ , where  $Q = 2\pi \int_0^r r u_1(r) dr$  is the mass flux through the nozzle, the maximum difference in the velocity field was  $0.008 U_B$  in the near-field region of interest ( $0 \leq r/d \leq 1$ ,  $0 \leq x/d \leq L/d$ ). For the entrainment flux (bottom right),  $v_1(x)/U_p = -c_2 \tanh[c_3(x-x_1)(x_2-x)/(x_2-x_1)^2]$  is specified (Fig. 5), with  $c_2 = 0.0785$  and  $c_3 = 50$ . These choices yield  $Q_e/Q \approx 1.8$ . A uniform-pressure condition is specified near the wall at the boundary of the domain exhaust, marked "outflow" in Fig. 5.

#### B. Potential-flow formulation

For axisymmetric flow, the continuity equation can be satisfied by expressing the velocity field in terms of a stream function,  $\psi(x, r)$ —i.e.,

$$u = \frac{1}{r} \frac{\partial \psi}{\partial r}, \quad v = -\frac{1}{r} \frac{\partial \psi}{\partial x}. \quad (4)$$

In the absence of swirl, the azimuthal vorticity  $\omega$  is related to the stream function by (e.g., Batchelor [28])

$$-r\omega = \frac{\partial^2 \psi}{\partial x^2} + \frac{\partial^2 \psi}{\partial r^2} - \frac{1}{r} \frac{\partial \psi}{\partial r} = r^2 \frac{dH}{d\psi}. \quad (5)$$

where  $H(\psi)$  is the Bernoulli constant.

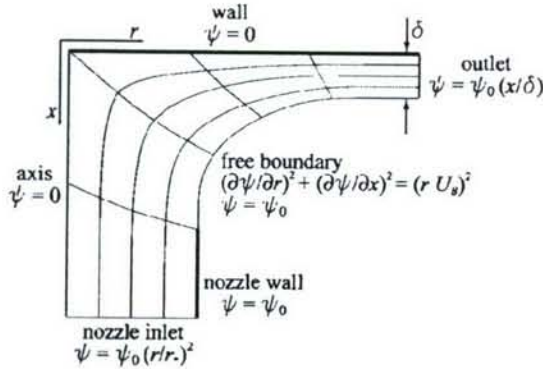


FIG. 6. Potential-flow simulation domain and boundary conditions.

$$H(\psi) \equiv \frac{1}{2}(u^2 + v^2) + \frac{p}{\rho}. \quad (6)$$

One approach to the inviscid impinging-jet problem is to specify an inlet axial velocity profile at some distance from the wall, determine  $H(\psi)$  at that location, and then solve Eq. (5) in a domain bounded by the axis of the jet, the wall, and specified inlet and outlet boundaries [1]. This approach is satisfactory provided the inlet conditions are not affected by the jet impingement.

In this study, we follow the conventional ideal-jet approach [24,25], where the interior flow is irrotational, the shear layers are infinitesimally thick, and the exterior flow is stagnant. Setting the right-hand side of Eq. (5) to zero, the equation for the stream function in the jet interior is then

$$\frac{\partial^2 \psi}{\partial x^2} + \frac{\partial^2 \psi}{\partial r^2} - \frac{1}{r} \frac{\partial \psi}{\partial r} = 0. \quad (7)$$

The surface of the jet is a streamline; hence,  $\psi(x_0, r_0) = \psi_0$ , where  $\psi_0$  is a constant and  $(x_0, r_0)$  are coordinates of any point on the surface of the jet. The location of the jet surface,  $(x_0, r_0)$ , is not known *a priori* and must be determined as part of the solution to satisfy the constant-pressure boundary condition

$$u^2 + v^2 = \frac{1}{r^2} \left[ \left( \frac{\partial \psi}{\partial x} \right)^2 + \left( \frac{\partial \psi}{\partial r} \right)^2 \right] = U_B^2. \quad (8)$$

where  $U_B$  is the Bernoulli velocity. Schach [20] solved this problem using an integral equation approach, assuming the nozzle outflow was not affected by proximity to the wall. Strand [21] used a truncated series solution (up to four terms) to solve for two cases:  $L/d \geq 1$  (ignoring wall-proximity effects) and  $L/d \ll 1$ . This approach, however, omits the transitional regime  $0.5 \leq L/d \leq 1.5$  of interest in this study.

The physical domain and boundary conditions are summarized in Fig. 6. Equation (7) was discretized using second-order centered finite differences on a fixed rectangular computational domain. This domain was mapped to the physical domain by the solution of two elliptic partial differential equations for the physical coordinates  $x$  and  $r$ . These equations were coupled to Eq. (7) through the boundary condition

of Eq. (8). The simultaneous solution of these equations determines the shape of the free constant-pressure boundary. To capture wall-proximity effects, a constant-diameter nozzle is included in the computational domain. Instead of prescribing the nozzle radius, a finite-velocity constraint is applied at the trailing edge of the nozzle. Uniform axial and radial velocity profiles were prescribed at the inlet and outlet of the domain, respectively. The inlet and outlet were positioned about four and eight nozzle radii from the wall stagnation point, respectively.

Second-order accuracy was verified by solving for infinite stagnation-point flow on grids generated from the solution of the impinging-jet problem at resolutions ranging from  $20 \times 80$  to  $80 \times 320$ . The analogous plane-flow impinging-jet problem was also solved and compared to the analytic solution outlined by Birkhoff and Zarantonello [24]. The error in the discharge coefficient was less than 1% with excellent agreement between the numerical and analytic free boundaries. For the axisymmetric impinging-jet problem, convergence studies were conducted at resolutions ranging from  $20 \times 80$  to  $80 \times 320$ . Differences in the centerline axial velocity were less than  $0.01 U_B$ . Sensitivity to the radial extent of the domain was studied by reducing the outlet radius to four nozzle radii. The difference in the centerline axial velocity was, again, less than  $0.01 U_B$ . The gradient of the centerline axial velocity decayed to almost zero at the nozzle inlet, indicating that the inlet was placed sufficiently far from the wall.

### C. Stream-function formulation

The one-dimensional solution for constant-density stagnation flows models the flow in terms of a local stream function  $\psi(x, r) = r^2 U(x)/2$ , which leads to  $u(x) = U(x)$  and  $v(x, r) = -r U'(x)/2$  [see Eq. (4)]. The axisymmetric Navier-Stokes equations can then be expressed in terms of the axial velocity,  $U(x)$ —i.e.,

$$\nu U''' - U U'' + \frac{1}{2} U'^2 = -\frac{2\Lambda}{\rho}, \quad (9)$$

where  $\Lambda$  is termed the radial-pressure eigenvalue of the problem.

$$\Lambda = \frac{1}{r} \frac{\partial p}{\partial r}, \quad (10)$$

which, in this formulation, must be a constant. Appendix A provides further discussion on the spatial variation in  $\Lambda$ . The third-order ordinary differential equation requires three boundary conditions at  $x=0$ . It is common to specify boundary conditions at  $x=0$  and  $x=\ell$  with  $0 < \ell \leq L$  some interior point, by adjusting the curvature boundary condition at  $x=0$  to achieve the desired boundary condition at  $x=\ell$ . A fourth boundary condition can be satisfied by adjusting  $\Lambda$ .

$$U(0) = 0,$$

$$U'(0) = 0,$$

$$U(\ell) = -U_1,$$

$$U'(\ell) = -U'_i, \quad (11)$$

Since  $u(\ell, r) < 0$  (flow is towards the stagnation plate), the negative signs are chosen for convenience to make the constants  $U_i$  and  $U'_i$  positive. Plug-flow boundary conditions—i.e.,  $U'(\ell) = 0$ —at the nozzle exit plane,  $\ell = L$ , are commonly specified with this formulation. The inviscid outer solution to Eq. (9) is a parabola. In the inviscid limit, the flow is irrotational if  $\Lambda = -\rho(U'_i)^2/4$ , for which the solution reduces to potential stagnation flow where the coefficient of the curvature term is identically zero—i.e., linear outer flow,  $U'_i = U_i/\ell$ . For more general boundary conditions, the resulting flow has vorticity, whereas the core of the experimental jet is irrotational. The introduction of vorticity to the flow is necessary to accommodate outer flows with curvature. The equations are solved using the CANTERA software package [4].

#### IV. RESULTS AND DISCUSSION

The experimental velocity data reported here were recorded at three nominal Reynolds numbers

$$Re = \frac{\rho d U_B}{\mu} \equiv 400, 700, \text{ and } 1400, \quad (12)$$

with actual values within  $\pm 35$ , in each case, and at three nozzle-to-stagnation plate separation distance to nozzle-exit-diameter ratios  $L/d \equiv 0.7, 1.0$ , and  $1.4$ . Figure 7 compares measured axial velocities, scaled by the Bernoulli velocity, for the three  $L/d$  ratios at the three Reynolds numbers. The velocity profiles collapse to a single curve, independent of  $L/d$ , if the axial velocity is scaled by the Bernoulli velocity. A centerline axial velocity deficit at the jet exit develops as the separation distance is decreased due to the influence of the stagnation point on the nozzle flow [11]. Notably, the velocity and its gradient adjust to maintain self-similarity, with the Bernoulli velocity scaling the flow.

Figure 8 shows the axisymmetric viscous simulation results at  $Re = 700$  and variable  $L/d$ . The velocity profiles follow a single curve when velocities are scaled by the Bernoulli velocity, consistent with the experimental results. Figure 9 gives pressure contours at  $L/d = 0.5$  and  $1.4$ , with pressures scaled by the Bernoulli pressure. The near-wall pressure field is not significantly altered by changes in the nozzle position. As the separation distance is reduced, the stagnation-point pressure field extends into the nozzle, altering the nozzle flow. Figure 10 compares the experimental data with the axisymmetric viscous calculations at  $L/d = 1.4$  and  $Re = 400, 700$ , and  $1400$ . The inset of Fig. 10 shows the residuals between the simulated,  $u_{sim}$ , and measured,  $u_{PSV}$ , velocities, normalized by the Bernoulli velocity  $U_B$ . The differences between experimental and numerical results for these three cases are less than  $0.015U_B$  root mean squared (rms), indicating that the experimental flow field is adequately modeled. Figure 11 compares particle-streak-image data and streamlines from the axisymmetric viscous simulations. Good qualitative agreement can be seen, even in the entrainment region where the velocities are low ( $< 0.02U_B$ ).

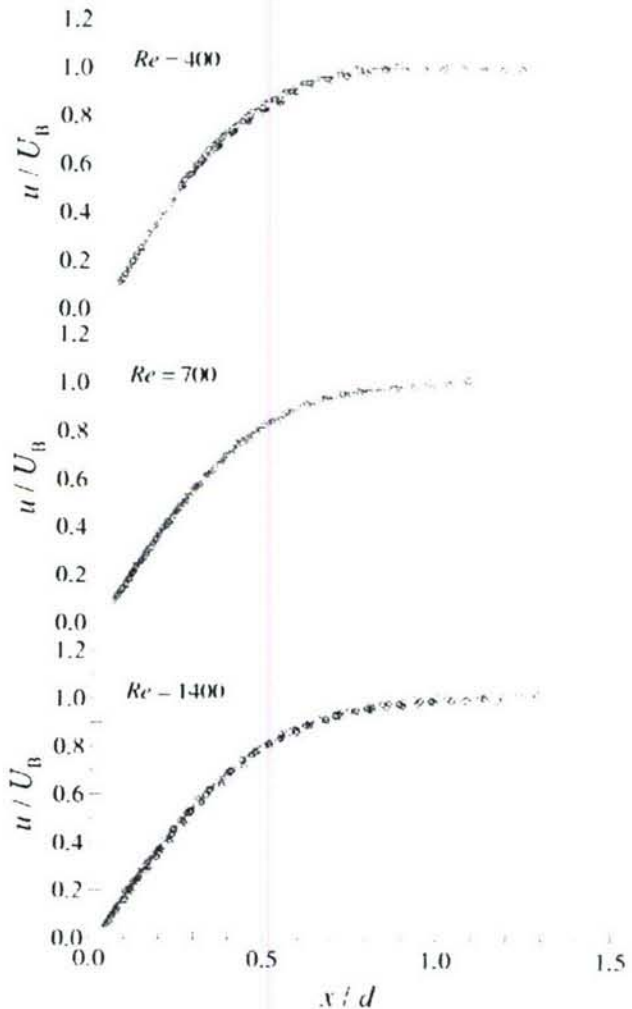


FIG. 7. (Color) Comparison of velocity versus axial distance from plate at three nominal Reynolds numbers. Velocities are scaled by the Bernoulli velocity and axial distances by the nozzle diameter. Experimental results for separation distances of  $L/d = 0.7$  ( $\times$ ),  $L/d = 1.0$  (+), and  $L/d = 1.4$  ( $\circ$ ).

Figure 12 compares the experimental data at the highest Reynolds number to the potential-flow results, with the normalized residuals between simulation and experiment plotted in the inset. Here the axial distance is normalized by the effective diameter  $d_e$ , where  $d_e$  is the nozzle diameter corrected for the nozzle-wall boundary-layer displacement thickness. One of the main effects of the Reynolds number in this flow is the change in the effective jet diameter through the boundary-layer displacement thickness. This effect should be removed before comparing the experiments to the inviscid potential-flow results, which are valid in the limit of infinite Reynolds number. The boundary-layer thicknesses are estimated from axisymmetric, viscous simulations of the nozzle flow. The small disagreement close to the wall is attributable to wall boundary-layer displacement effects. This discrepancy leads to a difference in the maximum centerline axial velocity gradient. As with the experimental results, the axial velocity profiles collapse independent of  $L/d$ .

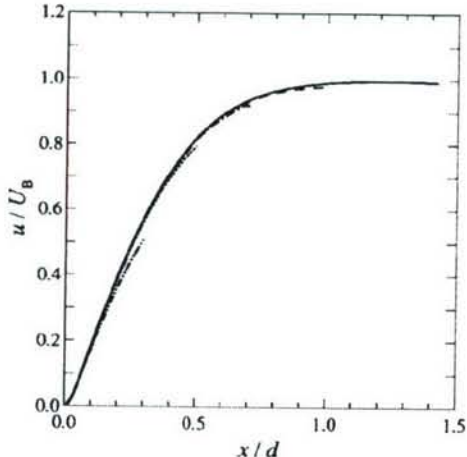


FIG. 8. Scaled velocity versus axial distance from plate. Viscous calculations at  $Re=700$  and  $L/d=0.3$  (dash-double-dotted line), 0.5 (dotted line), 0.7 (dash-dotted line), 1.0 (dashed line), and 1.4 (solid line).

Figure 13 compares the experimental axial velocity data, at  $Re=700$ , to four different one-dimensional simulations, with plug-flow boundary conditions and different choices of the interior boundary location  $\ell$ . Plug-flow boundary conditions capture the flow only for  $\ell/d=0.8$ . This is due to the fact that the outer solution to the one-dimensional equations is a parabola and cannot capture the free-jet behavior (zero-gradient region of flow) that is exhibited for  $x/d>1.0$ . Finite-velocity gradients are evident for  $x/d<0.8$ . The value of  $\ell/d=0.8$  is an intermediate case for which plug-flow boundary conditions capture the flow. The approximations invoked in arriving at the one-dimensional stream-function model are valid in the limit of an infinite-diameter jet impinging on a surface. However, from Fig. 13 it appears that the model should be able to capture the flow in the region  $0\leq x/d<0.8$  if appropriate boundary conditions are speci-

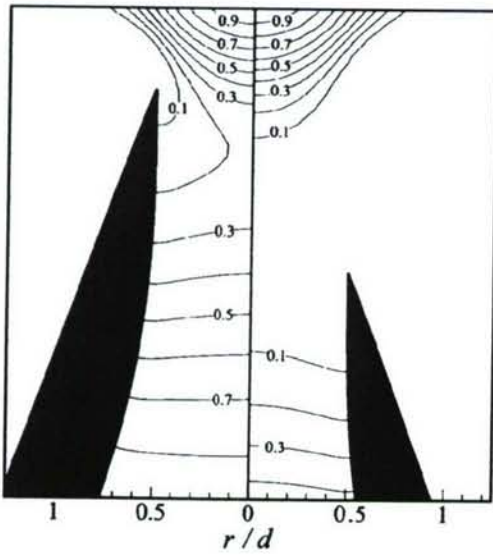


FIG. 9. Pressure contours, normalized by the Bernoulli pressure, at  $L/d=0.5$  (left) and  $L/d=1.4$  (right).

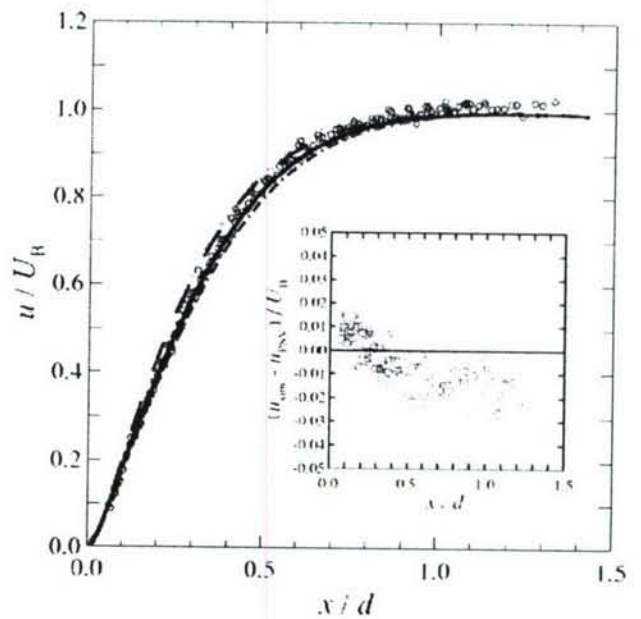


FIG. 10. (Color) Scaled velocity versus axial distance from plate. Viscous calculations (lines) and experimental data (symbols) at  $Re=400$  (dashed line,  $+$ ), 700 (solid line,  $\circ$ ), and 1400 (dash-dotted line,  $\times$ ). The inset shows the residuals between the simulated,  $u_{\text{sim}}$ , and measured,  $u_{\text{PSV}}$ , velocities, normalized by the Bernoulli velocity  $U_B$ . Symbols and colors correspond to the  $Re$  of the main plot.

fied. The velocity and velocity-gradient boundary conditions at a given axial location,  $U(\ell)$  and  $U'(\ell)$ , can be specified from an error-function fit to the experimental data [see Eq. (13)]. The one-dimensional solution calculated using this

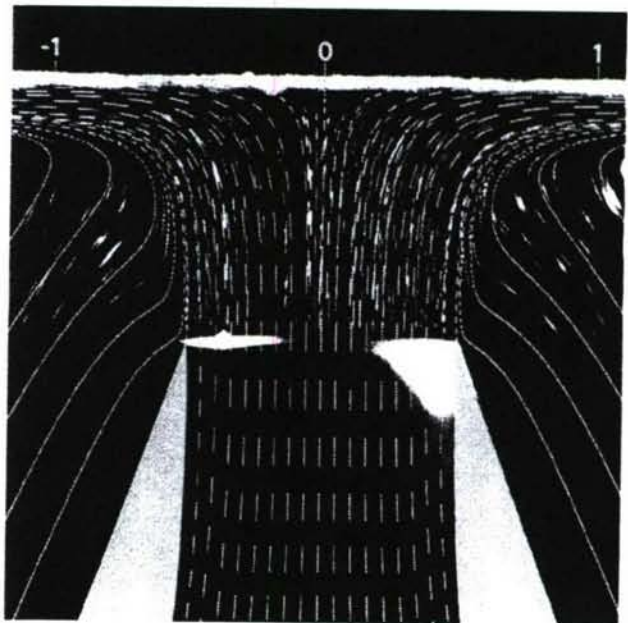


FIG. 11. (Color) Particle streak image (monochrome) detailing entrained flow with superimposed axisymmetric viscous calculation (blue lines) at  $Re=700$  and  $L/d=1.0$ .

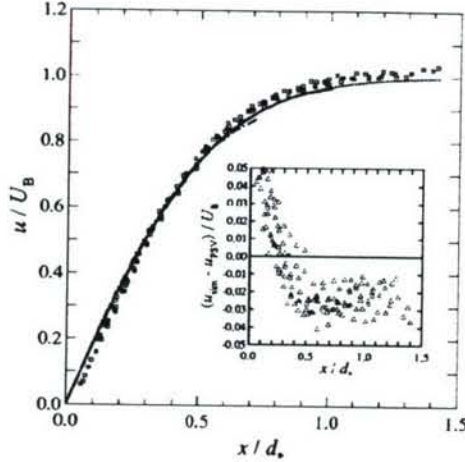


FIG. 12. Scaled velocity versus axial distance from plate normalized by the effective diameter  $d_*$ . Experimental data at  $Re = 1400$  ( $\square$ ) and potential-flow simulations (lines) at  $L/d_* = 0.7$  (dash-dotted line),  $L/d_* = 1.0$  (solid line), and  $L/d_* = 1.4$  (dotted line). The inset shows the residuals between the simulated,  $u_{\text{sim}}$ , and measured,  $u_{\text{PSV}}$ , velocities normalized by the Bernoulli velocity  $U_B$ .

method at  $Re = 700$ , over the range  $0.3 \leq \ell/d \leq 0.7$ , has a maximum error of less than  $0.03U_B$  when compared to axisymmetric viscous simulations. Figure 14 shows the one-dimensional simulation results compared to experimental data at  $Re = 700$ , with boundary conditions taken from the experimental data at  $\ell/d = 0.6$ . The normalized residuals between simulation and experiment are plotted as an inset.

In their study of turbulent jets, Kostiuk *et al.* [12] showed that opposed- or impinging-jet velocity data are well characterized by an error function and used the parameters obtained from the error-function fit to collapse their experimental data. Their error function contained three adjustable parameters: the velocity at infinity  $U_\infty$ , a strain-rate parameter  $\alpha$ , and a wall-offset length  $\delta/d$ .

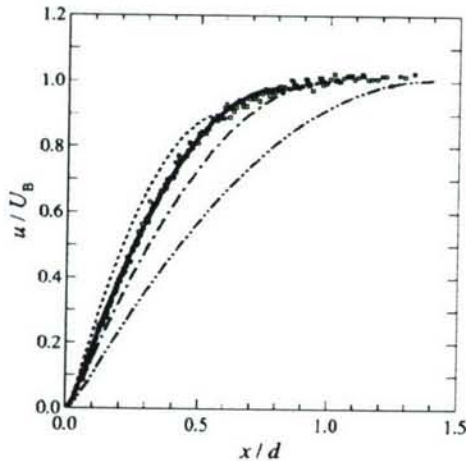


FIG. 13. Comparison of one-dimensional stream-function simulations with plug-flow boundary conditions (lines) to experimental results ( $\square$ ) at  $Re = 700$ , varying  $\ell$ :  $\ell/d = 0.6$  (dashed line),  $\ell/d = 0.8$  (solid line),  $\ell/d = 1.0$  (dash-dotted line), and  $\ell/d = 1.4$  (dash-double-dotted line).

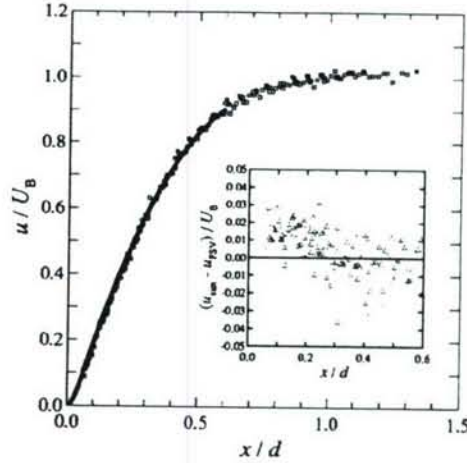


FIG. 14. Comparison of one-dimensional stream-function simulation (line) to experimental data ( $\square$ ) at  $Re = 700$ . Boundary conditions calculated from error-function fit to the data at  $\ell/d = 0.6$ . The inset shows the residuals between the simulated,  $u_{\text{sim}}$ , and measured,  $u_{\text{PSV}}$ , velocities normalized by the Bernoulli velocity  $U_B$ .

$$\frac{u(x)}{U_\infty} = \text{erf} \left[ \alpha \left( \frac{x}{d} - \frac{\delta}{d} \right) \right]. \quad (13)$$

The collapse of the experimental and numerical data discussed above suggests that the appropriate velocity scale for laminar impinging jets is the Bernoulli velocity—i.e.,  $U_\infty = U_B$ . From one-dimensional viscous stagnation-flow theory (see Appendix B), the scaled-offset length  $\delta/d$ , which is proportional to the scaled wall boundary-layer thickness, can be related to the strain-rate parameter  $\alpha$ , such that

$$\frac{\delta}{d}(\text{Re}, \alpha) = 0.755 \sqrt{\frac{1}{\text{Re} \alpha}}. \quad (14)$$

Thus, the only free parameter in this error-function fit to the data is the strain-rate parameter  $\alpha$ , which should be a func-

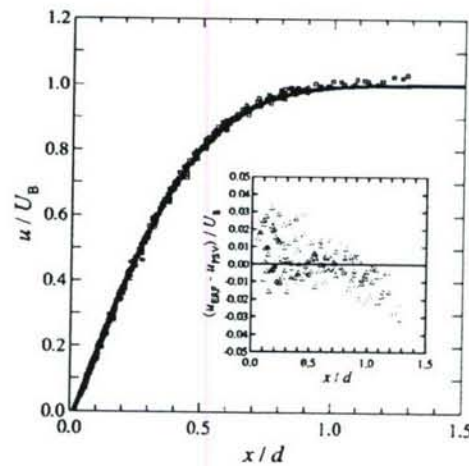


FIG. 15. Comparison of error-function fit (line) to experimental data ( $\square$ ) at  $Re = 1400$ . The inset shows the residuals between the error function,  $u_{\text{ERF}}$ , and measured,  $u_{\text{PSV}}$ , velocities normalized by the Bernoulli velocity  $U_B$ .

TABLE I. Error-function fit parameters and rms error  $\epsilon_{\text{rms}}$  of fits to experimental and viscous-simulation data.

Re	$\alpha$	$\delta/d$	Experiment $\epsilon_{\text{rms}}/U_B$	Simulation $\epsilon_{\text{rms}}/U_B$
400	2.21	0.027	0.017	0.014
700	2.00	0.020	0.010	0.009
1400	1.88	0.015	0.011	0.010

tion of Reynolds number alone—i.e.,  $\alpha = \alpha(\text{Re})$ . Therefore, the axial velocity field for an axisymmetric impinging laminar jet is fully specified by the Bernoulli velocity  $U_B$ , since the Reynolds number is, in turn, derived from it.

The error-function fit to the data at  $\text{Re} = 1400$  is plotted in Fig. 15, with the normalized residuals between the error function and experiment shown in the inset. The error function was fit to each experimental and viscous simulation case by adjusting  $\alpha$  such that the root-mean-squared (rms) error was minimized. For each Reynolds number, the strain-rate parameter  $\alpha$  was averaged over the range  $0.7 \leq L/d \leq 1.4$ . This single  $\alpha(\text{Re})$  dependence was subsequently used in all error-function fits to determine the resulting rms error  $\epsilon_{\text{rms}}$ . The fit parameters and  $\epsilon_{\text{rms}}$  are shown in Table I. The strain-rate parameter is found to scale with Reynolds numbers as  $\alpha = \alpha_0 + C_1/\text{Re}$ , with the constants  $\alpha_0 = 1.775$  and  $C_1 = 153$  determined by fitting the  $\alpha(\text{Re})$  values in Table I.

As previously mentioned, the main Reynolds number effect for this flow is through the nozzle-wall boundary-layer thickness. The effect of the nozzle-exit velocity profile is studied in Fig. 16 for profiles varying from a top-hat shape, representative of the outflow from a high-contraction ratio nozzle, to a parabolic profile, representative of laminar pipe flow. Real nozzle-exit velocity profiles will lie in between these two extremes (see Fig. 2). Intermediate cases are studied by specifying hyperbolic tangent profiles whose coeffi-

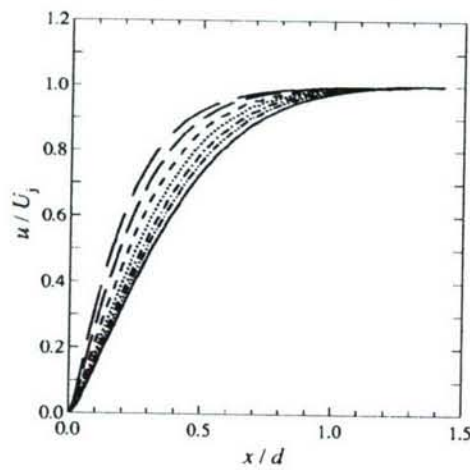


FIG. 16. Simulated velocity profiles at  $\text{Re} = 700$  and  $L/d = 1.4$  for variable nozzle-exit velocity profiles: parabolic ( $d^*/d = 0.71$ , long-dashed line), hyperbolic-tangent profiles with  $d^*/d = 0.76$  (medium-dashed line),  $d^*/d = 0.82$  (dashed line),  $d^*/d = 0.87$  (dotted line),  $d^*/d = 0.91$  (dash-dotted line),  $d^*/d = 0.95$  (dash-double-dotted line), and top-hat ( $d^*/d = 1.0$ , solid line) profiles.

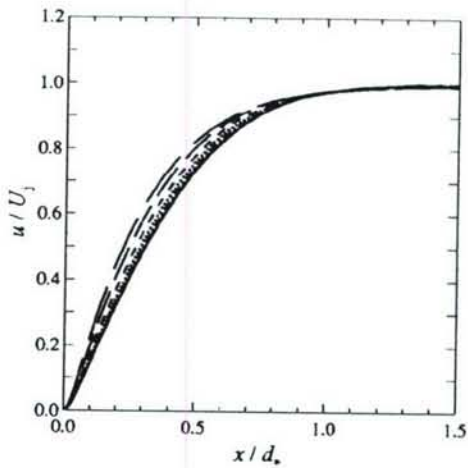


FIG. 17. Simulated velocity profiles versus axial distance from plate normalized by the effective diameter  $d^*$ , at  $\text{Re} = 700$  and  $L/d = 1.4$  for variable nozzle-exit velocity profiles. Legend as in Fig. 16.

cients are adjusted to obtain a variation of boundary-layer displacement thicknesses. The results in Figs. 16 and 17 are obtained by removing the nozzle interior from the axisymmetric-viscous-simulation domain and specifying the velocity profiles at the nozzle exit. Due to the lack of a plenum in the simulations, velocities are scaled by the velocity at the axis of the jet  $U_p$ , instead of the Bernoulli velocity. Figure 16 indicates that there is a significant effect of the nozzle-exit velocity profile on the resultant axial velocity field. Figure 17 plots the axial velocity profiles with the axial distance normalized by the boundary-layer thickness corrected diameter  $d^*$ . For  $d^*/d > 0.9$  this scaling results in a good collapse of the profiles.

From the previous results, the displacement-thickness-corrected diameter  $d^*$  is an appropriate scaling parameter for axial distances. Figure 18 shows the scaled velocity profiles from axisymmetric viscous simulations at four Reynolds numbers. For low Reynolds numbers ( $\text{Re} = 200$ ) viscous

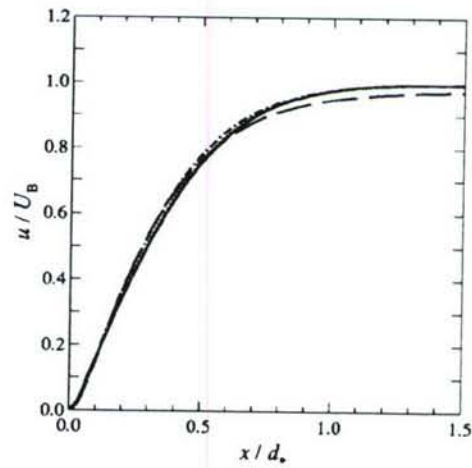


FIG. 18. Axisymmetric viscous simulation velocity profiles versus axial distance from plate normalized by the effective diameter  $d^*$ , at  $L/d = 1.4$  and  $\text{Re} = 200$  (long-dashed line), 400 (dash-dotted line), 700 (dotted line), and 1400 (solid line).

losses result in a jet-exit velocity that is less than the Bernoulli velocity. There is an additional weak Reynolds number effect exhibited for  $Re=200$  and 400 that is not fully captured by the current scaling and is manifested in the slope of the profiles. However, the velocity profiles collapse reasonably well using this scaling, and this allows the specification of an analytical expression for the velocity profile of the impinging jet in this Reynolds number range.

$$\frac{u(x)}{U_B} = \operatorname{erf} \left[ \alpha_* \left( \frac{x}{d_*} - \frac{\delta}{d} \right) \right], \quad (15)$$

where  $\alpha_* = 1.7$  and  $\delta/d_* = 0.016$  were found from fitting this error function to the axisymmetric-viscous-simulation data. The rms error of the error-function fit is less than 0.5% for  $Re=700$  and 1400 and less than 2% for  $Re=200$  and 400. In the limit of infinite Reynolds number, the wall boundary-layer thickness will tend to zero and the potential flow formulation will accurately model the flow. In this limit, the velocity field is given by  $u/U_B = \operatorname{erf}[\alpha_p(x/d_*)]$ , with  $\alpha_p = 1.59$  found by fitting this error function to the potential flow simulations. These expressions yield the velocity profile for an impinging jet with a measurement of the Bernoulli pressure across the nozzle contraction, the gas density and viscosity, the diameter ratio of the nozzle inlet and outlet, and the boundary-layer thickness at the nozzle exit.

## V. CONCLUSIONS

Scaling the centerline axial velocity for an impinging jet by the Bernoulli velocity, calculated from the static pressure drop across the nozzle contraction, collapses centerline axial-velocity data on a single curve that is independent of the nozzle-to-plate separation distance for separation-to-diameter ratios of  $L/d \geq 0.5$ . The axisymmetric viscous and potential-flow simulations reported here allow nozzle-to-wall proximity effects to be investigated by including the nozzle in the solution domain. Using this simulation domain, axisymmetric viscous simulations yield good agreement with experiment and confirm the velocity profile scaling. The potential-flow simulations reproduce the collapse of the data; however, at these Reynolds numbers, viscous effects result in disagreement with experiment. One-dimensional stream-function simulations provide an adequate approximation of the flow in the stagnation region if the boundary conditions are correctly specified.

The scaled axial velocity profiles are well characterized by an error function with one Reynolds-number-dependent parameter  $\alpha$ . The error function provides a good fit to both experimental and viscous-simulation data, with root-mean-squared errors of  $\epsilon_{rms} \leq 0.02U_B$ . In this Reynolds number range, viscous effects are captured by scaling the axial distance by the effective (displacement-thickness-corrected) diameter  $d_*$ . This scaling relies on thin nozzle boundary layers ( $d_*/d$  close to unity) and negligible viscous losses through the nozzle. These scalings allow the specification of an analytical expression for the velocity profile of an impinging laminar jet over the Reynolds number range investigated of  $200 \leq Re \leq 1400$ .

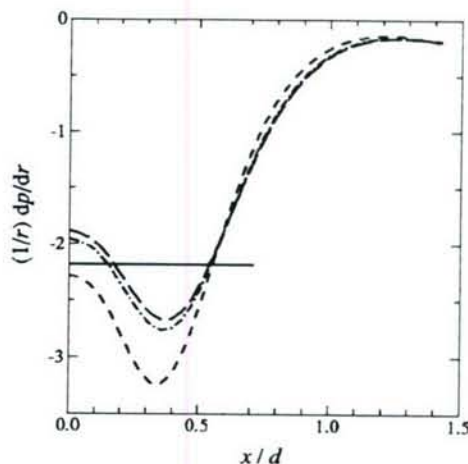


FIG. 19. Comparison of the radial-pressure eigenvalue profile at several radial locations,  $r/R=0$  (long-dashed line),  $r/R=0.2$  (dash-dotted line), and  $r/R=0.5$  (dashed line), to that of the one-dimensional model (solid line), which is constant in both  $x$  and  $r$ .

## ACKNOWLEDGMENTS

We would like to thank D. Lang for his contributions to the digital-imaging in this work, as well as G. Katzenstein for his assistance with experimental design and assembly. R. D. Henderson and H. Blackburn provided considerable assistance, as well as the codes that our axisymmetric viscous simulation code is based on. The work was funded by AFOSR Grant No. F49620-01-1-0006 and the DOE Caltech ASC Contract No. W-7405-ENG-48, whose support is gratefully acknowledged.

## APPENDIX A: RADIAL-PRESSURE EIGENVALUE

The one-dimensional formulation for stagnation flows relies on the introduction of a stream function to reduce the axisymmetric Navier-Stokes equations to a third-order ordinary differential equation. One of the assumptions used to derive this simplified model is that the radial-pressure eigenvalue  $\Lambda = (1/r)dp/dr$  must be a constant. In their study of cold and reacting opposed-jet flow, Frouzakis *et al.* [13] found that this quantity varies in the axial direction when the inlet axial velocity varies radially, while it is close to constant if plug-flow boundary conditions are specified. These authors found that the average value of  $\Lambda$  was approximately equal to that of the corresponding one-dimensional simulations. Figure 19 plots  $\Lambda$  as a function of the axial coordinate at several radii from the present axisymmetric-viscous simulations of impinging-jet flow at  $Re=700$ . It can be seen that the radial-pressure eigenvalue is nowhere constant in this flow, even for small  $x/d$  where the one-dimensional model appears to yield reasonable agreement with experiment. Near the axis, the radial-pressure eigenvalue is only a function of the axial direction and the radial variation is small. The good agreement between the one-dimensional simulations and either experimental data or two-dimensional simulations indicates that, for this flow, the axial velocity is not sensitively dependent on the spatial variation of  $\Lambda$ .

## APPENDIX B: WALL BOUNDARY-LAYER THICKNESS

From one-dimensional stagnation flow theory, the wall boundary-layer thickness is dependent only on the velocity gradient in the potential-flow region [17,18]. The solution to the boundary-layer equations is a linear function in the far field, with a viscous boundary layer close to the wall. The only free parameter in this flow is the far-field velocity gradient  $U'_\infty$ . In the far field, the high-order derivatives vanish ( $U'''_\infty, U''_\infty \rightarrow 0$ ) and, from Eq. (9), the radial pressure gradient eigenvalue is equal to  $\Lambda/\rho = -(U'_\infty)^2/4$ . The resulting equation can be nondimensionalized through the transformations  $\xi = x\sqrt{U'_\infty}/\nu$  and  $\phi = U(x)/\sqrt{U'_\infty}\nu$ , resulting in the following equation for  $\phi(\xi)$ :

$$2\phi''' - 2\phi\phi'' + (\phi')^2 = 1. \quad (B1)$$

The boundary conditions are  $\phi(0) = \phi'(0) = 0$  and  $\phi'(\infty) = 1$ . Equation (B1) can be solved using a shooting method, where  $\phi''(0)$  is adjusted to satisfy the boundary condition at infinity.

Figure 20 shows the solution to Eq. (B1). The nondimensionalized wall boundary-layer displacement thickness  $\delta_\xi$  can be calculated in the linear region of the flow ( $\xi > 5$ ).

$$\delta_\xi = \xi - \frac{\phi(\xi)}{\phi'(\xi)} = 0.80. \quad (B2)$$

Using Eq. (13), the velocity gradient can be computed at any point on the axis using the error-function fit

$$\frac{du(x)}{dx} = \frac{2U_B\alpha}{\sqrt{\pi d}} \exp\left[-\alpha^2\left(\frac{x}{d} - \frac{\delta}{d}\right)^2\right]. \quad (B3)$$

This yields a maximum velocity gradient of  $2U_B\alpha/(\sqrt{\pi d})$  at  $x = \delta$ . Therefore, the slope of the error function as it ap-

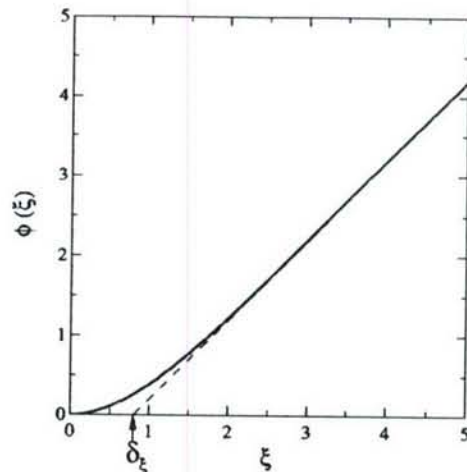


FIG. 20. One-dimensional stagnation flow solution with potential-flow boundary conditions (solid line) and linear fit (dashed line) showing wall boundary-layer offset  $\delta_\xi$ .

proaches the boundary layer is given by  $du/dx = 2U_B\alpha/(\sqrt{\pi d})$ . Equating this to  $U'_\infty$  allows the boundary-layer thickness to be determined analytically from the other error-function parameters  $U_B$  and  $\alpha$ . Thus, the wall boundary-layer displacement thickness in physical space is equal to

$$\frac{\delta}{d} = \delta_\xi \frac{(\pi)^{1/4}}{(2)^{1/2}} \sqrt{\frac{1}{\text{Re } \alpha}} = 0.755 \sqrt{\frac{1}{\text{Re } \alpha}}. \quad (B4)$$

where  $\text{Re} = dU_B/\nu$ , as defined previously. Since  $\alpha$  scales as  $\alpha = \alpha_\infty + C_1/\text{Re}$ ,  $\delta/d = 0.755/\sqrt{\text{Re}\alpha_\infty + C_1}$ .

---

[1] A. Rubel, AIAA J. **21**, 351 (1983).  
 [2] M. D. Deshpande and R. N. Vaishnav, J. Fluid Mech. **114**, 213 (1982).  
 [3] C. Houtman, D. Graves, and K. Jensen, J. Electrochem. Soc. **133**, 961 (1986).  
 [4] D. G. Goodwin, in *Proceedings of CVD XVI and EuroCVD Fourteen*, edited by M. D. Allendorf, F. Maury, and F. Teyssandier, (Electrochemical Society, New York, 2003), pp. 155–162.  
 [5] H. W. Smith, R. A. Schmitz, and R. G. Ladd, Combust. Sci. Technol. **4**, 131 (1971).  
 [6] M. Fang, R. A. Schmitz, and R. G. Ladd, Combust. Sci. Technol. **4**, 143 (1971).  
 [7] J. M. C. Mendes-Lopes, Ph.D. thesis, Cambridge University, 1983.  
 [8] J. M. Bergthorson, D. G. Goodwin, and P. E. Dimotakis, Proc. Combust. Inst. **30**, 1637 (2005).  
 [9] J. M. Bergthorson, Ph. D. thesis, California Institute of Technology, 2005.  
 [10] R. J. Kee, J. A. Miller, G. H. Evans, and G. Dixon-Lewis, Sym. (Int.) Combust., [Proc.] **22**, 1479 (1988).  
 [11] J. C. Rolon, D. Veyante, J. P. Martin, and F. Durst, Exp. Fluids **11**, 313 (1991).  
 [12] L. W. Kostiuk, K. N. C. Bray, and R. K. Cheng, Combust. Flame **92**, 377 (1993).  
 [13] C. E. Frouzakis, J. Lee, A. G. Tomboulides, and K. Boulouchos, Sym. (Int.) Combust., [Proc.] **27**, 571 (1998).  
 [14] C. C. Landreth and R. J. Adrian, Exp. Fluids **9**, 74 (1990).  
 [15] P. E. Dimotakis, F. D. Debussy, and M. M. Koochesfahani, Phys. Fluids **24**, 995 (1981).  
 [16] T. Echekki and M. G. Mungal, Sym. (Int.) Combust., [Proc.] **23**, 455 (1990).  
 [17] H. Schlichting, *Boundary Layer Theory* (McGraw-Hill, New York, 1960).  
 [18] R. J. Kee, M. E. Coltrin, and P. Glarborg, *Chemically Reacting Flow—Theory & Practice* (John Wiley & Sons, Hoboken, NJ, 2003).  
 [19] D. J. Phares, G. T. Smedley, and R. C. Flagan, Phys. Fluids **12**, 2046 (2000).  
 [20] W. Schach, Ing.-Arch. **6**, 51 (1935).  
 [21] T. Strand, AIAA Pap. **64**, 424 (1964).  
 [22] R. D. Henderson and G. E. Karniadakis, J. Comput. Phys. **122**, 191 (1995).  
 [23] G. E. Karniadakis and S. J. Sherwin, *Spectral/hp element*

*methods for CFD* (Oxford University Press, New York, 1999).

- [24] G. Birkhoff and E. H. Zarantonello, *Jets, Wakes and Cavities* (Academic Press, New York, 1957).
- [25] M. I. Gurevich, *Theory of Jets in Ideal Flows* (Academic Press, New York, 1965).
- [26] A. T. Patera, *J. Comput. Phys.* **54**, 468 (1984).
- [27] A. Leonard and A. Wray, in *Proceedings of the Eighth International Conference on Numerical Methods in Fluid Dynamics*, edited by E. Krause, *Lecture Notes in Physics*, Vol. 170 (Springer-Verlag, New York, 1982), pp. 335–342.
- [28] G. K. Batchelor, *An Introduction to Fluid Dynamics* (Cambridge University Press, New York, 1967).



Available online at [www.sciencedirect.com](http://www.sciencedirect.com)

SCIENCE @ DIRECT<sup>®</sup>

Proceedings of the Combustion Institute 30 (2005) 1637–1644

Proceedings  
of the  
Combustion  
Institute

[www.elsevier.com/locate/proc](http://www.elsevier.com/locate/proc)

## Particle streak velocimetry and CH laser-induced fluorescence diagnostics in strained, premixed, methane–air flames

Jeffrey M. Bergthorson<sup>a,\*</sup>, David G. Goodwin<sup>b</sup>, Paul E. Dimotakis<sup>a</sup>

<sup>a</sup> Graduate Aeronautical Laboratories, California Institute of Technology, Pasadena, CA 91125, USA

<sup>b</sup> Department of Mechanical Engineering, California Institute of Technology, Pasadena, CA 91125, USA

### Abstract

We present the use of simultaneous particle streak velocimetry (PSV) and CH planar laser-induced fluorescence (PLIF) diagnostics in the study of planar, strained, premixed, methane–air flames, stabilized in a jet-wall stagnation flow. Both PSV and PLIF data are imaged at high spatial resolution and sufficiently high framing rates to permit an assessment of flame planarity and stability. Concurrent measurements of mixture composition, (Bernoulli) static-pressure drop, and stagnation-plate temperature provide accurate boundary conditions for numerical simulations. The new PSV implementation is characterized by very low particle loading, high accuracy, and permits short recording times. This PSV implementation and analysis methodology is validated through comparisons with previous laminar flame-speed data and detailed numerical simulations. The reported diagnostic suite facilitates the investigation of strained hydrocarbon–air flames, as a function of nozzle-plate separation to jet-diameter ratio,  $L/d$ , and equivalence ratio,  $\Phi$ . Methane–air flames are simulated using a one-dimensional streamfunction approximation, with full chemistry (GRI-Mech 3.0), and multi-component transport. In general, we find good agreement between experiments and simulations if boundary conditions are specified from measured velocity fields. Methane–air flame strength appears to be slightly overpredicted, with the largest disagreements for lean flames. © 2004 The Combustion Institute. Published by Elsevier Inc. All rights reserved.

**Keywords:** Stagnation; One-dimensional; Flame speed; PLIF; Cantera

### 1. Introduction

Planar, strained flames provide a valuable development and validation testbed for transport and kinetics models that can then be used in any combustion environment. The high parametric dimensionality of these models requires many de-

tailed and accurate experiments over a sufficiently large range of conditions. Such experiments are enhanced by diagnostics that simultaneously permit detailed flow and chemical-species data to be measured and compared to model predictions. This paper describes a suite of diagnostics developed for this purpose and employed to probe planar, strained, methane–air flames, stabilized in a jet-wall stagnation flow. This setup yields a flow with boundary conditions that can be accurately specified, facilitating simulation and comparisons with experiment. This flow can also, with care,

\* Corresponding author. Fax: +1 626 395 4447.  
E-mail address: [jeffb@tyrvos.caltech.edu](mailto:jeffb@tyrvos.caltech.edu) (J.M. Bergthorson).

be stable to high Reynolds numbers. The diagnostics are optimized for accuracy, minimal flame disturbance, and rapid simultaneous recording of flow velocity and CH radical profiles.

Diagnostics documented here include extensions to and improvements of particle streak velocimetry (PSV), complemented by simultaneous CH planar laser-induced fluorescence (PLIF) imaging at 10 Hz. PLIF spectroscopy confirms the CH excitation and helps optimize dye-laser wavelength for signal-to-noise ratio. PLIF images are processed to extract CH radical profiles and to assess flame planarity. The 10 fps PLIF sequence permits an assessment of flame stability under all conditions. Only data from stable flame conditions are included.

Particle streak velocimetry (PSV) [1–3], a technique similar to particle tracking velocimetry [4], is used for instantaneous flow-field measurements and, in particular, axial velocities along the flow centerline. In combustion, PSV was previously used for qualitative flow descriptions (e.g., Sugiyama [5]). Extensions and improvements to PSV implemented here include digital imaging and processing, and new analysis techniques. The implementation yields a Lagrangian measurement of velocity that, in principle, requires only a single particle traversing a steady flame. The consequent PSV accuracy competes favorably with LDV and PIV techniques, while a 1–2 order of magnitude reduction in particle loading minimizes flame disturbances, and Mie-scattering and stray-light interference in PLIF images. Velocity data are used to specify boundary conditions for simulations and are compared to predictions.

The spatial distribution of the CH radical can be measured with PLIF. Its narrow spatial profile is well correlated with flame location and provides a sensitive test of direct predictions of strained-flame models.

Simultaneous measurements of air, fuel, and diluent mass fluxes, as well as of stagnation plate temperature, allow an accurate specification of boundary conditions for simulations.

Experimental profiles are compared to one-dimensional simulation predictions, using the *Cantera* software package [6]. The simulations incorporate GRI-Mech 3.0 kinetics [7] with multicomponent transport [8]. The simulations rely on a one-dimensional streamfunction formulation [9]. Few comparisons between this formulation and actual velocity data have been documented. Law and co-workers [10–13] studied methane-air, opposed-jet flames for lean, stoichiometric, and rich mixtures, using LDV and CARS for velocity, temperature, and major-species measurements to quantify the effect of stretch on flame structure. To compare experimental and simulated data, a potential-flow boundary condition with a variable inflow mass flux is used to visually match the profiles. The authors report general

agreement for temperature and major species profiles when flame location is adjusted to match the measurements.

The new PSV methodology is validated by comparing extrapolated laminar flame speeds with existing data and numerical simulations. Slightly lean, strained, methane-air flames are studied as a function of the nozzle-stagnation plate separation distance,  $L$ , to assess the simplified hydrodynamic model. Flame temperature dependence is studied by mixture dilution with excess nitrogen. The diagnostics are applied to methane-air flames, under similar strain-rate conditions, as a function of equivalence ratio,  $\phi$ . The approach and diagnostics permit an assessment of the numerical simulation predictions of strained-flames.

## 2. Experiments

A room-temperature, atmospheric-pressure jet is generated from a contoured nozzle with an exit diameter of  $d = 9.9$  mm that impinges on a constant-temperature (water-cooled) copper stagnation plate. Three K-type thermocouples are embedded on the centerline, spaced vertically between the stagnation and cooled surface, to allow monitoring of wall temperature and temperature gradients.

The pressure difference between the jet plenum interior and a point just outside the jet-core flow region is measured with a 1 Torr full-scale differential-pressure transducer (BOC Edwards W57401100 and W57011419). The Bernoulli

velocity,  $U_B = \sqrt{(2\Delta p)/(\rho[1 - (d/d_p)^4])}$ , is then calculated, where  $\Delta p$  is the nozzle static pressure drop,  $\rho$  is the fluid density,  $d$  is the nozzle exit diameter, and  $d_p$  is the plenum (inner) diameter. The Bernoulli velocity will be higher than the jet-exit velocity for  $L/d \leq 1$  due to the velocity deficit produced by streamline curvature at the nozzle-exit [14].

Fuel, oxidizer, and nitrogen-diluent mass flow rates are set using sonic metering valves and monitored concurrently (Omega FMA868-V-Methane, FMA872-V-Air, and FMA873V-Air, calibrated using a Bios DryCal ML-500). Estimated uncertainty in the mass-flow measurement of the air and fuel streams is, approximately, 1% each. Bernoulli pressure, mass-flow, and temperature data acquisition is synchronized with digital-image acquisition, allowing accurate specification of simulation boundary conditions.

### 2.1. Particle streak velocimetry

Flow velocities along the jet centerline are measured using particle streak velocimetry (PSV) [1–3]. The implemented PSV methodology yields

low-fractional-error axial-velocity data. The resulting accuracy is comparable to that obtained with LDV or PIV, while offering several advantages in flame environments. The reduced particle loading required for PSV minimizes flame disturbances introduced by particle seeding that can alter the effective thermal/heat-capacity environment, or the chemical kinetic/catalytic environment by providing surface-chemistry sites. Low PSV particle loading also reduces Mie-scattering interference in CH PLIF image-data, improving CH profile statistics. Particle loading required for accurate velocity measurements with PSV is an order of magnitude or more, lower than that required for LDV, or PIV. In a single PSV image frame, one or two particles traversing the vertical extent of the imaged region can suffice. In contrast, PIV measurements require a dispersion of particles throughout the domain in any one (short-time) exposure. With LDV, high particle number densities are required for converged statistics in a reasonable time.

A single PSV image captures the entire velocity field, making it ideal for short-run-time experiments. An example PSV image for a stagnation flame is shown in Fig. 1A. In axisymmetric, steady stagnation flow, axial velocities along the centerline can be reliably measured; particle paths do not cross or overlap, and occasional out-of-plane particle displacements are small and easily discernible (in-/out-of-focus streaks). The high sensitivity of the scattering cross-section to particle size, in the size range employed, allows easy identification of agglomerates that may not track high spatial-gradient regions in the flow. Streaks used for PSV processing are from in-plane, non-agglomerated particles. In a variable-velocity

field, particles track the flow if the dimensionless product of the local strain rate,  $\sigma = \partial u / \partial x$ , and the Stokes time,  $\tau_S \equiv \rho_p d_p^2 / (18\mu)$ , is small, i.e., provided  $\sigma \tau_S \ll 1$ . The measurements relied on alumina particles ( $\text{Al}_2\text{O}_3$  median size,  $d_p \equiv 0.8 \mu\text{m}$ ,  $\rho_p \equiv 3830 \text{ kg/m}^3$ ; Baikowski Malakoff, RC-SPT DBM). For the strain rates in these experiments,  $\sigma \tau_S \leq 3 \times 10^{-3}$ .

A Coherent I-90  $\text{Ar}^+$  laser, operated at 2–3 W, provides the PSV illumination source. Two cylindrical lenses generate a thin laser sheet ( $\approx 200 \mu\text{m}$ ) in the field of view. An Oriel (Model 75155) chopper with a 50% duty-cycle wheel modulates the laser beam. The chopper wheel is placed at a laser-beam waist to minimize on-off/off-on transition times. Chopping frequencies are in the range,  $1.6 \text{ kHz} \leq v_c \leq 2.4 \text{ kHz}$ , with  $v_c$  optimized depending on flow velocity.

PSV image data are recorded using the in-house-developed "Cassini" digital-imaging system that relies on a low-noise,  $1024^2$ -pixel CCD, with a (square)  $12 \mu\text{m}$  pitch. A PSV image frame rate of 4 sps is chosen to further minimize particle-loading requirements. Magnification ratios are in the range of 1:1.0–1:1.5 using a Nikon 105 mm, f/2.8 macro lens (with a 514.5 nm bandpass filter).

Local velocities,  $u(x)$ , are estimated from streak pairs as,  $u(x) \equiv \Delta X(x) / \Delta t$ , yielding  $u_I = L_I / \tau_c$  and  $u_{II} = L_{II} / \tau_c$  where  $\tau_c = 1/v_c$  (reciprocal of chopper frequency), and  $L_I = x_{2s} - x_{1s}$  and  $L_{II} = x_{2e} - x_{1e}$  are the distances from the start/end of one streak to the start/end of the next, respectively (cf. Fig. 1B). Using the same intensity threshold on a streak pair removes systematic errors in applying the Lagrangian time interval,  $\tau_c$ . This methodology is spatially second-order accurate and produces good agreement between velocity values derived from each streak pair. Streak lengths are estimated using bi-cubic fits on the 2-D streak-intensity image data, sampled to a 0.1-pixel resolution in both dimensions. An intensity threshold of  $\approx 0.3$  of the maximum intensity of each streak is used. The results do not depend on this choice and yield an r.m.s. error of  $\approx 0.01 U_j$ , where  $U_j$  is the jet-exit velocity.

The velocity estimate,  $u_I$ , is located at  $x_I = (x_{1s} + x_{2s})/2 + (w_1 + w_2)/4$ , where  $x_{is}$  is the spatial location of the start of the  $i$ th streak and  $w_i$  is the width of the  $i$ th streak (cf. Fig. 1B). Similarly,  $u_{II}$  is located at  $x_{II} = (x_{1e} + x_{2e})/2 - (w_1 + w_2)/4$ , where  $x_{ie}$  is the location of the end of the  $i$ th streak. PSV spatial resolution is comparable to that of other particle velocimetry techniques, e.g., PIV, LDV, that rely on comparable spatial displacements (e.g., 10–30 pix, or  $\approx 100$ – $300 \mu\text{m}$ , for this flow). These methods measure the distance travelled by a particle along a Lagrangian path in a fixed time (PIV, PSV), or the time required to traverse a number of fringes in space (LDV). Particle methods require care in regions of high fractional change in speed along individual particle track segments, here

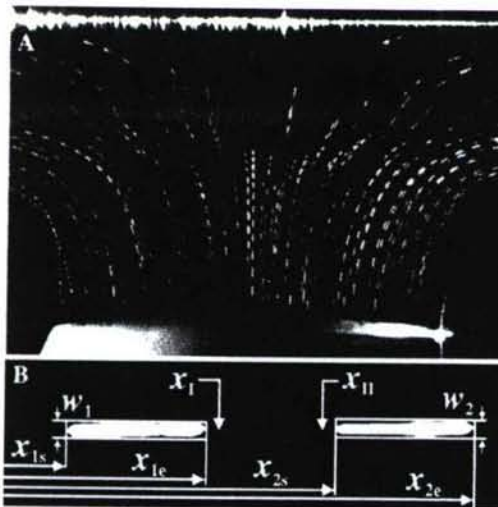


Fig. 1. (A) PSV in a strained premixed methane-air flame (image cropped in the vertical dimension).  $\phi = 0.87$ ,  $L/d = 0.8$ . (B) PSV processing implementation.

limited to measurements very close to the wall, or in regions of high velocity curvature.

## 2.2. Planar laser-induced fluorescence

CH fluorescence measurements are obtained by exciting the  $Q_1(7)$  transition of the  $B^2\Sigma-X^2\Pi(0,0)$  CH band at 390.30 nm, in the UV [15]. The UV beam is obtained from a tripled Nd:YAG (355 nm)-pumped dye laser (Spectra-Physics PRO-290 and Sirah PrecisionScan). Pulse duration is  $\approx 5$  ns with a linewidth of  $\approx 0.1$  cm $^{-1}$  (1.5 pm). Fluorescence is recorded from the A-X(1,1), A-X(0,0), and B-X(0,1) bands in the 420–440 nm range. Excitation to the B state yields a higher signal than excitation to the A state [16] and a large wavelength shift between excitation and fluorescence, facilitating filtering of Mie-and Rayleigh-scattering interference, which is important in particle-seeded flames. The  $Q_1(7)$  band provides a high signal level and low temperature sensitivity.

The output of the dye laser is passed through a pair of cylindrical lenses (150 and 500 mm at right angles) and yields a laser sheet with a Rayleigh range centered on the jet axis. Fluorescence is collected with a Nikkor 50 mm, f/1.2 lens at magnifications near 1:1, with a Schott KV-418 long-pass filter to reject scattering of the UV laser illumination, while transmitting approximately 90% of the fluorescence near 430 nm. Detection relies on a lens-coupled intensifier (Ultra-Blue Gen-III, Cooke VS-364) with a cooled CCD (Cooke Sensi-CAM<sup>QE</sup>, binned to 344 × 260 pix $^2$ ; a binned pixel maps into 46  $\mu\text{m}$  in the flow). A 70 ns gate time rejects chemiluminescence while retaining fluorescence. For the PLIF profiles presented here, a laser power of  $\approx 10$  mJ/pulse results in a saturated laser spectral intensity of  $I_v = E_p/(\tau_p A_b \text{SW}) \approx 10^8$  (W/cm $^2$ )/cm $^{-1}$ , where  $E_p$  is the pulse energy,  $\tau_p$  is the pulse length,  $A_b$  is the laser beam cross-sectional area, and SW is the laser spectral width [17]. A sample CH PLIF (single-exposure) image

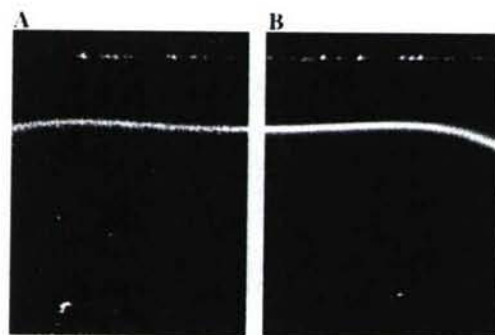


Fig. 2. Example CH PLIF images for a methane-air flame (344 × 260 pix $^2$ ,  $\Phi = 0.96$ ,  $L/d = 0.8$ ). (A) Single exposure. (B) Average of 1000 exposures.

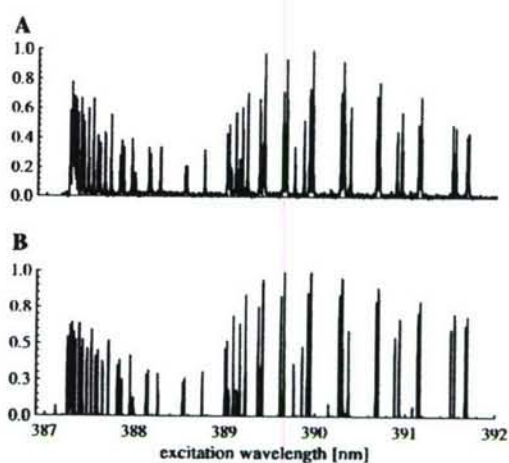


Fig. 3. Normalized experimental and simulated CH fluorescence spectra in a methane-air flame ( $\Phi = 0.96$ ,  $L/d = 0.8$ ). (A) Measured excitation/response scan. (B) Spectrum simulation performed using LIFBASE [18].

is reproduced in Fig. 2A, and an average of 1000 exposures is shown in Fig. 2B. To correct for dark current and Rayleigh scattering, an averaged image of the laser sheet (no flame) is subtracted from the image data. CH profiles are obtained from single-shot images by summing across the (flat) central portion of the flame. Single-image 60-column averaging, about the jet axis, yields good profile statistics.

Figure 3 shows an experimentally measured CH excitation scan, at a resolution of 0.5 pm. Spectrum simulations are performed with LIFBASE [18]. This scan was recorded with a laser power of 0.2 mJ/pulse, in a 1 mm × 2 cm sheet, producing a partially saturated laser spectral intensity of  $I_v \approx 2 \times 10^6 \approx I_v^{\text{sat}} \approx 10^6$  (W/cm $^2$ )/cm $^{-1}$ .

## 3. Numerical method

Stagnation flame simulations are performed using the *Cantera* reacting-flow software package [6]. The one-dimensional solution for stagnation flows models the flow in terms of a local streamfunction,  $\psi(x, r) = r^2 U(x)$ , with  $U(x) = \rho u/2$ , where  $u$  is the axial velocity [9]. The axisymmetric momentum equation then becomes

$$2U \frac{d}{dx} \left( \frac{1}{\rho} \frac{dU}{dx} \right) - \frac{1}{\rho} \left( \frac{dU}{dx} \right)^2 - \frac{d}{dx} \left[ \mu \frac{d}{dx} \left( \frac{1}{\rho} \frac{dU}{dx} \right) \right] = A. \quad (1)$$

In this formulation,  $A = (1/r)dp/dr$  must be a constant. By treating  $A$  as unspecified, four boundary conditions can be imposed on this third-order ordinary differential equation at  $x = 0$  and  $x = \ell$ , with  $0 < \ell \leq L$  a suitably chosen interior point, setting

$U(0) = 0$ ,  $U'(0) = 0$ ,  $U(\ell) = U_\ell$ ,  $U'(\ell) = U'_\ell$ . Exploiting the (cold) outer-flow solution to Eq. (1), which is a parabola, a quadratic is fit to the cold-flow data upstream of the flame.  $U_\ell$  and  $U'_\ell$  are then calculated from the fit, at  $x = \ell$ , minimizing errors that could be introduced by an inconsistent specification of flow boundary conditions or from data differentiation. Energy and species equations are solved with specification of inlet composition, inlet temperature, and stagnation-wall temperature. A no-flux boundary condition for species is applied at the wall. The simulations use a multi-component transport model and the GRI-Mech 3.0 kinetics mechanism [7,8]. Simulations of laminar flame speeds are performed using a freely propagating flame code with multi-component transport and the same kinetics mechanism [19].

#### 4. Results and discussion

The PSV methodology is validated by comparing extrapolated laminar flame speed measurements with previous data and numerical simulations. Figure 4A plots sample reference flame speed and strain-rate data, and the extrapolated flame speed. Vertical error bars are based on linear regression techniques. Horizontal error bars represent the estimated uncertainty in  $\Phi$  of 1.4%. Data at equivalence ratios of  $\Phi = 0.75$ , 0.84, and 0.95 are given in Fig. 4B, and compared to numer-

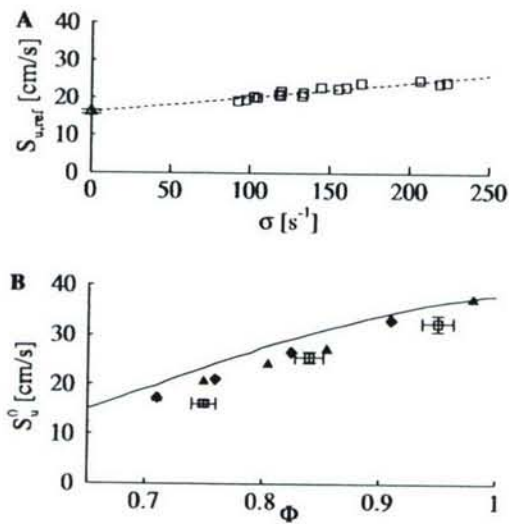


Fig. 4. (A) Flame speeds,  $S_{u,ref}$ , vs. strain rate,  $\sigma$ , for a  $\Phi = 0.75$ , methane-air flame. Extrapolation to zero strain rate yields laminar flame speed estimate,  $S_u^0$ , and error bar. (B) Estimated laminar flame speeds of methane-air flames (squares). Data by Yamaoka and Tsuji (triangles) [20] and Vagelopoulos et al. (diamonds) [21]. Numerical simulations use GRI-Mech 3.0 (line).

ical simulations and previous LDV-based data [20,21]. The measurements agree with previous data and, collectively, indicate lower flame speeds than predicted.

The diagnostic suite is applied to methane-air flames as a function of scaled separation distance,  $L/d$ , and  $\Phi$ . Table 1 lists the equivalence ratio, scaled separation distance, and dilution for the experiments reported here. The first subset of experiments is at  $\Phi \approx 1.0$ , with variable  $L/d$  (Table 1(a)). A diluted methane-air flame is also studied (Table 1(b)). Flame chemistry effects are probed at  $L/d = 0.8$  by varying equivalence ratio and dilution (Table 1(c)). The dilution level is chosen to maintain similar stretch conditions as mixture-fraction is varied.

Figure 5 shows the results for a near-stoichiometric ( $\Phi = 0.98$ ) methane-air flame, at  $L/d = 0.6$ . CH profiles, obtained from 60-column averages in single-exposure images, are normalized by peak values. The simulation predicts flame location with good agreement in both the flow field and CH profile. Thermophoresis will cause a particle drift in the high temperature-gradient region of the flow [11]. Utilizing the simulated temperature profile, thermophoretic corrections

Table 1  
Experimental conditions

	$\Phi$	$L/d$	% O <sub>2</sub> : (O <sub>2</sub> + N <sub>2</sub> )
(a)	0.98	0.6	21.0
	0.96	0.8	21.0
	0.97	1.0	21.0
	0.97	1.2	21.0
(b)	0.98	0.8	18.0
(c)	0.69	0.8	21.0
	0.76	0.8	21.0
	0.87	0.8	21.0
	1.08	0.8	18.0
	1.20	0.8	19.5
	1.31	0.8	21.0

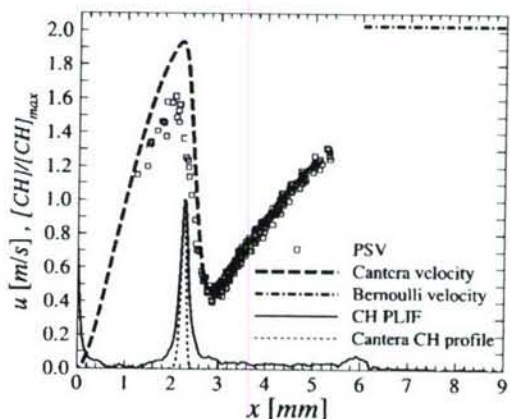


Fig. 5.  $\Phi = 0.98$ ,  $L/d = 0.6$ , methane-air flame profiles. Simulation boundary at  $\ell = 5$  mm.

yielded a maximum error of 3% in the high gradient region of the velocity profile (preheat zone). Velocity data in this region are used to visually assess simulation predictions and these (small) thermophoretic corrections are neglected; velocity data in the cold-flow region, where a quadratic is fit to determine flow boundary conditions, are unaffected by thermophoresis.

To compare simulations with experiments, the difference between measured and predicted peak CH concentration location,  $x_{\text{CH,PLIF}}$  and  $x_{\text{CH,sim}}$ , scaled by the simulated CH layer thickness,  $\delta_{\text{CH}}$ , is calculated. CH layer thicknesses are calculated as the full width at half maximum (FWHM) of Gaussian fits to simulated profiles. The difference between  $x_{\text{CH,PLIF}}$  and  $x_{\text{CH,sim}}$  is less than  $0.1\delta_{\text{CH}}$  in this case.

The scaled separation distance,  $L/d$ , is an important flow parameter. Figure 6 shows the results for a near-stoichiometric ( $\Phi = 0.96$ ) methane-air flame, at  $L/d = 0.8$ . Predicted and experimental peak CH locations agree within  $0.2\delta_{\text{CH}}$  for  $L/d = 0.6$ , 1.0, and 1.2, and within  $2\delta_{\text{CH}}$  for  $L/d = 0.8$ , at  $\Phi \approx 1.0$ . Experimental and predicted CH peak locations exhibit reasonable agreement at  $\Phi \approx 1.0$ , indicating good prediction of strained flame location for a variety of imposed hydrodynamic fields. The variation of flow conditions at constant  $\Phi$  indicates that the simplified hydrodynamic model can capture the experiment. For the remainder of this study, the scaled separation distance is fixed at  $L/d = 0.8$ .

To investigate flame-temperature effects, a diluted  $\Phi = 0.98$  flame is studied. Excess nitrogen is added to the premixture to reduce the flame temperature. Reasonable agreement was found between measured and predicted velocity and CH profiles, indicating that the simulations can capture variations in flame heat release and attendant temperature-dependent transport effects.

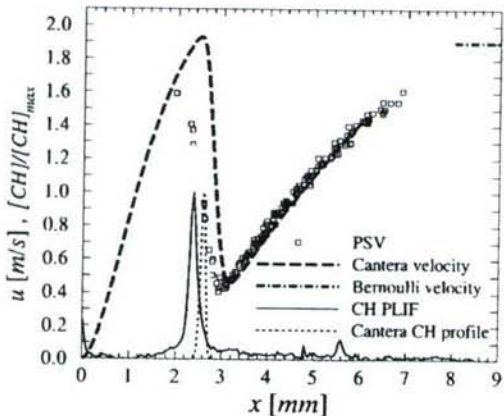


Fig. 6.  $\Phi = 0.96$ ,  $L/d = 0.8$ , methane-air flame profiles. Simulation boundary at  $\ell = 6$  mm.

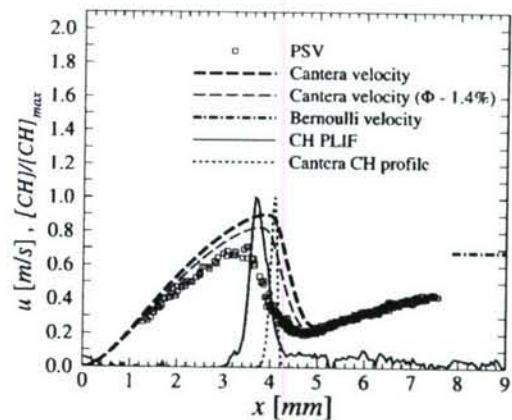


Fig. 7.  $\Phi = 0.69$ ,  $L/d = 0.8$ , methane-air flame profiles. Simulation boundary at  $\ell = 6$  mm.

The difference between simulated and measured CH peak locations is less than  $2\delta_{\text{CH}}$ .

Flame chemistry effects are probed by varying  $\Phi$ . Representative results are given in Figs. 7 and 8 that compare experimental and predicted profiles for a lean and rich flame, respectively. For the lean flame ( $\Phi = 0.69$ ), the predicted CH-profile is located upstream of the experimental one, consistent with an overprediction of strained-flame speed. Correspondingly, post-flame velocity is higher than that measured. For the rich flame ( $\Phi = 1.31$ ), good agreement is seen between experiment and simulation. Far from stoichiometry, the results are sensitive to inlet composition. A simulated velocity profile with  $\Phi$  decreased by 1.4% (the direction required for agreement) is also included in Fig. 7. The 1.4% increment represents the estimated maximum uncertainty in  $\Phi$ . For lean and rich flames, simulations exhibit high sensitivity to the inlet composition and its measurement uncertainty.

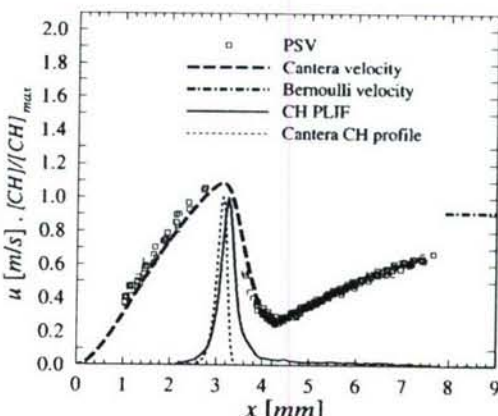


Fig. 8.  $\Phi = 1.31$ ,  $L/d = 0.8$ , methane-air flame profiles. Simulation boundary at  $\ell = 6$  mm.

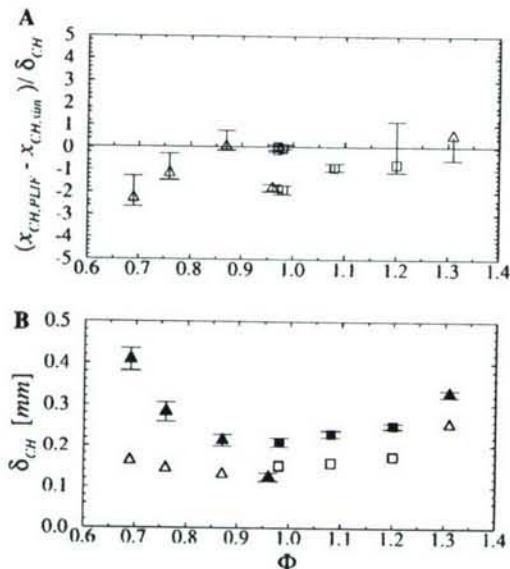


Fig. 9. (A) Difference in measured ( $x_{CH,PLIF}$ ) and predicted ( $x_{CH,sim}$ ) peak locations of CH, scaled by the simulated CH profile thickness ( $\delta_{CH}$ ), as a function of equivalence ratio. (B) Experimental (closed) and simulated (open) CH profile thicknesses (FWHM). Experimental data are referenced to the  $\Phi = 0.96$  undiluted flame. Undiluted flames marked with triangles; diluted flames with squares.

Results for methane-air flames over a range of equivalence ratios are presented in Fig. 9. In an attempt to reduce the number of parameters varied between experiments, strong burning flames ( $\Phi \approx 1.1, 1.2$ ) are diluted with excess nitrogen to maintain an approximately constant flame temperature [22]. This permits a similar strain-field to be established as equivalence ratio is varied, allowing some decoupling of the various effects. We note reasonable agreement for methane-air flames, with a maximum scaled error between measured and predicted CH peak locations of  $\approx 2.3 \delta_{CH}$  for the leanest flame (cf. Fig. 9A). Error bars represent the results from simulations with  $\Phi$  increased and decreased by its maximum estimated uncertainty of 1.4%. For the richest flame ( $\Phi = 1.31$ ), a solution could not be found with  $\Phi$  increased by 1.4% and the error bar represents a decrease of 1.4% in  $\Phi$ .

Figure 9B compares experimental and simulated CH profile thicknesses, referenced to the  $\Phi = 0.96$  flame. Measured CH-profile thickness is an ensemble average of the FWHM of individual Gaussian fits to single-exposure profiles (60-column average over the flat, central portion of the flame). For the  $\Phi = 0.96$ ,  $L/d = 0.8$  flame, the measured CH-profile thickness is approximately twice the simulated value. The point spread function (PSF) of the imaging system

and the true CH profile can be approximated by Gaussians. A measured PLIF profile will then also be a Gaussian that is a convolution of the two, with a composite width (squared),  $\delta_{PLIF}^2$ , that is the sum of the PSF,  $\delta_{PSF}^2$ , and true CH profile,  $\delta_{CH}^2$ , widths squared, i.e.,  $\delta_{PLIF}^2 \cong \delta_{PSF}^2 + \delta_{CH}^2$ . PSF width squared is estimated based on the undiluted,  $\Phi = 0.96$ ,  $L/d = 0.8$  flame by subtracting the measured and simulated widths squared. This PSF width is systematically applied to study the difference between predicted and measured reference profile thicknesses as a function of equivalence ratio. Figure 9B plots the mean FWHM calculated from multiple shots,  $700 < n \leq 1000$ , and error bars (one standard deviation). Simulations underpredict variations in  $\delta_{CH}$  with  $\Phi$  and dilution. Beam-steering, lensing, or profile-broadening artifacts are estimated not to be significant, or  $\Phi$ -dependent, and cannot account for this discrepancy.

## 5. Conclusions

Combined PSV and CH PLIF diagnostics are presented that yield high-accuracy measurements of velocity fields and of the spatial extent of relative CH-concentration profiles. The new PSV implementation requires very low particle loading, resulting in minimal flame disturbances and improving statistics in simultaneous PLIF measurements. This implementation and analysis methodology is validated through good agreement with previous laminar flame-speed data and detailed numerical simulations. Numerical simulations overpredict laminar flame speeds for lean flames.

The diagnostic suite facilitates investigation of strained premixed flames, performed here for methane-air mixtures, as a function of the nozzle-plate separation and equivalence ratio. Axial velocity and CH profiles are extracted from PSV and PLIF field data, and compared to one-dimensional simulations. Strained flames are simulated using a one-dimensional streamfunction approximation, with detailed chemistry (GRI-Mech 3.0) and multi-component transport. The diagnostics permit a complete boundary-condition specification to the one-dimensional flow-transport-kinetic model, allowing detailed comparisons of measured and predicted velocity and CH profiles in strained stagnation flames.

Near-stoichiometric, strained, methane-air flames are studied, as a function of the nozzle-stagnation plate separation distance, to assess the simplified hydrodynamic model employed. Reasonable agreement is seen for all cases, provided cold-flow (upstream of the flame) boundary conditions are specified from measurements. Flame-temperature effects are probed by nitrogen dilution. Results indicate that the simulations can

capture the hydrodynamics, as well as effects caused by variations in flame temperature.

Flames investigated over a range of compositions used both undiluted air–methane mixtures and diluted air–methane mixtures to maintain an approximately constant post-flame temperature rise. Along with the variation in  $L/d$ , these preliminary experiments target the convective, transport, and kinetic components of the model. Reasonable agreement is seen for methane–air flames, with the results suggesting that flame strength is slightly overpredicted, especially for lean flames. The results from these preliminary investigations suggest that a complete study would provide further insight.

### Acknowledgments

We acknowledge discussions with K. Sone and assistance by D. Lang with digital-imaging, and by G. Katzenstein with mechanical design and assembly. The work was funded by AFOSR Grant F49620-01-1-0006, whose support is gratefully acknowledged.

### References

- [1] P.E. Dimotakis, F.D. Debussy, M.M. Koochesfahani, *Phys. Fluids* 24 (1981) 995–999.
- [2] A.A. Adaczyk, L. Rimal, *Exp. Fluids* 6 (1988) 373–380.
- [3] C.M. Vagelopoulos, *An Experimental and Numerical Study on the Stability and Propagation of Laminar Premixed Flames*, Ph.D. thesis, University of Southern California, 1999.
- [4] T. Echekki, M.G. Mungal, *Proc. Combust. Inst.* 23 (1990) 455–461.
- [5] G. Sugiyama, *Proc. Combust. Inst.* 25 (1994) 601–608.
- [6] D.G. Goodwin, in: *Proceedings of CVD XVI and EuroCVD Fourteen*, Electrochem. Soc., 2003, pp. 155–162.
- [7] G.P. Smith, D.M. Golden, M. Frenklach, N.W. Moriarty, B. Eiteneer, M. Goldenberg, C.T. Bowman, R.K. Hanson, S. Song, W.C. Gardiner, V.V. Lissianski, Z. Qin. Available from: [http://www.me.berkeley.edu/gri\\_mech/](http://www.me.berkeley.edu/gri_mech/).
- [8] R.J. Kee, M.E. Coltrin, P. Glarborg, *Chemically Reacting Flow—Theory and Practice*, Wiley, New Jersey, 2003.
- [9] R.J. Kee, J.A. Miller, G.H. Evans, G. Dixon-Lewis, *Proc. Combust. Inst.* 22 (1988) 1479–1494.
- [10] C.K. Law, C.J. Sung, G. Yu, R.L. Axelbaum, *Combust. Flame* 98 (1994) 139–154.
- [11] C.J. Sung, C.K. Law, R.L. Axelbaum, *Combust. Sci. Technol.* 99 (1994) 119–132.
- [12] C.J. Sung, J.S. Kistler, M. Nishioka, C.K. Law, *Combust. Flame* 105 (1996) 189–201.
- [13] C.J. Sung, J.B. Liu, C.K. Law, *Combust. Flame* 106 (1996) 168–183.
- [14] J.C. Rolon, D. Veyante, J.P. Martin, F. Durst, *Exp. Fluids* 11 (1991) 313–324.
- [15] C.D. Carter, J.M. Donbar, J.F. Driscoll, *Appl. Phys. B* 66 (1998) 129–132.
- [16] J. Luque, R.J.H. Klein-Douwel, J.B. Jeffries, D.R. Crosley, *Appl. Phys. B* 71 (2000) 85–94.
- [17] J.W. Daily, E.W. Rothe, *Appl. Phys. B* 68 (1999) 131–140.
- [18] J. Luque, D.R. Crosley, *LIFBASE: database and spectral simulation program (Version 1.5)*, Report No. MP 99-009, SRI International, 1999.
- [19] J.F. Grcar, R.J. Kee, M.D. Smooke, J.A. Miller, *Proc. Combust. Inst.* 21 (1986) 1773–1782.
- [20] I. Yamaoka, H. Tsuji, *Proc. Combust. Inst.* 20 (1984) 1883–1892.
- [21] C.M. Vagelopoulos, F.N. Egolfopoulos, C.K. Law, *Proc. Combust. Inst.* 25 (1994) 1341–1347.
- [22] D.L. Zhu, F.N. Egolfopoulos, C.K. Law, *Proc. Combust. Inst.* 22 (1988) 1537–1545.

### Comment

Christopher Cadou, University of Maryland, USA. How would you determine velocity in regions away from the centerline, where the streaklines are curved?

*Reply.* Data in flow regions with both axial and radial velocities can be processed to give both vector components. The start-to-start (or end-to-end) distance from a streak pair can be measured in both the axial and radial directions. These two lengths are converted to two velocity components by dividing them by the chopping period. The resultant velocity data ( $u, v$ ) can be applied at the loca-

tion ( $x, r$ ) that corresponds to the midpoint of the trajectory. As with any particle tracking method, such as Particle Image Velocimetry (PIV), choosing an appropriate Lagrangian time that is represented by the chopping period in this technique can minimize error. In areas of large curvature, the Lagrangian time must be small to minimize the error introduced by approximating the profiles as piecewise linear segments. Particle Streak Velocimetry can be used to extract data in high-curvature regions of the flow in an equivalent manner to PIV, with the data obtained from individual particle trajectories.

# Charge-Injection Noise in CCDs

Brian Kern

**Abstract**—An analysis of the noise associated with electronic charge injection in charge-coupled devices (CCDs) is presented, including the effects of diffusion currents. The capacitance of the injection circuit determines the charge-injection noise, and specification of the noise requires consideration of the quoted capacitance; for large charge packets, the noise has a characteristic variance of  $kTC/2$  or  $kTC$ , depending on whether the capacitance is defined by microscopic (internal) or macroscopic (external) potentials. The variance is Poissonian for small charge packets. The noise values presented in this paper may serve as a target when optimizing charge-injection operation of a CCD.

**Index Terms**—Charge-coupled devices (CCDs), diffusion processes, MOSFETs, shot noise.

## I. INTRODUCTION

**C**HARGE-INJECTION circuits were a necessary component of the first charge-coupled devices (CCDs) when their primary application was to serve as a memory device [1]. Charge-injection circuits generate charge packets whose sizes are related to input voltages, allowing memory to be written. After DRAM dominated the market for solid-state memory and CCD-based memory development was largely abandoned, the need for charge injection was mostly limited to diagnostic applications, and many CCD designs omitted any charge-injection circuits.

There has been a renewed interest in electronic charge injection with the optimization of CCDs for astronomical X-ray imaging. X-ray CCDs have flown on sounding rockets [2] and on the ASCA [3], XMM-Newton [4], Chandra [5], HETE-2 [6], Swift [7], and Suzaku [8] X-ray satellites as well as the failed SAC-B and Astro-E missions. X-ray CCDs are generally intended to record individual isolated X-ray photons, whose energy can be determined by the size of the charge packet generated in a small number of neighboring pixels. Low charge transfer efficiency (CTE) degrades this energy resolution, and the CTE of CCDs in orbit degrades over time due to radiation damage [9]. Electronic charge injection can be used to fill those traps before the photogenerated signal charge is collected and read out, improving CTE and restoring energy resolution [10], [11]. However, charge-injection noise also degrades the energy resolution, so care must be taken to minimize charge-injection noise for this technique to have a net benefit on the energy resolution.

Using a MOSFET analogy, early theoretical calculations predicted an injected-charge variance of  $2/3 kTC$  [12], [13],

with  $C$  being the characteristic capacitance of the potential well into which the charge is injected. Of published measurements of charge-injection noise, the lowest are approximately  $kTC$  [14]–[16]. The “soft reset” of CMOS active pixel sensor (APS) devices is similar to charge injection, and theory and experiment have shown  $kTC/2$  levels of noise [17], [18]. In recent years, CCD read noise has dropped to the  $1\text{--}3 e^-$  level, and the charge packets being injected may be as small as tens of  $e^-$ , prompting a refined analysis of the fundamental limit of charge-injection noise.

This paper describes two calculations of charge-injection noise appropriate to the conditions in which charge injection is currently used. First, a one-dimensional (1-D) model is described that allows a thorough algebraic analysis and admits some insight into the process. Second, a two-dimensional (2-D) model is described and solved numerically, with the intent that this model should be relevant to the X-ray Imaging Spectrometer (XIS) CCDs on board Suzaku [16].

## II. CHARGE INJECTION TECHNIQUE

Charge-injection is commonly performed using a “surface potential equilibration” technique [19], which is commonly referred to as “fill and spill.” An input diode and input gate are added to the end of a serial register, as shown in Fig. 1. The process involves three steps: fill, spill, and transfer. First, the input diode is brought low, which fills the channel under the input gate and the collecting well with electrons. Next, the input diode is brought high, which allows the charge to spill back into the diode. In the absence of diffusion, this spilling would stop when the collecting-well potential equals the channel potential under the input gate (equilibration). With diffusion present, the spill continues beyond equilibration at a reduced current. Last, at some predetermined time, the remaining charge is transferred down the serial register as the injected charge. The amount of charge injected is determined by the difference in the externally applied voltages at the collecting well and the input gate ( $V_W - V_G$ ) and can be varied by changing either voltage (or both).

If diffusion were negligible [no current in Fig. 1(c)], the current flow would stop when the channel potentials are equal (equilibration) ( $\phi_G = \phi_W$ ), where  $\phi_G$  and  $\phi_W$  are the gate and collecting-well channel potentials. The number of electrons in the collecting well at equilibration [ $N_0 = N(t_0)$ ] would be

$$N_0 = N_{tr} = C(V_W - V_G)/q \quad (1)$$

where  $V_W$  and  $V_G$  are externally applied voltages, and  $N_{tr} = N(t_{tr})$  is the number of electrons in the collecting well when serial transfer begins.

Manuscript received December 30, 2005; revised July 10, 2006. The review of this paper was arranged by Editor J. Hynecik.

The author was with the California Institute of Technology, Pasadena, CA 91125 USA. He is now with the Jet Propulsion Laboratory, Pasadena, CA 91019 USA (e-mail: Brian.D.Kern@jpl.nasa.gov).

Digital Object Identifier 10.1109/TED.2006.882271

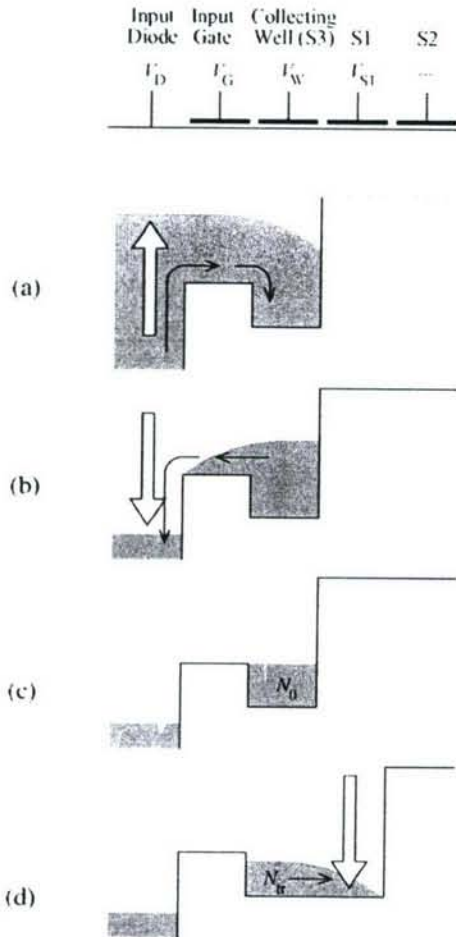


Fig. 1. Fill-and-spill sequence. The input diode and input gate are shown attached to the end of an ordinary serial register (with phases S3, S1, S2, etc.). Broad white arrows show a change in channel potential due to a change in the external gate or diode voltages; thin arrows show flow of electrons. In (a), the input diode is pulsed low (up on the plot), filling the potential wells with electrons. In (b), the input diode is brought high, allowing electrons to spill out of the CCD. When the channel well potential equilibrates with the potential under the input gate, at  $t = 0$ , the number of electrons in the collecting well is  $N_0$ . In (c), the spill operation continues, but the current is now dominated by diffusion, which is shown with a shaded arrow. In (d), serial transfer begins at time  $t_{tr}$ , carrying the remaining  $N_{tr} < N_0$  electrons out through the serial register, as the injected charge.

Diffusion processes, however, play a dominant role in charge injection. The diffusion processes involved have a natural thermal scaling. The thermal potential  $\phi_T$  is

$$\phi_T = kT/q \quad (2)$$

where  $q$  is the electron charge. It will be assumed throughout this analysis that the CCD is operated cooled to 150 K, giving  $\phi_T = 0.013$  V. This potential also implies a thermal electron number  $N_T$ , which is defined dimensionally as

$$N_T = C\phi_T/q \quad (3)$$

$$= kTC/q^2 \quad (4)$$

where  $C$  is the characteristic capacitance of the collecting well. The characteristic  $C$  is very different for the 1-D and 2-D models;  $N_T$  in this analysis ranges from 1000 for the 1-D model

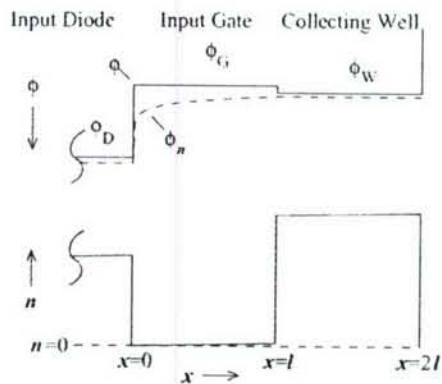


Fig. 2. Representative channel potential  $\phi$ , electron quasi-Fermi potential  $\phi_n$ , and electron density  $n$ , as functions of position, which are shown during a spill operation once  $\phi_W > \phi_G$  (i.e.,  $t > 0$ , after equilibration), for a 1-D model. The dotted line in the top plot is electron quasi-Fermi potential  $\phi_n$ , which is continuous everywhere (even at  $x = 0$ ). The electron density  $n$  has a constant nonzero slope under the input gate.

to  $\sim 10$  for a 2-D model (more closely approximating the real world), depending on the operating conditions. Typical spill operations may last on the order of microseconds; except where noted otherwise, this analysis assumes  $t_{tr} = 1 \mu\text{s}$ , where  $t = 0$  is defined by equilibration (the time between the beginning of the spill and equilibration is negligible compared to  $1 \mu\text{s}$ ). As an order of magnitude assumption, the end result is that  $N_0 - N_{tr} \sim 6-10 N_T$ , i.e., the total charge spilled after equilibration is several  $N_T$ .

### III. 1-D ANALYSIS

In 1-D, analogous to obsolete surface channel devices, the channel potentials are nearly constant under each gate but discontinuous between gates (see Fig. 2). The analysis presented here assumes that diffusion currents dominate over drift currents, with a consistency check to justify this assumption. The noise in the injected charge is then calculated.

#### A. 1-D Current

The 1-D geometry, when  $\phi_W > \phi_G$  (i.e., after equilibration), is shown in Fig. 2. The gates all have length  $l$  ( $l$  is measured in the  $x$ -direction). The channel potential  $\phi(x)$  is approximately constant with  $x$  except at gate boundaries; it takes on values of  $\phi_D$ ,  $\phi_G$ , and  $\phi_W$  in the channel under the input diode, input gate, and collecting well, respectively. The electron density  $n(x)$  at every point is defined by the channel potential  $\phi(x)$  and the electron quasi-Fermi potential  $\phi_n(x)$

$$n(x) = n_0 e^{(\phi(x) - \phi_n(x))/\phi_T} \quad (5)$$

where  $n_0$  is the bulk concentration of electrons (i.e.,  $N_D$  number density of donors, for  $n$ -type Si). The electron current, incorporating both drift and diffusion components, is [20]

$$J_n(x) = q\mu_n n(x) \frac{\partial}{\partial x} \phi_n(x) \quad (6)$$

where  $J_n$  is the electron current density, and  $\mu_n$  is the electron mobility. Approximately, in the collecting well,  $n$  is large,

and  $(\partial/\partial x)\phi_n$  is small. Under the input gate,  $n$  is small, and  $(\partial/\partial x)\phi_n$  is large (see Fig. 2).

The first assumption to be made, hereafter referred to as (A1), is that the input diode is held high [ $\phi_D - \phi_G > 100\phi_T$  (a few volts)], so that  $n(0^+) = n(0^-) e^{-(\phi_D - \phi_G)/\phi_T} \sim 0$ . The second assumption (A2) is that the electron density under the input gate is significantly smaller than that in the collecting well (true shortly after equilibration), which is arbitrarily quantified as  $\phi_W - \phi_G > 3\phi_T$ .

The third assumption (A3) is that  $\phi(x)$  under the input gate can be treated as a constant for  $0 < x < l$ , i.e.,  $\phi(x) = \phi_G$ , when evaluating (5). This implicitly assumes that diffusion dominates. The fourth assumption (A4) is that  $J_n(x)$  is constant for  $0 < x < l$ , i.e.,  $|q(\partial/\partial t)n| = |(\partial/\partial x)J_n| \ll |J_n/l|$ . Taking all these assumptions together, the solution to (5) and (6) gives

$$n(x) = n(l^-) x/l, \quad \text{for } 0 < x < l. \quad (7)$$

Approximating  $n(x) = n_W$  as a constant with  $x$  for  $l < x < 2l$  (i.e., in the collecting well), which is a consequence of (A2)

$$n(l^-) = n_W e^{-(\phi_W - \phi_G)/\phi_T}. \quad (8)$$

The number of electrons in the collecting well is then

$$N = whl n_W \quad (9)$$

$$= N_0 - C(\phi_W - \phi_G)/q \quad (10)$$

where  $w$  and  $h$  are characteristic width and height (whose values are not important). Here,  $N$  is not a function of  $x$  (it is a sum over  $l < x < 2l$ ) and always refers to the number of electrons in the collecting well. This simplifies (7) for the electron density under the input gate to

$$n(x) = (N/whl) e^{(N-N_0)/N_T} x/l. \quad (11)$$

Using a diffusion-only current equation [instead of the full current in (6) and (11), the current  $I$  under the input gate is

$$I = qD_n wh \frac{\partial}{\partial x} n(x) \quad (12)$$

$$= (q/\tau_D) N e^{(N-N_0)/N_T} \quad (13)$$

where  $D_n$  is the electron diffusion coefficient (Einstein relation is  $D_n = \mu_n \phi_T$ ), and  $\tau_D$  is the diffusion timescale

$$\tau_D = l^2/D_n. \quad (14)$$

Recognizing that  $I = -q(d/dt)N$ , (13) can be solved for  $N$ , giving

$$\Gamma(0, N/N_T) = \Gamma(0, N_0/N_T) + t/\tau_D e^{-N_0/N_T} \quad (15)$$

where  $\Gamma(i, z)$  is the upper incomplete gamma function,  $\Gamma(i, z) = \int_z^\infty e^{-y} y^{i-1} dy$ , and  $t$  is the elapsed time since equilibrium (when  $N = N_0$ ). Note that all the variables in (15) are constant during a spill except for  $N$  and  $t$ .

The gamma function in (15) has two simple limiting forms for large and small  $N/N_T$ . For  $N/N_T \gg 1$

$$\Gamma(0, N/N_T) \sim e^{-N/N_T}/(N/N_T) \quad (16)$$

$$N \sim N_0 - N_T \ln [(N/N_T)t/\tau_D + 1]. \quad (17)$$

Note that  $N$  appears on both sides of this equation. For  $N/N_T \ll 1$

$$\Gamma(0, N/N_T) \sim -\ln(N/N_T) - \gamma \quad (18)$$

$$N \sim N_T e^{-[\Gamma(0, N_0/N_T) + t/\tau_D e^{-N_0/N_T} + \gamma]} \quad (19)$$

where  $\gamma$  is the Euler–Mascheroni constant ( $\gamma \approx 0.577$ ). The general features of these approximations are that for large  $N/N_T$ ,  $N$  decreases nearly logarithmically in time, and for small  $N/N_T$ ,  $N$  is exponential with time. At a given time, for large  $N/N_T$ , (17) gives a value of  $N$  that is strictly larger than the true  $N$  from (15), and for small  $N/N_T$ , (19) gives a value of  $N$  that is strictly smaller than the true  $N$ .

The second assumption (A2) listed above required that  $\phi_W - \phi_G > 3\phi_T$ , which is rewritten as  $N_0 - N > 3N_T$ . This does not preclude the injection of small charge packets; for  $t_{tr} = 1 \mu\text{s}$ ,  $N_0 = 3300$  ( $N_0 = 3.3N_T$ ) gives  $N_{tr} = 1$ . A spill operation beginning with  $N_0 = 3300$  ceases to violate assumption (A2) after 150 ns, so even in this most restrictive practical case ( $N_{tr} = 1$ ), the majority of the 1- $\mu\text{s}$  spill time is spent in agreement with the assumption.

To confirm Assumption (A3) by calculating the drift currents under the input gate, the electron densities given by (11) are assumed to give rise to small deviations of  $\phi(x)$  from  $\phi_G$  that create electric fields (self-induced drift)

$$\phi(x, t) = \phi_G - [q N e^{(N-N_0)/N_T} / C] (x/l). \quad (20)$$

The ratio of drift to diffusion currents  $R$ , which must satisfy  $R < 1$  to justify (A3) neglecting the deviations in  $\phi(x)$ , is

$$R = \left[ q\mu_n n \frac{\partial}{\partial x} \phi \right] / \left[ qD_n \frac{\partial}{\partial x} n \right] \quad (21)$$

$$< (N/N_T) e^{(N-N_0)/N_T} \quad (22)$$

where the variation of  $n/(\partial/\partial x)n$  with  $x$  is ignored (it is evaluated at its maximum, for  $x = l$ ). Because  $R$  is monotonically increasing with  $N$ , and (17) gives  $N$  strictly larger than those of (15), evaluating (22) using  $N$  from (17) gives a sufficient constraint. Combining (17) and (22), after some rearranging, the constraint  $R < 1$  is guaranteed when  $t > \tau_D$ .

The assumption that the current is constant under the input gate (A4) is  $|q(\partial/\partial t)n| = |(\partial/\partial x)J_n| \ll |J_n/l|$ . Since  $J_n/l = I/(whl) = -(q/whl)(d/dt)N$ , (A4) becomes

$$\left| q/(whl) \frac{d}{dt} \left( N e^{(N-N_0)/N_T} \right) \right| \ll \left| q/(whl) \frac{d}{dt} N \right| \quad (23)$$

$$(N/N_T + 1) e^{(N-N_0)/N_T} \ll 1. \quad (24)$$

The difference between this equation and (22), which is the constraint on (A3), will be ignored here because  $t > \tau_D$  is exceeded by factors of  $> 100$  for the times of interest.

The constraints imposed by the four itemized assumptions (A1)–(A4), are summarized here:

$$(A1) \phi_D - \phi_G > 148 \phi_T \quad (25)$$

$$(A2) N_0 - N > 3N_T \quad (26)$$

$$(A3) t > \tau_D \quad (27)$$

$$(A4) t > \tau_D. \quad (28)$$

In all practical cases, these conditions are all met for the majority of the spill time.

### B. 1-D Injection Noise

Because diffusion currents carry the charge during most of the spill operation, the current noise is shot noise. The diffusion current at the input gate/input diode boundary flows only in one direction (reverse current is smaller by  $> e^{100}$ ), which is analogous to a saturated weakly inverted (subthreshold) MOSFET or a saturated reverse-biased p-n junction diode. As such, the shot noise comes from the current flowing in only one direction (half the unsaturated shot noise), and the noise current  $\Delta I$  has autocorrelation

$$\langle \Delta I(t') \Delta I(t'') \rangle = qI(t')\delta(t' - t'') \quad (29)$$

where  $\delta$  is the Dirac delta function [21]–[23].

The analysis of noise in the spill operation cannot be performed in the frequency domain, as the spill operation is not periodic (it never reaches a steady-state equilibrium), and the instantaneous current noise is a function of the (nonperiodic) current. Following exactly the prescription of Demir *et al.* [24] for time-domain analysis of a circuit with additive white noise, we assume that the current noise is a perturbation on the noise-free behavior, and we write a stochastic differential equation relating the noise-free  $N$  to a stochastic process

$$\frac{d}{dt}N - \left( \frac{d^2}{dt^2}N / \frac{d}{dt}N \right)N + \left( -\frac{d}{dt}N \right)^{1/2} \nu = 0 \quad (30)$$

where  $\nu$  is a standard white Gaussian stochastic process. There is a corresponding ordinary differential equation specifying the evolution of the integrated time-dependent noise variance  $K(t) = \langle \Delta N(t)^2 \rangle$

$$dK/dt = 2 \left( \frac{d^2}{dt^2}N / \frac{d}{dt}N \right) K - \frac{d}{dt}N. \quad (31)$$

Given a functional form for  $N$  and an initial value for  $K$ , (31) can be solved to determine the noise at any time  $t$ . Equation (31) is evaluated for a range of values of  $N_0$ , assuming  $N_T = 1000$ ,  $\tau_D = 6$  ns, and  $t_{tr} = 1 \mu\text{s}$  in Fig. 3.

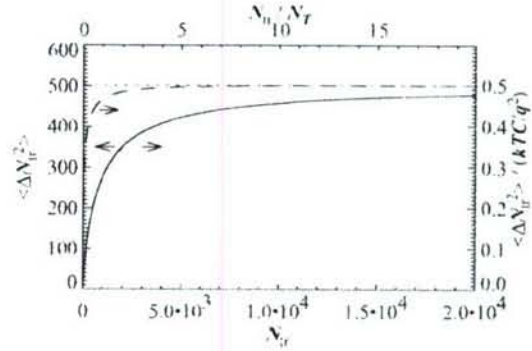


Fig. 3. Variance of number of electrons injected  $\langle \Delta N_{tr}^2 \rangle$  versus injected charge  $N_{tr}$  for a 1-D device. The solid line represents  $\langle \Delta N_{tr}^2 \rangle$  and is referenced both on the left  $y$ -axis in electron counts and on the right  $y$ -axis normalized by  $N_T = kTC/q^2$ . The dashed line references only the right  $y$ -axis and is  $\langle \Delta N_{tr}^2 \rangle$  normalized by  $kTC_{ext}/q^2$ , with the external capacitance  $C_{ext}$  defined relative to the external voltages rather than the internal potentials. Horizontal arrows denote which  $y$ -axis labels apply to each plot. The dotted line shows the asymptotic value of  $\langle \Delta N_{tr}^2 \rangle / N_T = 1/2$ .

There are two useful limiting cases of (31): for  $N/N_T \gg 1$  and for  $N/N_T \ll 1$ . When  $N/N_T \gg 1$  and  $t/\tau_D \gg 1$ , (17) gives  $(d/dt)N \sim -N_T/t$ , and assuming  $K(0) = 0$

$$\langle \Delta N(t)^2 \rangle = N_T/2. \quad (32)$$

When  $N/N_T \ll 1$ , (19) gives

$$\langle \Delta N(t)^2 \rangle = N(t). \quad (33)$$

In both of these cases, the form of (31) makes the dependence of  $K(t)$  on  $K(0)$  decay exponentially on timescales of  $\tau_D$  (note that  $(d^2/dt^2)N/(d/dt)N < 0$ ), so  $K(0)$  can safely be set to zero without practical consequences. To summarize, the diffusion noise leaves large charge packets with  $kTC/2$  variance and small charge packets with Poisson variance.

The capacitance  $C$  in (4) and (10) has been assumed to be constant at all times and for all values of  $N$ . This capacitance is essentially defined by  $C = q\partial N/\partial\phi_W$  [see (10)]. The collecting-well potential  $\phi_W$  is not measurable externally. If one defines an external capacitance as  $C_{ext} = q(dN_{tr}/dV_W)$ , where  $V_W$  is the externally applied collecting-well voltage, the noise follows the dashed line in Fig. 3, which is much closer to  $\langle \Delta N_{tr}^2 \rangle = (1/2)kTC_{ext}/q^2$ . The values of  $C_{ext}$  used in Fig. 3 were calculated numerically from (15).

### IV. 2-D ANALYSIS

The 2-D analysis is complicated by the fact that the potentials in the buried channel cannot be approximated algebraically from the applied gate voltages, but must be approximated numerically in  $x$ , across gate structures, and in  $z$ , perpendicular to the CCD surface. The calculations estimate the potentials, electron densities, and current densities in two dimensions as a function of applied gate voltages and total number of electrons in the collecting well.

### A. Iterative Analysis Procedure

The continuous spilling of electrons is calculated here at a number of snapshots in time, calculating the instantaneous potentials, electron densities, and currents at each snapshot. The time between snapshots is then estimated from the instantaneous current densities and the change in electron densities between snapshots.

The instantaneous potentials, electron densities, and current densities are determined iteratively in three steps. First, given the gate voltages and an estimate of the electron densities, the potentials are calculated using Gauss' law. Second, given the potentials and electron densities, the electron quasi-Fermi potentials can be determined, which determine the currents. Third, the currents are integrated for a very short time to determine the changes in the electron densities, which are then renormalized to the total number of electrons in the collecting well, and fed back into the first step. The time for irregular distributions of electrons and current in 2-D to relax to a quasi-steady state solution, where the current is limited by flow over the input gate, is short compared to the time for the total electron population in the collecting well to decrease significantly. As such, from arbitrary initial distributions for an individual snapshot, iterating these three steps will yield a quasi-steady state solution that accurately represents the instantaneous conditions (potentials, electron, and current densities). It is worth noting that the thermal electron number  $N_T$  is not constant here, as the capacitance varies strongly with  $N$ .

### B. Numerical-Analysis Results

The geometry assumed throughout this analysis was intended to represent the CCDs in the XIS instrument on Suzaku. These are deep-depletion CCDs on high-resistivity silicon, which are approximated here with abrupt p-n junctions, with a donor number density of  $N_D = 2 \times 10^{16} \text{ cm}^{-3}$  to a depth of  $0.6 \mu\text{m}$ , and an acceptor number density  $N_A = 5 \times 10^{14} \text{ cm}^{-3}$  extending to the substrate. A  $0.1\text{-}\mu\text{-thick}$   $\text{SiO}_2$  layer separates the gates from the silicon. The width of the collecting well is half that of the input diode and input gate at  $3 \mu\text{m}$  instead of  $6 \mu\text{m}$ . During the spill operation, the gate voltages were held fixed, with  $V_D = 8 \text{ V}$  (the input diode is held high),  $V_G = 5 \text{ V}$ , and  $V_{S1} = 0 \text{ V}$  ( $V_{S1}$  acts as a barrier phase until serial transfer, as in Fig. 1). For a given charge-injection cycle,  $V_W$  is constant and determines the number of electrons in the collecting well as a function of time. In this analysis,  $V_W$  ranged from  $5.5$  to  $8 \text{ V}$ . In practice, it would likely be more practical to hold  $V_W$  fixed and vary  $V_G$  to control the charge injection, but the results should depend almost exclusively on  $V_W - V_G$ .

The calculated 2-D potentials show maxima that are confined to a narrow range of  $z$  (the depth dimension). As such, the pertinent variations in physical parameters can be plotted in one dimension  $x$ . A sample plot of potential and electron quasi-Fermi potential is shown in Fig. 4.

After a series of snapshot, quasi-steady state solutions for different  $V_W$  and  $N$  are calculated, the elapsed time between successive snapshots is estimated from the calculated currents. Given a total spill time, which is  $t_{tr} = 1 \mu\text{s}$  in this case, a

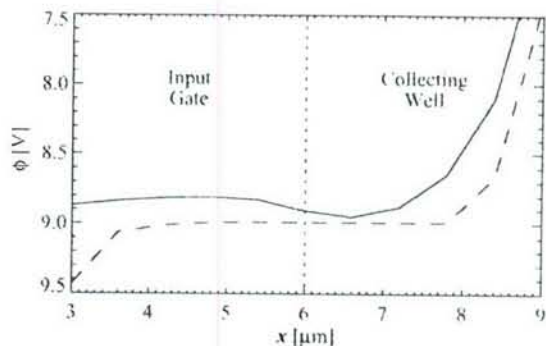


Fig. 4. Sample plot of potential (solid) and electron quasi-Fermi potential (dashed) versus  $x$  (across gates) for  $V_W = 5.62 \text{ V}$  and  $V_G = 5 \text{ V}$  at  $t_{tr} = 1 \mu\text{s}$  for a 2-D device. This is calculated at  $T = 150 \text{ K}$  and corresponds to  $N_{tr} = 106$ . The input gate extends from  $x = 0 \mu\text{m}$  to  $x = 6 \mu\text{m}$ , and the collecting well extends from  $x = 6 \mu\text{m}$  to  $x = 9 \mu\text{m}$ . In the region of the input gate for  $x < 3 \mu\text{m}$ , which is not plotted here, the electric fields are large and the electron densities are very small; the electrons that diffuse over the potential minimum at  $x \sim 5 \mu\text{m}$  are quickly carried away by the electric fields (there is no return current). Note that the electrons are confined to a small region near  $x \sim 6.5 \mu\text{m}$ ; the collecting-well capacitance decreases as  $N$  decreases.

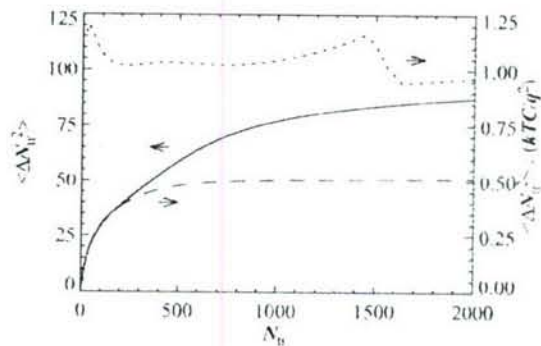


Fig. 5. Noise variance of the injected charge  $\langle \Delta N_{tr}^2 \rangle$  versus the injected charge  $N_{tr}$  for a 2-D calculation. The solid line represents  $\langle \Delta N_{tr}^2 \rangle$  measured in electrons, referenced only to the left  $y$ -axis, the dashed line represents  $\langle \Delta N_{tr}^2 \rangle$  normalized by  $C_{int}$ , referenced only to the right  $y$ -axis, and the dotted line represents  $\langle \Delta N_{tr}^2 \rangle$  normalized by  $C_{ext}$ , referenced only to the right  $y$ -axis. Horizontal arrows denote which  $y$ -axis labels apply to each plot. It is not known if the deviations of  $\langle \Delta N_{tr}^2 \rangle / (kTC_{ext}/q^2)$  from unity (dotted line) are artifacts of the numerical analysis.

one-to-one relationship is established between gate voltages and number of electrons  $N_{tr}$  remaining at the end of the spill operation.

The noise can be calculated from the numerical estimates of current versus time. As in the 1-D analysis, the first step is to determine the conditions under which the current is dominated by diffusion. Calculating the ratio of drift to diffusion currents  $R$  using (21), for all cases considered here, the currents become diffusion dominated ( $R < 1$ ) by  $t \sim 1 \text{ ns}$ . Comparing this to  $t_{tr} = 1 \mu\text{s}$ , it is safe to say that the currents are diffusion dominated under all conditions.

The noise variance, which is calculated according to (31), is shown in Fig. 5 along with the noise variance normalized by two different estimates of the capacitance. The internal capacitance can be defined by  $C_{int} = q\partial N/\partial\phi_W$  and evaluated at  $t = t_{tr}$ . The external capacitance can be defined by  $C_{ext} = qdN_{tr}/dV_W$ . The asymptotic behavior for large  $N_{tr}$  normalized to  $C_{int}$  is  $\langle \Delta N_{tr}^2 \rangle = (1/2)kTC_{int}/q^2$ . When normalized by

$C_{\text{ext}}$ ,  $\langle \Delta N_{\text{tr}}^2 \rangle \approx kTC_{\text{ext}}/q^2$  for nearly all cases. For small  $N_{\text{tr}}$ ,  $\langle \Delta N_{\text{tr}}^2 \rangle \sim N_{\text{tr}}$ , just as in the 1-D case.

## V. DISCUSSION

For virtually all charge-injection levels of interest, where the injected charge is on the order of thousands of electrons or less and the spill time is on the order of microseconds, the currents during the spill operation are dominated by diffusion. The noise in the injected charge is then governed by shot noise, resulting in a noise variance of  $kTC/2$  for one choice of capacitance. In a 2-D analysis, however, the only measurable capacitance  $C_{\text{ext}}$  defined by varying the input voltages and examining the resulting injected charge normalizes the noise variance to  $kTC_{\text{ext}}$ .

At a practical level, these answers are not dramatically different from the previously calculated  $(2/3)kTC$  using strongly inverted MOSFET analogies [12], [13], and the  $(1/2)kTC$  large-signal answer agrees with the analysis of soft resets of CMOS APS devices [17], [18]. As with the APS soft-reset analyses, the drift currents are negligible compared to the diffusion currents (analogous to weakly inverted MOSFETs), but this analysis points out the need to carefully define the pertinent capacitance  $C$ . For small charge packets, this analysis predicts Poisson variance, as is predicted for APS soft resets [18].

The actual behavior of the XIS CCDs, which this analysis intended to represent, is reported by Prigozhin *et al.* [16] to show  $\sim kTC_{\text{ext}}$  noise (see [16, Fig. 3]). Their reported performance does not extend much below  $N_{\text{tr}} = 100$ , where this analysis would predict Poisson variance, so this prediction remains untested. While CCD geometry and operating conditions analyzed here differ somewhat from the actual XIS CCDs, and this analysis extends only to two dimensions, the prediction of  $kTC$  noise (as opposed to  $kTC/2$ ) is in modest agreement, although exact numerical correspondence is loose.

The analysis presented here is derived purely from first principles of charge transport, using electron quasi-Fermi potentials to calculate both drift and diffusive currents, showing that diffusion dominates and presenting a noise analysis of the diffusion currents. This approach differs from the APS soft-reset analyses in that their calculations have used a MOSFET analogy, which should be applicable but tend to obscure the mechanics (diffusion) of the processes, and the noise calculations rely on implicit assumptions that may not be obvious (absence of short-channel effects, etc.).

The approach taken in this analysis also applies to CCD blooming calculations, where diffusion carries charge over potential barriers, as has been calculated by rules-of-thumb [1] and more careful analysis [25]. However, both these blooming analyses invoked thermionic emission as the mechanism governing the current flow between buried channels at different potentials; simple drift-diffusion transport is the mechanism, as is captured consistently with quasi-Fermi potentials, while thermionic emission is applicable to the current flow across an interface between dissimilar media. In related contexts, the standard thermionic formulation can lead to inconsistencies for small barrier heights (below  $kT/q$ ) [26], as when the "interface" is between similar (or, in this case, identical) media.

The blooming analyses cited here are unchanged by using a drift-diffusion formulation, but as a semantic note, the derivation of currents should invoke diffusion rather than thermionic emission.

## ACKNOWLEDGMENT

This analysis began as a tangent to a discussion with E. Atlas and D. Lang, which was then pointed in the right direction by Prof. C. Stubbs and Prof. P. Dimotakis.

## REFERENCES

- [1] J. R. Janesick, *Scientific Charge-Coupled Devices*. Bellingham, WA: SPIE, 2001.
- [2] J. A. Mendenhall and D. N. Burrows, "CCD sounding rocket observation of the high-latitude soft X-ray background," *Astrophys. J.*, vol. 563, no. 2, pp. 716–723, Dec. 2001.
- [3] B. E. Burke, R. W. Mountain, P. J. Daniels, M. J. Cooper, and V. S. Dolat, "CCD soft X-ray imaging spectrometer for the ASCA satellite," *IEEE Trans. Nucl. Sci.*, vol. 41, no. 1, pp. 375–385, Feb. 1994.
- [4] H. Soltan *et al.*, "Performance of the *pn*-CCD X-ray detector system designed for the XMM satellite mission," *Nucl. Instrum. Methods Phys. Res. A. Accel. Spectrom. Detect. Assoc. Equip.*, vol. 377, no. 2, pp. 340–345, Aug. 1996.
- [5] B. E. Burke, J. A. Gregory, M. W. Bautz, G. Y. Prigozhin, S. E. Kissel, B. B. Kosicki, A. H. Loomis, and D. J. Young, "Soft-X-ray CCD imagers for AXAF," *IEEE Trans. Electron Devices*, vol. 44, no. 10, pp. 1633–1642, Oct. 1997.
- [6] R. Vanderspek, J. Villaseñor, J. Doty, J. G. Jernigan, A. Levine, G. Monnelly, and G. R. Ricker, "GRB observations with the HETE soft X-ray cameras," *Astron. Astrophys. Suppl. Ser.*, vol. 138, no. 3, pp. 565–566, Sep. 1999.
- [7] D. N. Burrows *et al.*, "The Swift X-ray telescope," *Proc. SPIE*, vol. 5165, pp. 201–216, 2004.
- [8] H. Matsumoto *et al.*, "X-ray imaging spectrometers (XIS) of Astro-E2," *Nucl. Instrum. Methods Phys. Res. A. Accel. Spectrom. Detect. Assoc. Equip.*, vol. 541, no. 1/2, pp. 357–364, Apr. 2005.
- [9] J. Janesick, T. Elliott, and F. Pool, "Radiation damage in scientific charge-coupled devices," *IEEE Trans. Nucl. Sci.*, vol. 36, no. 1, pp. 572–578, Feb. 1989.
- [10] L. K. Townsley, P. S. Broos, G. P. Garnire, and J. A. Nousek, "Mitigating charge transfer inefficiency in the Chandra X-ray observatory advanced CCD imaging spectrometer," *Astrophys. J.*, vol. 534, no. 2, pp. L139–L142, May 2000.
- [11] H. Tomida, H. Matsumoto, M. Ozaki, Y. Tazawa, H. Awaki, T. Tsuru, K. Koyama, H. Tsunemi, and K. Yamamoto, "Radiation damage on X-ray CCDs and restoration technique for space astronomy," *Publ. Astron. Soc. Jpn.*, vol. 49, no. 3, pp. 405–412, 1997.
- [12] K. K. Thomsen, "Noise suppression in charge transfer devices," *Proc. IEEE*, vol. 60, no. 9, pp. 1113–1114, Sep. 1972.
- [13] S. P. Emmons and D. D. Buss, "Noise measurements on the floating diffusion input for charge-coupled devices," *J. Appl. Phys.*, vol. 45, no. 12, pp. 5303–5306, Dec. 1974.
- [14] A. M. Mohsen, M. F. Thompson, and C. H. Sequin, "Noise measurements in charge-coupled devices," *IEEE Trans. Electron Devices*, vol. ED-22, no. 5, pp. 209–218, May 1975.
- [15] R. W. Brodersen and S. P. Emmons, "Noise in buried channel charge-coupled devices," *IEEE J. Solid-State Circuits*, vol. SSC-11, no. 1, pp. 147–155, Feb. 1976.
- [16] G. Prigozhin, B. Burke, M. Bautz, S. Kissel, B. LaMarr, and M. Freytsis, "X-ray CCD with charge injection structure," *Proc. SPIE*, vol. 5501, pp. 357–365, 2004.
- [17] H. Tian, B. Fowler, and A. El Gamal, "Analysis of temporal noise in CMOS photodiode active pixel sensor," *IEEE J. Solid-State Circuits*, vol. 36, no. 1, pp. 92–101, Jan. 2001.
- [18] E. R. Fossum, "Charge transfer noise and lag in CMOS active pixel sensors," in *Proc. IEEE Workshop Charge Coupled Devices and Adv. Image Sens.*, Schloss Elmau, Germany, 2003, pp. 1–6.
- [19] M. F. Thompson, "Surface potential equilibration method of setting charge in charge-coupled devices," *IEEE Trans. Electron Devices*, vol. ED-22, no. 6, pp. 305–309, Jun. 1975.
- [20] R. F. Pierret, *Semiconductor Fundamentals*. Reading, MA: Addison-Wesley, 1988.

- [21] R. Sarpeshkar, T. Delbruck, and C. A. Mead, "White noise in MOS transistors and resistors," *IEEE Circuits Devices Mag.*, vol. 9, no. 6, pp. 23–29, Nov. 1993.
- [22] A. van der Ziel, *Noise in Solid State Devices and Circuits*. Reading, MA: Wiley, 1986.
- [23] R. D. Thornton, *Characteristics and Limitations of Transistors*. New York: Wiley, 1966.
- [24] A. Demir, E. W. Y. Liu, and A. L. Sangiovanni-Vincentelli, "Time-domain non-Monte Carlo noise simulation for nonlinear dynamic circuits with arbitrary excitations," *IEEE Trans. Comput.-Aided Design Integr. Circuits Syst.*, vol. 15, no. 5, pp. 493–505, May 1996.
- [25] S. Kawai, N. Mutoh, and N. Teranishi, "Thermionic-emission-based barrier height analysis for precise estimation of charge handling capacity in CCD registers," *IEEE Trans. Electron Devices*, vol. 44, no. 10, pp. 1588–1592, Oct. 1997.
- [26] G. Chen, "Diffusion-transmission interface condition for electron and phonon transport," *Appl. Phys. Lett.*, vol. 82, no. 6, pp. 991–993, Feb. 2003.



**Brian Kern** received the Ph.D. degree in astronomy from Caltech, Pasadena, CA, in 2002, working on astronomical instrumentation.

After a postdoctoral appointment with Caltech working on interferometry and high-speed charge coupled devices (CCDs) detectors, he joined the Jet Propulsion Laboratory, Pasadena, CA, in 2005. His research interests are low-noise and high-speed CCD detectors, and optical interferometry and coronagraphy for astronomy.

J. M. Bergthorson · P. E. Dimotakis

## Particle velocimetry in high-gradient/high-curvature flows

Received: 4 November 2005 / Revised: 10 February 2006 / Accepted: 27 February 2006  
© Springer-Verlag 2006

**Abstract** Particle-velocimetry techniques typically rely on the assumption that particle velocities match fluid velocities. However, this assumption may be invalid if external forces or inertia cause the particle motion to differ from that of the flow. In this paper, particle motion through premixed stagnation flames is modeled, including Stokes-drag and thermophoretic forces. The finite time interval employed in particle-tracking techniques can act as a low-pass filter in flow regions with large curvature in the velocity field. To account for this effect, the modeled-particle-tracking profile for a specified time interval is estimated from the predicted particle position in time and compared to measurements. The implementation presented here is applicable to other simulated flow fields and allows direct comparisons with particle-velocimetry measurements. Expressions are also derived that allow particle-tracking data to be corrected for these effects.

### 1 Introduction

Particle-tracking techniques, such as particle image velocimetry (PIV) and particle streak velocimetry (PSV), rely on the measurement of the spatial displacement of a particle over a specified time interval (e.g., Adrian 1991). Most implementations assume that particle velocities match fluid velocities. However, particle-inertia, external forces, and possibly other effects may invalidate this assumption. The work presented here derives from studies of premixed flames in stagnation flows, where PSV is utilized to estimate axial velocities along the

centerline of strained premixed flames, augmented by planar laser induced fluorescence (PLIF) of CH radicals in the reaction zone (Bergthorson et al. 2005). Experimental data are compared to numerical predictions using the Cantera software package (Goodwin 2003). The simulations rely on a one-dimensional hydrodynamic model, with detailed chemistry models, multicomponent transport, and suitable boundary conditions. For the methane-air flames in this paper, the GRI-Mech 3.0 chemical-thermal-transport model (Smith et al. 2006) is utilized to simulate the stagnation-flame profiles.

A schematic of the stagnation-flame experimental geometry and a sample PSV image are given in Fig. 1. Flames generate regions with high spatial gradients and curvature in the velocity, density, and temperature fields. The flow field of a premixed stagnation flame can be described as arising from two stagnation flows joined through a region of high acceleration due to dilatation from the flame heat release (see Fig. 2). The dilatation in the flame preheat zone and the (cold) primary stagnation flow produce a local velocity minimum upstream of the flame, while the dilatation and the (hot) secondary stagnation flow produce a local maximum in the velocity field downstream of the flame. The large gradients that arise in the flame-front and wall thermal-viscous boundary-layer regions challenge particle-velocimetry techniques. Particles may lag the flow in high-velocity-gradient regions because of their inertia. Large temperature gradients impose thermophoretic forces in a direction opposite the temperature gradient. In addition, the finite time interval employed in particle-tracking techniques can act as a low-pass filter, but is dictated by cold-flow measurement requirements upstream of the flame. In aggregate, such effects can lead to systematic measurement errors and uncertainties.

Errors attributable to particle-inertia effects have been widely studied. Gilbert et al. (1955) investigated the velocity lag of particles through the reaction zone of a laminar flame. These authors solved the equation of particle motion, with the Stokes drag term as the only force, for the case of a linearly varying flow field and

J. M. Bergthorson (✉) · P. E. Dimotakis  
Graduate Aeronautical Laboratories,  
California Institute of Technology, Pasadena  
CA 91125, USA  
E-mail: jeffb@tyrvos.caltech.edu  
Tel.: +1-626-3954445  
Fax: +1-626-3954447

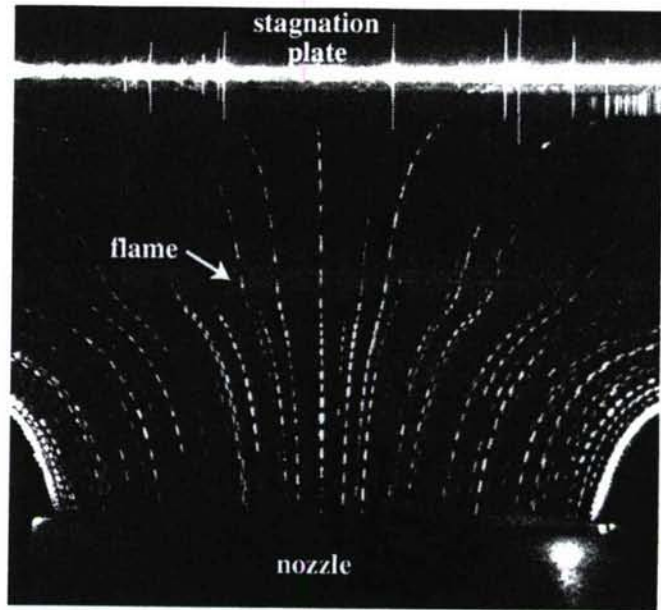
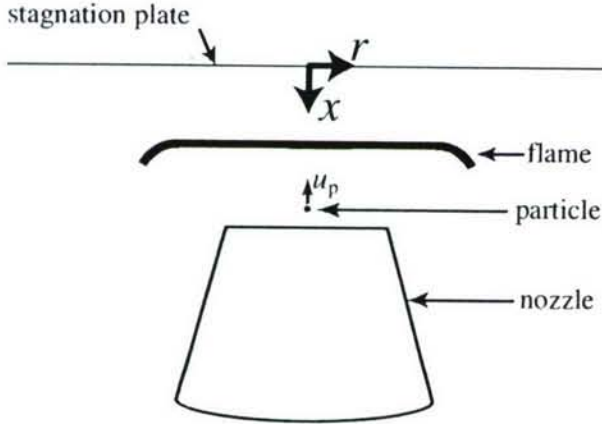


**Fig. 1** *Left:* Sketch of stagnation-flame experimental geometry. *Right:* sample PSV image in a  $\Phi=0.8$ , methane-air flame. Position through the flame,  $x$ , is measured from the stagnation wall and  $-u$  is plotted in all figures. Increasing particle time corresponds to decreasing  $x$

found significant lag in the reaction zone, even for small particles. Haghgoie et al. (1986) investigated laser Doppler velocimetry (LDV) techniques in turbulent flows and found that particles of 1 or 2  $\mu\text{m}$  in diameter should adequately follow velocity fluctuations in the flow up to 10 or 2 kHz respectively. Samimy and Lele (1991) studied the behavior of particles in a compressible shear layer, and recommend that the ratio of the Stokes time (see Eq. 13) to the flow time be kept below 0.05 for accurate flow visualizations. Melling (1997) discusses tracer particles and seeding for PIV and finds that a maximum particle size of 1  $\mu\text{m}$  is required to achieve a frequency response of 10 kHz, in accord with the findings of Haghgoie et al. (1986).

In combustion, additional considerations arise because of large temperature variations in the flow. The high spatial temperature gradients produce thermophoretic forces that influence particle motion through the reaction zone. This thermophoretic force results from the momentum imbalance between faster molecules striking the hot side of the particle and slower molecules colliding with the cold side of the particle. The momentum difference per unit time produces a net force that drives the particle away from the high-temperature region of the flow (see Talbot 1980). Sung et al. (1994) studied thermophoretic effects on seeding particles in LDV measurements of counterflow premixed flames. They found significant lag between the fluid and particle velocities in the preheat zone of the flame. In a subsequent study, Sung et al. (1996) studied lean methane-air flames and compared measured velocity profiles, using LDV, to simulated velocity profiles. These authors noted discrepancies between measurement and simulation in the reaction zone and the region

of the velocity maximum (high-temperature zone). They also compared their measurements to a velocity profile corrected for the effects of particle inertia and thermophoresis. The corrections bring the predicted and experimental profiles closer together, although the corrected profiles are still at variance with measurements in the region of maximum velocity. Using similar techniques, Jackson et al. (2003) compared laser Doppler velocimetry measurements in premixed methane-hydrogen counterflow flames at high strain rates to simulated velocity profiles and predicted particle profiles. Inclusion of inertial and thermophoretic effects in the particle profiles brings measurement and prediction into closer agreement, but the profiles again remain at variance in the region of maximum velocity. Egolfopoulos and Campbell (1999) studied dusty reacting flows numerically with thermal coupling between the gas and solid phases. They found that thermophoresis is significant for micron-sized particles in flames. Gravitational effects were found to be small for particles smaller than 5  $\mu\text{m}$ . Stella et al. (2001) investigated the application of PIV to combusting flows. They found that thermophoretic effects were significant for micron-sized particles, but noted that the main effect was a shift between the particle and fluid velocity profiles. These authors also discuss other sources of error that need to be considered when investigating turbulent reacting flows. Specifically, non-homogeneity and time-dependence of the refractive-index field was investigated as a source of light-sheet deflection, or beam steering, as well as image distortion. These authors find that at the laboratory scale, uncertainties associated with beam-steering effects can be neglected. The image distortion effect is only experienced in flames with time-dependent

index-of-refraction fields, and thus can be neglected in studies of steady laminar flames, such as those reported here.

In this paper, particle motion through the flow field of premixed stagnation flames is modeled in terms of Stokes drag and thermophoretic forces. For a given particle size and density, this yields a predicted particle velocity profile derived from the simulated (fluid) flow fields. From the predicted particle location in time, the profile measured by the particle-tracking technique for any chosen time interval can be estimated. The resulting modeled-particle-tracking (modeled-PT) profile can then be directly compared to measurements. The implementation is not flow-specific and may be applied to other simulated flows to permit direct comparison with particle-tracking velocimetry experiments. In addition, expressions are derived that allow particle-tracking velocimetry data to be corrected for particle-inertia and finite particle-track interval effects.

## 2 Particle motion in high-gradient/high-curvature flows

The equation of motion for a (fixed-mass) particle can be expressed using Newton's Second Law as

$$\sum \mathbf{F} = m_p \mathbf{a}_p = m_p \frac{d\mathbf{u}_p}{dt}, \quad (1)$$

where  $\sum \mathbf{F}$  is the sum of the forces acting on the particle,  $m_p = \pi \rho_p d_p^3 / 6$  is the mass for a spherical particle,  $\rho_p$  is the particle density,  $d_p$  is the particle diameter,  $\mathbf{a}_p$  is the particle acceleration, and  $\mathbf{u}_p$  is the particle velocity. For solid particles in gas-phase flows, fluid density is almost three orders of magnitude lower than particle density, and force terms containing the gas density (e.g., apparent-mass, unsteady-drag) can be neglected (Sung et al. 1994). The forces acting on the particle that must be considered are,

$$\sum \mathbf{F} = \mathbf{F}_G + \mathbf{F}_{SD} + \mathbf{F}_{TP}, \quad (2)$$

where  $\mathbf{F}_G = m_p \mathbf{g}_0 = -\mathbf{e}_3 m_p g_0$  is the gravitational force (for a particle traveling upward, along  $\mathbf{e}_3$ ),  $\mathbf{F}_{SD}$  is the Stokes-drag force, and  $\mathbf{F}_{TP}$  is the thermophoretic force. For flows typical of laminar flames,  $a_p = |\mathbf{a}_p| \gg g_0$ , as particles are subject to accelerations in the range  $a_p \cong 10^2\text{--}10^4 \text{ m/s}^2$ , or more, compared to  $g_0 \cong 10 \text{ m/s}^2$ . For micron-sized particles in stagnation flames, the gravitational force may be neglected (Egolfopoulos and Campbell 1999). The resulting equation of motion for a particle in one dimension then becomes

$$m_p \frac{du_p}{dt} = F_{SD} + F_{TP}. \quad (3)$$

The ability of a particle to accurately track the flow through a stagnation flame depends on its inertia and the local Stokes-drag and thermophoretic forces.

### 2.1 Stokes drag

The drag force exerted on a sphere in low Reynolds number flow was first described by Stokes in 1851. To account for rare-gas (Knudsen-number) effects, the Stokes drag formula is typically modified to introduce a slip factor (Allen and Raabe 1985) given by,

$$F_{SD} = \frac{-3\pi\mu d_p (u_p - u_f)}{C_{KW}}, \quad (4)$$

where  $\mu$  is the fluid viscosity,  $d_p$  is the particle diameter,  $u_p$  and  $u_f$  are the particle and (local) fluid velocities, respectively, and

$$C_{KW} = 1 + Kn \cdot \left[ \alpha + \beta \exp\left(\frac{-\gamma}{Kn}\right) \right] \quad (5)$$

is the Knudsen-Weber slip-correction factor. In this expression,  $Kn$  is the Knudsen number, and  $\alpha = 1.142$ ,  $\beta = 0.558$ , and  $\gamma = 0.999$  are empirical (best-fit) constants (Allen and Raabe 1985). The Knudsen number is defined as the ratio of the mean free path,  $\lambda$ , to the length scale of the flow, e.g.,  $r_p = d_p/2$ , the particle radius, i.e.,

$$Kn = \frac{\lambda}{r_p} = \frac{2\lambda}{d_p}. \quad (6)$$

In this work, we follow Talbot et al. (1980) and use the viscosity-based value for the mean free path,

$$\lambda = \frac{2\mu}{\rho_f \bar{c}}, \quad (7)$$

where  $\rho_f$  is the fluid density and

$$\bar{c} = \sqrt{\frac{8R_g T}{\pi}} \quad (8)$$

is the mean molecular speed of the gas mixture (Talbot et al. 1980). In this expression,  $T$  is the fluid temperature,  $R_g = R_u/M$  is the specific gas constant,  $R_u = 8,314 \text{ J/(kmol K)}$  is the universal gas constant, and  $M$  is the mean molar mass (molecular weight) of the gas mixture.

### 2.2 Particle lag in a uniform velocity gradient

A particle in a flow with a uniform velocity gradient,  $d u_f / dx = \text{constant} = \sigma$ , experiences an acceleration of,

$$a_p = \frac{du_p}{dt} = \frac{du_p}{dx_p} \frac{dx_p}{dt} \cong \frac{du_f}{dx} u_p \cong \sigma u_p, \quad (9)$$

where  $x_p(t)$  is the particle position in time. A particle in this flow will move toward the stagnation point,  $x = 0 \text{ mm}$ , and thus the velocity is negative ( $u = dx/dt < 0$ ). In this paper,  $-u$  is plotted in the figures to make the velocity profiles positive. In uniform-temperature flow, the Stokes drag is the only active force ( $F_{TP} = 0$ ), and the ratio of particle-to-fluid velocity can be estimated as,

$$m_p a_p = \left( \frac{\pi \rho_p d_p^3}{6} \right) a_p = \frac{-3\pi \mu d_p (u_p - u_f)}{C_{KW}} = F_{SD} \quad (10)$$

$$-\frac{\rho_p d_p^2}{18\mu} C_{KW} \sigma u_p \cong (u_p - u_f) \quad (11)$$

$$\frac{u_p}{u_f} \cong \frac{1}{1 + C_{KW} \tau_S \sigma}, \quad (12)$$

where

$$\tau_S \equiv \frac{\rho_p d_p^2}{18\mu} \quad (13)$$

is the particle Stokes time. For a particle decelerating in a stagnation flow,  $\sigma < 0$ , and particle velocity exceeds that of the fluid. Good particle tracking requires  $(C_{KW} \tau_S \sigma) \ll 1$ . The dimensionless product provides a first-order estimate for the fractional difference between particle and fluid velocities. From a measured (particle) velocity and velocity gradient at any point in the flow, fluid velocity can be calculated using Eq. 12. Particle lag exhibits a  $d_p^2$  dependence on particle size (Eq. 13), as often noted.

### 2.3 Particle-inertia effects

Figure 2 shows the effect of increasing particle size on estimated particle velocity profiles in a near-stoichiometric ( $\Phi = 0.9$ ) methane-air stagnation-point premixed flame. Four representative particles are assumed: a 1  $\mu\text{m}$  alumina particle ( $\rho_p = 3,830 \text{ kg/m}^3$ ), and ceramic microspheres 3, 5, and 7  $\mu\text{m}$  in diameter ( $\rho_p = 2,400 \text{ kg/m}^3$ ). Fluid velocity, temperature, species, and other profiles are solved for this flame using the Cantera software package (Goodwin 2003), with multicomponent transport and the GRI-Mech 3.0

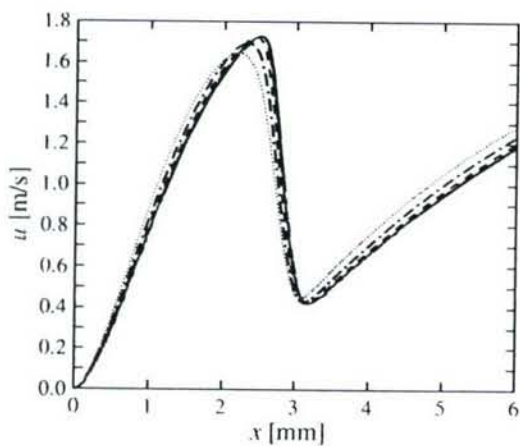


Fig. 2 Velocity profiles in a  $\Phi = 0.9$  premixed methane-air flame considering Stokes drag only ( $F_{TP} = 0$ ). Solid line simulated velocity profile ( $u_f$  vs.  $x$ ). Particle velocity profiles ( $u_p$  vs.  $x_p$ ) for different particle diameters: long-dash  $d_p = 1 \mu\text{m}$ , short-dash  $d_p = 3 \mu\text{m}$ , dash-dot  $d_p = 5 \mu\text{m}$ , and dot  $d_p = 7 \mu\text{m}$

chemical-thermal-transport model (Smith et al. 2006). The simulation boundary conditions are derived from experimental measurements of stagnation flames (Bergthorson et al. 2005). In the experiments, premixed fuel and air exit from a contoured nozzle 10 mm in diameter. The flow impinges on a temperature-controlled (water-cooled) stagnation plate. The measured wall temperature is specified at the stagnation point,  $x = 0 \text{ mm}$ , as well as  $u_f(0) = du_f/dx(0) = 0$ . For this flow, the simulation inlet is located at  $x = 6 \text{ mm}$  and the nozzle is at  $x = 8 \text{ mm}$ . The gas composition is controlled and measured with mass flow meters and specified at the simulation inlet. The velocity and velocity gradient at the simulation inlet are specified from parabolic fits to the PSV data in the cold-flow region of the profile, where a parabola is the analytical solution to the one-dimensional hydrodynamic model (Bergthorson et al. 2005). The inlet velocity specified in the simulations is corrected for particle lag using Eq. 12. Particle motion is solved using a Lagrangian technique to integrate particle position, velocity, and acceleration as a function of time through the simulated flame fields, with the particle initialized at  $x = 6 \text{ mm}$  at  $t = 0$ . For this figure, Eq. 3 was used with  $F_{TP} = 0$ . The initial particle velocity is given using Eq. 12. The initial acceleration can be estimated from the Stokes drag to be  $a_p(t=0) = -3\pi \mu d_p (u_p - u_f)/(C_{KW} m_p)$ . As expected, particle lag increases in regions of high velocity gradients and with increasing particle size.

### 2.4 Thermophoretic force

The thermophoretic force is felt by a particle as it travels through a high-temperature-gradient region, as occurs in a premixed flame front where gradients can reach  $10^6 \text{ K/m}$ . Measurements of the thermophoretic effect are difficult, experimental data with which to validate theory are sparse, and data and theories remain controversial (e.g., Talbot 1980; Santachiara et al. 2002). However, the different formulations basically predict similar behavior and vary only in the (constant) scaling factors (Bergthorson 2005, Sect. A.3). In this work, we follow previous combustion investigators and utilize the Brock-Talbot formulation of the thermophoretic force (e.g., Sung et al. 1994; Egolfopoulos and Campbell 1999).

In the slip-flow regime,  $Kn < 1$ , Brock (1962) derived an expression for the thermophoretic force using a hydrodynamic analysis with appropriate slip boundary conditions. The thermophoretic force can be expressed as

$$F_{TP} = -\frac{6\pi\mu v d_p C_s (\kappa_f/\kappa_p + C_t Kn)}{(1 + 3C_m Kn)(1 + 2\kappa_f/\kappa_p + 2C_t Kn)} \frac{\nabla T}{T}, \quad (14)$$

where  $v = \mu/\rho_f$  is the gas kinematic viscosity,  $\kappa_f$  and  $\kappa_p$  are the fluid and particle thermal conductivities, and  $C_s$ ,  $C_m$ , and  $C_t$  are the thermal slip, momentum exchange, and thermal exchange coefficients specified by the kinetic

theory of gases (Talbot et al. 1980). For polyatomic gases, one should use the translational thermal conductivity,

$$\kappa_f = \kappa_{tr} = \frac{15}{4} R_g \mu. \quad (15)$$

In the original analysis (Brock 1962), a value of  $C_s = 3/4$  was used but yielded poor agreement with experiment (Talbot 1980; Talbot et al. 1980). Talbot et al. proposed using Eq. 14 as a "fitting formula" throughout the entire range of Knudsen numbers, and suggested  $C_s = 1.17$ ,  $C_m = 1.14$ , and  $C_1 = 2.18$  as the best values from kinetic theory. With these values, the modified Brock theory gave the best agreement with their experimental results.

Particle velocity profiles inferred from the combined influence of Stokes drag and thermophoretic forces for several representative particles are depicted in Fig. 3. Particle velocity profiles are calculated by integrating Eq. 3 in time, evaluating the location, velocity, and acceleration of the particle at each time step. The slip-corrected form of the Stokes drag (Eq. 4) and the Brock-Talbot expression for the thermophoretic force (Eq. 14) are used to simulate particle motion. The temperature, temperature gradient, fluid viscosity, mean molar mass, and other profiles are interpolated from simulated stagnation-flame profiles at the particle location, at each time step. The gas translational thermal conductivity is calculated from the viscosity and the mean molar mass according to Eq. 15. The thermal conductivity of the aluminum-oxide ( $\text{Al}_2\text{O}_3$ ) particles,  $\kappa_p$ , is taken from standard tables (Incropera and DeWitt 1990; Table A.2). Due to the small size and high thermal conductivity of the particles, their temperature is assumed equal to the local gas temperature. The initial particle velocity is given by Eq. 12 at the inlet to the simulation domain ( $x = 6 \text{ mm}$ ), using the simulated fluid velocity and velocity gradient values. In the cold-flow region,

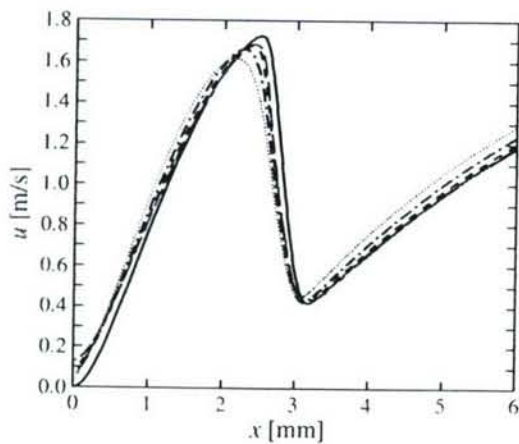


Fig. 3 Velocity profiles in a  $\Phi = 0.9$  premixed methane-air flame considering Stokes-drag and thermophoretic forces. Solid line simulated velocity profile ( $u_f$  vs.  $x$ ). Particle velocity profiles ( $u_p$  vs.  $x_p$ ) for different particle diameters: long-dash  $d_p = 1 \mu\text{m}$ , short-dash  $d_p = 3 \mu\text{m}$ , dash-dot  $d_p = 5 \mu\text{m}$ , and dot  $d_p = 7 \mu\text{m}$

thermophoretic forces are negligible, and the initial acceleration can be estimated from the Stokes drag as,  $a_p(t=0) = -3\pi\mu d_p (u_p - u_f)/(C_{\text{kw}} m_p)$ . Increased lag is evident for the larger particles. Particle velocity profiles do not go to zero in the near-wall region because of thermophoretic forces imposed by the temperature gradient between the hot post-flame products and the cooled stagnation surface.

### 3 Finite particle-track interval effects

Velocities inferred by particle-velocimetry techniques may not match fluid velocities even if particles accurately track the flow. This is especially true in flows with large spatial variations (high-gradient and high-curvature regions) in the velocity field, as in flames. The time interval between particle images can act as a low-pass filter on measured profiles. To account for this effect, the predicted particle location in time,  $x_p(t)$ , determined using the Lagrangian technique discussed above, can be used to model the experimental analysis technique.

Choosing a time interval,  $\tau$ , allows the modeled-PT velocity field,  $u_{\text{PT}}(x_{\text{PT}})$ , to be estimated as,

$$u_{\text{PT}}(x_{\text{PT}}) = \frac{x_p(t + \tau) - x_p(t)}{\tau}, \quad (16)$$

where,

$$x_{\text{PT}} = \frac{x_p(t + \tau) + x_p(t)}{2} \quad (17)$$

is the position at which the particle-tracking velocity estimate is placed, taken as the average location of the start and end of the particle trajectory over the Lagrangian time interval,  $\tau$ . These expressions can be evaluated for each time step in the particle-motion integration, resulting in a spatially smooth modeled-PT profile. As the Lagrangian time interval,  $\tau$ , is made arbitrarily small,  $u_{\text{PT}}(x_{\text{PT}})$  will converge to  $u_p(x_p)$ . However, for finite Lagrangian times, the particle-tracking velocity estimate will not match the particle velocity as a result of spatial averaging of the velocity profiles. Unfortunately,  $\tau$  cannot be made arbitrarily small because the particle displacement,  $\Delta x_p$ , in the time interval,  $\tau$ , must be sufficiently large in units of the detector spatial resolution to facilitate its estimation. Typically,  $\tau$  is chosen to ensure that the minimum velocities of interest can be accurately measured, imposing dynamic-range limitations on the measured flow field. To illustrate the effect of finite particle-track interval, a particle is tracked through the same flame as in Figs. 2 and 3. The velocity profile as a function of time in the particle frame is given in Fig. 4. Various particle-track intervals,  $\tau$ , applied to the particle position-time profile yield the results in Fig. 5. As  $\tau$  increases, modeled-PT profiles deviate from the particle velocity field in the post-flame region. This flow region is characterized by high velocities and high curvature of

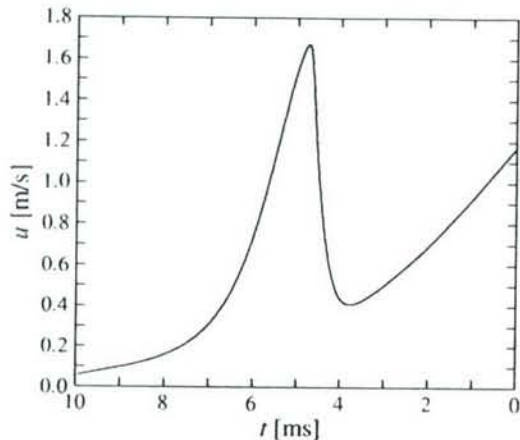


**Fig. 4** Velocity profile as a function of time in the particle frame ( $u_p$  vs.  $t$ ,  $d_p = 3 \mu\text{m}$ ,  $\rho_p = 2,400 \text{ kg/m}^3$ ) in a  $\Phi=0.9$  methane-air flame. Note that particle motion and increasing time is from right to left

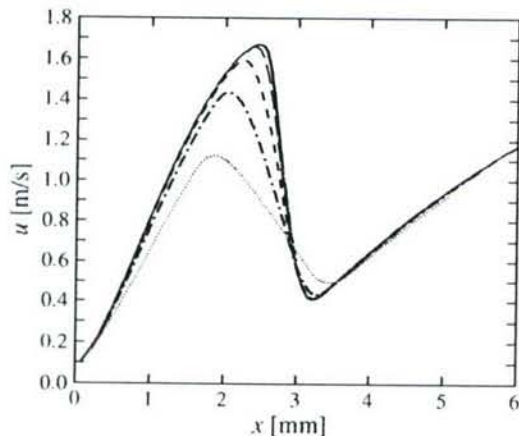


**Fig. 5** Particle-tracking profiles ( $u_{PT}$  vs.  $x_{PT}$ ) in a premixed methane-air flame ( $\Phi=0.9$ ) for various particle-track intervals. Solid line calculated particle velocity profile ( $u_p$  versus  $x_p$ ,  $d_p = 3 \mu\text{m}$ ,  $\rho_p = 2,400 \text{ kg/m}^3$ ); long dash line 0.2 ms, dash line 0.5 ms, dash-dot line 1 ms, dotted line 2 ms

the velocity field, both of which contribute to the reduced accuracy of the particle technique in this zone. The particle-tracking technique acts as a low-pass filter that performs a moving average of the velocity over an axial distance proportional to the fluid velocity at that point. In Fig. 5, the largest values of the particle-track interval,  $\tau$ , are included to illustrate the low-pass filtering effect on the profiles when measurements are performed with inadequate spatial resolution. These conditions should be avoided in experimental implementations.

### 3.1 Modeled-particle-tracking (modeled-PT) summary

The motion of a particle through a simulated stagnation-point flame is modeled using Eq. 3. A particle is

released at the inlet of the simulation domain at  $t=0$ , and particle position,  $x_p(t)$ , velocity,  $u_p(t)$ , and acceleration,  $a_p(t)$ , are solved as a function of time. Appropriate choices of  $u_p(t=0)$  and  $a_p(t=0)$  can remove initial/transient effects. Modeling particle motion can remove systematic errors that result from assuming the particle accurately tracks the flow. The resulting description of particle position as a function of time,  $x_p(t)$ , can be used to model the particle-tracking technique, using Eqs. 16 and 17, and the experimental particle-track time,  $\tau$ . The modeled-PT profile,  $u_{PT}(x_{PT})$ , accounts for the systematic errors and uncertainties in the diagnostic and should be used when comparing predictions to experimental data.

### 4 Finite particle-track interval corrections

In high-gradient/high-curvature flows, particle-tracking techniques introduce errors attributable to the approximation that flow velocity can be calculated from a measurement of the spatial displacement of a particle over a fixed time interval. Corrections for these errors are derived for flows that can be locally approximated by a parabola. The procedure outlined here is general and can be applied to other flow profiles of interest.

For a particle moving in a flow with constant curvature near a velocity maximum, we have  $u(x) = u_{\max} [1 - \beta^2(x - x_{\max})^2]$ . A local coordinate system is defined centered at a position  $x_1$  in the flow,  $X = x - x_1$ , yielding  $u(X) = u_{\max} [1 - \beta^2 (X + x_1 - x_{\max})^2] = u_1 [1 + \gamma_1 X - \gamma_2^2 X^2]$ . Therefore,  $u_1 = u(x_1)$ ,  $\gamma_1 = -2\beta^2 (x_1 - x_{\max}) (u_{\max}/u_1)$ , and  $\gamma_2^2 = \beta^2 (u_{\max}/u_1)$ . The time to traverse a (particle-track) distance  $l$  is then,

$$\tau = \int_{t_1}^{t_2} dt = \int_{-l/2}^{l/2} \frac{dX}{u(X)} = \frac{1}{u_1} \int_{-l/2}^{l/2} \frac{dX}{1 + \gamma_1 X - \gamma_2^2 X^2}. \quad (18)$$

A parabola capturing a velocity maximum has two real roots. The integral is,

$$\tau = \frac{l}{u_1} \frac{1}{\beta l} \frac{u_1}{u_{\max}} \tanh^{-1} [\beta (X + x_1 - x_{\max})] \Big|_{-l/2}^{l/2}, \quad (19)$$

yielding a correction factor,

$$\begin{aligned} f_{\max} &= \frac{u_1}{(l/\tau)} \\ &= \frac{u_1}{\beta l u_{\max}} [\tanh^{-1} [\beta (x_1 - x_{\max} + l/2)] \\ &\quad - \tanh^{-1} [\beta (x_1 - x_{\max} - l/2)]]. \end{aligned} \quad (20)$$

In the vicinity of velocity minima, the flow can be approximated by,  $u(x) = u_{\min} [1 + \beta^2 (x - x_{\min})^2]$ , with two imaginary roots. The resulting correction factor is then,

$$\begin{aligned}
f_{\min} &= \frac{u_1}{(l/\tau)} \\
&= \frac{u_1}{\beta l u_{\min}} \left[ \tan^{-1} [\beta(x_1 - x_{\min} + l/2)] \right. \\
&\quad \left. - \tan^{-1} [\beta(x_1 - x_{\min} - l/2)] \right]. \quad (21)
\end{aligned}$$

In flows with a gradient and negligible curvature, the profile can be approximated by  $u(x) = u_{\text{ref}} [1 + a(x - x_{\text{ref}})]$ . A local coordinate system is again defined, yielding,  $u(X) = u_{\text{ref}} [1 + a(X + x_1 - x_{\text{ref}})] = u_{\text{ref}} [1 + a(x_1 - x_{\text{ref}}) + aX] = u_1 [1 + \alpha X]$ , where  $u_1 = u(x_1)$  and  $\alpha = a(u_{\text{ref}}/u_1)$ . The time to traverse a (particle-track) distance  $l$  is then given by,

$$\begin{aligned}
\tau &= \int_{x_1}^{x_2} dt = \int_{-l/2}^{l/2} \frac{dX}{u(X)} = \frac{1}{u_1} \int_{-l/2}^{l/2} \frac{dX}{1 + \alpha X} \\
&= \frac{1}{u_1 \alpha} \ln \left( \frac{1 + \alpha l/2}{1 - \alpha l/2} \right). \quad (22)
\end{aligned}$$

corresponding to a correction factor,

$$f_{\text{grad}} = \frac{u_1}{(l/\tau)} = \frac{1}{\varepsilon} \ln \left( \frac{1 + \varepsilon/2}{1 - \varepsilon/2} \right), \quad (23)$$

that must be applied with  $\varepsilon = \alpha l = a(l(u_{\text{ref}}/u_1) = \Delta u/u_1)$ . This correction is important in regions of the flow where the velocity change,  $\Delta u$ , during the time interval,  $\tau$ , is significant, as compared to the average velocity over the interval,  $u_1$ .

These expressions allow (measured) particle-tracking velocity profiles to be corrected in high-curvature regions near minima or maxima and regions of high-gradient. Measured flow profiles that contain such features can be fit locally with either a parabola or line, as

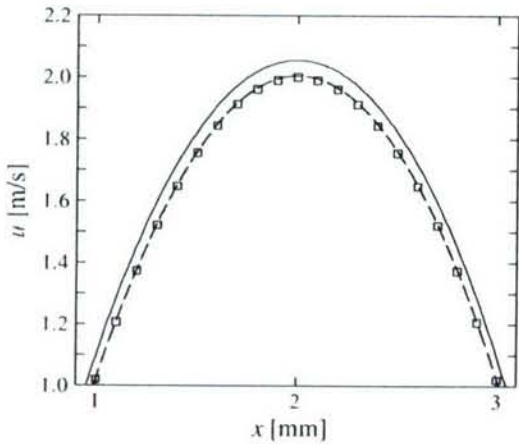


**Fig. 6** Particle-tracking velocimetry correction near velocity-profile maxima. Squares particle-track velocity profile corresponding to specified parabola. Solid line corrected particle velocity profile ( $u_p$  vs.  $x_p$ ) using Eq. 20. Dash line modeled-particle-tracking (modeled-PT) profile ( $u_{\text{PT}}$  vs.  $x_{\text{PT}}$ , see Sect. 3) determined by Lagrangian integration of the corrected velocity profile ( $u_p$  vs.  $x_p$ ). In this example,  $x_{\max} = 2$  mm,  $u_{\max} = 2$  m/s,  $\beta = 700 \text{ m}^{-1}$ , and  $\tau = 0.4$  ms

appropriate, to allow the associated correction factor to be estimated and applied. The expressions contain the local velocity,  $u_1$ , which can be approximated as the (measured) particle-tracking velocity to be corrected,  $u_{\text{PT}}$ . To illustrate their application, the specific case of flow near a velocity maximum is considered. Figure 6 gives a sample particle-tracking profile, specified with  $x_{\max} = 2$  mm,  $u_{\max} = 2$  m/s, and  $\beta = 700 \text{ m}^{-1}$ , that is representative of the flow near the post-flame velocity maximum in a stoichiometric methane-air stagnation flame. Simulated particle-tracking data (squares) are created using this specified parabola and the correction (Eq. 20) is applied to find the corrected (true spatial) particle velocity profile (solid line). The correction is approximately 3% near the peak of the profile. In this example, the particle-track distance,  $l$ , is estimated using  $l = u_{\text{PT}}/\tau$ , with  $\tau = 0.4$  ms (corresponds to PSV chopping frequency of  $v_c = 2,500$  Hz). As a test of the methodology presented in Sect. 3 (Eqs. 16, 17), the particle-tracking profile (dashed line) is estimated from the corrected particle velocity profile (solid line). The particle position and velocity are found as a function of time using Lagrangian integration. The particle velocity is interpolated at the current particle location from the corrected particle velocity profile at each time step. Utilizing the same particle-track interval,  $\tau = 0.4$  ms, the estimated particle-tracking profile (dashed line) gives good agreement with the original (specified) particle-tracking profile (squares), with a maximum error less than 0.5% of the local velocity.

## 5 Comparison with experiment

Figure 7 compares the experimental PSV profile for a  $\phi = 0.9$  methane-air flame to the simulated fluid velocity profile,  $u_f(x)$ , the modeled particle trajectory,  $u_p(x_p)$ , and the modeled-PT velocity profile,  $u_{\text{PT}}(x_{\text{PT}})$ . A  $3 \mu\text{m}$

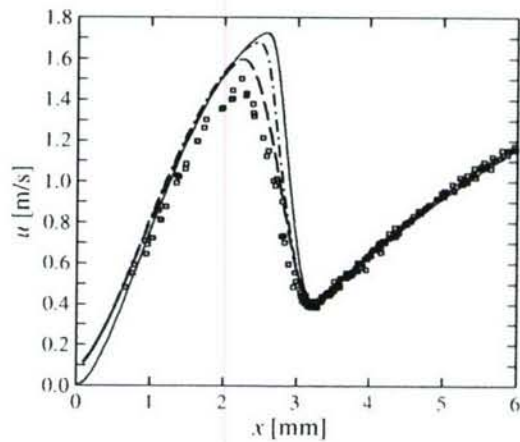


**Fig. 7** Velocity profiles in a premixed methane-air flame ( $\phi = 0.9$ ). Squares PSV data, solid line simulated fluid velocity profile ( $u_f$  vs.  $x$ ), dash-dot line calculated particle profile ( $u_p$  versus  $x_p$ ,  $d_p = 3 \mu\text{m}$ ,  $\rho_p = 2,400 \text{ kg/m}^3$ ), dash line modeled-PT profile ( $u_{\text{PT}}$  vs.  $x_{\text{PT}}$ , particle-track interval  $\tau = 0.5$  ms)

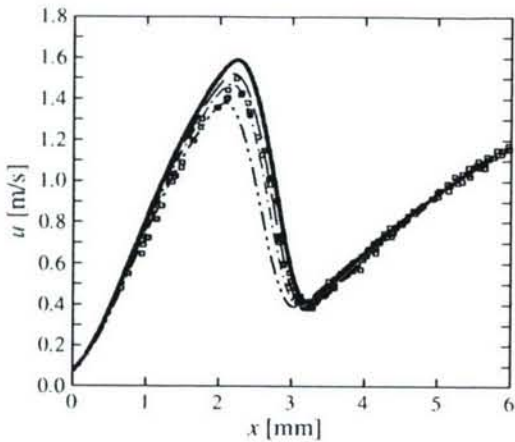


**Fig. 8** Modeled-particle-tracking profiles compared to experimental data for a  $\Phi = 0.9$  methane-air flame. Simulations are performed with the pre-exponential rate constant of the main chain-branching reaction reduced to artificially lower the predicted flame speed. *Solid line* no reduction, *long dash* 5% reduction, *dash-dot* 10% reduction, *dash-dot-dot* 15% reduction. All profiles calculated using  $d_p = 3 \mu\text{m}$ ,  $\rho_p = 2,400 \text{ kg/m}^3$ , and  $\tau = 0.5 \text{ ms}$

ceramic microsphere ( $\rho_p = 2,400 \text{ kg/m}^3$ ) and a chopping frequency of  $v_c = 2,000 \text{ Hz}$  ( $\tau = 0.5 \text{ ms}$  particle-track interval) are utilized, corresponding to experiment. Further details on the experimental methodology and the PSV diagnostic may be found in Bergthorson et al. (2005). The modeled-PT profile includes the effects of particle inertia, Stokes drag, thermophoretic forces, and finite particle-track interval. Improved agreement is seen between the modeled-PT and measured PSV profiles in the post-flame region. The modeled-PT profile lies above the measurements, consistent with the findings of Sung et al. (1996).

To explore the remaining discrepancy, simulations were performed with artificially lowered flame speeds by reducing the pre-exponential factor of the main chain-branching reaction,  $\text{H} + \text{O}_2 \rightleftharpoons \text{OH} + \text{O}$ . Figure 8 presents profiles with variable predicted flame speeds. As the rate of the main chain-branching reaction is reduced to 85% of its original value, the reference flame speed (minimum of velocity profile upstream of flame) varies from 0.415 to 0.387 m/s, a change of 7%. These profiles yield reference flame speeds both above and below the measured minimum of 0.399 m/s. The maximum of the modeled-PT velocity profiles varies from 1.589 to 1.379 m/s, a relative change of 13%. The resulting velocity maxima span the measurements. From Fig. 8, it is seen that a predicted flame speed that is slightly higher than measured yields a large discrepancy in the region of the velocity maximum. Velocity differences in the cold-flow region are amplified by the density drop through the reaction zone that results from the flame heat release.

Figures 9 and 10 compare velocity profiles for methane-air flames at equivalence ratios of  $\Phi = 0.7$  and 1.3, respectively. The flames are simulated with the GRI-Mech 3.0 model using the procedure described above.

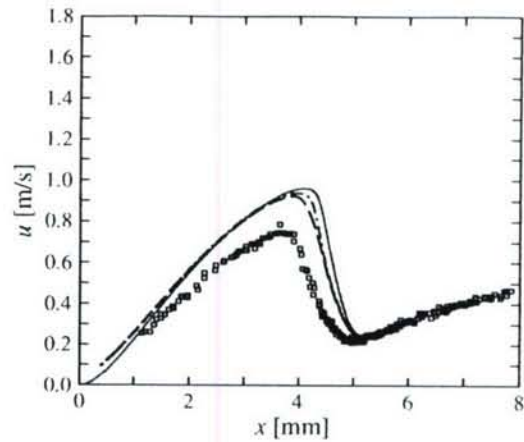


**Fig. 9** Velocity profiles in a premixed methane-air flame ( $\Phi = 0.7$ ). *Squares* PSV data, *solid line* simulated fluid velocity profile ( $u_f$  vs.  $x$ ), *dash-dot line* calculated particle profile ( $u_p$  vs.  $x_p$ ,  $d_p = 3 \mu\text{m}$ ,  $\rho_p = 2,400 \text{ kg/m}^3$ ), *dash line* modeled-PT profile ( $u_{\text{PT}}$  vs.  $x_{\text{PT}}$ , particle-track interval  $\tau = 0.625 \text{ ms}$ )

The particle and modeled-PT velocity profiles are calculated using the same particle properties and particle-track intervals as in the experiments. For the lean,  $\Phi = 0.7$ , methane-air flame, the predicted flame speed is higher than experiment and both the minimum and maximum of the profile lie above the experimental measurements. For the rich,  $\Phi = 1.3$ , methane-air flame, good agreement is seen between the modeled-PT and experimentally measured profiles. These results are consistent with the results of previous investigators, who find that the predicted flame speed using GRI-Mech 3.0 matches experiment for rich flames, but lies above the data for stoichiometric to lean flames (e.g., Bosschaart and de Goey 2004).

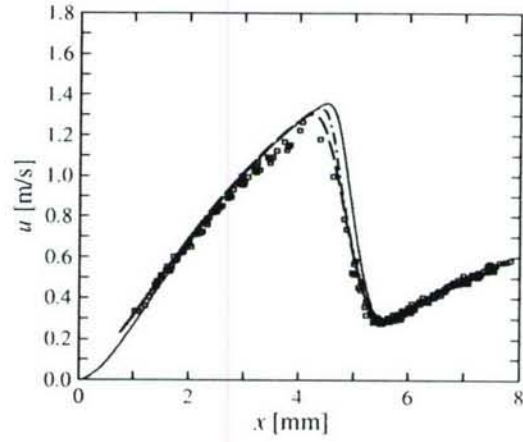


**Fig. 10** Velocity profiles in a premixed methane-air flame ( $\Phi = 1.3$ ). *Squares* PSV data, *solid line* simulated fluid velocity profile ( $u_f$  vs.  $x$ ), *dash-dot line* calculated particle profile ( $u_p$  vs.  $x_p$ ,  $d_p = 3 \mu\text{m}$ ,  $\rho_p = 2,400 \text{ kg/m}^3$ ), *dash line* modeled-PT profile ( $u_{\text{PT}}$  vs.  $x_{\text{PT}}$ , particle-track interval  $\tau = 0.5 \text{ ms}$ )

## 6 Conclusions

Detailed comparisons between simulation and experiment require that uncertainties and systematic effects in the diagnostics be estimated and accounted for. In particle-velocimetry techniques, particles may not accurately track the fluid velocity due to the combined effects of external forces and particle inertia. In addition, the finite time interval employed in particle-tracking techniques can act as a low-pass filter. These effects can be accounted for using the methodology presented in this paper. Application of these techniques brings modeled-PT profiles, derived from numerical simulations of premixed stagnation flames, and the corresponding particle-tracking velocimetry measurements in closer agreement. The methodology is not flow-specific and can be applied to any simulated flow field to permit improved direct comparisons between theory, simulation, and experiment. In situations where simulations are not available for comparison, experimental data in regions of velocity gradients can be corrected for particle-inertia effects using the results presented in Sect. 2.2. Errors due to the finite particle-track interval can be accounted for in regions of velocity gradients, maxima, and minima, as discussed in Sect. 4. Arbitrary flow profiles can be segmented and fit, piecewise, to allow appropriate particle-track corrections to be applied in each region.

**Acknowledgements** We would like to acknowledge discussions with L. Benezech, and assistance by D. Lang and G. Katzenstein with the experiments, and D. Goodwin with the Cantera software package. This work was funded by AFOSR Grant F49620-01-1-0006, whose support is gratefully acknowledged.

## References

Adrian RJ (1991) Particle-imaging techniques for experimental fluid mechanics. *Annu Rev Fluid Mech* 23:261–304

Allen MD, Raabe OG (1985) Slip correction measurements of spherical solid aerosol particles in an improved Millikan apparatus. *Aerosol Sci Technol* 4:269–286

Bergthorson JM (2005) Experiments and modeling of impinging jets and premixed hydrocarbon stagnation flames. PhD Thesis, California Institute of Technology, <http://resolver.caltech.edu/CaltechETD:etd-05242005-165713>

Bergthorson JM, Goodwin DG, Dimotakis PE (2005) Particle streak velocimetry and CH laser-induced fluorescence diagnostics in strained, premixed, methane-air flames. *Proc Combust Inst* 30:1637–1644

Bosschaart KJ, de Goey LPH (2004) The laminar burning velocity of flames propagating in mixtures of hydrocarbons and air measured with the heat flux method. *Combust Flame* 136:261–269

Brock JR (1962) On the theory of thermal forces acting on aerosol particles. *J Colloid Sci* 17:768–780

Egolfopoulos FN, Campbell CS (1999) Dynamics and structure of dusty reacting flows: inert particles in strained, laminar, premixed flames. *Combust Flame* 117:206–226

Gilbert M, Davis L, Altman D (1955) Velocity lag of particles in linearly accelerated combustion gases. *Jet Propul* 25:26–30

Goodwin DG (2003) An open-source, extensible software suite for CVD process simulation. In: *Proceedings of CVD XVI and EuroCVD Fourteen*, Electrochemical Society, pp 155–162

Haghgoie M, Kent JC, Tabaczynski RJ (1986) Verification of LDA and seed generator performance. *Exp Fluids* 4:27–32

Incropera FP, DeWitt DP (1990) *Fundamentals of heat and mass transfer*, 3rd edn. Wiley, New York

Jackson GS, Sai R, Plaia JM, Boggs CM, Kiger KT (2003) Influence of H<sub>2</sub> on the response of lean premixed CH<sub>4</sub> flames to high strained flows. *Combust Flame* 132:503–511

Melling A (1997) Tracer particles and seeding for particle image velocimetry. *Meas Sci Technol* 8:1406–1416

Samimy M, Lele SK (1991) Motion of particles with inertia in a compressible free shear layer. *Phys Fluids* 3:1915–1923

Santachiara G, Prodi F, Cornetti C (2002) Experimental measurements on thermophoresis in the transition region. *J Aerosol Sci* 33:769–780

Smith GP, Golden DM, Frenklach M, Moriarty NW, Eiteneer B, Goldenberg M, Bowman CT, Hanson RK, Song S, Gardiner WC Jr, Lissianski VV, Qin Z (2006) GRI-Mech 3.0, [http://www.me.berkeley.edu/gri\\_mech/](http://www.me.berkeley.edu/gri_mech/)

Stella A, Guj G, Kompenhans J, Raffel M, Richard H (2001) Application of particle image velocimetry to combusting flows: design considerations and uncertainty assessment. *Exp Fluids* 30:167–180

Sung CJ, Law CK, Axelbaum RL (1994) Thermophoretic effects on seeding particles in LDV measurements of flames. *Combust Sci Technol* 99:119–132

Sung CJ, Kistler JS, Nishioka M, Law CK (1996) Further studies on effects of thermophoresis on seeding particles in LDV measurements of strained flames. *Combust Flame* 105:189–201

Talbot L (1980) Thermophoresis—a review. In: Fisher SS (ed) *Rarefied gas dynamics—part I*, vol 74. American Institute of Aeronautics and Astronautics, New York, pp 467–488

Talbot L, Cheng RK, Schefer RW, Willis DR (1980) Thermophoresis of particles in a heated boundary layer. *J Fluid Mech* 101:737–758

# Planar shock cylindrical focusing by a perfect-gas lens

P. E. Dimotakis and R. Samtaney<sup>a)</sup>

Graduate Aeronautical Laboratories, California Institute of Technology, Pasadena, California 91125

(Received 15 December 2005; accepted 10 February 2006; published online 17 March 2006)

We document a gas lensing technique that generates a converging shock wave in a two-dimensional wedge geometry. A successful design must satisfy three criteria at the contact point between the gas lens and the wedge leading edge to minimize nonlinear reflected and other wave effects. The result is a single-point solution in a multidimensional parameter space. The gas lens shape is computed using shock-polar analysis for regular refraction of the incident shock at the gas lens interface. For the range of parameters investigated, the required gas-lens interface is closely matched by an ellipse or hyperbola. Nonlinear Euler simulations confirm the analysis and that the transmitted shock is circular. As the converging transmitted shock propagates down the wedge, its shape remains nearly uniform with less than 0.1% peak departures from a perfect circular cylinder segment. Departure from the design criteria leads to converging shocks that depart from the required shape. The sensitivity to incident shock Mach number, as well as the qualitative effects of the presence of boundary layers are also discussed. © 2006 American Institute of Physics.

[DOI: 10.1063/1.2186553]

Converging shocks occur in such contexts as inertial confinement fusion,<sup>1</sup> supernova collapse,<sup>2</sup> sonoluminescence,<sup>3</sup> shock-wave lithotripsy,<sup>4</sup> accelerating or maneuvering aircraft that can generate "superbooms,"<sup>5</sup> concave detonation-driven shocks,<sup>6</sup> and in others. Interest in them derives from their ability to concentrate energy in a small volume, especially if the focusing is in three dimensions. Although two- and three-dimensional focusing of linear (acoustic/optical) waves is straightforward, finite-amplitude shocks exhibit instabilities that amplify initial shape imperfections<sup>7</sup> and focusing is complicated by nonlinear wave interactions. For these and other reasons, shocks are difficult to focus in typical laboratory environments.

This Letter documents a two-dimensional (2D) gas lens that nonlinearly refracts a planar incident shock into a 2D circular (cylindrical) transmitted shock and focuses it as it propagates down a suitably configured wedge (Fig. 1). A properly focused shock is a prerequisite for laboratory investigations of the Richtmyer-Meshkov instability in a converging geometry, which will require the presence of a second gas interface in the converging test section. The incident planar shock,  $I$ , will, in general, refract and reflect at the gas interface contact surface,  $C$ , which can be implemented via a suitably supported thin membrane that it will also deflect. The half-angle of the wedge,  $\theta_w$ , and the shape of  $C$  must generate a transmitted shock that is congruent with a circular arc centered at the wedge apex and a flow that is radial towards the wedge apex. In what follows, a subscript 0 denotes flow/gas properties ahead of the incident shock and to the left of the  $C$  interface,  $I$  denotes flow/gas properties behind the incident shock and to the left of  $C$ , and 2 denotes conditions in the undisturbed region to the right of  $C$ .

The parameters governing the interaction of  $I$  with  $C$  are:

the strength of the incident planar normal shock, given by its Mach number  $M_i$ ; for matched temperature and pressure across  $C$ , the gas properties expressed as the density ratio  $\eta = \rho_2 / \rho_0$  across the contact interface, the ratios of specific heats  $\gamma_0$  and  $\gamma_2$  of the gas on the left and right of  $C$ , respectively; and the geometrical parameters:  $\theta_w$ , the angle  $\alpha_0$  between the incident shock and the contact surface at the point  $P$ , and the initial shape of  $C$ . At the junction  $P$ , the requirements for the initiation of a converging-shock flow solution are: (a) The transmitted shock must be perpendicular to the wedge face, (b) the reflected wave must be canceled to minimize nonlinear wave reflections from the wedge walls, and (c) the angle  $\theta_t$  by which the flow turns across the transmitted shock should be such that the flow is radial immediately behind the transmitted shock—the flow-turning angle must equal the wedge half-angle, i.e.,  $\theta_t = \theta_w$  at  $P$ .

Assuming ( $T_0 = T_2$ ,  $p_0 = p_2$ ,  $\eta$ ,  $\gamma_0$ , and  $\gamma_2$ ), a gas lens, if it exists, must satisfy the three conditions and represents an inverse-design solution in the three-dimensional parameter space: ( $M_i$ ,  $\alpha_0$ ,  $\theta_w$ ). The solution can be determined using Newton's method to define the shock polars and determine their intersections to satisfy the three criteria (details omitted in the interest of brevity). The problem differs from linear-wave focusing in that the finite-amplitude wave deflects the "lens," as it interacts with it (Fig. 2), and must be such as to cancel the reflected wave at the wedge leading edge,  $P$ . No solutions exist if  $\gamma_0 = \gamma_2$ ; a hot gas to the left and the same lower-temperature gas to the right of  $C$  cannot lead to perfect focusing. Further, the need to cancel the reflected shock at  $P$  generally limits the solution to weak, or moderate-strength, incident shocks. Strong-shock refraction at a fast-slow interface typically transitions from regular refraction to irregular refraction with a Mach stem, while weak to modest shock refraction transitions from a reflected shock wave to a reflected rarefaction.<sup>8</sup>

For  $\eta = 1.4$ ,  $\gamma_0 = 1.5$ , and  $\gamma_2 = 1.4$ , e.g., corresponding to a

<sup>a)</sup>Present address: Princeton Plasma Physics Laboratory, Princeton University, Princeton, NJ 08543.

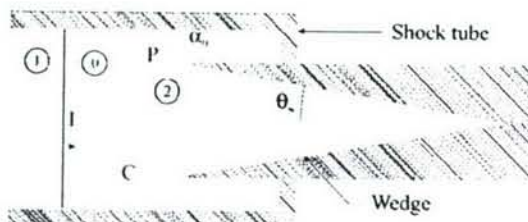


FIG. 1. Setup of the physical domain. The incident shock (1) is initialized upstream of a gas interface/contact (C).

mixture for gas 0 and nitrogen for gas 2, the solution is ( $M_i=1.3122$ ,  $\alpha_0=51.856^\circ$ ,  $\theta_w=11.617^\circ$ ). Solutions for different gas properties, if they exist, can be found by analytic continuation.

The procedure used to compute the interface shape of C is now briefly described, followed by results from nonlinear Euler simulations demonstrating the correctness of the approximate analytical solution and the ability of the computed interface to focus a planar shock. Violation of any of the three confluence conditions is shown to foil the quality of the transmitted shock and the attendant focusing, where “quality” denotes the degree of congruency with a circular arc centered at the wedge apex. A sensitivity analysis in terms of incident shock strength is also presented. Finally, we comment on the influence of boundary layers in an experimental design.

The initial configuration is that of an interface with a shock upstream of it (Fig. 1). At an intermediate time, the configuration is as in Fig. 2. Assuming that the refraction is regular, all waves meet at a single node. In a small neighborhood of the node, all waves and contact surfaces are assumed to be straight, i.e., local-curvature effects are neglected. The incident shock I reaches P at  $t=t_i$ , having traversed the interface C, and generates a transmitted shock T that must be a circular arc of radius R, while canceling the local reflected wave. We now solve the initial interface contour C that leads to the desired transmitted-shock configuration. When I refracts at C, the transmitted shock is assumed to move in a direction normal to its front, i.e., along rays emanating from the apex of the wedge. At any time  $t$ , let  $\alpha(t)$  be the angle between the I and C, and let the transmitted shock front make an angle  $\beta(t)$  with respect to I. At  $t=0$ , we have  $\beta(0)=\alpha(0)=0$ , whereas at  $t=t_i$ ,  $\beta(t_i)=\theta_w$ , and  $\alpha(t_i)=\alpha_0$ .

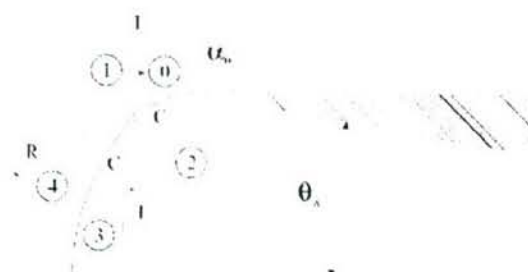


FIG. 2. (Color online) Shock-interface configuration for  $t < t_i$ , before the incident shock has traversed the interface C. Regular refraction of the incident shock I at C, R is the reflected wave and T is the transmitted wave that at  $t_i$  is a circular arc centered on the wedge apex.

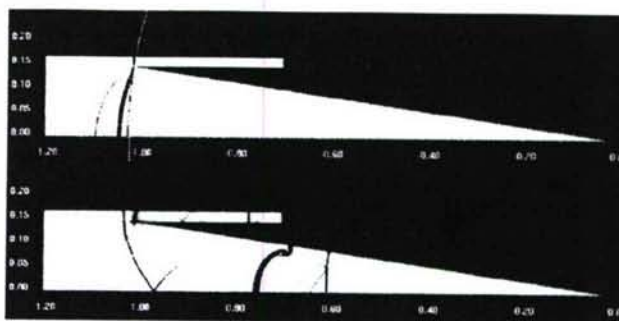


FIG. 3. (Color online) Numerical Schlieren at time  $t_i$  (top) and at time  $t=6.2t_i$ . The white curve (top panel) is a circular arc shown for reference at time  $t_i$ . Parameters:  $M_i=3.0$ ,  $\eta=1.4$ ,  $\gamma_0=1.5$ ,  $\gamma_2=1.4$ ,  $\theta_w=8.37^\circ$ , and  $\alpha_0=50.0^\circ$ .

At  $t=0$ , the transmitted shock strength can be estimated as a one-dimensional shock contact interaction and is  $M_{t0}=1.34521$  for the parameters chosen. Then,  $t_i$  is calculated using

$$t_i = \frac{R(1 - \cos \theta_w)}{M_i c_0 - M_{t0} c_2}, \quad (1)$$

where  $c_0$  and  $c_2$  are the unshocked sound speeds in gases 0 and 2, respectively. During the time  $t_i$ , the incident and transmitted shocks travel a distance  $L_i=M_i c_0 t_i$  and  $L_t=M_{t0} c_2 t_i$ , respectively. Measuring  $x$  from the wedge apex, the foot of the interface is at  $x_i=-(R+L_t)$ . The nonlinear function  $\alpha(t)$  is then solved by an iterative bisection procedure at each time  $t \in [0, t_i]$ .

$$\begin{aligned} \mathcal{F}[\alpha(t)] = & \{R + M_m[\alpha(t)]c_2(t_i - t)\}\cos \beta(t) - (R + L_t) \\ & + M_i c_0 t = 0, \end{aligned} \quad (2)$$

where  $M_m$  is the normal Mach number of the transmitted shock,  $\alpha(t)$  is the local angle between I and C and a function of the parameters:  $M_i$ ,  $\eta$ ,  $\gamma_0$ , and  $\gamma_2$ .  $M_m$  and  $\beta(t)=\beta[\alpha(t)]$  are computed using local shock-polar analysis that, for regular refraction, as described in Ref. 9. With  $\alpha(t)$  determined, the C interface coordinates are derived by

$$x_r = -[R + M_m c_2(t_i - t)]\cos \beta(t), \quad (3a)$$

$$y_r = [R + M_m c_2(t_i - t)]\sin \beta(t). \quad (3b)$$

For the design case, the required initial contact curve is (very close to) an ellipse of aspect ratio 4.448, centered at  $x=2.14R$  (to the right of the wedge apex).

Results from simulations of the compressible Euler equations are now presented. The level-set method is employed to handle the wedge and “cookie-cutter” boundary geometry. Details of the numerical method are in Refs. 10 and 11. The initial conditions are a planar shock upstream of the gas interface computed in the previous section. Figure 3 shows the numerical equivalent of a Schlieren image for parameter set ( $M_i=3.0$ ,  $\eta=1.4$ ,  $\gamma_0=1.5$ ,  $\gamma_2=1.4$ ,  $\theta_w=8.37^\circ$ , and  $\alpha_0=50.0^\circ$ ), corresponding to a case in which the correct refracted shock is generated at P, but the other two conditions are not satisfied. The two faint vertical lines that may be discernible are features associated with weak left-moving

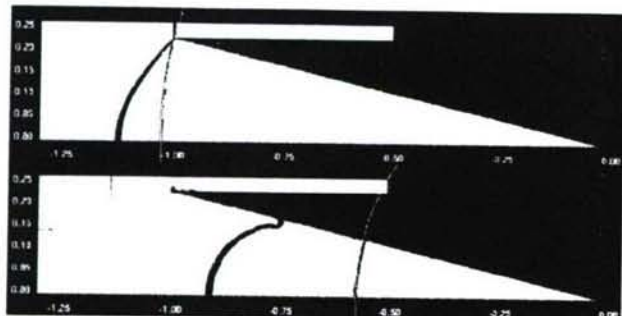


FIG. 4. (Color online) Numerical Schlieren at time  $t_i$  (top) and at time  $t = 3.2t_i$ . White circular arcs are shown for reference. Parameters:  $M_i = 1.59$ ,  $\eta = 1.4$ ,  $\gamma_0 = 1.4$ ,  $\gamma_2 = 1.4$ ,  $\theta_w = 13.45^\circ$ , and  $\alpha_0 = 61.28^\circ$ .

startup waves that occur as the initially sharp incident shock adjusts itself onto the discrete mesh. They are of no consequence to the subsequent development of the flow. The transmitted shock is circular at time  $t_i$ . For linear waves, this condition would suffice for focusing. However, as the finite-amplitude shock propagates into the wedge, secondary reflected waves interact with the leading shock and circularity is violated.

Figure 4 simulates a Schlieren image for the parameters:  $M_i = 1.59$ ,  $\eta = 1.4$ ,  $\gamma_0 = 1.4$ ,  $\gamma_2 = 1.4$ ,  $\theta_w = 13.45^\circ$ , and  $\alpha_0 = 61.28^\circ$ . This case satisfies the first two conditions, but not the one for radial flow behind the transmitted shock at P, and corresponds to nearly the maximum incident Mach number for regular refraction for this combination of gases. Although the transmitted shock is circular at  $t_i$  and the reflected shock strength vanishes at P, circularity deteriorates with increasing time. For the  $M_i = 3.0$  and  $M_i = 1.59$  cases depicted in Figs. 3 and 4, respectively, the shock-polar analysis leads to an initial interface curve that closely matches a section of a hyperbola.

The design case is depicted in Fig. 5. The transmitted shock departure from circularity at  $t_i$  is smaller than the numerical smearing from shock capturing. Reflected shock

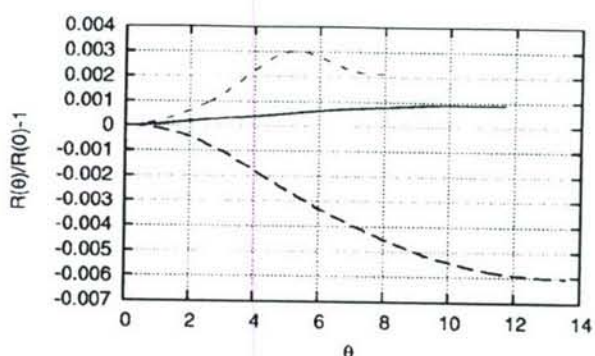


FIG. 6. Normalized shock radius, vs azimuthal angle  $\theta$ , for  $M_i = 1.59$  at  $t = 4.2t_i$  (solid),  $M_i = 1.59$  at  $t = 3.2t_i$  (lower dashed), and  $M_i = 3.0$  at  $t = 6.2t_i$  (upper dashed).

strength is seen to vanish at P at  $t_i$ . Figure 6 depicts the normalized shock radius, some distance down the wedge, as a function of the azimuthal angle  $\theta$  for the off-design and the design cases. The shocks are seen to be very nearly circular, with less than 1% deviation from a perfect circle, and less than 0.1% for the design case.

Although the design procedure yields a nearly circular transmitted shock that eventually focuses, at least for inviscid flow, the pressure behind the shock is not perfectly uniform. To leading order, the pressure behind the transmitted shock at  $t_i$  varies as  $p_i(\theta) - p_i(0) = \kappa \sin^2 \theta + O(\sin^4 \theta)$ , where  $\theta$  is the polar angle measured from the wedge apex,  $p_i(0)$  is the centerline pressure behind the transmitted shock (foot of the interface), and  $\kappa$  is a small parameter that depends only on  $M_i$ ,  $\eta$ ,  $\gamma_0$ , and  $\gamma_2$ . As a consequence, there is a weak azimuthal flow behind the shock that will tend to spoil the desired circular symmetry. This, however, is mitigated by the fact that the converging shock accelerates as it travels down the wedge, leaving the small initial azimuthal disturbances behind. As well, the flow behind the shock is guided by the wedge (cf. results in Figs. 5 and 7).

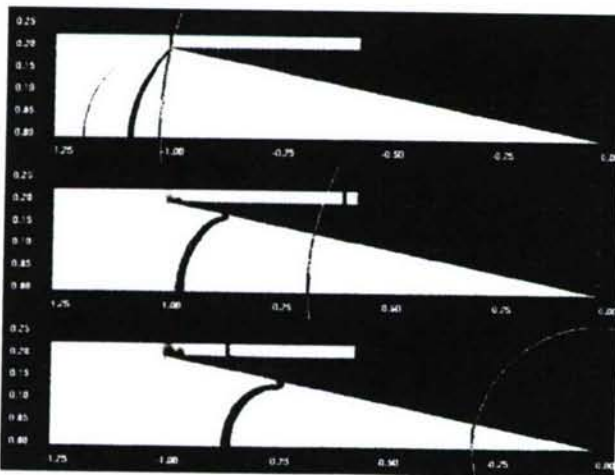


FIG. 5. (Color online) Numerical Schlieren for design case at  $t = t_i$  (top), at  $t = 4.2t_i$  (middle panel), and at  $t = 7.5t_i$  (bottom panel). Solution parameters:  $M_i = 1.3122$ ,  $\eta = 1.4$ ,  $\gamma_0 = 1.5$ ,  $\gamma_2 = 1.4$ ,  $\theta_w = 11.617^\circ$ , and  $\alpha_0 = 51.86^\circ$ . White circular arcs are shown for reference.

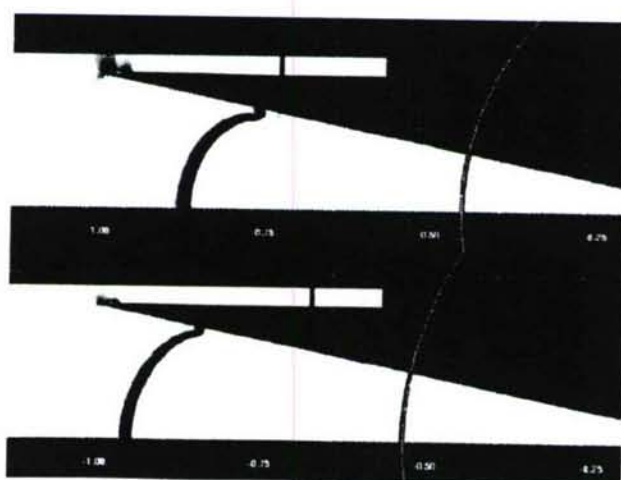


FIG. 7. (Color online) Numerical Schlieren corresponding to  $\pm 5\%$  off-design incident Mach numbers at times. Top:  $M_i = 1.3778$  at  $t = 5.9t_i$ , Bottom:  $M_i = 1.2466$  at  $t = 5.8t_i$ . The white circular arc is shown for reference.

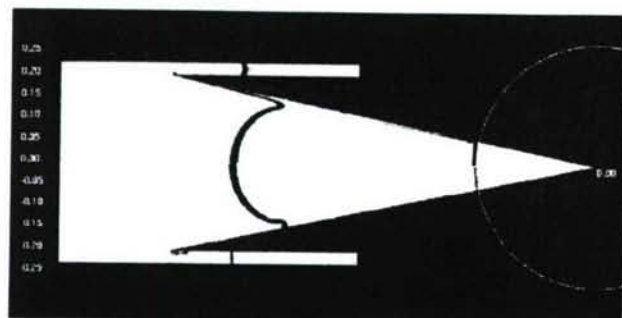


FIG. 8. (Color online) Numerical Schlieren at  $t = 7.5t_0$ . Top: design case with boundary-layer effects. Bottom: The inviscid computation shown flipped about the  $x$  axis for comparison. The white circular arc is shown for reference.

In shock-tube experiments, the incident shock Mach number,  $M_i$ , can be controlled to within 1–2%, or so. We examine the sensitivity of the performance of the computed gas lens to  $M_i$ , varying it by  $\pm 5\%$  from the optimal design value. Numerical results depicted in Fig. 7 indicate a robust focusing solution with respect to variations in  $M_i$ , for the gas choices in the example considered here, for which shock polars intersect at a shallow angle.

Another consideration is the formation of boundary layers behind the shock. Their negative displacement thickness introduces flow obliquity in the vicinity of the wall, which straightens and slows the shock down as it proceeds down the wedge. In straight shock tubes, the trailing contact surface is also accelerated so, in concert with the deceleration of the shock, shock-tube test time between shock and contact-surface arrivals attains a maximum value, independent of shock-tube length.<sup>12,13</sup> To qualitatively explore and highlight boundary layer effects in this geometry, the design case was simulated using a compressible Navier-Stokes code with no-slip boundary conditions. The Reynolds number was chosen to be about two orders of magnitude lower than in planned experiments, corresponding to boundary-layer displacement effects about one order of magnitude larger than expected. No changes in the conditions at  $P_0$  or in the required design procedure for  $C$ , are required as no boundary layers will have formed as yet. The transmitted shock at time  $t_0$  is circular, as expected. Figure 8 compares the viscous solution (top) to the inviscid solution (bottom), at a later time. The weak waves that emanate from the shock-wave junction with the wedge wall are minor grid-induced artifacts of the numerical simu-

lation. Boundary layers are responsible for some influence at later times, as expected. In particular, the converging shock with a boundary layer in its wake lags the inviscid solution at the same time. Boundary layers are also seen to have a small but discernible influence on the shape of the shock, spoiling congruence with a circular arc. These effects will be amplified further, as the ratio of the converging shock arc length to the boundary-layer displacement thickness increases with time. If the three conditions at  $P$  are satisfied and  $C$  has been designed as described previously, the expected convergence ratio for shocks contained by a wedge in the laboratory will be limited by boundary layer effects.

The authors would like to acknowledge discussions with Paul Miller, Omar Hurricane, and Karnig Mikaelian of the Lawrence Livermore National Laboratory (LLNL), as well as discussions and exchanges with Hans Hornung, Dale Pullin, Dan Meiron, Amy Lam, and David Hill of Caltech. This work was performed under the auspices of the U.S. Department of Energy by the U.C. LLNL, under Contract No. W-7405-Eng-48, DOE/Caltech ASC/ASAP Subcontract No. B341492.

- <sup>1</sup>D. L. Lindl, R. L. McCrory, and E. M. Campbell, "Progress toward ignition and burn propagation in inertial confinement fusion," *Phys. Today* **45** (9), 32 (1992).
- <sup>2</sup>W. D. Arnett, J. N. Bahcall, R. P. Kirshner, and S. E. Woosley, "Supernova 1987A," *Annu. Rev. Astron. Astrophys.* **27**, 629 (1989).
- <sup>3</sup>S. J. Puterman, "Sonoluminescence—sound into light," *Sci. Am.* **272**, 1107 (1995).
- <sup>4</sup>D. Howard and B. Sturtevant, "In vitro study of the mechanical effects of shock-wave lithotripsy," *Ultrasound Med. Biol.* **23**, 1107 (1997).
- <sup>5</sup>D. J. Maglieri and K. J. Plotkin, *Aeroacoustics of Flight Vehicles* (Acoustical Society of America, New York, 1995).
- <sup>6</sup>D. A. Holder, A. V. Smith, C. J. Barton, and D. L. Youngs, "Mix experiments using a two-dimensional convergent shock-tube," *Laser Part. Beams* **21**, 403 (2003).
- <sup>7</sup>D. W. Schwendeman and G. B. Whitham, "On converging shock waves," *Proc. R. Soc. London, Ser. A* **413**, 297 (1987).
- <sup>8</sup>A. M. Abd-El-Fattah and L. F. Henderson, "Shock waves at a fast-slow gas interface," *J. Fluid Mech.* **86**, 15 (1978).
- <sup>9</sup>R. Samtaney and N. J. Zabusky, "Circulation deposition on shock-accelerated planar and curved density-stratified interfaces: models and scaling laws," *J. Fluid Mech.* **269**, 45 (1994).
- <sup>10</sup>J. Cummings, M. Aivazis, R. Samtaney, R. Radovitzky, S. Mauch, and D. Meiron, "A virtual test facility for the simulation of dynamic response in materials," *J. Supercomput.* **23**, 39 (2002).
- <sup>11</sup>M. Arienti, P. Hung, E. Morano, and J. E. Shepherd, "A level set approach to Eulerian-Lagrangian coupling," *J. Comput. Phys.* **185**, 213 (2003).
- <sup>12</sup>A. Roshko, "On flow duration in low-pressure shock tubes," *Phys. Fluids* **3**, 835 (1960).
- <sup>13</sup>H. Mirels, "Test time in low-pressure shock tubes," *Phys. Fluids* **6**, 1201 (1963).

# Laser Scanning of Three-Dimensional Time-Varying Fluid Phenomena

Daniel Lang

Santiago Lombeyda

Jan Lindheim

Paul Dimotakis

California Institute of Technology

## 1 Introduction

Time-varying three-dimensional CFD simulations have been at the center of many of the modern computational, physical, and movie special-effect challenges. Results are presented on the first full-field, three-dimensional, time-varying scanning of fluid phenomena. The discussion includes a description of the acquisition hardware, the data-acquisition methodology, the geometrical (space and time) and image corrections applied, and the visualization results and analysis. The results of the three-dimensional field capability on computational and physical models, new challenges it brings to the visualization field, and new possible applications are also discussed.

## 2 Experiment

The experimental and infrastructure development is based on laser scanning and the acquisition of three-dimensional data, high-volume data storage, a repository of basic phenomena, and visualization and analysis of the results. The developed infrastructure is already proving useful. In reference to turbulence, the primary research focus, it is yielding large data sets for visualization and subsequent analysis. Visualization and analysis of the first data sets has dictated the design and implementation of a new class of experiments that is in progress, targeting the exploration of flow structure and new phenomena over a wide range of Reynolds numbers, the assessment of turbulence theories, and the validation of direct and large-eddy numerical simulations (DNS and LES).

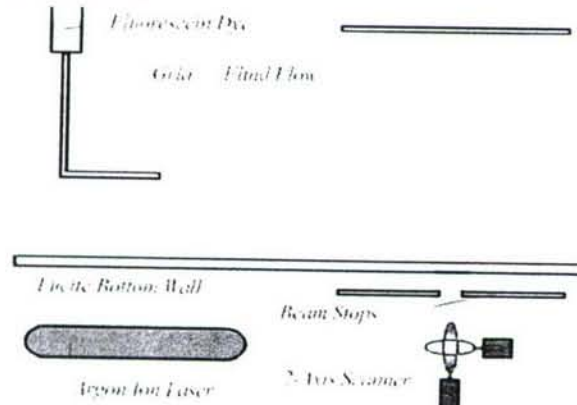


Figure 1. Side view of the Free Surface Water Tunnel. Three-Dimensional Laser Scanner Experimental Setup

The KFS camera system was designed and fabricated in-house. The KFS camera head contains a low-noise CCD (KFS CCD) designed at JPL by Mark Wadsworth and has  $1024 \times 1024$  pixel resolution based on  $12 \mu\text{m}^2$  pixels and 32 output channels. The 32 CCD output channels are buffered and fed to an 8-channel A/D converter board. Each converter board has four 12-bit 40 MHz converters that cover the 32 output channels of the KFS CCD. Real-time lossless image compression reduces image storage requirement by a factor of 1.5 to 3, depending on the data SNR. The integrated KFS camera system has a measured noise of  $25.8 \text{ e}^-$  at room temperature at 200 fps (frames/s).

Each A/D converter board transfers the real-time data to the data-storage clusters via S-Link fiber-optic links, at rates up to 160 MB/s per channel, for an aggregate rate of 1.28 GB/s for 8 channels. This permits the acquisition of terabytes of data, limited only by the speed of the disk arrays. By way of example, at the 100 fps rate in this experiment, this corresponds to a data rate of  $10^8$  12-bit measurements per second.

The first experiments address the dispersion of a scalar marker from a continuous (steady) point release. A fluorescent dye is released into turbulent flow in water, generated by a grid with  $1/4$ " grid wires spaced by 1". The laser-scanning system sweeps a laser beam across the measurement volume, causing the dye to fluoresce. See Fig. 1.

The KFS camera system image acquisition is synchronized with the volume sweeps. During the readout time, the beam is moved in the 3<sup>rd</sup> direction to prepare for the next sweep. In the first implementation described here, less than 1/3 of a second was required to perform 32 sweeps, image readouts, and data transfer to high-speed disk storage.

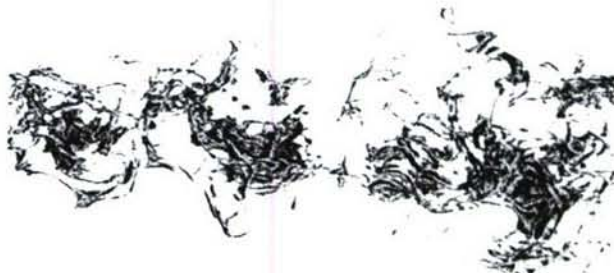


Figure 2. Volume rendering of a sample volume frame after intensity and geometric corrections

## 3 Discussion and Conclusions

Previous three-dimensional scalar data have been limited to scanning of relatively small volumes in the flow. The present experiments and data-acquisition, -storage, and -visualization infrastructure captures the full scalar-dispersion field and permits its topology to be recorded. A single volume frame that visualizes the resulting data, with intensity and geometric corrections applied, color-coded in terms of the concentration of the passive-contaminant scalar marker, is depicted in Fig. 2. Classically, one expects a Gaussian dispersion (mean) profile some distance downstream of the injection point. The experiments indicate a rather sparse (intermittent) worm-like concentration field whose topology is much like the enstrophy (vorticity squared,  $|\omega|^2$ ) field observed in direct numerical simulations, as opposed to previous smaller-scale volume-scanning experiments that concluded that the field is more sheet-like.

The experimental setup and data-acquisition and -processing infrastructure can also be extended to the special-effects industry and allows an internal digital volumetric model representation of the fluid that can be used to interact with digital characters.

## Reynolds-number effects and anisotropy in transverse-jet mixing

By JERRY W. SHAN AND PAUL E. DIMOTAKIS

Graduate Aeronautical Laboratories, California Institute of Technology, Pasadena, CA 91125, USA

(Received 23 May 2005 and in revised form 8 January 2006)

Experiments are described which measured concentration fields in liquid-phase strong transverse jets over the Reynolds-number range  $1.0 \times 10^3 \leq Re_j \leq 20 \times 10^3$ . Laser-induced-fluorescence measurements were made of the jet-fluid-concentration fields at a jet-to-freestream velocity ratio of  $V_r = 10$ . The concentration-field data for far-field ( $x/d_j = 50$ ) slices of the jet show that turbulent mixing in the transverse jet is Reynolds-number dependent over the range investigated, with a scalar-field PDF that evolves with Reynolds number. A growing peak in the PDF, indicating enhanced spatial homogenization of the jet-fluid concentration field, is found with increasing Reynolds number. Comparisons between transverse jets and jets discharging into quiescent reservoirs show that the transverse jet is an efficient mixer in that it entrains more fluid than the ordinary jet, yet is able to effectively mix and homogenize the additional entrained fluid. Analysis of the structure of the scalar field using distributions of scalar increments shows evidence for well-mixed plateaux separated by sharp cliffs in the jet-fluid concentration field, as previously shown in other flows. Furthermore, the scalar field is found to be anisotropic, even at small length scales. Evidence for local anisotropy is seen in the scalar power spectra, scalar microscales, and PDFs of scalar increments in different directions. The scalar-field anisotropy is shown to be correlated to the vortex-induced large-scale strain field of the transverse jet. These experiments add to the existing evidence that the large and small scales of high-Schmidt-number turbulent mixing flows can be linked, with attendant consequences for the universality of small scales of the scalar field for Reynolds numbers up to at least  $Re = 20 \times 10^4$ .

### 1. Introduction

The turbulent jet discharging into a crossflow, or transverse jet, is a turbulent free-shear flow of both environmental and technological significance. A common-place occurrence of the transverse jet is the plume emitted from a smokestack on a windy day. Plumes generated by volcanoes, thunderstorms, or forest fires can also rise to heights in the atmosphere where significant crossflow exists. Other transverse jets arise in diverse situations including effluent discharge into rivers, steering jets for missiles and ships, VTOL/STOL aircraft aerodynamics, and blade-and-endwall cooling in gas turbines. The transverse jet has also been proposed as a means for fuel injection in high-speed air-breathing propulsion, i.e. SCRAMJETS (Gruber *et al.* 1999). Buoyancy can be important to different degrees in the various applications of transverse jets; however, this study restricts its attention to momentum-driven jets in crossflow.

A large body of work has focused on the velocity fields and vortex dynamics of the turbulent jet in crossflow (Gordier 1959; Keffer & Baines 1963; McMahon, Hester & Palsky 1971; Chassaing *et al.* 1974; Fearn & Weston 1974; Moussa, Trischka &

Eskinazi 1977; Andreopoulos & Rodi 1984; Karagozian 1986; Kelso & Smits 1995; Kelso, Lim & Perry 1996; Cortelezzi & Karagozian 2001; extensive literature reviews are given by Margason 1993 and Morton & Ibbetson 1996). In comparison, less attention has been paid to scalar transport and mixing, despite the fact that, as noted by Niederhaus, Champagne & Jacobs (1997), 'the majority of applications require knowledge of the transport of either heat or mass.' A number of early studies focused on classical measures of jet mixing such as scalar trajectories, centreline concentration decay, and mean scalar fields (e.g. Patrick 1967; Kamotani & Greber 1972). Broadwell & Breidenthal (1984) made an important contribution by modelling the transverse jet as an axial vortex pair that arises as a global consequence of the transverse lift force imparted by the jet to the crossflow. The analysis of Broadwell & Breidenthal provided analytical models for the rate at which mean concentration decays on the centreline. Broadwell & Breidenthal also performed experiments measuring 'flame length' in liquid-phase transverse jets, and reported the flame length to be independent of Reynolds number above a circulation-based Reynolds number of  $\Gamma/\nu \simeq 300$ .

Smith & Mungal (1998) reported on experiments on the mixing and structure of gas-phase transverse jets. They identified different regions of the transverse jet for which different scalings held: the vortex interaction region, the near field, and the far field. Based on decay rates of mean concentration on the jet centreline, they found the location of a branch point separating the near and far fields to be insensitive to Reynolds number over the range  $8.4 \times 10^3 \leq Re_j \leq 33 \times 10^3$ , where Reynolds number is based on jet-exit velocity and nozzle diameter. Hasselbrink & Mungal (2001) used similarity analysis to find scaling laws for the mean centreline concentration decay in the near and far fields. Reasonable agreement was found with the data of Smith & Mungal (1998). Su & Mungal (2004) have reported on simultaneous measurements of velocity and scalar fields in transverse jets. Other studies of turbulent mixing in transverse jets with additional complexity have been reported, e.g. for jets with swirl (Niederhaus *et al.* 1997), sonic jets injected into a supersonic crossflow (VanLerberghe *et al.* 2000), and fully modulated jets (Johari, Pacheco-Tougas & Hermanson 1999).

Relatively little attention appears to have been paid to the evolution of mixing with Reynolds number in transverse jets. Smith & Mungal (1998) found that the mean concentration decay rate on the jet centreline was approximately constant over a Reynolds-number range of  $8.4 \times 10^3 \leq Re_j \leq 33 \times 10^3$ . However, no comparison was made of probability distribution functions (PDFs) of the scalar field for different Reynolds numbers. As discussed in § 3, mean quantities such as the mean concentration decay rate are measures of entrainment, rather than measures of mixing. Moreover, experience with liquid-phase axisymmetric turbulent jets discharging into a quiescent reservoir shows that the details of scalar fields mixed by turbulence can depend on Reynolds number. For example, scalar-field distributions and root-mean-squared (r.m.s.) scalar fluctuations vary with jet Reynolds number over a range of at least  $3.0 \times 10^3 \leq Re_j \leq 24 \times 10^3$  (Miller & Dimotakis 1991; Catrakis & Dimotakis 1996). This paper addresses the issue of Reynolds-number dependence of scalar mixing by examining the probability distribution of jet fluid in strong liquid-phase transverse jets at a fixed far-downstream location (§ 3). In addition, high-Schmidt-number mixing is compared between transverse jets and ordinary jets to investigate possible differences in mixing for fully developed (but finite-Reynolds-number) turbulent flows.

A detailed examination of the structure of the mixed-fluid concentration fields is also made with scalar increments (also known as scalar differences). The distribution of

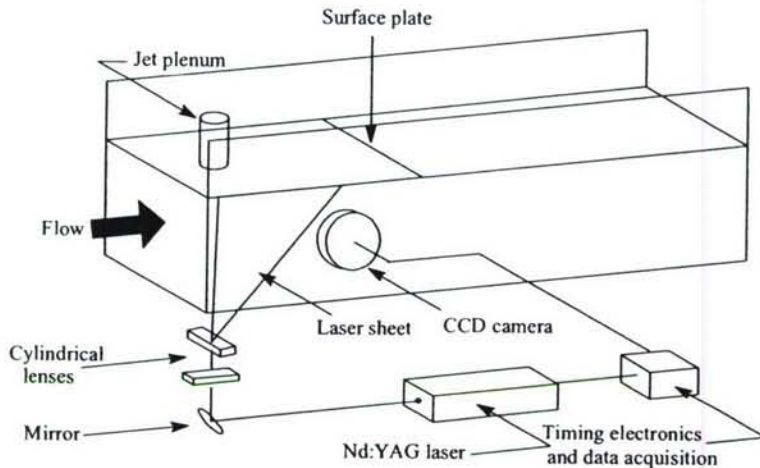


FIGURE 1. Experimental facility and imaging configuration for streamwise views of a transverse jet.

scalar increments,  $f(\Delta, C)$ , defined as the probability distribution of the instantaneous concentration difference between two spatially separated points in the scalar field,

$$f(\Delta, C) \equiv f(C(\mathbf{x} + \mathbf{r}, t) - C(\mathbf{x}, t)), \quad (1)$$

describes the probability of finding a concentration  $C + \Delta C$  at a distance  $\mathbf{r}$  away from a point of concentration  $C$ . The scalar increment statistics, which are connected to intermittency and the structure of the scalar field, are examined in §4 to explore the internal structure of the jet-fluid concentration field.

The experiments reported here also examine other aspects of the internal structure of the scalar field in liquid-phase transverse jets. In particular, the issue of local anisotropy is addressed with two-dimensional power spectra, scalar microscales and scalar increments in two directions. An attempt is made to quantify the observed small-scale anisotropy and identify its cause. Based on an observed correlation between the small-scale anisotropy and the mean strain field, it is suggested that the large-scale vortex dynamics of the transverse jet are responsible for the local scalar anisotropy in the far field (§5).

## 2. Experiments and visualization

Experiments on high-Schmidt-number turbulent mixing in the transverse jet were conducted in the GALCIT free-surface water tunnel (FSWT), a closed-circuit facility having a 50.8 cm wide  $\times$  76.2 cm deep (20 in.  $\times$  30 in.) test section. The FSWT was operated as a water tunnel with square cross-section for these experiments by fitting a surface plate at the free-surface; for all experiments, the water level in the test section was maintained at a depth of 50.8 cm (20 in.). A neutrally buoyant jet of water was injected downward into the crossflow from the top of the surface plate (figure 1). Flow was initiated by pressurizing an inverted liquid-filled plenum with air; the jet flowed out of a nozzle block that was fitted flush to the surface plate. The jet nozzle was convex contoured to suppress formation of Görtler vortices and had an area-contraction ratio of 43. The nozzle was 31.8 mm (1.25 in) long and had an internal exit diameter of 7.62 mm (0.300 in). Once filled, the plenum was allowed to settle for at least 30 min before each run to allow flow disturbances to die down.

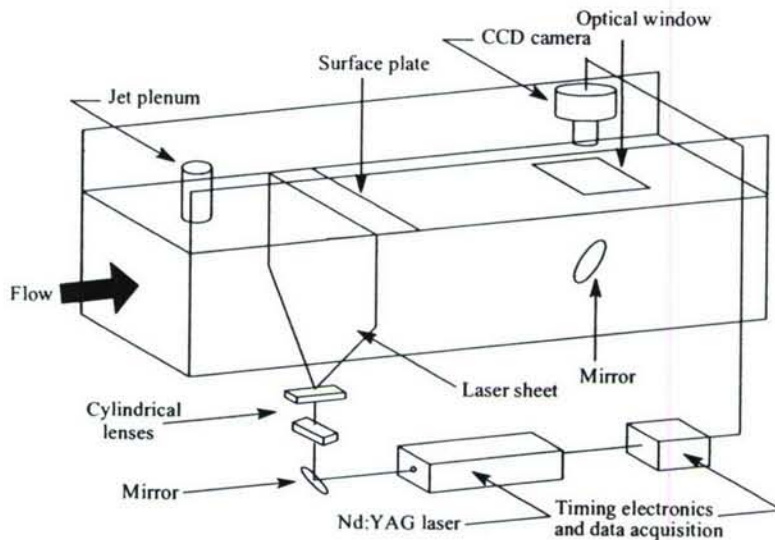


FIGURE 2. Imaging configuration for perpendicular cross-sections of transverse jet at  $x/d_j = 50$ .

Experiments were conducted at fixed jet-to-free-stream velocity ratio  $V_r \equiv U_j/U_\infty = 10$  for several Reynolds numbers. Selected experiments were performed at a higher velocity ratio,  $V_r = 32$ , for visualization purposes, but all quantitative data discussed in this paper came from jets at  $V_r = 10$ . Particular attention was paid to the transverse jet at  $V_r = 10$  because that velocity ratio was identified as a critical ratio for 'strong' jets, in the sense that wall (pressure) effects on the jet trajectory can be neglected in favour of entrainment effects for  $V_r \geq 10$ . Hasselbrink & Mungal (2001) show that the similarity analysis of Broadwell & Breidenthal (1984), which predicts the well-known power-law trajectory for transverse jets, implicitly assumes that  $V_r \geq 10$ . In addition, the  $V_r = 10$  jet is of interest because that velocity ratio has been identified as a critical ratio for the appearance of jet fluid in the wake; higher velocity-ratio jets were observed to have jet fluid in the wake, while lower velocity ratio jets did not (Smith & Mungal 1998). Velocity ratios between 10 and 20, depending on the assumed stoichiometry, have also been reported to result in minimum flame lengths (Broadwell & Breidenthal 1984; Smith & Mungal 1998).

For all but some limited visualizations, the velocity ratio was thus maintained constant at  $V_r = 10$  while the jet Reynolds number was varied in the range  $1.0 \times 10^3 \leq Re_j \equiv U_j d_j / \nu \leq 20 \times 10^3$  by suitably adjusting the jet and free-stream velocities. Streamwise slices of the jet were taken at  $Re_j = 1.0, 2.0, 5.0$  and  $10 \times 10^3$ , whereas transverse slices were taken at  $x/d_j = 50$  for  $Re_j = 1.0, 2.0, 5.0, 10$  and  $20 \times 10^3$ . The crossflow boundary layer (the boundary layer on the surface plate) was laminar and thin, calculated to be between  $0.067d_j$  and  $0.30d_j$  at the jet exit, depending on Reynolds number. Table 1 summarizes the experimental conditions for the primary case of interest, the transverse slices at  $x/d_j = 50$ .

### 2.1. Imaging technique

Digital imaging of laser-induced fluorescence (LIF) was used to measure mixed-fluid concentration fields (Walker 1987) in the transverse jet (figure 2). The jet plenum was filled with a dilute mixture of rhodamine-6G chloride and water, in molar concentrations of  $1.4 \times 10^{-6}$  M (streamwise views) and  $1.4 \times 10^{-5}$  M (transverse views).

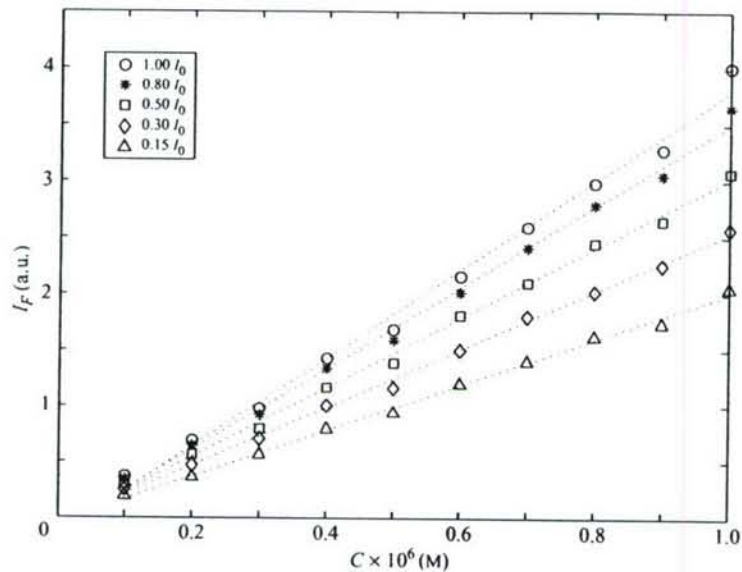


FIGURE 3. Variation of fluorescence intensity with dye concentration, over the indicated range of laser intensities.  $I_0 = 10^{11} \text{ W m}^{-2}$ .

Upon excitation at  $\lambda_L = 532 \text{ nm}$  with a frequency-doubled Q-switched Nd:YAG laser (Continuum YG661), the dyed jet fluid fluoresced at  $\lambda_F = 555 \text{ nm}$  while the undyed tunnel fluid remained dark (e.g. Pringsheim 1949). The laser provided  $250 \text{ mJ pulse}^{-1}$  (in the green) with a pulse duration of approximately 6 ns. An optical low-pass filter (Kodak no. 21) was used to isolate the fluorescence emission from the laser wavelength spectrally. Experiments were performed in a darkened laboratory to further minimize noise from ambient light.

The suitability of rhodamine-6G dye and a high-powered pulsed Nd:YAG laser for quantitative measurement of the scalar field was verified in separate experiments (Shan, Lang & Dimotakis 2004). To summarize, the fluorescence intensities,  $I_F$ , of various rhodamine-6G solutions were measured in a cuvette for concentrations and laser intensities similar to those of the jet-imaging experiment. The fluorescence of aqueous solutions of rhodamine-6G (at similar concentrations to those occurring in the present experiments) was found to be approaching saturation owing to the high instantaneous power of the pulsed laser. Although the fluorescence was not linear with illumination intensity, the fluorescence was nonetheless linearly proportional to concentration (figure 3). This enabled quantitative measurement of the jet-fluid concentration field, using the procedure described below.

Because of the linearity of fluorescence with concentration, the imaged intensity of fluorescence,  $I_F(x_1, x_2, t)$ , of a time-varying concentration field,  $c(x_1, x_2, t)$ , can be written as,

$$I_F(x_1, x_2, t) = g [I_L(x_1, x_2), S(x_1, x_2)] c(x_1, x_2, t) + I_{back}(x_1, x_2), \quad (2a)$$

where  $g(I_L, S)$  is an undetermined function of the local laser intensity,  $I_L(x_1, x_2)$  and the pixel-by-pixel sensitivity,  $S(x_1, x_2)$ , of the imaging system.  $I_{back}$  is the cumulative background level due to dark noise, offsets, etc. in the CCD camera. The imaged intensity for a reference, uniform-concentration field would be,

$$I_{F,ref}(x_1, x_2) = g [I_L(x_1, x_2), S(x_1, x_2)] c_{ref} + I_{back}(x_1, x_2), \quad (2b)$$

where  $c_{ref}$  is a known concentration. The laser-illumination fields for the jet image, (2a), and the reference image, (2b), are the same, or nearly so, because the laser attenuation due to absorption is negligible.<sup>†</sup> In this case then, the mixed-fluid concentration field, referenced to the known concentration, may be computed by subtracting the background-illumination images and normalizing by the uniform-concentration images (cf. (2a) and (2b)), i.e.

$$\frac{c(x_1, x_2, t)}{c_{ref}} = \frac{I_F(x_1, x_2, t) - \langle I_{back}(x_1, x_2) \rangle}{\langle I_{F, ref}(x_1, x_2) \rangle - \langle I_{back}(x_1, x_2) \rangle}. \quad (3a)$$

This result relies on linearity with respect to concentration, as demonstrated in figure 3, but is independent of the precise functional form of  $g(I, S)$ . Thus, the ability to make quantitative measurements of scalar concentration using pulsed-laser LIF depends only on weak absorption and the linearity of fluorescence with concentration, which were both verified for the present experiments.

Fluorescence images of the mixed-fluid concentration field were recorded in both streamwise (figure 1) and perpendicular (figure 2) cross-sectional views of the transverse jet. For both cases, a laser sheet was formed in order to illuminate a thin slice of the jet-fluid concentration field. A negative-focal-length cylindrical lens expanded the beam into a laser sheet, while a long-focal-length cylindrical lens focused the sheet to a thin waist centred in the field of view. The sheet was 0.19 mm thick at its waist, and had a Rayleigh range of 20 cm. Images of streamwise cross-sections of the jet were recorded on the centreline for a square field of view of dimensions 40 cm (16 in or  $53 d_j$ ) on a side. Images of transverse cross-sections were recorded for a field of view of 24 cm (9.3 in or  $31 d_j$ ) on a side, at a downstream location of  $x/d_j = 50$ . The pixel (in-plane) resolution in transverse images was 0.23 mm, which is comparable to the laser-sheet thickness of 0.19 mm. The pixel resolution in the streamwise images was 0.40 mm. Additional discussion of the resolution of the experiment is given in §2.3.

As shown in figures 4–7, the coordinate system is taken to have its origin at the jet exit, with  $y$  in the direction of jet injection (downward),  $x$  in the crossflow direction, and  $z$  in the spanwise direction.

A digital camera was custom-designed and constructed to record the images of the mixed-fluid concentration field. The camera used a low-noise high-dynamic-range CCD image detector developed by NASA's Jet Propulsion Laboratory for the Cassini spacecraft. This 'Cassini' imaging system was capable of true 12-bit dynamic range at  $(1024 \times 1024)$ -pixel resolution at a framing rate of 10 Hz. Sequences of 508 images were recorded for perpendicular cross-sections of the jet, and 254 images for streamwise cross-sections.

Background images,  $I_{back}(x_1, x_2)$ , were recorded shortly before each run, with the laser firing and an optical low-pass filter on the camera lens, but without starting the fluorescent-dye-seeded jet. Then, after the jet was run, reference images,  $I_{F, ref}(x_1, x_2)$ , of a uniform concentration field were recorded by immersing a transparent acrylic container filled with well-mixed dye of known concentration,  $c_{ref}$ , in the test section. Using these background and reference images, the effects of CCD sensitivity variation, illumination non-uniformity, and optical transfer function were removed using (3). The imaged jet-fluid concentration was referenced to the jet-plenum dye concentration,  $c_0$ ,

<sup>†</sup> The low concentrations used in the jet experiment, and near-saturation of fluorescence, caused absorption to be a small fraction of the initial laser intensity,  $I_{L,0}$  (Shan *et al.* 2004). It was verified in fluorescence measurements of a uniform-concentration field that laser attenuation due to absorption was small for the mean-concentration-pathlength of the jet images.

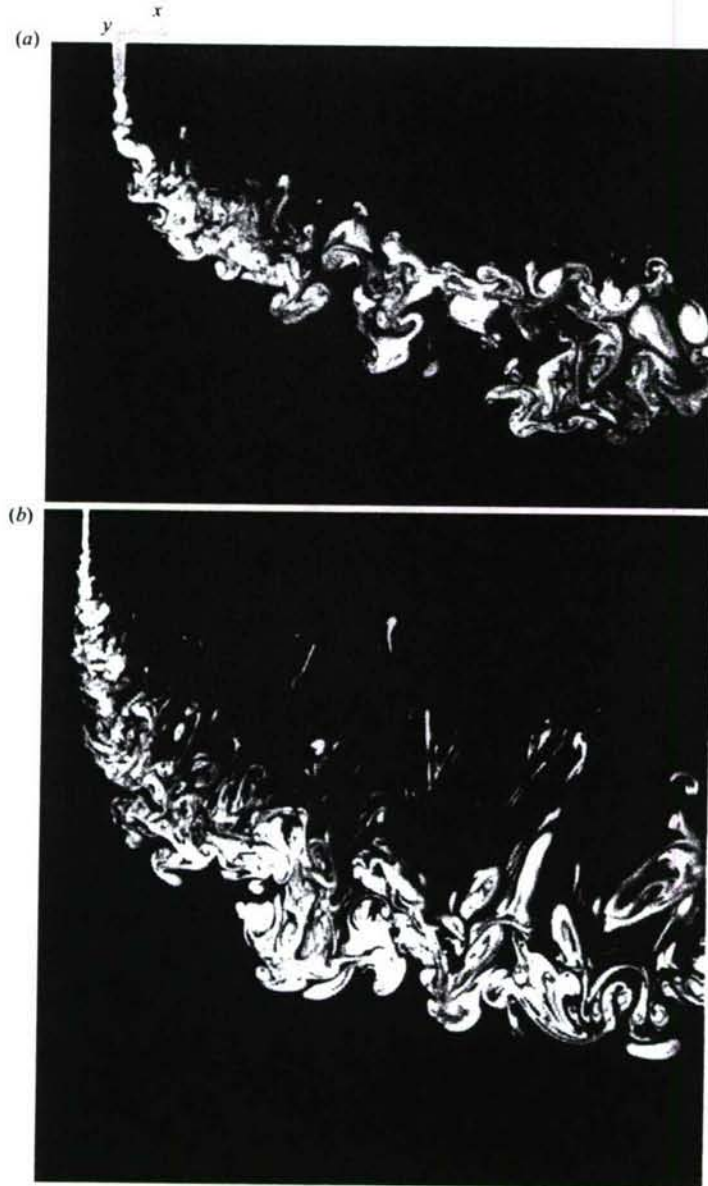


FIGURE 4. Mixed-fluid concentration in a streamwise cross-section of the transverse jet at  $Re_j = 1.0 \times 10^3$ . The intensity of the image shown has scaled by  $x^{1/2}$  to compensate for downstream decay. (a)  $V_r \simeq 10$ . (b)  $V_r \simeq 32$ .

by scaling by  $c_{ref}/c_0$ , which is known *a priori*. This ultimately yields the mixed-fluid-concentration values, normalized to the plenum concentration, so that

$$0 \leq C(x_1, x_2, t) \equiv \frac{c(x_1, x_2, t)}{c_0} = \frac{c(x_1, x_2, t)}{c_{ref}} \frac{c_{ref}}{c_0} \leq 1. \quad (3b)$$

In this way, the scalar-field measurements were normalized so that  $C = 1$  corresponds to unmixed jet fluid (at the jet exit) and  $C = 0$  corresponds to pure crossflow (free-stream) fluid.

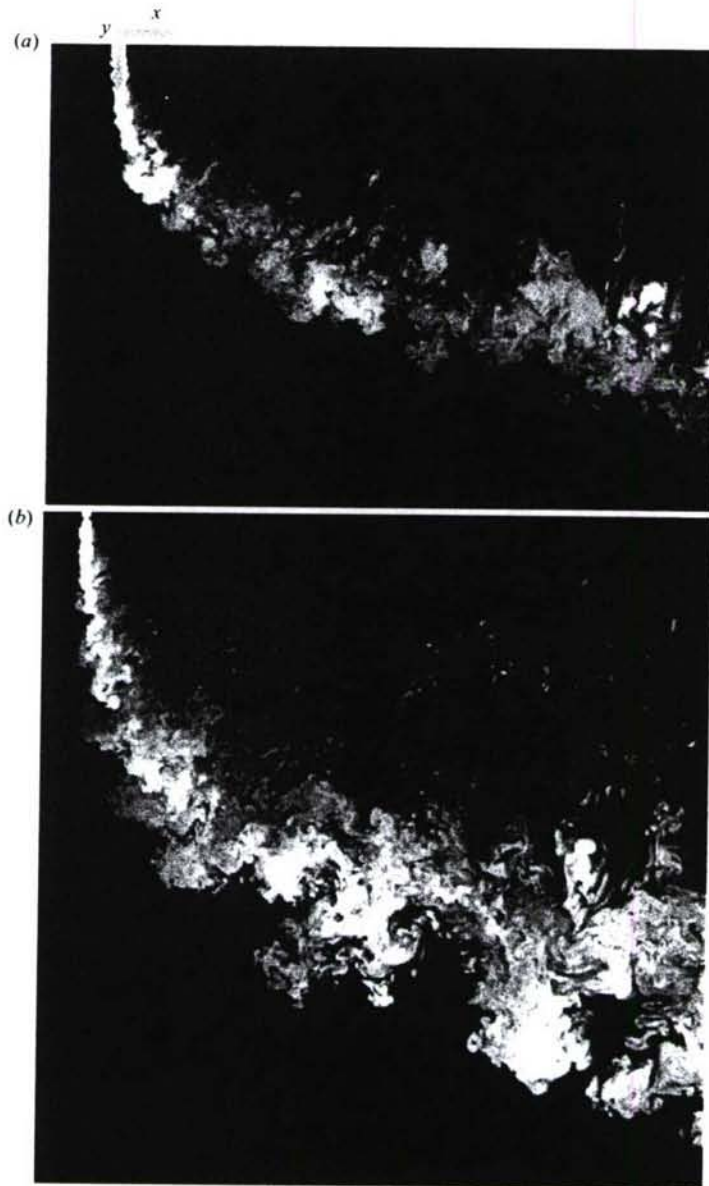


FIGURE 5. As for figure 4, but  $Re_j = 10 \times 10^4$ .

For streamwise slices of the jet, any possible shot-to-shot variations in the power of the pulsed laser were measured and normalized by monitoring the fluorescence-intensity fluctuations at the jet exit. This was made possible by the fact that the jet exit remained visible in the streamwise images, and that the jet-exit concentration never varied. For transverse slices of the jet, the jet exit was no longer visible and an alternative reference cell was required. In that case, a fibre-optic probe was used to deliver a fraction of the laser output to a test tube containing a small sample of fluorescent dye. An image of the test-tube fluorescence was recorded on an unused corner of the CCD array and used to detect and normalize any shot-to-shot power fluctuations of the laser. In other LIF experiments, which typically use

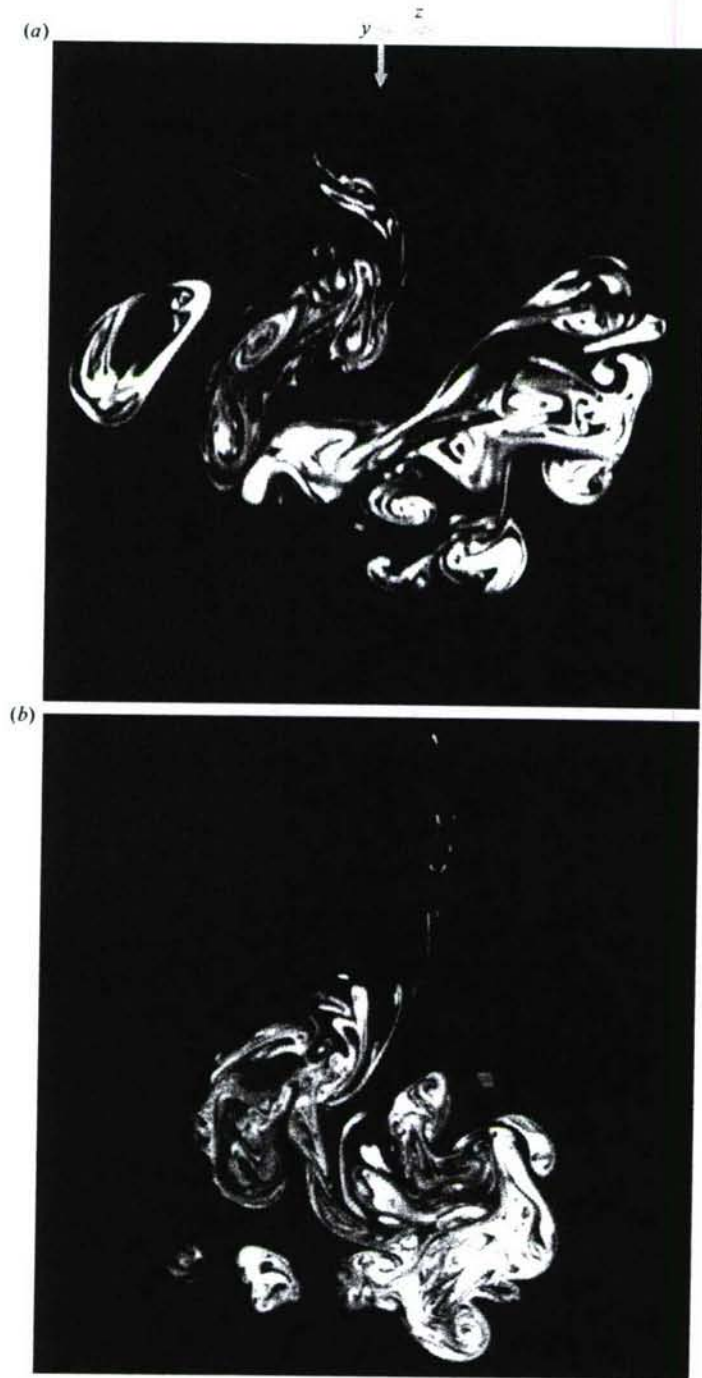


FIGURE 6. Mixed-fluid concentration in a perpendicular cross-section of the jet at  $Re_j = 1.0 \times 10^3$ . (a)  $V_r \simeq 10$  and  $x/d_j = 50$ . (b)  $V_r \simeq 32$ .

continuous-wave lasers, previous investigators have used reference cells in a similar fashion to account for temporal variations, attenuation and other non-idealities in the optical system (e.g. Koochesfahani & Dimotakis 1986; Dahm & Dimotakis 1990).

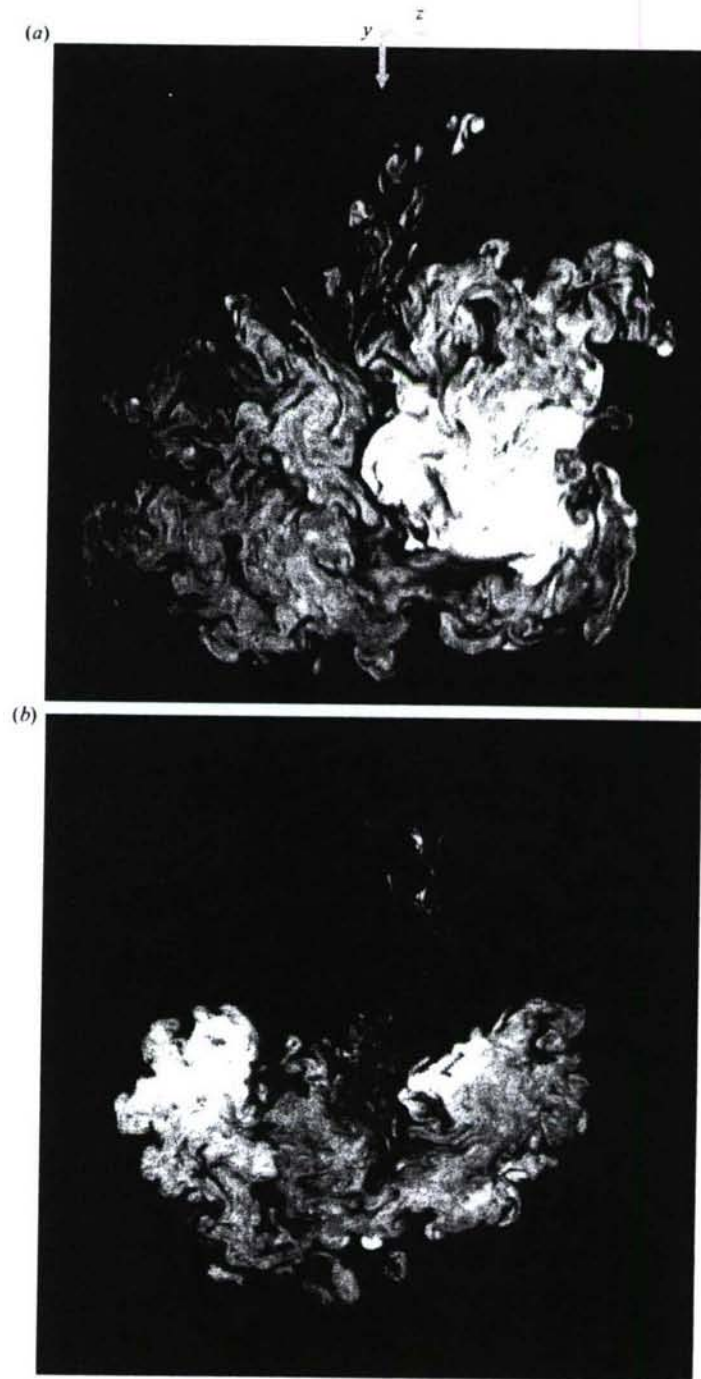


FIGURE 7. As figure 6, but  $Re_j = 10 \times 10^3$ .

Figures 4 and 5 show examples of streamwise cross-sectional images at Reynolds numbers of  $1.0 \times 10^3$  and  $10 \times 10^3$ , respectively. (For display purposes only, the images shown in figures 4 and 5 have been scaled to compensate for the downstream decay

in concentration and image intensity. The images intensity was adjusted by a factor proportional to the square root of the downstream distance (i.e.  $x^{1/2}$ ) starting just upstream of the jet exit. This scaling, of course, was not applied to the data used for quantitative analysis.) The upper images are for a jet-to-crossflow velocity ratio of 10, and the lower images for a velocity ratio of 32. In the low-Reynolds-number case, the jet core remained laminar for several  $d_j$  after exiting the nozzle; however, at the higher Reynolds number, the jet's potential core transitioned and mixed within approximately one  $d_j$ . From the images, it can also be seen that the transverse jet's scalar field has very small-scale structure at its upper half (the 'wake' region); the jet is noticeably smoother on the bottom. Also clearly visible on the jet centreline at  $V_r = 32$ , and still present but less noticeable at  $V_r = 10$ , are the filaments ('hairs' or 'fingers') of jet fluid extending upward from the jet body toward the injection wall. These thin filaments have a preferred orientation in the vertical direction, and contribute to the local anisotropy of the scalar field, as will be discussed in § 5.

Figures 6 and 7 show examples of transverse cross-sections of the jet at  $Re_j = 10^3$  and  $Re_j = 10 \times 10^3$ , respectively. A kidney-shaped structure is seen which is associated with a counter-rotating vortex pair. From a time sequence of images, the jet position and the size of the scalar 'lobes' can be seen to vary over time. As was the case with the streamwise view of the jet, thin vertical filaments can be seen in the wake region; these filaments extend from the middle of the counter-rotating vortex pair up toward the injection wall. These fine-scale features in the wake region are more apparent in the transverse slices than in the streamwise slices because, in the cross-sectional views, they are captured even if they do not fall precisely on the jet centreline.

The appearance of jet fluid in the wake, which is seen from the data for  $V_r \geq 10$ , has been previously reported by Lozano *et al.* (1993) and Smith & Mungal (1998) to occur at velocity ratios between 10 and 15. Fric and Roshko (1994) concluded, based on the absence of jet fluid in the wake for high velocity ratios, that the boundary layer on the plate (i.e., the crossflow boundary layer), and not the jet boundary layer (originating within the jet nozzle), was the source of vorticity for the organized vortices that they observed in the wake region of the transverse jet. The fact that jet fluid is observed in the wake for  $V_r \geq 10$  implies that Fric & Roshko's reasoning does not apply for high-velocity-ratio jets; their conclusion may still be correct, however. Smith & Mungal (1998) have proposed that wake vortices, when stretched, could have strong axial flows that would pull fluid from the jet into the wake region. This explanation would reconcile the observation that the jet fluid appears in the wake with Fric & Roshko's proposal that the wake vortices arise from the crossflow boundary layer. However, the observed presence of jet fluid in the wake means that it cannot be completely ruled out based on existing arguments that the vorticity in the wake region arises from a source other than the crossflow boundary layer.

## 2.2. Local Reynolds number and circulation

Unlike the axisymmetric jet discharging in a quiescent reservoir, the local Reynolds number of the jet in crossflow changes with increasing downstream distance. It is shown in the following that the local Reynolds number,  $Re_T$ , based on the circulation of a counter-rotating vortex pair, decays in power-law fashion with downstream distance.

Following the analysis of Broadwell & Breidenthal (1984), a jet is considered which discharges perpendicularly at velocity  $U_j$  into a crossflow of velocity  $U_\infty$ . The jet becomes a point source of momentum in the limit in which the jet momentum flux,  $\dot{m}_j U_j = \rho_j \pi (d_j/2)^2 U_j^2$ , is held constant as jet diameter,  $d_j$ , decreases, and the discharge

velocity,  $U_j$ , increases. This point source of normal momentum, i.e. a 'lift' force of vanishing drag, generates a counter-rotating vortex pair that is analogous to the tip-vortices behind a finite-span wing generating lift. Broadwell & Breidenthal argue that viscosity has no global role but only serves to dissipate energy at the small scales; thus, the only global length scale possible from dimensional analysis is:

$$l = \left( \frac{\dot{m}_j U_j}{\rho_\infty U_\infty^2} \right)^{1/2}, \quad (4)$$

For the case of equal density fluids, as is the case in the present experiments, the global length scale reduces to  $l = (\pi/4)^{1/2} d_j V_r$ .

The circulation,  $\Gamma$ , of one vortex of the vortex pair is related to the vortex-core separation distance,  $R$ , and the vortices' vertical velocity,  $dy/dt$ :

$$\frac{dy}{dt} = \frac{c_1 \Gamma}{R}. \quad (5)$$

Also, the fluid impulse per unit length,  $P$ , of the vortex is:

$$P = c_2 \rho_\infty \Gamma R. \quad (6)$$

The values of the constants  $c_1$  and  $c_2$  in (5) and (6) depend on the spatial distribution of vorticity; for example,  $c_1 = \pi/4$  and  $c_2 = 2$  for ideal line vortices. It should be noted that (5) and (6) assume that the jet takes the form of a single counter-rotating vortex pair. (If the circulation is divided between more than two vortices, each vortex could have different induced velocities,  $dy/dt$ , and differing trajectories. The basic case, in which a single vortex pair is found, is considered for this discussion.) A similarity form is assumed in which the flow is independent of the global length scale  $l$  in the far field, so that  $R$  is proportional to  $y$ . Then, (5) and (6) may be combined to eliminate  $\Gamma$ , and the result integrated, assuming  $R \propto y$ , to find the trajectory:

$$y = c_3 \left( \frac{P}{\rho_\infty} \right)^{1/3} t^{1/3}. \quad (7)$$

With the far-field transformation  $x = U_\infty t$ , and noting that  $P = \dot{m}_j U_j / U_\infty$ , the trajectory of the transverse jet is,

$$\frac{y}{l} = c_3 \left( \frac{x}{l} \right)^{1/3}, \quad (8)$$

as found by Broadwell & Breidenthal (1984).

It can be seen from the preceding equations that the circulation of each vortex in the transverse-jet decreases with downstream distance,  $x$ , as:

$$\frac{\Gamma}{U_\infty l} = c_4 \left( \frac{x}{l} \right)^{-1/3}. \quad (9)$$

Equation (9) can be expected to hold in the far field of high-velocity ratio transverse jets, in particular, for  $x > l$ , where  $l \equiv V_r d_j$ . An alternative definition of the far field has been proposed by Smith & Mungal (1998) based upon centreline concentration decay measurements. By their measure, the far field begins for  $s/d_j > 0.3 V_r^2$ , where  $s$  is the arclength along the jet trajectory. Regardless of which definition is used, the measurements of jet cross-sections at  $x/d_j = 50$  that are described in the following sections are in the far field.

It should also be noted that the decreasing circulation of the vortex pair (equation (9)) is not a consequence of viscous decay of vorticity because the analysis

$Re_j$	$V_r$	$\Theta/d_j$	$Re_\Gamma$	$Re_\lambda$	$\lambda_v/\lambda_p$	$\lambda_x/\lambda_p$
$1.0 \times 10^3$	10	0.30	$0.58 \times 10^3$	32	281	5.3
$2.0 \times 10^3$	10	0.21	$1.2 \times 10^3$	45	167	3.2
$5.0 \times 10^3$	10	0.13	$2.9 \times 10^3$	71	84	1.6
$10 \times 10^3$	10	0.094	$5.8 \times 10^3$	100	50	0.94
$20 \times 10^3$	10	0.067	$12 \times 10^3$	141	30	0.56

TABLE 1. Experimental conditions and imaging resolution of the LIF measurements at  $x/d_j = 50$ .  $\lambda_p$  is the in-plane pixel resolution for the transverse slices. The momentum thickness,  $\Theta$ , is computed at jet exit. The circulation-based ( $Re_\Gamma$ ) and Taylor ( $Re_\lambda$ ) Reynolds numbers are computed at  $x/d_j = 50$ .

assumes inviscid flow. Hasselbrink & Mungal (2001) argue that the decrease in circulation is a result of the circulation integral being taken across a decreasing number of vortex lines as one moves downstream. Because the vorticity is not contained in a single vortex tube, circulation measured in transverse planes need not be conserved, even in the inviscid limit. (The actual circulation that would be measured in an experiment would be even less owing to the viscous decay of two opposite-signed vortices in proximity to one another.)

Based upon the circulation, a local Reynolds number for the transverse jet at any far-field downstream location  $x > l$  can be defined,

$$Re_\Gamma(x) \equiv \frac{\Gamma}{v} = c_4 \frac{U_\infty l}{v} \left( \frac{x}{l} \right)^{-1/3}. \quad (10)$$

The local Reynolds number,  $Re_\Gamma(x)$ , is related to the jet-exit Reynolds number,  $Re_j$ , as

$$Re_\Gamma(x) = c_5 \frac{U_j d_j}{v} \left( \frac{x}{l} \right)^{-1/3} = c Re_j \left( \frac{x/d_j}{V_r} \right)^{-1/3}, \quad (11a)$$

where  $c_5$  and  $c$  are constants. The value of the constant,  $c$ , can be estimated by noting that the local Reynolds number,  $Re_\Gamma(x)$ , should approach (or at least be of the same order of magnitude as) the jet-exit Reynolds number,  $Re_j$ , as one moves closer to the jet exit (i.e.  $c$  is of order one so that  $Re_\Gamma(x)/Re_j$  is of order one as  $x/l \rightarrow 1$ ). It is reasonable then to define  $c = 1$ , with the resulting expression for the local, circulation-based Reynolds number as:

$$Re_\Gamma(x) = \left( \frac{x/d_j}{V_r} \right)^{-1/3} Re_j. \quad (11b)$$

Thus, at downstream location  $x/d_j = 50$ , the jet-exit Reynolds number,  $Re_j$ , is related to the local (outer-scale) Reynolds number by a factor of 0.6 for  $V_r = 10$ . Both Reynolds numbers are summarized in table 1 for the experimental conditions of this paper.

Finally, the Taylor Reynolds number, based upon the root-mean-squared fluctuation of one component of velocity and the Taylor microscale,  $\lambda_T$ , can be estimated as

$$Re_\lambda \equiv \frac{u_{rms} \lambda_T}{v} \simeq Re^{1/2},$$

for high Reynolds number (e.g. Frisch 1995). For the present experiment, the highest Taylor Reynolds number attained is  $Re_\lambda \simeq 141$  (table 1). The scalar-species equivalent of the Péclet number for this flow,  $Re_\lambda Sc$ , is estimated to reach a maximum of  $3.9 \times 10^5$ .

The proceeding discussion, which found the local Reynolds number for the transverse jet, has consequences for the dissipation scales of the current experiment. The smallest scales of the transverse jet, and the imaging resolution, are discussed in the following section.

### 2.3. Dissipation scales and resolution

The resolution requirement for scalar concentration measurement is set by the scalar diffusion scale,  $\lambda_\delta$ , which is itself a multiple of the viscous scale,  $\lambda_v$ ,

$$\lambda_\delta \simeq Sc^{-1/2} \lambda_v. \quad (12)$$

The Schmidt number,  $Sc$ , is the ratio of kinematic viscosity to scalar species diffusivity. For high molecular-weight dyes in liquid-phase flows, the Schmidt number is much larger than unity and the finest features in the scalar field can be significantly smaller than those in the velocity or vorticity fields. (The Schmidt number for rhodamine-6G in water is  $Sc \simeq 2800$  (e.g. Xu & Yeung 1997).)

To estimate the viscous scale, it is possible to take the scale at which turbulence spectra deviate at high wavenumbers from  $-5/3$  power-law behaviour. Based upon data from a variety of flows (wakes, grid turbulence, boundary layers, jets, etc.) across a wide range of Reynolds numbers ( $23 \leq Re_\lambda \leq 3180$ ), Dimotakis (2000) has estimated the viscous scale to be 50 times larger than the Kolmogorov scale,  $\lambda_K$ , i.e.

$$\lambda_v \simeq 50 \lambda_K. \quad (13)$$

The Kolmogorov scale,  $\lambda_K$ , is in turn defined as

$$\lambda_K \equiv \left( \frac{v^3}{\epsilon} \right)^{1/4}. \quad (14a)$$

When no measured values for the dissipation rate are available, an alternative approximation to the Kolmogorov scale can be used:

$$\frac{\lambda_K}{\delta(x)} \simeq c_6 Re(x)^{-3/4}. \quad (14b)$$

The constant,  $c_6$  is of order unity, based upon the energy-dissipation measurements of Freihe, Van Atta & Gibson (1971) in turbulent jets (Dimotakis 2000).

For the transverse jet, the jet width is a sensible outer scale, and the Reynolds number can be taken to be the local circulation-based Reynolds number  $Re_{\ell}$ . Based on the jet width and the circulation-based Reynolds number, the scalar diffusion scales for the conditions of the present experiments can be computed; these estimates of the required spatial resolution to fully resolve the flow are shown in table 1. In the table, the scalar diffusion scale is compared to the measurement resolution,  $\lambda_p$ , which is determined by either the pixel resolution of the images, or the thickness of the laser sheet, whichever is greater. For the transverse cross-sectional images of the jet, the pixel image resolution was 0.23 mm and the laser-sheet thickness was 0.19 mm. Thus, comparing the image resolution to the estimated scalar-diffusion scale, the LIF measurements of concentration are seen to be resolved for transverse slices at  $x/d_j = 50$  for Reynolds numbers up to  $10 \times 10^3$ , and not fully resolved for  $Re_j = 20 \times 10^3$ .

The consequences of inadequate spatial resolution when making measurements of passive scalar fields were discussed by Breidenthal (1981) and Koochesfahani & Dimotakis (1986). Koochesfahani & Dimotakis found for liquid-phase mixing layers that inadequate resolution mimicked the qualitative effect of enhanced molecular

diffusion. However, a ten-fold degradation of measurement resolution did not change the mean concentration and only increased the probability of finding mixed fluid by approximately 10% on the centreline of the mixing layer. Thus, while the marginal spatial resolution for the  $Re_j = 20 \times 10^3$  transverse jet may artificially sharpen the peak of the probability distribution, it is unlikely to change the measured distribution of jet fluid significantly. Moreover, the Reynolds-number effects seen in the flow (§ 3) begin at Reynolds numbers which are well resolved, and thus are unlikely to result from degrading resolution.

#### 2.4. Space-time visualization

The global structure of the jet can be visualized by stacking a contiguous time-resolved sequence of images of the jet. The transverse jet is particularly amenable to such space-time visualizations because Taylor's hypothesis holds reasonably well in the far-field of this flow and can be used to transform between time and space coordinates. For the transverse jet, the streamwise velocity deficit (the velocity of the wake relative to the free-stream velocity), decays rapidly with downstream distance, so that the streamwise velocity is approximately the free-stream velocity at a far-downstream location, i.e.  $U_x \simeq U_\infty$  for the far field (e.g. Mungal & Lozano 1996; Yuan & Street 1998). In this case, the space-time visualizations provide a reasonable approximation to the instantaneous three-dimensional jet. It should be noted, however, that the growth of the jet with downstream distance is not captured by the space-time data. In a sense, however, alternative information is recorded; the space-time data sets, while not instantaneous spatial data, are nonetheless a three-dimensional slice of the four-dimensional space-time domain of the unsteady turbulent jet. The space-time images that are presented here are similar in spirit to the visualizations of Mungal & Lozano (1996) of burning plumes in crossflow. Their visualizations, taken from video films of burning Kuwaiti oil wells, are qualitative images of burning plumes, rather than the quantitative LIF slices of density-matched jets considered in the present work. Mungal & Lozano find, based on assembled side views (i.e. streamwise views) of the jet, that the downstream side (the wake side) of the jet displays considerably more complexity than the upstream side of the jet. Yoda, Hesselink & Mungal (1992) have provided similar volume renderings of a turbulent jet without crossflow.

Visualizations of level-sets of jet-fluid concentration, i.e.  $C(x, t) = C_{iso}$ , are of particular interest because the area of the level sets affects the overall rate of reaction that would occur if the two fluids contained chemically reacting species. In figures 8 and 9, sequences of instantaneous images are assembled into three-dimensional space-time visualizations of the scalar jet at two Reynolds numbers,  $Re_j = 1.0 \times 10^3$  and  $Re_j = 2.0 \times 10^3$ . Taylor's hypothesis is used to transform time into an approximate streamwise distance. The  $C \simeq 0.006$  isosurface is highlighted for both cases by selecting only a small concentration range centred at that concentration to be opaque and reflecting.

From the space-time visualizations, the scalar structure of the transverse jet at both Reynolds numbers can again be seen to be dominated by a pair of kidney-shaped, counter-rotating vortices. A deep cleft separates the two main lobes of the counter-rotating vortices, and fine-scale filaments extend up from the cleft into the wake, as was also seen in the individual images (figure 6). The wake side of the jet has more complex smaller-scale features than the upstream side, as previously seen by Mungal & Lozano (1996). Comparing the two Reynolds numbers, a small tertiary vortex is seen at  $Re_j = 1.0 \times 10^3$  which is not seen at  $Re_j = 2.0 \times 10^3$ . Rotation of the tertiary vortex is evident in the spiral wrapping of thin scalar filaments. For the



FIGURE 8. Space-time visualization of isosurface of  $C \simeq 0.06$  for transverse jet at  $Re_j = 1.0 \times 10^3$ ,  $V_r = 10$ , and  $x/d_j = 50$ .



FIGURE 9. Space-time visualization of isosurface of  $C \simeq 0.06$  for a  $Re_j = 2.0 \times 10^3$ ,  $V_r = 10$ , transverse jet.

lower-Reynolds-number jet, the main lobes of the scalar field are not equal in size because of the jet fluid entrained in the tertiary vortex. Only two main lobes, approximately equal in size, are seen in the higher-Reynolds-number case,  $Re_j = 2.0 \times 10^3$ .

These limited visualizations are qualitatively consistent with the experiments of Kuzo (1995), which found a transition between asymmetric and symmetric counter-rotating vortices in the transverse jet above a critical Reynolds number. Using particle image velocimetry to measure velocity and vorticity fields, Kuzo reported the existence of tertiary, and even quaternary vortices, at low Reynolds numbers. At  $V_r = 10$ , the initially asymmetric jets appeared to transition to a symmetric flow state as the Reynolds number was increased above a critical value of  $Re_j \simeq 6.0 \times 10^3$ . Of course, the scalar-field measurements of the present study are not directly comparable to measurements of vorticity and velocity fields. However, the present data do indicate asymmetric structure and decreasing asymmetry with increasing Reynolds number in the flow-regime investigated. The general asymmetry of the transverse jet at downstream locations has been noted in experimental studies by Kamotani & Greber (1972) and Smith & Mungal (1998), among others. Smith and Mungal (1998) review the evidence for asymmetry in the transverse jet and conclude that it is quite common in experiments, although symmetry is often assumed in computational investigations.

### 3. Reynolds-number effects and flow dependence

By some measures, the behaviour of turbulent jets in crossflow appears to be insensitive to Reynolds number. Gross structural features, such as the jet size and trajectory, are insensitive to Reynolds number within the range that was investigated. Figure 10 shows two different 'sizes' of the jet cross-section at  $x/d_j = 50$ . The size,  $\delta_h$ , is defined as the horizontal extent of the jet for which the mean concentration is greater than a given percentage (either 3 % or 5 %) of the peak concentration. As seen in the figure, the horizontal size is approximately independent of Reynolds number over the range  $1.0 \times 10^3 \leq Re_j \leq 20 \times 10^3$ . Despite the different growth rates of the transverse jet and jet discharging in a quiescent reservoir, their sizes are comparable at  $x/d_j = 50$ , where  $\delta_h \simeq 23$  (cf. Dahm & Dimotakis 1990). A further discussion of the relative entrainment rates of transverse jets and ordinary jets will be postponed until §3.2.

Reynolds number also appears to have little effect on jet trajectories. Mean jet trajectories, defined as the locus of points of maximum mean-concentration on the jet centreline, are shown in figure 11 for the same velocity ratio at two different Reynolds numbers,  $Re_j = 1.0 \times 10^3$  and  $10 \times 10^3$ . The trajectories essentially overlap, and both exhibit a power-law dependence of penetration depth on downstream distance. (For the higher-Reynolds-number jet, the trajectory dips slightly around  $x/d_j \approx 10^{1.25} = 18$  before continuing on at the same slope. The slight dip in jet trajectory is associated with a near-plateau that occurs in the mean concentration field at that location (see figure 11); a similar dip occurs at the same downstream location in the trajectory reported by Smith & Mungal (1998, their figure 7) for the  $V_r = 10$  jet.) Early experiments by Pratte & Baines (1967) found power-law trajectories with an exponent of 0.28, and, as discussed in §2, subsequent modelling work by Broadwell & Breidenthal (1984) predicted a power-law trajectory with an exponent of 1/3. For comparison, lines of slope 0.28 and 1/3 are shown in figure 11. The trajectory of the present data is closer to that of Broadwell & Breidenthal. It should be noted that the scalar trajectories are generally shallower than trajectories based on the maximum velocity or mean nozzle streamlines (e.g. Kamotani & Greber 1972; Yuan, Street & Ferziger 1999). Differences between scalar and velocity trajectories are also discussed by Su *et al.* (2000) and Hasselbrink & Mungal (2001).

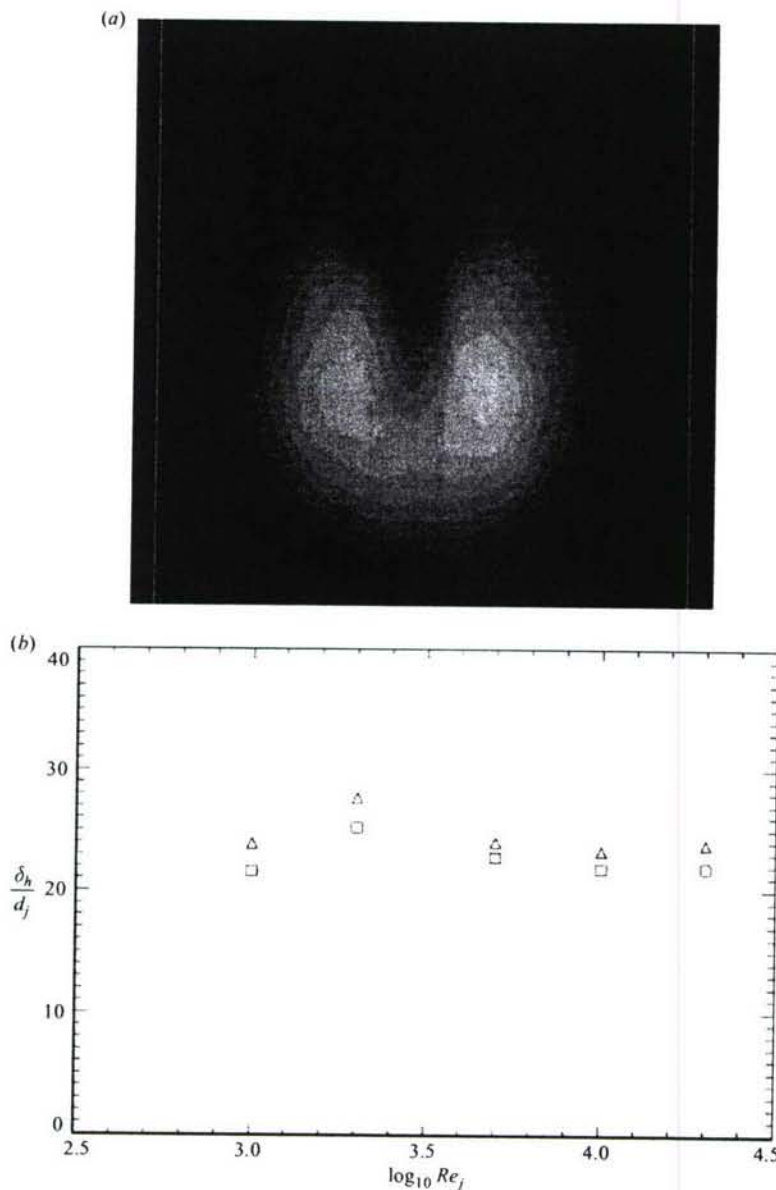


FIGURE 10. 'Size' of the  $V_r = 10$  transverse jet in cross-section, defined as the average horizontal extent,  $\delta_h$ , of mean scalar field at  $x/d_j = 50$ . (a) Ensemble-averaged scalar field for  $Re_j = 20 \times 10^3$ . Lines show horizontal extent of 3% of maximum mean-concentration. (b) Size versus Reynolds number.  $\triangle$ , 3% of maximum mean-concentration.  $\square$ , 5% of maximum mean-concentration.

The decay of mean-concentration on the jet centreline is also insensitive to Reynolds number, over the range of values investigated. Figure 12 shows the centreline mean-concentration decay for  $Re_j = 1.0 \times 10^3$  and  $Re_j = 10 \times 10^3$ . The lower-Reynolds-number jet has a longer potential core and initially decays more slowly with penetration depth (cf. figures 4 and 5). However, by about  $x/d_j \simeq 6$ , the decay of the low-Reynolds-number jet has caught up to that of the higher-Reynolds-number case.

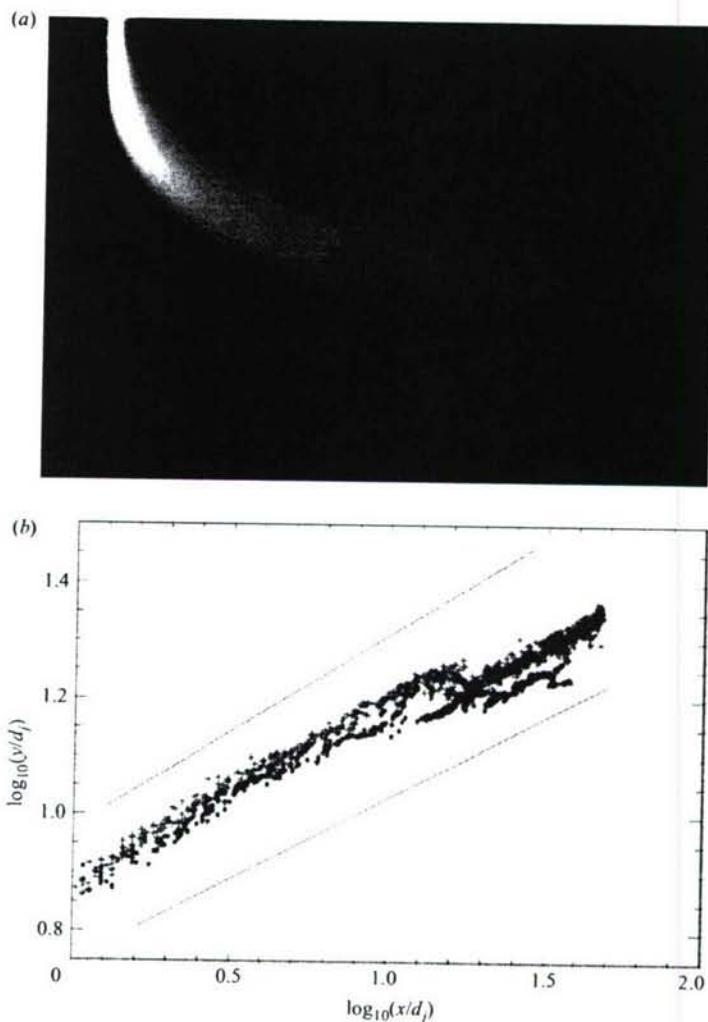


FIGURE 11. Mean concentration field and jet-centreline trajectory for  $V_r = 10$ . (a) Ensemble-averaged concentration field for  $Re_j = 10 \times 10^3$ . (b) Penetration depth versus downstream distance. Circles show  $Re_j = 1.0 \times 10^3$  and crosses show  $Re_j = 10 \times 10^3$ . The lower comparison line is based on experiments of Pratte & Baines (1967) and shows  $y/d_j \propto (x/d_j)^{0.28}$ . The upper comparison line is based on predictions of Broadwell & Breidenthal (1984) and shows  $y/d_j \propto (x/d_j)^{1/3}$ .

Figure 13 depicts the concentration decay with downstream distance normalized in two ways,  $x/d_j$  and  $x/V_r d_j$ . Apart from a difference due to potential-core lengths, the decay rates of the jet at the two Reynolds numbers are nearly indistinguishable.

As an aside, it should be noted that Smith & Mungal (1998) reported a ‘branch point’ in the centreline concentration decay, representing, in their words, ‘a transition in the flow field from enhanced mixing to reduced mixing compared to the free jet.’ They identified the transition point as occurring around  $s/V_r^2 d_j \simeq 0.3$ , or, approximately,  $x/V_r d_j \simeq 1.6$  (Smith & Mungal 1998, their figure 24). That location is marked in figure 13 with an arrow. For the  $Re_j = 10 \times 10^3$  case shown, a very slight change in the slope of the centreline concentration decay can be seen. While

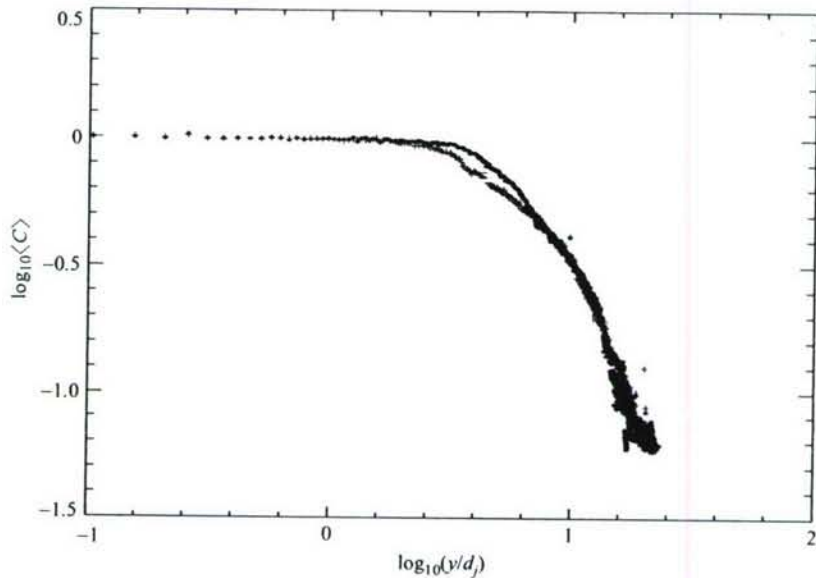


FIGURE 12. Decay of maximum mean-concentration with penetration depth at  $V_r = 10$ . Small circles show  $Re_j = 1.0 \times 10^3$ , and small crosses show  $Re_j = 10 \times 10^3$ .

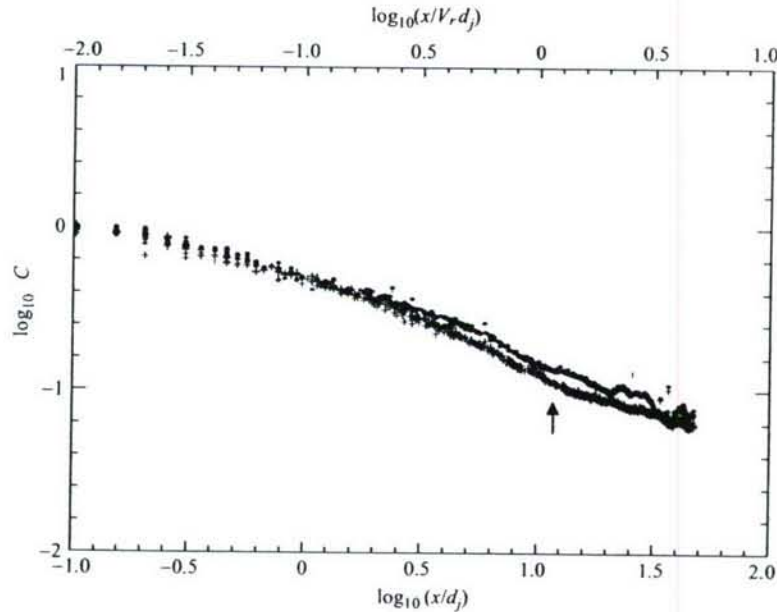


FIGURE 13. Decay of maximum mean-concentration with downstream distance at  $V_r = 10$ .  $Re_j = 1.0 \times 10^3$  is shown with circles,  $Re_j = 10 \times 10^3$  with crosses. The top axis shows downstream distance normalized by  $V_r d_j$ , while the bottom axis shows downstream distance normalized by  $d_j$ . The arrow marks the location of a slight change in the slope of the decay reported by Smith & Mungal (1998) at  $\log(x/V_r d_j) \simeq 0.15$ .

not conclusive, the present data are consistent with Smith & Mungal's (1988) findings of a slight change in slope of the mean-concentration decay rate on the centreline of the transverse jet.

However, it should be noted that mean quantities, such as mean-concentration decay rate or mean jet width, are not actual measures of mixing, but rather measures of entrainment. In particular,  $\langle C \rangle$  is a measure of the ratio of jet fluid to total (jet fluid plus entrained crossflow fluid) mass flux. By definition, the mean concentration is the same for any probability distribution function having the same first moment. Thus, the mean cannot distinguish between perfectly homogenized fluids (one Dirac delta function), completely unmixed fluids (two Dirac delta functions), or intermediate states with the same first moment. To assess mixing, and its Reynolds-number dependence, measures other than mean quantities must be examined.

### 3.1. Distribution of jet fluid

A description of mixing involves knowledge of the probability density function of the conserved passive scalar, in this case, the jet-fluid concentration. The distribution,  $f(C; Re_j)$ , of mixed-fluid concentration is normalized so that its definite integral is the probability that  $C$  lies between the limits of integration:

$$Pr\{C_1 \leq C < C_2\} = \int_{C_1}^{C_2} f(c) dc = F(C_2) - F(C_1). \quad (15)$$

It should be noted that the distributions discussed in this paper are based on the probability of occurrence of a particular concentration  $C$  in an instantaneous two-dimensional image, rather than on the frequency of occurrence at a fixed point in space. Thus, they are spatial rather than temporal probability distributions. The spatial PDF is computed as the normalized magnitude of the differential area associated with various concentration values. In two dimensions, the PDF is (Kuznetsov & Sabel'nikov 1990; Dimotakis & Catrakis 1996),

$$f(C) = \frac{1}{A_{tot}} \left| \frac{dA(C)}{dC} \right|, \quad (16a)$$

where  $A(C)$  is the area associated with a specified value of the scalar concentration, and  $A_{tot}$  is the total area (domain) of the measured scalar field. Generalized to  $d$ -dimensions, the PDF would be computed as,

$$f_n(C) = \frac{1}{V_{d,tot}} \left| \frac{dV_d(C)}{dC} \right|, \quad (16b)$$

where  $V_d(C)$  is the  $d$ -dimensional volume associated with  $C$ , and  $V_{d,tot}$  is the total,  $d$ -dimensional volume (domain) of the scalar field. Experimentally measured probability-density functions depend in general on the dimensionality of the measurement, as well as on the form of the scalar field (see the Appendix). Thus, the PDFs described in the following discussion are more precisely the distribution of jet-fluid concentration in two-dimensional slices of the four-dimensional scalar field  $C(x, y, z, t)$ .

In contrast with structural measures such as the jet size and trajectory, or mean measures such as the decay of centreline concentration, the data indicate that the distribution of mixed fluid in the far field of a high-Schmidt-number strong transverse jet varies strongly with Reynolds number. The PDF of jet-fluid concentration at a fixed far-field location does not reach an asymptotic state, up to at least  $Re_j = 20 \times 10^3$ . Figure 14 shows scalar PDFs for five different Reynolds numbers,  $Re_j = 1.0, 2.0, 5.0, 10$  and  $20 \times 10^3$ . The measurement location was fixed at  $x/d_j = 50$  and the velocity ratio was maintained at  $V_j = 10$  in all cases. At the lowest Reynolds number, the PDF is qualitatively similar to the probability distribution of a two-dimensional diffusive concentration field (derived in the Appendix). The distribution is

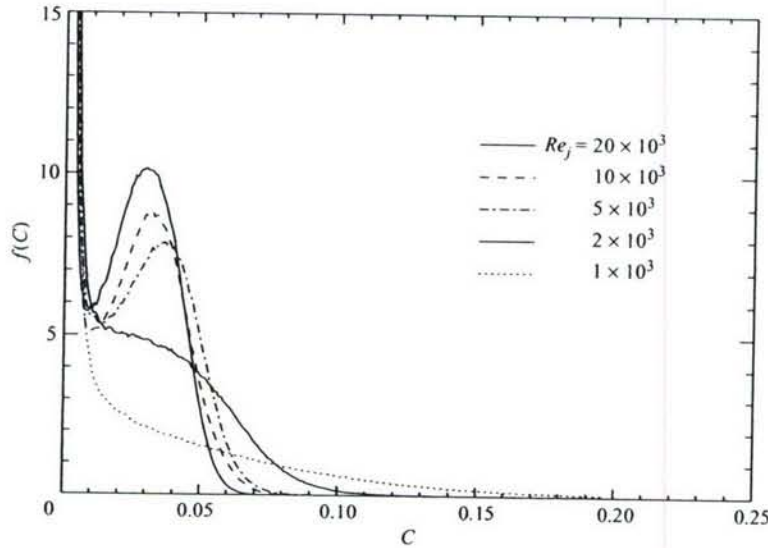


FIGURE 14. Distribution of jet-fluid-concentration for varying Reynolds number at  $V_r = 10$ . Measurements made at  $x/d_j = 50$  for  $Re_j = 1.0, 2.0, 5.0, 10$  and  $20 \times 10^3$ . Increasingly peaked PDFs with increasing Reynolds number.

broad, decreases monotonically, and peaks at very low jet-fluid concentration ( $C \approx 0$ ). As the Reynolds number is increased, the distribution of mixed fluid no longer decreases monotonically but develops a peak, i.e. there develops a most-probable concentration in the scalar field. The peak occurs by  $Re_j = 5.0 \times 10^3$ . The preferred-concentration peak grows in height with increasing Reynolds-number up to the highest Reynolds numbers investigated,  $Re_j = 20 \times 10^3$ . The scalar field is increasingly stirred and becomes more spatially homogeneous with increasing Reynolds number.

The image data themselves show additional evidence for a shift from a relatively unmixed to a well-mixed nearly homogeneous distribution with increasing Reynolds number. Figure 15 shows scalar fields for concentrations straddling the peak of the mixed-fluid PDF at high Reynolds numbers. Jet-fluid concentrations between  $C = 0.025$  and  $C = 0.045$  are highlighted in the image at two Reynolds numbers,  $Re_j = 1.0 \times 10^3$  and  $Re_j = 10 \times 10^3$ . For the lower-Reynolds-number case, the concentration range,  $0.035 \leq C \leq 0.045$ , is confined to a thin region on the boundary of the jet. Everywhere else, the scalar field is relatively unmixed, with high concentration regions near the core of the jet and pure free-stream fluid outside. For the higher Reynolds-number jet, the specified concentration range is found throughout much of the body of the jet. The jet fluid is much more homogeneously mixed owing to the turbulent stirring. Thus, the measured growth of PDF peaks with increasing Reynolds number is a direct consequence of the enhanced homogenization of the concentration field. It should also be noted that the PDF for each Reynolds number contains  $5.3 \times 10^8$  individual measurements of the scalar field (508 frames at  $(1024 \times 1024)$ -pixel resolution). For the length of the recording, approximately four large-scale structure passages are captured at the lowest Reynolds number, and over 75 at the highest.

The most-probable concentration (i.e. the location of the PDF peak) and the width of PDF both vary with Reynolds number over the range  $1.0 \times 10^3 \leq Re_j \leq 20 \times 10^3$ . Figure 16 shows the concentrations associated with the peaks of the jet-fluid

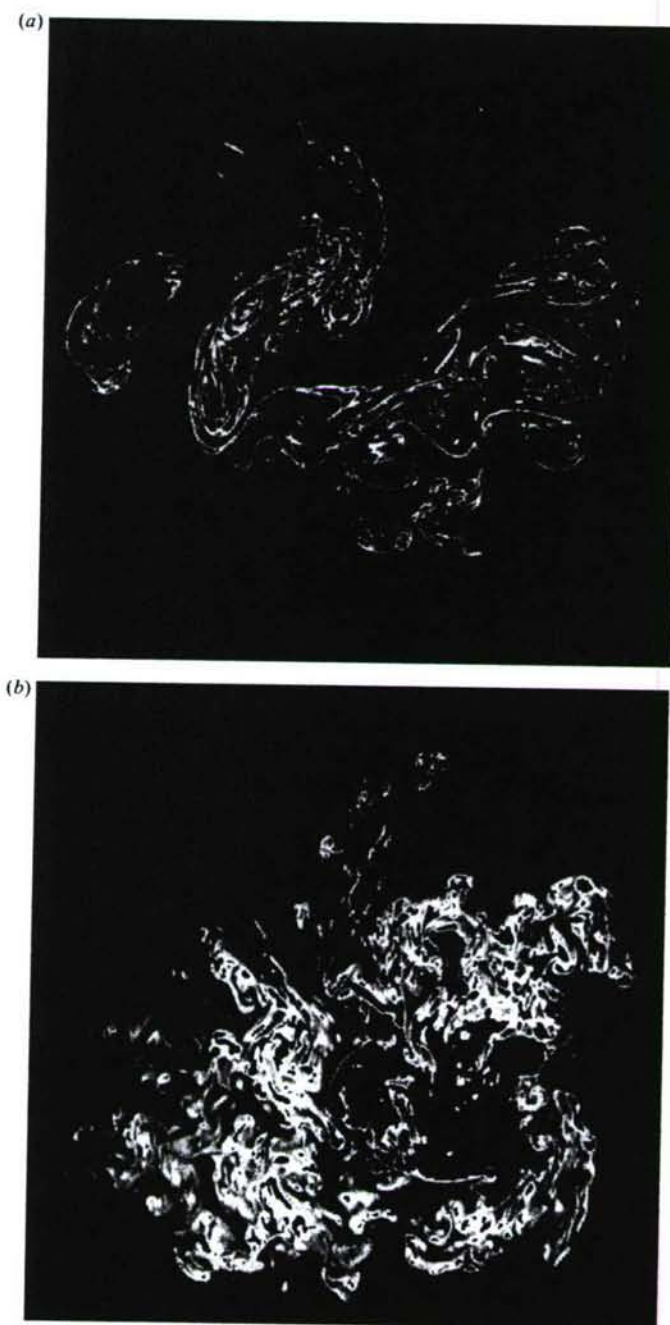


FIGURE 15. Concentrations in the range  $0.025 \leq C \leq 0.045$  for (a)  $Re_j = 1.0 \times 10^3$  and (b)  $Re_j = 10 \times 10^3$  at  $V_r = 10$ . Compare with figures 6 and 7.

distribution. The most-probable concentration shifts to lower values with increasing Reynolds number, but the incremental change diminishes at the higher Reynolds numbers. Another concentration of interest is the mean mixed-fluid concentration,  $C_{mixed}$ , defined as the mean of all concentrations greater than a chosen value representing a cutoff between mixed and unmixed fluid. In this case, the cutoff

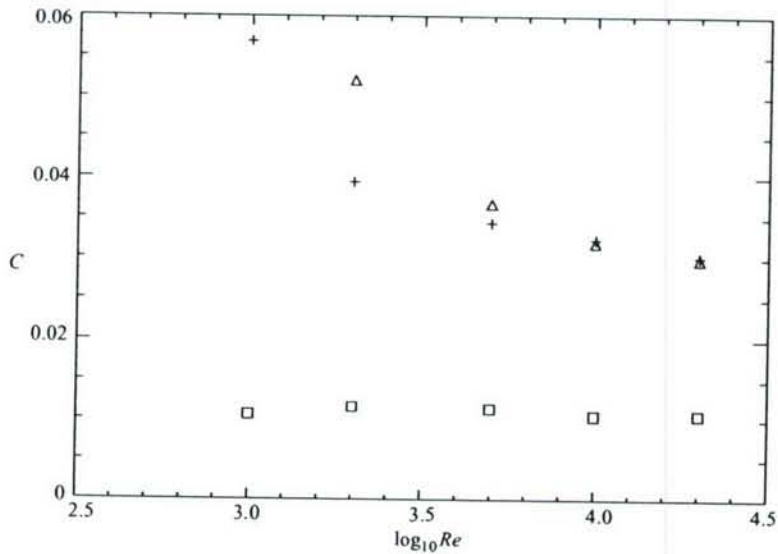


FIGURE 16. Peak, mixed-fluid, and mean concentrations versus Reynolds number for  $V_r = 10$ .  $\square$ , mean concentration,  $\bar{C}$ ;  $+$ , mean mixed-fluid concentration,  $C_{mixed}$ , for  $C > 0.01$ ;  $\Delta$ , peak concentration,  $C_{peak}$ , defined as point of zero slope (for  $Re_j = 5.0, 10$  and  $20 \times 10^3$ ), or as point of maximum negative curvature (for  $Re_j = 2.0 \times 10^3$ ).

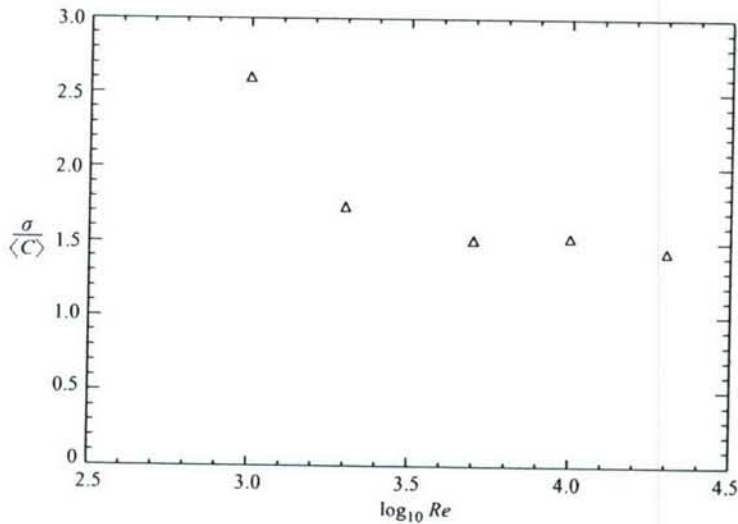


FIGURE 17. Normalized r.m.s. fluctuations of the scalar field versus Reynolds number for  $V_r = 10$ .

concentration,  $C = 0.01$ , was chosen to coincide with a local minimum that occurs in the PDF. The mean mixed-fluid concentration also asymptotes at the highest Reynolds numbers. Finally, the width of the PDF also declines and asymptotes with increasing Reynolds number. As seen in figure 17, the normalized standard deviation decreases rapidly before levelling off around  $Re_j = 10 \times 10^4$ . The asymptotic levelling off of measures such as standard deviation and most-probable concentration for the transverse jet is consistent with a mixing transition that has been documented in other

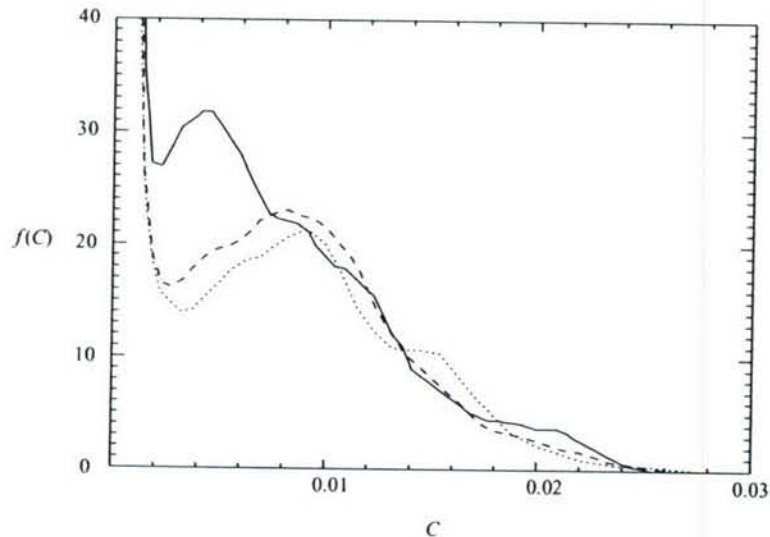


FIGURE 18. Jet-fluid concentration PDFs for jets discharging in a quiescent reservoir. Lines of increasing solidity denoting increasing  $Re_j = 4.5, 9$  and  $18 \times 10^3$  (Catrakis & Dimotakis 1996, adapted from their figure 8).

flows to occur at comparable outer-scale Reynolds numbers of order  $10^4$  (Dimotakis 2000).

It can be shown from control-volume analysis that the mean concentration in a transverse cross-section of the jet should remain constant for any Reynolds number, provided the velocity ratio is unchanged. The mean concentration,  $\bar{C}$ , depends linearly on velocity ratio,

$$\bar{C} = \int_{-\infty}^{\infty} C f(C) dC \simeq C_0 V_r \frac{A_j}{A}. \quad (17)$$

In the above expression,  $A_j$  is the area of the nozzle exit, and  $A$  is the area of a transverse plane whose boundary completely encloses the cross-section of the jet. When jet-plenum concentration,  $C_0$ , and velocity ratio,  $V_r$ , are fixed, as they are in the case of the present experiments, the mean concentration should be independent of the Reynolds number. This provides a test for the quantitative accuracy of the concentration measurements, and further verifies that the plenum concentrations and jet velocity ratios were well controlled for the test series. As shown in figure 16, the invariance of the mean concentration,  $\bar{C}$ , was verified for the present set of experiments.

### 3.2. Entrainment and stirring compared with jets in quiescent reservoirs

Differences in turbulent mixing can be seen between transverse jets and jets discharging into a quiescent reservoir. For comparison to the transverse-jet data (figure 14), figure 18 shows measured distributions of jet-fluid concentration for varying Reynolds number in the far-field ( $x/d_j = 275$ ) of liquid-phase, quiescent-reservoir jets. These jet measurements were made by Catrakis & Dimotakis (1996) for a similar Reynolds-number range to the current transverse-jet experiments. At the lowest Reynolds number,  $Re_j = 4.5 \times 10^3$ , the jet-fluid-concentration PDF of the quiescent-reservoir-jet displays a well-defined peak much like the PDF of the transverse jet at similar Reynolds numbers. However, as the Reynolds number

increases, the height of the peak measured from the local minimum decreases, i.e. the relative height of the peak decreases. For jets without crossflow, the trend with increasing Reynolds number seems to be towards a smooth monotonic-decreasing distribution. We anticipate that the peak will disappear altogether with further increases in Reynolds number for the quiescent-reservoir jet. In contrast, for the transverse jet, the relative height of the distribution peak increases with Reynolds number. The trend in the transverse jet appears to be toward a strongly peaked distribution, as the scalar field is increasingly homogenized. The current data suggest that, for Reynolds numbers up to  $Re_j = 20 \times 10^3$ , the trends in turbulent mixing with Reynolds number may be different between transverse ( $V_r = 10$ ) and quiescent-reservoir jets. Additional comparisons at different downstream locations and velocity ratios would be required to confirm this hypothesis.

It is necessary to consider possible differences in entrainment between ordinary and transverse jets, because entrainment is a key step in what has been described as the three-stage process of turbulent mixing (e.g. Eckart 1948; Dimotakis 1986): entrainment; stirring; and molecular diffusion. (Entrainment is the engulfment of irrotational flow into the turbulent-flow region, stirring is the kinematic motion responsible for creating interfacial area between mixing species, and molecular mixing is due to diffusion.) The rate of entrainment of unmixed fluid, relative to the rate at which stirring and molecular diffusion act to homogenize the previously entrained fluid, helps to determine the distribution of the scalar field. This idea is illustrated in figure 19. The jet is modelled in a Lagrangian sense as a balloon being filled from a tap in similar fashion to the model developed for shear layers by Dimotakis & Hall (1987). The balloon is initially filled with a fixed volume  $V_0$  of  $C = 1$  fluid while the tap pours in  $C = 0$  fluid at varying volume flow rate  $\dot{V} = e(t)$ . For mixing jets, the original fluid in the balloon represents a parcel of plenum fluid that is injected into the crossflow, while the fluid that is poured in represents the fluid that is entrained into the jet in a convective frame moving with the jet fluid. The contents of the balloon are a Lagrangian parcel combining jet fluid and entrained crossflow fluid which cannot detract, since entrainment and mixing can only proceed one way. Thus, the size of balloon (and the jet it represents) grows monotonically with time and downstream distance in an average sense. In the complete absence of stirring and molecular diffusion, the PDF of the contents of the balloon would be the sum of two delta functions, i.e.  $f(C) = (1 - C_{mean})\delta(C) + C_{mean}\delta(C - 1)$  (Dimotakis & Miller 1990). However, if stirring and diffusion act to mix the fluid, then intermediate, mixed concentrations would be generated within the balloon. In that case, the PDF would tend toward a delta function,  $f(C) = \delta(C - C_{mean})$ , centred at the mean concentration, if stirring and molecular mixing rates are fast compared to the entrainment rate.

The mean concentration,  $C_{mean}$ , is determined by the ratio of jet fluid to entrained fluid, regardless of mixing rate, and is given by

$$C_{mean} = \frac{V_0}{V_0 + \int_0^\infty e(t) dt} = \frac{1}{1 + E/V_0}, \quad (18)$$

where  $V_0$  is the original volume of  $C = 1$  fluid,  $e(t)$  is the entrainment rate, and  $E/V_0$  is the volume ratio of entrained to original fluid for that Lagrangian parcel of fluid.

The total mass flux of fluid through a plane perpendicular to the jet axis is

$$\dot{m} = \int_{A_{jet}} \rho \mathbf{u} \cdot d\mathbf{A}, \quad (19)$$

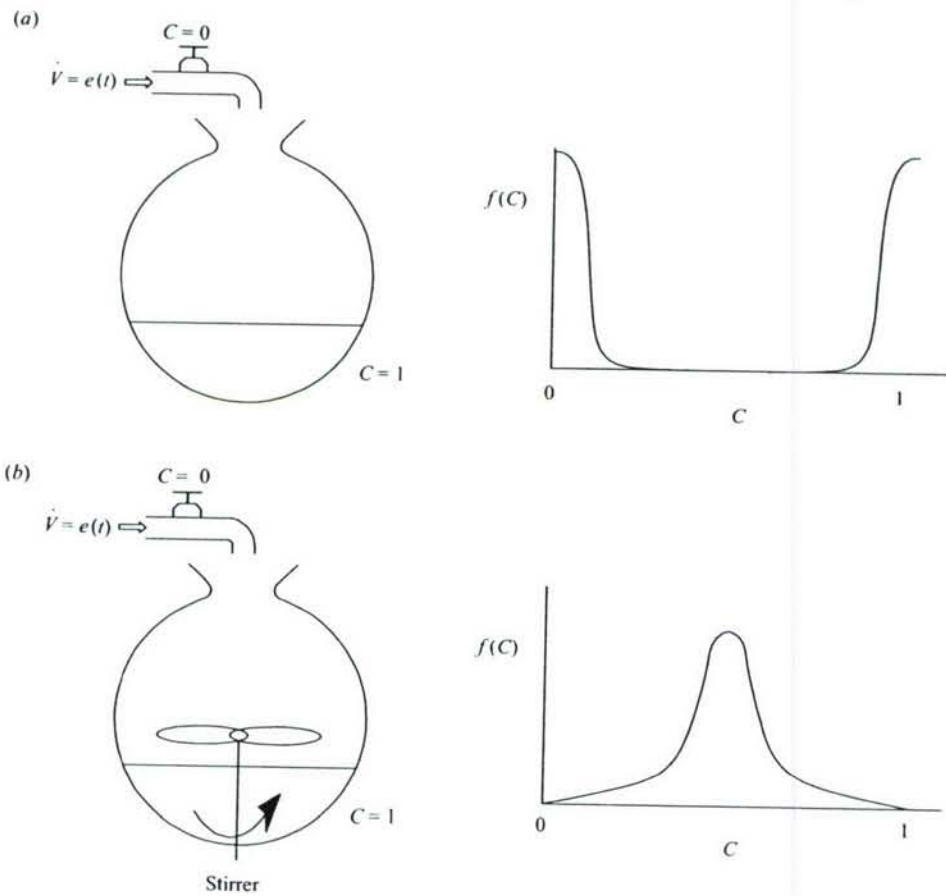


FIGURE 19. The jet-mixing process represented as a balloon being filled from a tap. The balloon represents a Lagrangian control-volume for a parcel of fluid initially comprised of pure jet fluid that entrains reservoir/crossflow fluid and mixes with it (a) Limited mixing (b) Mixing with enhanced stirring.

while the mass flux of dye is

$$\dot{m}_{dye} = \int_{A_{jet}} C \rho \mathbf{u} \cdot d\mathbf{A}, \quad (20)$$

where  $d\mathbf{A}$  has unit normal parallel to the jet axis. The mass flux of dye is conserved, and must be equal to the initial flux at the nozzle, i.e.  $\dot{m}_{dye} = \dot{m}_0$ , since  $C = 1$  at the nozzle. In the far field of the jet, where  $\mathbf{u} \simeq U_\infty \hat{\mathbf{x}}$ , the ratio of mass fluxes is,

$$\frac{\dot{m}_{dye}}{\dot{m}} \simeq \frac{\int_{A_{jet}} C dA}{\int_{A_{jet}} dA} = \frac{\int_{A_{jet}} C dA}{A_{jet}}. \quad (21)$$

This ratio of dye flux to total flux is simply the mean flux,  $C_{mean}$ , which can be measured from the image data. Thus, the entrainment of transverse jets can be deduced from measurements of concentration and compared to expressions proposed by previous investigators.

It should be noted that the mean concentration,  $C_{mean}$ , discussed above is the average concentration of a Lagrangian parcel of jet fluid mixed with entrained fluid. It differs subtly from the  $\bar{C}$  that was previously defined in (17) as the measured mean concentration over a field of view containing a cross-section of the jet as well as surrounding tunnel fluid. Because the field-of-view of the measurement contains additional (un-entrained) surrounding fluid in addition to the mixed jet fluid,  $C_{mean} \geq \bar{C}$ . (The equality would hold only if concentration is measured for an area containing only the jet fluid and entrained tunnel fluid, i.e. excluding the surrounding tunnel fluid.) On the other hand, the mean concentration,  $C_{mean}$ , is less than the mixed-fluid concentration,  $C_{mixed}$ , which was previously defined as the average over the measurement plane of all concentrations greater than  $C = 0.01$  (figure 16). The mean concentration is thus constrained to be,

$$\bar{C} \leq C_{mean} < C_{mixed}, \quad (22)$$

Based on measurements at  $x/d_j = 50$  for the transverse jet,  $C_{mixed} = 0.03$  and  $\bar{C} = 0.01$  (see figure 16). Using (18) and the measured  $C_{mixed}$  and  $\bar{C}$  for the  $V_r = 10$  jet, the ratio of entrained fluid to jet fluid at  $x/d_j = 50$  is found to be within the limits:

$$32 < \frac{E}{V_0} \leq 99. \quad (23)$$

For comparison, Hasselbrink & Mungal (2001) and Hanm, Orozco & Mungal (2000) estimated the entrainment rate of transverse jets by considering the momentum exchange between crossflow and jet fluid necessary to turn the jet to an experimentally determined trajectory. They proposed an expression for total mass flux through a section perpendicular to the jet axis in the transverse jet as:

$$\frac{\dot{m}}{\dot{m}_0} = 1 + \frac{V_r}{AB} \left( \frac{x}{V_r d_j} \right)^{1-B}, \quad (24)$$

where  $A \simeq 2.1$  and  $B \simeq 0.29$  are experimentally determined constants. This expression is valid in the far field, for  $s/V_r^2 d_j \geq 0.3$  by the definition of Smith & Mungal (1998), where  $s$  is the arclength from the jet exit. Substituting (24) into (21) then yields:

$$C_{mean} \simeq \frac{1}{1 + \frac{V_r}{AB} \left( \frac{x}{V_r d_j} \right)^{1-B}}. \quad (25)$$

This predicts a mean concentration  $C_{mean}(x/d_j = 50) \simeq 0.02$  and entrained-to-crossflow fluid ratio  $E/V_0 \simeq 51$  for the  $V_r = 10$  jet, which is consistent with the range of values inferred from the concentration measurements (equations (22) and (23)).

For a turbulent, axisymmetric jet in a quiescent reservoir, the total mass flow rate was found by Ricou & Spalding (1960) to be:

$$\frac{\dot{m}}{\dot{m}_0} = 1 + 0.32 \frac{s}{d_j}. \quad (26)$$

This is plotted in figure 20 along with the normalized mass flux versus arclength,  $s$ , from the jet exit for the  $V_r = 10$  transverse jet. In the figure, the lines transition from dashed to solid lines at the beginning of the far field for transverse and regular jets, as defined by Smith & Mungal (1998) and Dahm & Dimotakis (1990), respectively. At the downstream location of the present experiments,  $x/d_j = 50$  (equivalent to  $s/d_j = 67$ ), the  $V_r = 10$  transverse jet has 2.3 times the total mass-flow rate of an

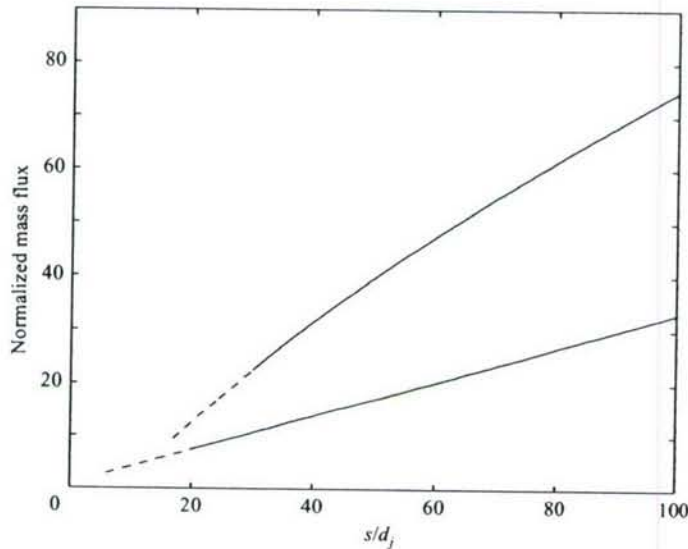


FIGURE 20. Normalized total mass flux,  $\dot{m}/\dot{m}_0$ , versus arclength from jet exit. Upper line: transverse jet for  $V_r = 10$ . Lower line: jet in quiescent reservoir.

ordinary jet of the same initial mass-flow rate. If extrapolated further, the two lines will eventually cross in the extreme far field, as  $\dot{m}/\dot{m}_0 \propto (s/d_j)^{1-B}$ , where  $B \simeq 0.29$  for the transverse jet, while  $\dot{m}/\dot{m}_0 \propto s/d_j$  for the ordinary jet. However, for the  $V_r = 10$  transverse jet, the estimated cross-over in mass flux occurs at  $s/d_j \simeq 2800$ . Thus, for most practical purposes, the high-velocity-ratio transverse jet has entrained more fluid than a jet of the same initial mass flux discharging in a quiescent reservoir.

As discussed in the previous section, the growing peaks in the PDF of jet-fluid concentration indicate that the scalar field of the transverse jet is increasingly homogenized with increasing Reynolds numbers. This implies that stirring, relative to entrainment rate, is enhanced at higher Reynolds numbers. Yet, in comparison to the jet discharging in a quiescent reservoir, the  $V_r = 10$  transverse jet has a greater entrainment rate and total mass flux at  $x/d_j = 50$ . The spatial homogenization of the scalar field in the far field occurs in spite of the transverse jet's relatively high entrainment rate. The high-velocity ratio, turbulent transverse jet is an efficient mixer in the sense that it rapidly entrains unmixed free-stream fluid, and homogenizes the jet-fluid-concentration field.

#### 4. Scalar increment statistics

While the statistics of concentration fields in transverse jets can be described with scalar PDFs (§3), the structure of the scalar field can be assessed in terms of the distribution of spatial differences,  $f(\Delta, C)$ . As introduced in (1), the probability distribution of scalar differences, also known as scalar increments, gives the probability of finding a concentration  $C + \Delta C$  at a vector distance  $\mathbf{r}$  away from a point of concentration  $C$ . The statistics of scalar differences are connected to the structure functions for a turbulent scalar field and have implications for the Kolmogorov-Oboukhov-Corrsin (KOC) theory of turbulent mixing of passive scalars (Oboukhov 1949; Corrsin 1951; an overview of passive-scalar turbulence is given by Shraiman &

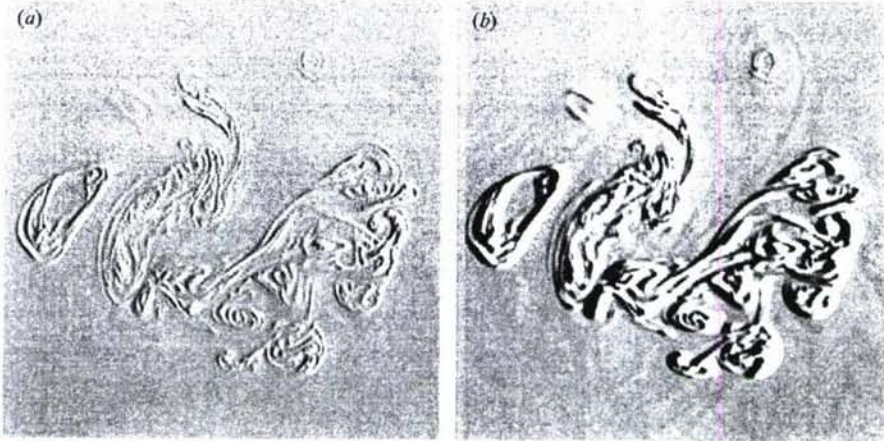


FIGURE 21. Scalar-difference field for  $Re_j = 1.0 \times 10^3$ ,  $V_r = 10$  jet. (a) Horizontal shift of  $0.3 \times 10^{-2} \delta_h$ . (b) Horizontal shift of  $2.1 \times 10^{-2} \delta_h$ .  $\Delta, C = 0$  is shown as grey, and negative and positive values are shown as black and white, respectively.

Siggia 2000). In this paper, the distribution of scalar differences is investigated primarily for the evidence they provide for intermittency and anisotropy in the scalar field.

Scalar increments are typically studied with point measurements of the scalar field, for example, with temperature probes (Antonia *et al.* 1984; Ould-Rouis *et al.* 1995; Mydlarski & Warhaft 1998). However, two-dimensional image data of the type collected in the present experiments allow novel whole-field measurement of scalar increments of the concentration field (figure 21). Normalized and calibrated images measuring scalar concentration fields are spatially displaced by a vector distance  $r$  and subtracted from themselves. For instance, figure 21 shows two-dimensional scalar-difference fields for small and large horizontal displacements,  $r/\delta_h = 0.3 \times 10^{-2} \hat{z}$  and  $r/\delta_h = 2.1 \times 10^{-2} \hat{z}$ , respectively. The probability distribution of scalar increments is then computed as the normalized histogram of the scalar-difference field. To prevent the PDF from being dominated by differences between the completely unmixed crossflow fluid and the jet, the distribution of scalar differences is conditioned on both measurement ‘points’ being within the instantaneous body of the jet. This is accomplished by making the distribution conditional on the intersection between shifted and unshifted jet body, defined from the image data by a minimum scalar threshold. The procedure is conceptually equivalent to requiring that the two measurement ‘probes’ lie within the jet body. (The condition is necessary because of the inhomogeneity and spatial confinement of the image data. Without it, the distribution of scalar difference would be dominated at large separation distances by differences between points within the jet and points outside of the jet. In that case, the distribution of scalar increments for a spatially confined scalar field would simply tend toward the concentration PDF,  $f(C)$  and its reflection,  $f(-C)$  for large  $r$ .)

#### 4.1. Intermittency and the distribution of scalar increments

Distributions of conditional scalar increments at two Reynolds numbers,  $Re_j = 2.0 \times 10^3$  and  $Re_j = 20 \times 10^3$ , are shown in figure 22. The distributions were computed

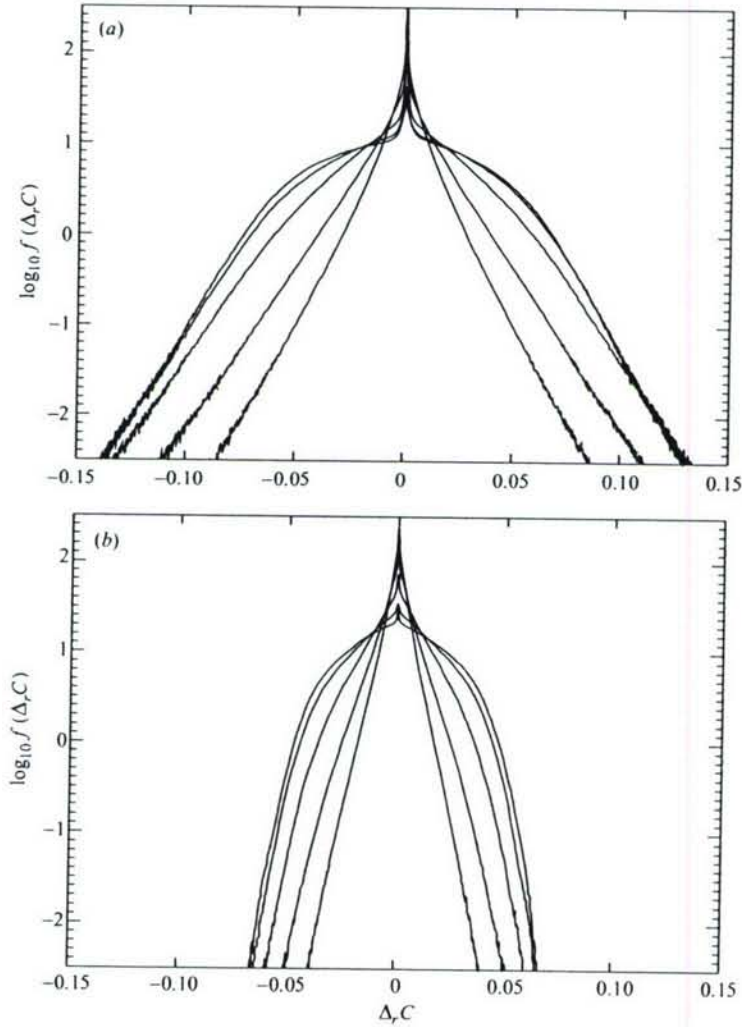


FIGURE 22. Scalar-increment PDFs at  $V_r = 10$  for two different Reynolds numbers and varying horizontal separation distances,  $r$ . Innermost, triangular PDFs are for smallest separation distances and outermost, broad-shouldered PDFs are for largest separations. (a)  $Re_j = 2.0 \times 10^3$  and separation distances  $r/\delta_h = 0.2, 0.4, 1.7, 7.0$ , and  $14 \times 10^{-2} \hat{z}$ . (b)  $Re_j = 20 \times 10^3$  and separation distances  $r/\delta_h = 0.3, 0.5, 2.0, 8.1$  and  $16 \times 10^{-2} \hat{z}$ .

for varying horizontal separation distances in the range  $0.2 \times 10^{-2} \leq |r|/\delta_h \leq 14 \times 10^{-2}$ , where  $\delta_h$  was previously defined (§ 3) to be the horizontal size of the jet based on mean concentration. As seen from the figure, the PDF becomes narrower with increasing Reynolds number at all separation distances, i.e. the probability for large differences in the scalar field decreases with increasing Reynolds number. Large differences in mixed-fluid concentration between two spatially separated points become rarer as the jet fluid is increasingly homogenized at high Reynolds numbers. This increased spatial homogenization of the scalar field was also seen in the growing preferred-concentration peaks in the PDF of jet-fluid concentration (figure 14), and the decreasing variance of the scalar field (figure 17).

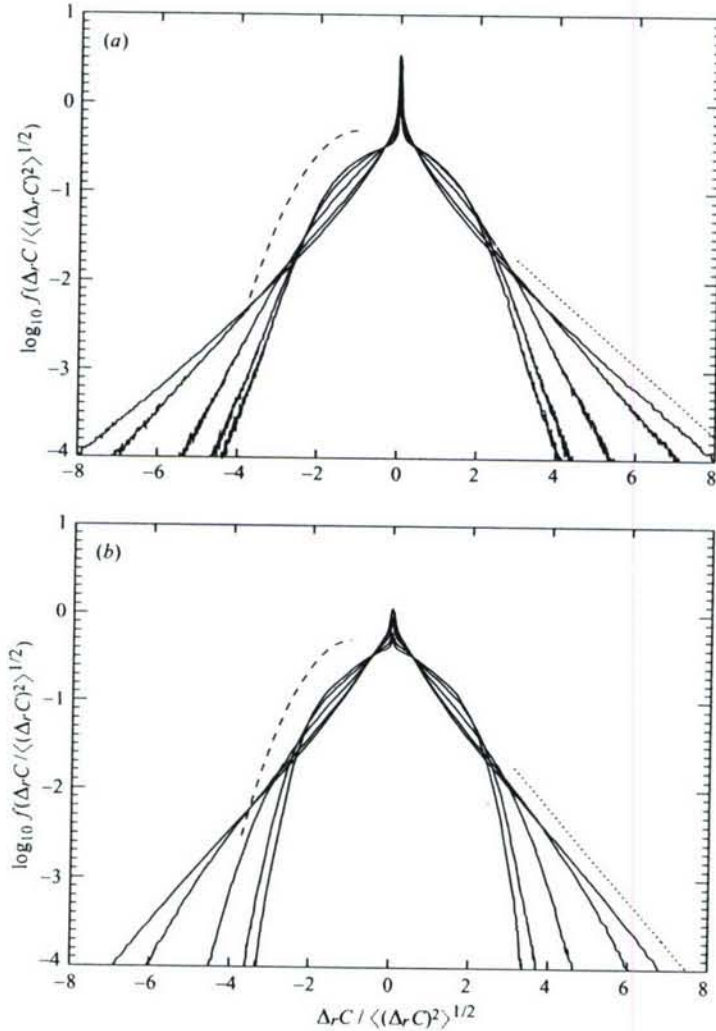


FIGURE 23. Standard-deviation-normalized PDFs of scalar increments at  $V_r = 10$  for two Reynolds numbers and varying horizontal separation distances,  $r$ . Gaussian (dashed) and exponential (dotted) distributions shown for comparison. Exponential-tailed triangular PDFs are for smallest separation distances and Gaussian-shouldered innermost PDFs are for largest separations. (a)  $Re_j = 2.0 \times 10^3$  and separation distances  $r/\delta_h = 0.2, 0.4, 1.7, 7.0$  and  $14 \times 10^{-2} \hat{z}$ . (b)  $Re_j = 20 \times 10^3$  and separation distances  $r/\delta_h = 0.3, 0.5, 2.0, 8.1$  and  $16 \times 10^{-2} \hat{z}$ .

As the separation distance changes for a given Reynolds number, the shape of the scalar increment PDF evolves from a broad-shouldered distribution to a long-tailed distribution. Figure 23 shows scalar increment PDFs normalized by their own standard deviation. The distributions are plotted for varying horizontal separation distances,  $r$ . A growing 'spike' is seen at  $\Delta_r C \simeq 0$  as the separation distance decreases. At the largest distances, the PDF has narrow tails and shoulders which are Gaussian in shape. For smaller separation distances, the PDF is long-tailed and has an exponential or stretched-exponential form. For comparison, exponential and Gaussian distributions are plotted in the figure. The observed exponential or

stretched-exponential behaviour of the distributions is consistent with previous results for scalar temperature increments in Rayleigh–Bénard convection (Ching 1991), grid turbulence (Mydlarski & Warhaft 1998), boundary layers (Ould-Rouis *et al.* 1995), and plane jets (Antonia *et al.* 1984). Using novel whole-field measurements of scalar increments, the present experiments extend the list of turbulent flows for which long-tailed distributions of scalar increments are found to liquid-phase transverse jets. (In making comparisons, it should be noted that the Schmidt number of the present experiment is two orders of magnitude higher than the Prandtl number of the previous temperature measurements.)

The long tails and peak at the origin of the scalar-increment distribution are believed to arise from plateau-cliff structures in the scalar field. Such structures, consisting of integral-scale-sized ‘plateaux’ of nearly homogeneously mixed fluid separated by intense gradient sheets, or ‘cliffs’, have been documented in a variety of turbulent mixing flows (discussed below), and are also seen in the scalar field of the transverse jet. Figure 24 shows the jet-fluid concentration in a transect of the transverse jet at  $Re_j = 10 \times 10^3$ . In this transect, the concentration is arranged in three bands (plateaux), separated by large jumps (cliffs) in concentration. Relatively small fluctuations in concentration occur within the bands. Such an intermittent scalar field can produce a spiked long-tailed distribution of scalar increment in the following manner. Plateaux of nearly constant scalar concentration in the transverse jet contribute to the large small-concentration-difference peak at the origin of the distribution of  $\Delta C$ , while cliffs separating the concentration plateaux produce large fluctuations which contribute to the long tails of the scalar-increment distribution. The spiked long-tailed distribution of scalar increments is thus evidence that the scalar field is intermittent and contains plateaux and cliffs which persist for Reynolds number up to  $Re_j \leq 20 \times 10^3$ .

Large-scale plateaux of well-mixed fluid, separated by cliffs of sharp concentration gradients, appear to be characteristic of a wide variety of turbulent mixing flows. Such scalar plateaux and cliffs in physical space (or, equivalently, ramp-cliffs for time-series measurements) have previously been observed in experiments on mixing in turbulent shear flows such as wakes (Gibson, Friehe & McConnell 1977), boundary layers (Mestayer *et al.* 1976; Gibson *et al.* 1977), and jets (Uberoi & Singh 1975; Sreenivasan, Antonia & Britz 1979; Antonia *et al.* 1986; Dahm & Dimotakis 1990; Yoda *et al.* 1992). Such ramp-cliff structures have also been found in grid turbulence with a superimposed mean-temperature profile (Budweig, Tavoularis & Corrsin 1985; Thoroddsen & Van Atta 1992; Tong & Warhaft 1994), despite the absence of mean shear, entrainment and large-scale anisotropy of the velocity field. Numerical simulations in two- (Holzer & Siggia 1994) and three- (Pumir 1994) dimensions show the same basic structure of the scalar field in physical space: relatively well-mixed regions separated by cliffs where the scalar gradient is very large. As noted by Warhaft (2000), it is remarkable that ramp-cliff structures are observed in the two-dimensional simulations of Holzer & Siggia, which assumed a Gaussian random velocity field rather than a velocity field that is a solution of the Navier–Stokes equations. Experiments (Antonia *et al.* 1986) and simulations (Pumir 1994) indicate that cliffs tend to develop where the flow is hyperbolic (at a diverging separatrix), while elliptic regions are better mixed. Based on experiments in heated grid turbulence, Tong & Warhaft (1994) concluded that the cliffs persist and become even sharper and more intense with increasing Reynolds number up to at least  $Re_j = 130$ . In doing so, the cliff-plateau structures contribute deeper and deeper into the tails of the scalar-derivative PDF with increasing Reynolds number. (The scalar-increment

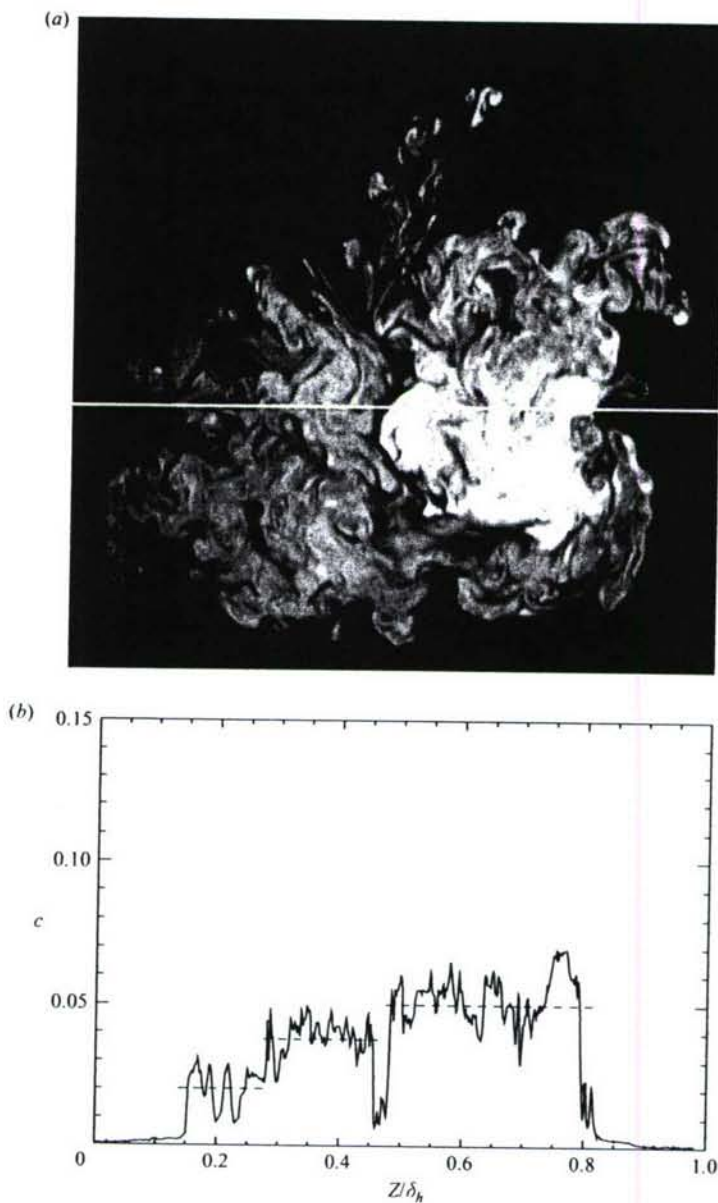


FIGURE 24. Concentration in a transect of the jet at  $Re_j = 10 \times 10^3$  and  $V_r = 10$ .  
 (a) Location of transect. (b) Concentration versus position.

PDF would approach the scalar-derivative PDF in the limit of  $r \rightarrow 0$ .) The basic plateau-cliff or ramp-cliff structure of the scalar field has also been associated with small-scale anisotropy, an issue that is discussed in the following sections.

#### 4.2. Anisotropy and scalar increments in differing directions

The measured distributions of scalar increments suggest that the large scales (plateaux) of the scalar field are separated by small scales (cliffs). In a sense, this is a coupling of

the large and small scales, which introduces the possibility that the scalar field may be anisotropic even at small length scales (e.g. reviews by Sreenivasan & Antonia 1997; Shraiman & Siggia 2000; Warhaft 2000). There has long been evidence of a lack of scalar isotropy in turbulent mixing flows at both inertial and dissipation scales. A persistent (even at high Reynolds numbers) non-zero skewness of the scalar derivative has been reported in shear flows (Mestayer *et al.* 1976; Gibson *et al.* 1977; Sreenivasan *et al.* 1979) as well as isotropic grid turbulence with a linear temperature profile (Tavoularis & Corrsin 1981; Budwig *et al.* 1985; Tong & Warhaft 1994). The skewness of the scalar derivative is a consequence of the ramp-cliff structures in the scalar field, which can be preferentially aligned in a turbulent flow. In shear flows, the converging-diverging separatrices that form the cliffs are inclined along the principal-strain direction on average (Antonia *et al.* 1986). In flows without mean shear, the separatrices are randomly aligned; however, those that happen to be aligned with the mean scalar gradient will tend to create ramp-cliff structures (Holzer & Siggia 1994; Warhaft 2000). In either case, the cliffs in the scalar field are preferentially oriented and sharp, thus resulting in scalar anisotropy at both large and small scales. In addition to the reported non-zero skewness of the scalar field, experiments have investigated the morphology of turbulent scalar fields with three-point correlations,  $\langle C(x_A)C(x_B)C(x_C) \rangle$ , where the net result depends on the distribution of cliff orientations and the geometry of the triangle formed by the three measurement points. Experiments on heated grid turbulence found scalar anisotropy using such measures at both the dissipation and inertial scales of the scalar field (Mydlarski & Warhaft 1998). In similar spirit to the three-point correlations of the scalar field, the probability distribution of differences between two points in the scalar field can be measured for separations in different directions to investigate possible anisotropy and structure at different length scales in the scalar field.

Figure 25 shows distributions of scalar increments for separations in two orthogonal directions at  $Re_j = 2 \times 10^3$ . At the larger separation distance ( $1.7 \times 10^{-2} \delta_h$ ), the PDFs are nearly identical for horizontal and vertical separations of the same distance. However, at a smaller separation distance ( $0.2 \times 10^{-2} \delta_h$ ), the distributions are markedly different. The PDF is narrower for vertical increments than horizontal increments, indicating the scalar field has less variation in the vertical than in the horizontal direction. Increments in different directions for  $Re_j = 20 \times 10^3$  also show anisotropy of the scalar field (figure 26). Thus, the difference in the distributions of scalar increments for separations in two directions suggests that the scalar field has small length-scale, vertically aligned (y-axis) structure for the Reynolds-number range investigated.

More insight into the spatial localization and possible sources of the small-scale anisotropy of the scalar field can be gained by directly visualizing the scalar difference field  $\Delta C$  for small separations in two directions. Figure 27 compares scalar-difference fields for small horizontal and vertical displacements of  $0.2 \times 10^{-2} \delta_h$ . The same linear intensity scaling is used to display concentration values in both images. Higher contrast in the images indicates larger differences in concentration, which contribute to the tails of  $f(\Delta, C)$ . Visual examination of the scalar-increment fields reveals that large scalar differences (high contrast, nearly white or black features in the images) are more prominent and common for horizontal separations than vertical separations of the same distance. This difference in contrast is visual evidence of anisotropy, indicating that there is a preferred vertical orientation for the small scales of the scalar field. The small-scale scalar anisotropy appears strongest near the centreline of the jet (between the counter-rotating cores), where wispy 'fingers' extend up into the

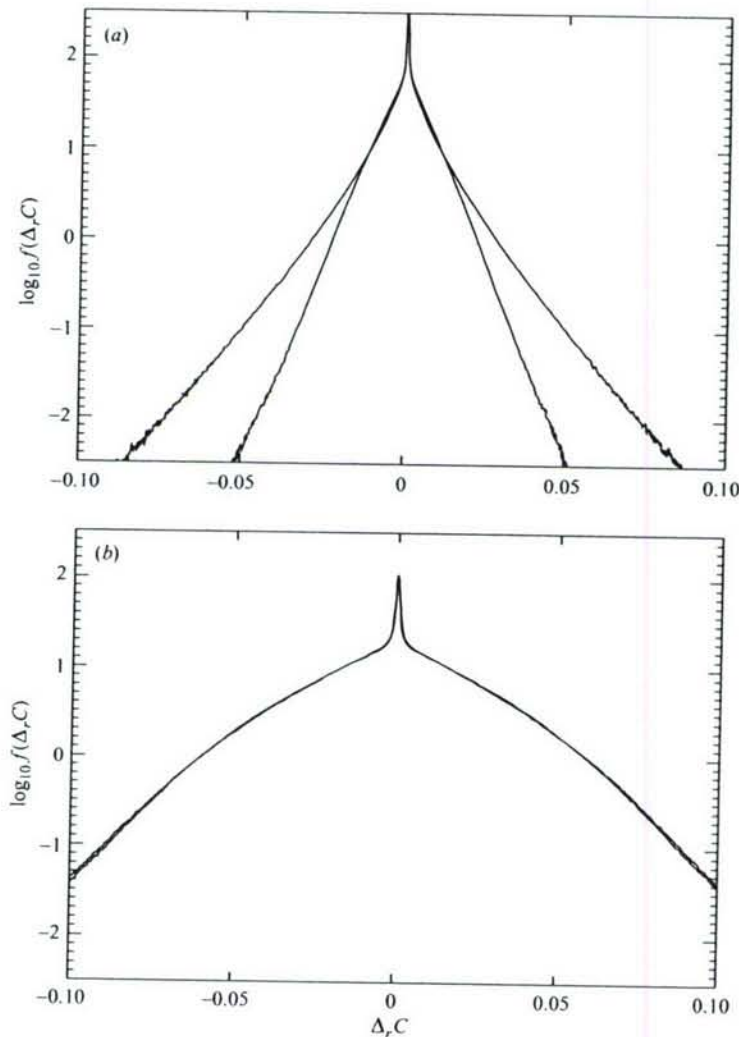


FIGURE 25. PDFs of scalar increments at  $V_r = 10$  for the same horizontal and vertical separations.  $Re_j = 2.0 \times 10^3$  and  $x/d_j = 50$ . (a) Outer PDF is for horizontal separations of  $\mathbf{r}/\delta_h = 2.2 \times 10^{-3} \hat{\mathbf{z}}$ , and inner PDF is for vertical separations of  $\mathbf{r}/\delta_h = 2.2 \times 10^{-3} \hat{\mathbf{y}}$ . (b)  $\mathbf{r}/\delta_h = 17 \times 10^{-3} \hat{\mathbf{z}}$  and  $17 \times 10^{-3} \hat{\mathbf{y}}$ .

wake. In the following section, additional evidence is presented for local anisotropy of the scalar field of the transverse jet, and a possible mechanism for the anisotropy is presented.

### 5. Anisotropy of scalar field

The anisotropy of the scalar field that was seen in the distribution of scalar increments can also be seen in measures such as one- and two-dimensional power spectra. One-dimensional power spectra can be computed from image data of the concentration field by taking transects of the scalar field. The spectra are computed for each row or column of the image and then ensemble-averaged over the entire

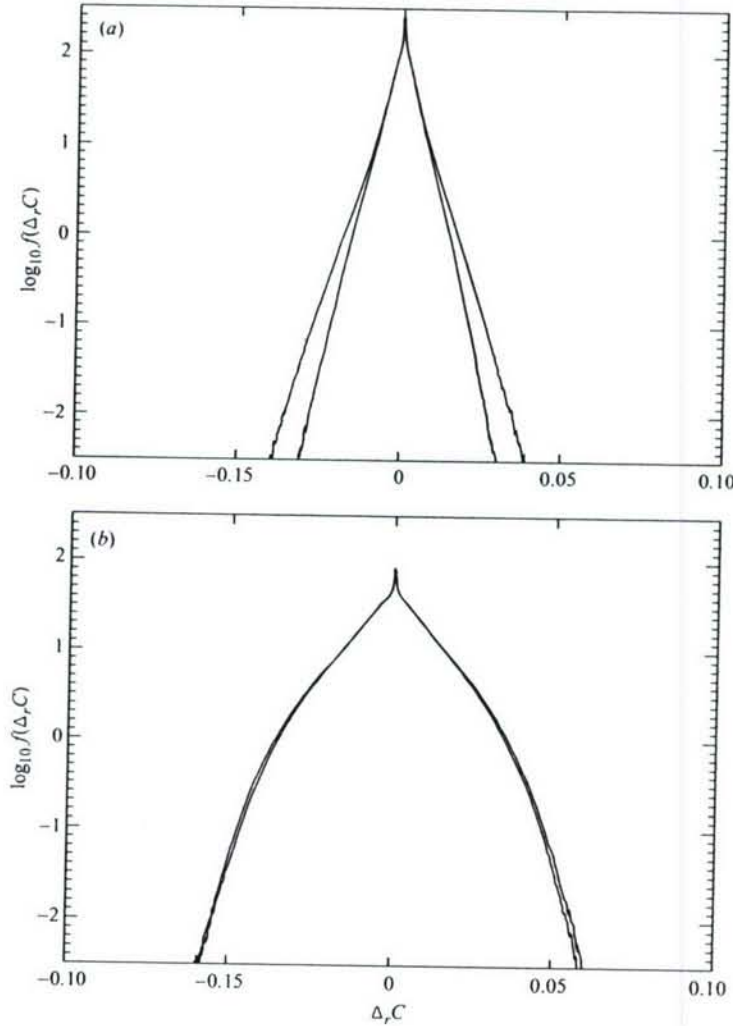


FIGURE 26. As figure 25, but for  $Re_j = 20 \times 10^3$ . (a) Outer PDF is for horizontal separations of  $r/\delta_h = 2.5 \times 10^{-3} \hat{z}$ , and inner PDF is for vertical separations of  $r/\delta_h = 2.5 \times 10^{-3} \hat{y}$  pixels. (b)  $r/\delta_h = 20 \times 10^{-3} \hat{z}$  and  $20 \times 10^{-3} \hat{y}$ .

image and averaged again over the sequence of 508 images. Hann-windowing is used to prevent aliasing. The scalar power spectra are normalized by the scalar variance and non-dimensionalized by the mean width of the jet,  $\delta_h$ , i.e.

$$\hat{S}_C \equiv \frac{S_C(k\delta_h)}{\delta_h \langle C'^2 \rangle}, \quad (27a)$$

where the variance is,

$$\langle C'^2 \rangle = \frac{2}{\delta_h} \int_0^\infty S_C(k\delta_h) d(k\delta_h). \quad (27b)$$

The wavenumber  $k$  is non-dimensionalized by the mean width of the jet as  $k\delta_h$ .

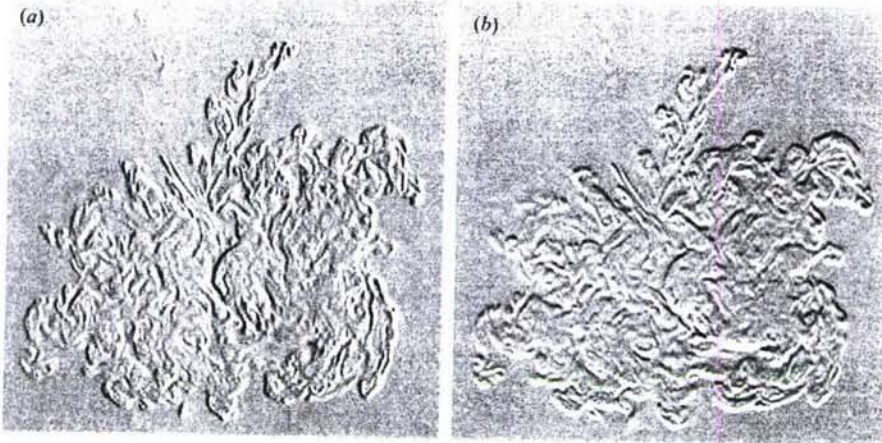


FIGURE 27. Scalar difference field,  $\Delta_r C$ , for increments in different directions at  $Re_j = 10 \times 10^3$  and  $V_r = 10$ . (a) Horizontal increment of  $r/\delta_h = 0.2 \times 10^{-2} \hat{z}$ . (b) Vertical shift of the same magnitude.

As seen in figure 28, the one-dimensional spectra for vertical and horizontal transects at  $Re_j = 1.0 \times 10^3$  are essentially identical at low wavenumbers, but deviate beginning at moderate wavenumbers of  $k\delta_h \simeq 40$ . A deviation between the spectra for horizontal and vertical transects is also seen at moderate wavenumbers for  $Re_j = 10 \times 10^3$ . The spectra show that less energy is contained in the higher wavenumbers of the vertical transects than the horizontal ones, implying that scalar gradients are larger horizontally than vertically. This is consistent with the observation based on the distributions of scalar increments that the scalar field of the transverse jet has vertically aligned structure at small length scales (§4.2). In the case of the transverse jet, the deviation between vertical and horizontal power spectra begins in the inertial range. The Kolmogorov wavenumber,

$$k_K \delta_h \equiv \frac{\delta_h}{\lambda_K} \simeq Re_j^{3/4}, \quad (28)$$

is estimated to be  $k_K \delta_h \simeq 118$  for  $Re_j = 1.0 \times 10^3$  and  $k_K \delta_h \simeq 665$  for  $Re_j = 10 \times 10^3$ , while the deviations in the spectra begin near  $k\delta_h = 40$  and  $k\delta_h = 16$  for the two Reynolds numbers, respectively. In other experiments, for instance, heated grid-turbulence measurements, scalar anisotropy has been seen to begin in the inertial range and continuing into the dissipation range (e.g. Warhaft 2000).

Small-scale anisotropy of the scalar field can also be seen in two-dimensional power spectra of the transverse-jet concentration field. Such power spectra can be calculated from two-dimensional Hann-windowed concentration fields. Two-dimensional spectra are computed for each instantaneous image, and ensemble-averaged over 508 realizations at each Reynolds number. The two-dimensional spectra are shown as contour plots of constant scalar power in figure 29. In contrast to the circular contours of the power spectra of an axisymmetric scalar field such as the round jet discharging in a quiescent reservoir (see Catrakis & Dimotakis 1996), the transverse-jet spectra are anisotropic. In fact, the contours are increasingly elliptical with increasing wavenumbers. The horizontal elongation of the contours once again suggest that scalar gradients are steeper in the horizontal direction than in the vertical

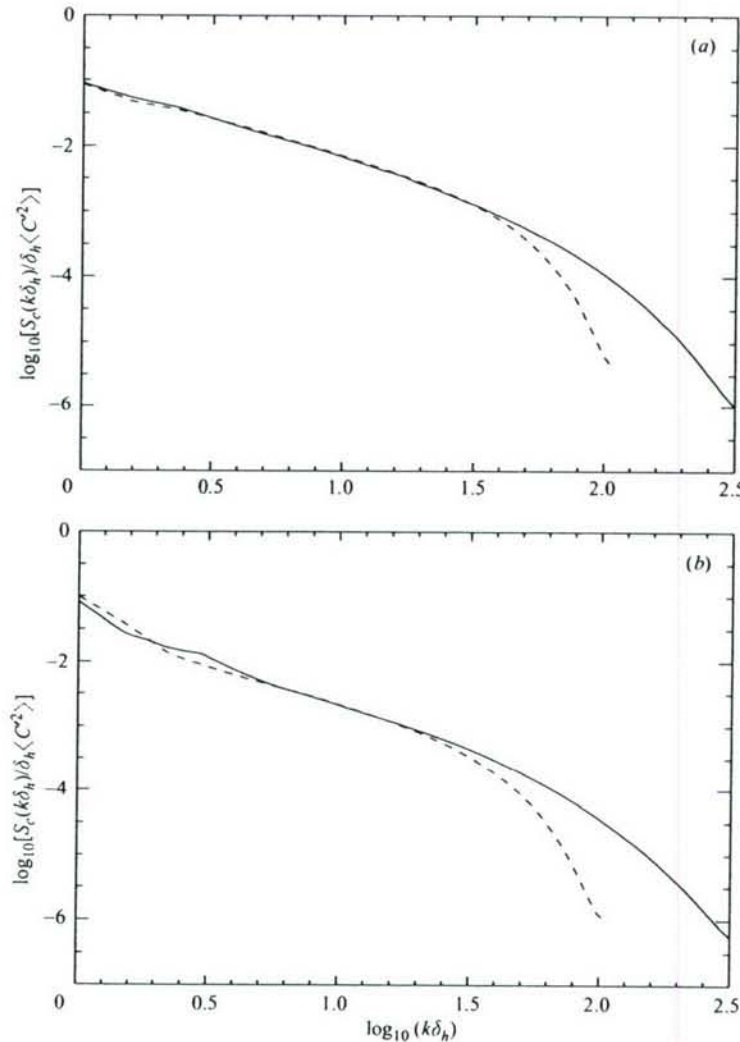


FIGURE 28. Power spectra of one-dimensional transects of the scalar field at  $x/d_j = 50$  for  $V_r = 10$  jet. Solid line is for horizontal transects, and dashed line for vertical transects. Wavenumber,  $k$ , normalized by the scalar width of the jet,  $\delta_h$ . (a)  $Re_j = 1.0 \times 10^3$ . (b)  $Re_j = 10 \times 10^3$ .

direction. For both  $Re_j = 1.0 \times 10^3$  and  $Re_j = 10 \times 10^3$  jets, the small length scales (higher wavenumbers) differ more, i.e. are more anisotropic, than the large length scales. Further evidence for small-scale anisotropy, and for its spatial localization, are discussed in the following section.

### 5.1. Scalar microscale in differing directions

The scalar microscale, computed for gradients in different directions, is another measure of the over-all anisotropy of the scalar field. It can also be computed for specific regions of the jet to determine whether or not the anisotropy is localized

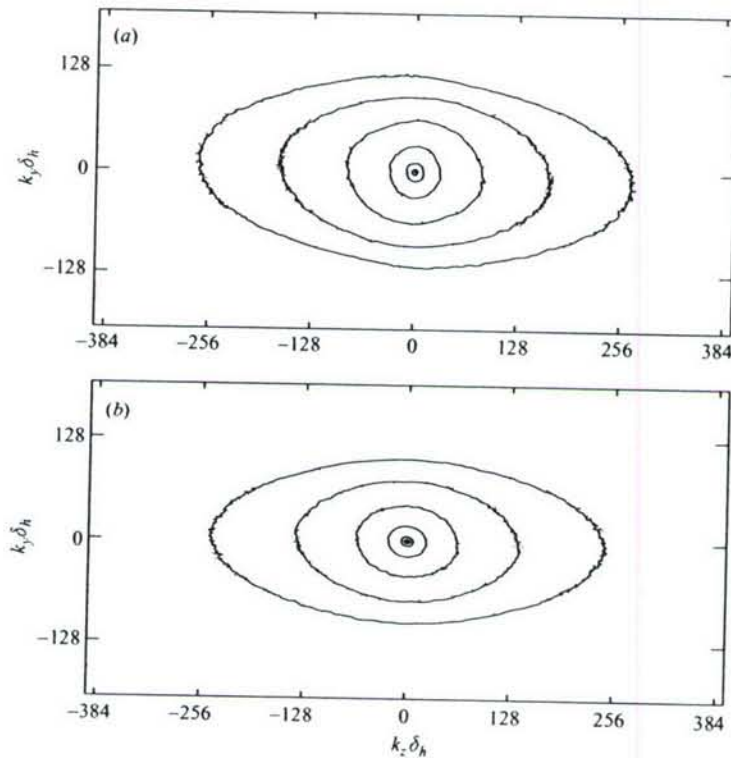


FIGURE 29. Two-dimensional power spectra of the scalar field at  $x/d_j = 50$  for  $V_r = 10$  jet. Wavenumber,  $k$ , normalized by width of the jet,  $\delta_h$ . Contour plot in  $\log_{10}$  increments of 1. (a)  $Re_j = 1.0 \times 10^3$ . (b)  $Re_j = 10 \times 10^3$ .

to specific regions, and help identify possible sources of the observed small-scale anisotropy. A microscale for fluctuations of a scalar field can be defined analogously to the Taylor microscale for velocity fields. For an isotropic scalar field, the scalar microscale,  $\lambda_C$ , is defined as (Tennekes & Lumley 1972):

$$\lambda_C^2 \equiv \frac{\langle C'^2 \rangle}{\langle (\partial C' / \partial x)^2 \rangle}. \quad (29a)$$

For anisotropic scalar fields, a generalized scalar microscale which can vary with direction may be defined as,

$$\lambda_{C,i}^2 \equiv \frac{\langle C'^2 \rangle}{\langle (\partial C' / \partial x_i)^2 \rangle}, \quad (29b)$$

where  $i$  denotes the direction in which the gradient and microscale is computed (Cook & Dimotakis 2001).

Scalar microscales in two orthogonal directions are computed for measured concentration fields in the transverse jet. The microscales are computed for horizontal and vertical gradients for each concentration field, and then ensemble averaged over 508 images. Figure 30 shows the computed scalar microscales in two directions for  $Re_j = 1, 2, 5, 10$ , and  $20 \times 10^3$ . For the Reynolds-number range of the present experiment, the vertical microscales are consistently larger than the horizontal

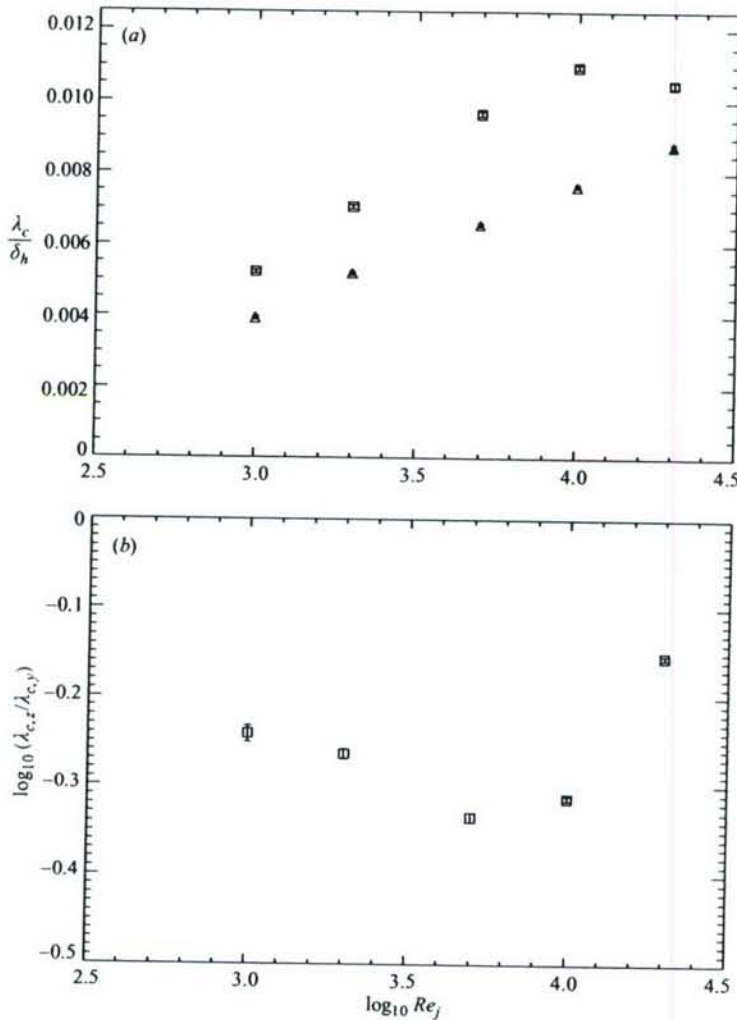


FIGURE 30. Scalar microscale as a function of jet Reynolds number for  $V_r = 10$ . (a) Scalar microscale with Reynolds number.  $\square$ , vertical and  $\triangle$ , horizontal microscale. (b) Ratio of horizontal to vertical microscales (logarithmic coordinates).

microscales. Ratios of horizontal to vertical microscales are plotted in figure 30 for varying Reynolds number. The degree of anisotropy increases with Reynolds number until  $Re_j \simeq 10 \times 10^3$ , and then appears to decrease with further increases in Reynolds number. The evidence is thus that the vertical length scales are larger than the horizontal length scales, which is entirely consistent with the indications of the power spectra and the directional PDFs of scalar increments. Similar anisotropy in the scalar microscales, persisting as the flow developed, was found in direct numerical simulations of three-dimensional Rayleigh–Taylor flow (Cook & Dimotakis 2001). In the Rayleigh–Taylor flow, the transverse scales (in the direction of gravity) were found to be larger than the horizontal scales. Moreover, the vertical length scales of the scalar field, unlike the horizontal scales, did not collapse with mixing-zone height for different initial conditions in that flow. The Rayleigh–Taylor flow is driven by a directed body force, and the dynamics responsible for generation of vertical

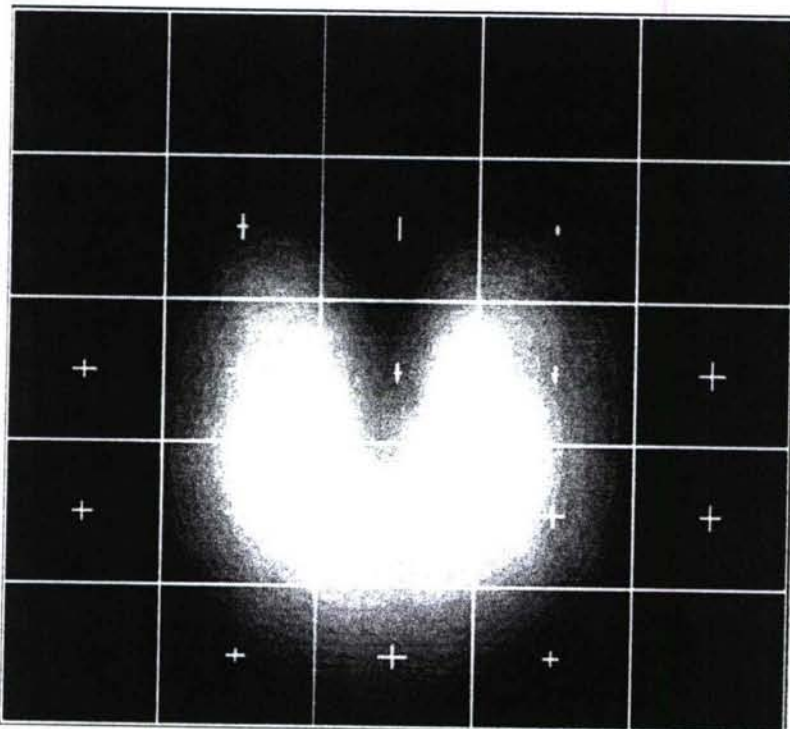


FIGURE 31. Scalar microscales in various regions of the  $V_r = 10$  jet at  $Re_j = 20 \times 10^3$ , superimposed on the mean concentration field. Microscales are computed in each section and ensemble averaged over 508 images. Crosses have dimensions  $4\lambda_{C,z} \times 4\lambda_{C,y}$ .

scales, even in the interior of the mixing zone, are coupled to the outer scales. In the Rayleigh-Taylor flow the indications are that the small length scales of the scalar field are anisotropic, at least in part, because they are coupled to anisotropic outer scales.

To localize the small-scale anisotropy and perhaps identify a coupling to outer scales which could explain it, the scalar microscale can be computed in specific regions of the jet. The instantaneous scalar field is subdivided into 16 smaller regions, so that the scalar microscales in two orthogonal directions can be computed for each section of each image. The instantaneous local microscales for each region are then ensemble averaged over 508 images. Figure 31 shows the scalar microscales computed for various subsections of the jet, superimposed on an image of the mean concentration field. A cross in each region represents the computed horizontal and vertical microscales within that region. The horizontal and vertical dimensions of each cross are four times the vertical and horizontal scalar microscales computed at each location, i.e. each cross has height and width  $4\lambda_{C,z} \times 4\lambda_{C,y}$ . As seen in figure 31, differences between the vertical and horizontal microscales are greatest in the upper-central portion of the jet, in the wake region between the vortex centres. This location is where thin, vertical filaments, or 'fingers', of jet-fluid were seen in the wake of the transverse jet, as discussed in § 2. In the following section, a possible explanation is presented for the observed small-scale anisotropy in the wake region of the transverse jet.

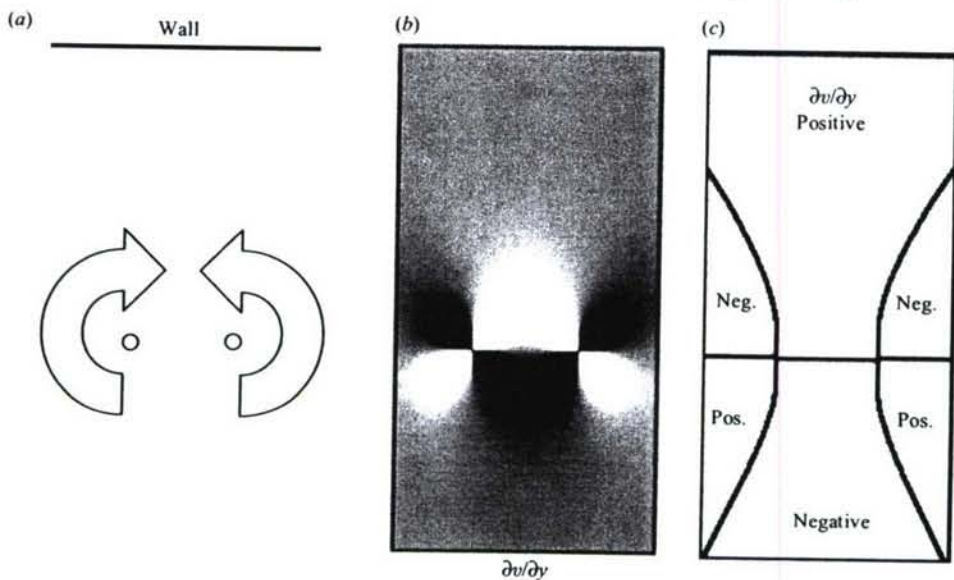


FIGURE 32. The vertical strain rate  $\partial v / \partial y$  that would be induced by inviscid flow of counter-rotating line vortices close to a wall. The no-through-flow condition at the wall is satisfied using image vortices. (a) Location and sense of rotation of the line vortices. (b) Vertical strain-rate field  $\partial v / \partial y$ . (c) Boundaries of extensional and compressive vertical strain.

### 5.2. Origins of anisotropy

The location of the greatest difference between horizontal and vertical microscales suggests that the observed scalar anisotropy may be connected to the large-scale dynamics of the transverse jet. The dynamics of the far field of the transverse jet have been modelled as a counter-rotating vortex pair (Broadwell & Breidenthal 1984). Hasselbrink & Mungal (2001) suggest that a more realistic picture of the vorticity field is an ensemble of stretched vortex rings, inclined at an angle of  $\tan^{-1}(1/V_r)$  to the crossflow direction. For high-velocity-ratio jets, the angle of inclination is slight (5.7° for  $V_r = 10$ ), and Hasselbrink & Mungal's model of the vorticity field approaches that of a pair of line vortices nearly parallel to the wall.

Thus, as a lowest-order approximation, the large-scale dynamics of the transverse jet are represented as two infinite line vortices close to a wall. Assuming inviscid flow, the vertical strain rate  $\partial v / \partial y$  in the far field of the transverse jet can be computed. Figure 32 shows the vertical strain field produced by such an arrangement of vortices. In figure 32(b), the strain rate is represented by intensity, with the brightest regions showing the highest extensional strain ( $\partial v / \partial y > 0$ ), and darkest regions showing the greatest compressive ( $\partial v / \partial y < 0$ ) vertical strain. Boundaries between regions of extension and compression are also shown. As seen in the figure, positive strain is generated in the wake region, with peak extensional strain produced close to the jet centreline. The positive strain in the vertical direction is hypothesized to stretch the scalar field, thus producing the thin vertical filaments, or 'fingers' seen in the wake of the jet. Although the line vortex pair is an admittedly simple model for vorticity in the transverse jet, the general behaviour should hold for the real flow. A downward (injection direction) velocity is induced between the regions of opposite-signed vorticity, and this downwash, coupled with a no-through-flow condition imposed by the wall, necessarily produces extensional strain in the vertical

direction in the wake. The correlation between the observed anisotropy of the scalar field and location of the maximum vertical strain rate suggests that the small-scale anisotropy is a consequence of the large-scale dynamics of the transverse jet.

Although these observations are based on measurements at  $x/d_j$  of the  $V_r = 10$  transverse jet, the observed local anisotropy of the scalar field is likely to be characteristic of the far field of high-velocity-ratio transverse jets in general, since the counter-rotating vortex pair is a robust feature of the far field of strong transverse jets. In addition, the conclusion that the large-scale dynamics can impose itself on the small scales of the scalar field has possible implications for other turbulent mixing flows. One consequence is that the small-scale structure of turbulent mixing is likely to depend on the flow geometry. This is consistent with the results of mixing experiments by Villermaux, Innocenti & Duplat (2001) in a turbulent jet, which showed that the injection features of the scalar persist. (The mixing time of the axisymmetric jet was found by Villermaux *et al.* (2001) to scale with the injection scale, independent of Reynolds number. In addition, the dependence of the mixing times on scalar diffusivity was reported to be a weak (logarithmic) function of Schmidt number.) Another consequence of the apparent connection between large and small scales is that scalar fields produced by turbulent mixing may be anisotropic at small length scales, as observed not only in the transverse jet, but also for other turbulent flows. For instance, as previously discussed, a link has been reported between large-scale anisotropic dynamics and the small scales of the scalar field (even within the mixing zone) for Rayleigh–Taylor flows (Cook & Dimotakis 2001). The link between large and small scales has also been noted in other flows such as heated grid turbulence (Warhaft 2000). The heated grid-turbulence experiments, of course, were quite different from scalar mixing of the transverse jet. In particular, for the heated grid-turbulence flows, the velocity and vorticity fields were isotropic, but the scalar field had an initial large-scale anisotropy (a linear temperature profile) which manifested itself in small-scale scalar anisotropy. In contrast, the transverse jet has large organized vorticity which produces small-scale anisotropy in the scalar field. In both cases, however, the source for the small-scale anisotropy is postulated to be a coupling between large and small scales of the turbulent mixing flows.

## 6. Conclusions

In summary, enhanced mixing, in the sense of better spatial homogenization of the scalar field, is found with increasing Reynolds number in the far field of high-velocity ratio liquid-phase transverse jets over the range  $1.0 \times 10^3 \leq Re_j \leq 20 \times 10^3$ . Many classical measures, such as scalar trajectories, decay of mean concentration on the centreline, and the spatial extent of the jet, are essentially independent of Reynolds number. However, the mixed-fluid distribution, as quantified by the PDF of jet-fluid concentration, evolves with Reynolds number at fixed location in the far field of the transverse jet. With the enhanced stirring that comes with increasing Reynolds number, the scalar field develops a preferred concentration, and the jet-fluid-concentration PDF evolves from a monotonically decreasing function to a strongly-peaked distribution. This behaviour, which occurs despite the greater entrainment rate of the transverse jet (at  $x/d_j = 50$ ) as compared to the jet discharging in a quiescent reservoir, suggests that the transverse jet is an efficient mixer.

Whole-field scalar increments show the concentration field of the turbulent transverse jet to be intermittent, with plateaux of nearly constant concentration separated by cliffs of sharp changes in concentration. The distribution of scalar

differences is seen to tend toward long-tailed exponential distributions with decreasing separation distance. These long-tailed PDFs of scalar differences, which persist for the Reynolds number range studied, are similar to results reported for grid-turbulence, Rayleigh-Bénard convection, and other turbulent flows. The long exponential tails and strongly peaked shape of the PDF of scalar differences is consistent with the physical picture of well-mixed plateaux, separated by cliffs, in the scalar field.

The scalar field of the liquid-phase high-Schmidt-number transverse jet is found to be anisotropic at even the smallest length scales. For instance, scalar power spectra for the far field of the jet are found to be essentially axisymmetric for lower wavenumbers, but increasingly elliptical for higher wavenumbers. The small-scale anisotropy is also seen in the difference between PDFs of scalar increments in different directions. Probability distributions of scalar increments have narrower shapes for vertical separations than for horizontal separations. These results indicate that the scalar field has less variation (in terms of PDFs of scalar increments, and power spectra) in the vertical direction than in the horizontal direction. Thus, the fine scales of the concentration field appear to have preferential orientation in the vertical direction. The small-scale anisotropy of the scalar field persists from the lowest Reynolds numbers investigated,  $Re_j = 1.0 \times 10^3$ , to the highest Reynolds numbers studied,  $Re_j = 20 \times 10^3$ . Further evidence for the anisotropy of the scalar field is seen in the scalar microscales computed for different directions. The difference between scalar microscales in two directions is greatest in the wake region of the jet, between the body of the jet and the wall. The observed local anisotropy is believed to be a consequence of the strain field produced by the counter-rotating vorticity in the transverse jet. Thus, the large-scale vortex structure of the transverse jet appears to impose itself on even the smallest features of the advected scalar field. The scalar anisotropy that is found in the  $V_r = 10$  jet is expected in other high-velocity-ratio jets, since the counter-rotating vortex pair is a characteristic feature of strong transverse jets.

One consequence of the apparent link between large and small scales that is observed in these experiments (and which has been previously reported for other turbulent flows) is that local scalar isotropy need not exist for turbulent mixing flows having anisotropic large scales. In addition, the long-tailed and peaked scalar-increment distribution found in the transverse jet is a consequence of intermittent, well-mixed plateaux in the scalar field separated by cliffs, and thus can be found in many other turbulent mixing flows. Furthermore, as a consequence of the connection between large-scale dynamics and the small scales of the scalar field, the detailed structure of turbulent mixing may depend on flow geometry. These conclusions, which are drawn from the study of liquid-phase transverse jets up to Reynolds numbers of  $20 \times 10^3$ , add to the existing evidence that the universality of small scales of the scalar field is not typical of turbulent-mixing flows. Additional experimental and numerical work is desirable to further analyse the behaviour of the transverse jets and other turbulent-mixing flows at yet higher Reynolds numbers and different Schmidt or Prandtl numbers.

We are grateful for assistance of D. Lang with the Cassini digital imaging system, and of S. Lombeyda with the three-dimensional visualizations. We also thank P. Svitek for his help with mechanical design and the operation of the GALCIT free-surface water tunnel. M. Gharib, H. Hornung, A. Leonard and Z. Warhaft provided helpful comments on the text. This work was supported by the Air Force Office of Scientific Research (F49620-98-1-0052 and F49620-01-1-0006) and a NDSEG

fellowship. J.W.S. acknowledges the support of P. Atsavapranee and I.-Y. Koh for the revision of this text. Development of the Cassini system was supported by DURIP grant F49620-95-1-0199, and AFOSR grants F49620-94-1-0283 and F49620-00-1-0036. The three-dimensional visualizations were made possible by NSF MRI grant 0079871.

### Appendix. PDFs for higher-dimensional diffusive fields

The PDF for a distribution,  $C(\mathbf{r})$ , in  $d$ -dimensional space is the differential  $d$ -dimensional volume,  $dV_d(C)$ , associated with a differential concentration,  $dC$ , equation (16b).

Normalization by the total volume,  $V_{d,tot}$ , is necessary so that the PDF has the properties discussed in § 3, and proper dimensions of inverse concentration.

Consider, for instance, the Gaussian scalar distribution,

$$C(\mathbf{r}, t) = \frac{1}{2^d(\pi\mathcal{D}t)^{d/2}} \exp(-r^2/4\mathcal{D}t) = \frac{1}{(2\pi)^{d/2}\sigma^d} \exp(-r^2/2\sigma^2). \quad (\text{A1})$$

This is the solution to the  $d$ -dimensional initial-value problem for the diffusion equation on an infinite domain with initial conditions of a delta function at the origin,  $C(\mathbf{r}, t = 0) = \delta(\mathbf{r})$ . Here,  $\sigma^2 = 2\mathcal{D}t$ . The differential length,  $dr$ , at any given time (i.e.  $\sigma = \text{constant}$ ) is related to  $dC$  by

$$\frac{dr}{dC} = -\frac{(2\pi)^{d/2}\sigma^d}{2r} \exp(r^2/2\sigma^2). \quad (\text{A2a})$$

Using (A 1),  $dr/dC$  can be written as a function of  $C$  alone:

$$\frac{dr}{dC} = \frac{1}{2Cr} = \frac{1}{2\sigma C \{ -2 \ln [(2\pi)^{d/2}\sigma^d C] \}^{1/2}}. \quad (\text{A2b})$$

The differential  $d$ -dimensional volume  $dV_d(C)$  may then be expressed as a function of  $C$  using (A 1) and (A2) to yield the form of the PDF for a  $d$ -dimensional Gaussian distribution:

$$f_d(C) \propto \frac{[\ln(1/C)]^{d/2-1}}{C}. \quad (\text{A3})$$

For one-, two- and three-dimensional Gaussian concentration distributions, the PDFs are then:

$$f_1(C) \propto \frac{1}{C [\ln(1/C)]^{1/2}}. \quad (\text{A4a})$$

$$f_2(C) \propto \frac{1}{C}. \quad (\text{A4b})$$

$$f_3(C) \propto \frac{[\ln(1/C)]^{1/2}}{C}. \quad (\text{A4c})$$

These functions are shown in figure 33. The distribution for the one-dimensional case has two peaks, at  $C = 0$  and  $C = 1$ , while the distributions for the two- and three-dimensional cases each have a peak at  $C = 1$ . The PDF decreases monotonically to zero at  $C = 1$  for the three-dimensional Gaussian, and to a non-zero minimum for the two-dimensional Gaussian.

Since  $d$ -dimensional transects of a higher-dimensional Gaussian are themselves  $d$ -dimensional Gaussians, the PDFs above can be viewed as PDFs of concentration

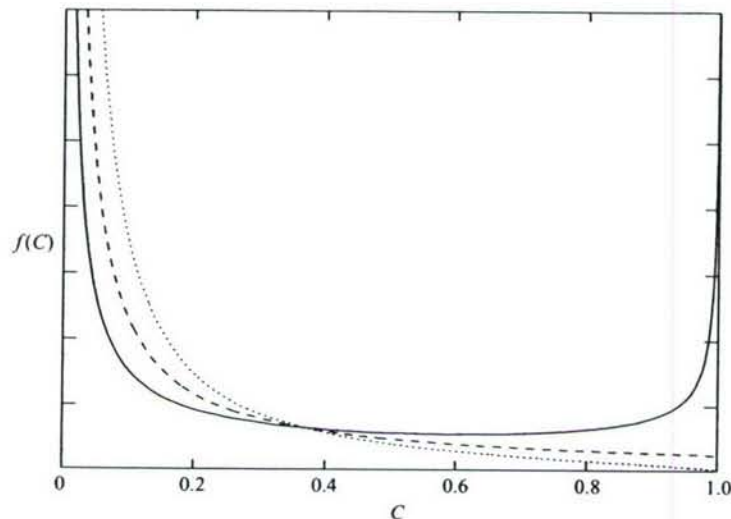


FIGURE 33. PDFs of diffusive (Gaussian) distributions. Solid line: one-dimensional; dashed line: two-dimensional; dotted line: three-dimensional.

distributions in  $d$ -dimensional space, or as  $d$ -dimensional measurements of a higher-dimensional distribution. Thus, a PDF can depend on the dimensionality of the space (or measurement), as well as the concentration field,  $C(\mathbf{r})$ .

#### REFERENCES

ANDREOPoulos, J. & RODI, W. 1984 An experimental investigation of jets in a crossflow. *J. Fluid Mech.* **138**, 93–127.

ANTONIA, R. A., BROWNE, L. W. B., BRITZ, D. & CHAMBERS, A. J. 1984 A comparison of properties of temporal and spatial temperature increments in a turbulent plane jet. *Phys. Fluids* **27**, 87–93.

ANTONIA, R. A., CHAMBERS, A. J., BRITZ, D. & BROWNE, L. W. B. 1986 Organized structures in a turbulent plane jet: topology and contribution to momentum and heat transport. *J. Fluid Mech.* **172**, 211–229.

BREIDENTHAL, R. E. 1981 Structure in turbulent mixing layers and wakes using a chemical reaction. *J. Fluid Mech.* **109**, 1–24.

BROADWELL, J. E. & BREIDENTHAL, R. E. 1984 Structure and mixing of a transverse jet in incompressible flow. *J. Fluid Mech.* **148**, 405–412.

BUDWIG, R., TAVOURARIS, S. & CORRSIN, S. 1985 Temperature fluctuations and heat flux in grid-generated isotropic turbulence with streamwise and transverse mean-temperature gradients. *J. Fluid Mech.* **153**, 441–460.

CATRAKIS, H. J. & DIMOTAKIS, P. E. 1996 Mixing in turbulent jets: scalar measures and isosurface geometry. *J. Fluid Mech.* **317**, 369–406.

CHASSANG, P., GEORGE, J., CLARIA, A. & SANANES, F. 1974 Physical characteristics of subsonic jets in a cross-stream. *J. Fluid Mech.* **62**, 41–64.

CHING, E. S. C. 1991 Probabilities for temperature differences in Rayleigh–Bénard convection. *Phys. Rev. A* **44**, 3622–3629.

COOK, A. W. & DIMOTAKIS, P. E. 2001 Transition stages of Rayleigh–Taylor instability between miscible fluids. *J. Fluid Mech.* **443**, 69–99.

CORRSIN, S. 1951 On the spectrum of isotropic temperature fluctuations in isotropic turbulence. *J. Appl. Phys.* **22**, 469–473.

CORTELEZZI, L. & KARAGOZIAN, A. R. 2001 On the formation of the counterrotating vortex pair in transverse jets. *J. Fluid Mech.* **446**, 347–373.

DAHM, W. J. A. & DIMOTAKIS, P. E. 1990 Large Schmidt number mixing of a conserved scalar in the self-similar far field of turbulent jets. *J. Fluid Mech.* **217**, 299–330.

DIMOTAKIS, P. E. 1986 Two-dimensional shear-layer entrainment. *AIAA J.* **24**, 1791–1796.

DIMOTAKIS, P. E. 2000 The mixing transition in turbulence. *J. Fluid Mech.* **409**, 69–98.

DIMOTAKIS, P. E. & CATRAKIS, H. J. 1996 Turbulence, fractals, and mixing. NATO Advanced Studies Institute series, *Mixing: Chaos and Turbulence*. *GALCIT Rep.* FM97–1.

DIMOTAKIS, P. E. & HALL, J. L. 1987 A simple model for finite chemical kinetics analysis of supersonic turbulent shear layer combustion. *AIAA/SAE/ASME/ASEE 23rd Joint Propulsion Meeting*, Paper 87–1879.

DIMOTAKIS, P. E. & MILLER, P. L. 1990 Some consequences of the boundedness of scalar fluctuations. *Phys. Fluids A* **2**, 1919–1920.

ECKART, C. 1948 An analysis of the stirring and mixing processes in incompressible fluids. *J. Mar. Res.* **7**, 265–275.

FEARN, R. & WESTON, R. P. 1974 Vorticity associated with a jet in a cross flow. *AIAA J.* **12**, 1666–1671.

FRIC, T. F. & ROSHKO, A. 1994 Vortical structure in the wake of a transverse jet. *J. Fluid Mech.* **279**, 1–47.

FRIEHE, C. A., VAN ATTA, C. W. & GIBSON, C. H. 1971 Jet turbulence: Dissipation rate measurements and correlations. *Turbulent Shear Flows AGARD Conf. Proc.* **93**, 18.1–7.

FRISCH, U. 1995 *Turbulence*. Cambridge University Press.

GIBSON, C. H., FRIEHE, C. A. & MCCONNELL, S. O. 1977 Structure of sheared turbulent fields. *Phys. Fluids* **20**, part II, S156–S167.

GORDIER, R. L. 1959 Studies on fluid jets discharging normally into moving liquid. St Anthony Falls Hyd. Lab., U. Minnesota, Tech. Paper 28, Series B.

GRUBER, M. R., BAURLE, R. A., MATHUR, T. & HSU, K.-Y. 1999 Fundamental studies of cavity-based flameholder concepts for supersonic combustors. *AIAA/SAE/ASME/ASEE 23rd Joint Propulsion Meeting*, Paper 99–2248.

HAN, D., OROZCO, V. & MUNGAL, M. G. 2000 Gross-entrainment behavior of turbulent jets injected obliquely into a uniform crossflow. *AIAA J.* **38**, 1643–1649.

HASSELBRINK, E. F. & MUNGAL, M. G. 2001 Transverse jets and jet flames. Part 1. Scaling laws for strong transverse jets. *J. Fluid Mech.* **443**, 1–25.

HOLZER, M. & SIGGIA, E. D. 1994 Turbulent mixing of a passive scalar. *Phys. Fluids* **6**, 1829–2176.

JOHARI, H., PACHECO-TOUGAS, M. & HERMANSON, J. 1999 Penetration and mixing of fully modulated turbulent jets in crossflow. *AIAA J.* **37**, 842–850.

KAMOTANI, Y. & GREBER, I. 1972 Experiments on a turbulent jet in a cross flow. *AIAA J.* **10**, 1425–1429.

KARAGOZIAN, A. R. 1986 An analytical model for the vorticity associated with a transverse jet. *AIAA J.* **24**, 429–436.

KEFFER, J. F. & BAINES, W. D. 1963 The round turbulent jet in a cross-wind. *J. Fluid Mech.* **15**, 481–496.

KELSO, R. M., LIM, T. T. & PERRY, A. E. 1996 An experimental study of round jets in cross-flow. *J. Fluid Mech.* **306**, 111–144.

KELSO, R. M. & SMITS, A. J. 1995 Horseshoe vortex systems resulting from the interaction between a laminar boundary layer and a transverse jet. *Phys. Fluids* **7**, 153–158.

KOOCHESFAHANI, M. M. & DIMOTAKIS, P. E. 1986 Mixing and chemical reactions in a turbulent liquid mixing layer. *J. Fluid Mech.* **170**, 83–112.

KUZNETSOV, V. R. & SABEL'NIKOV, V. A. 1990 *Turbulence and Combustion*. Hemisphere.

KUZO, D. M. 1995 An experimental study of the turbulent transverse jet. PhD thesis, California Institute of Technology, Pasadena, CA.

LOZANO, A., SMITH, S. H., MUNGAL, M. G. & HANSON, R. K. 1993 Concentration measurements in a transverse jet by planar laser-induced fluorescence of acetone. *AIAA J.* **32**, 218–221.

MCMAHON, H. M., HESTER, D. D. & PALFERY, J. G. 1971 Vortex shedding from a turbulent jet in a cross-wind. *J. Fluid Mech.* **48**, 73–80.

MARGASON, R. J. 1993 Fifty years of jet in cross flow research. *AGARD Meeting on Computational and Experimental Assessment of Jets in Cross Flow*, April, 1993.

MESTAYER, P. G., GIBSON, C. H., COANTIC, M. F. & PATEL, A. S. 1976 Local anisotropy in heated and cooled turbulent boundary layers. *Phys. Fluids* **19**, 1279–1287.

MILLER, P. L. & DIMOTAKIS, P. E. 1991 Reynolds number dependence of scalar fluctuations in a high Schmidt number turbulent jet. *Phys. Fluids A* **3**, 1156–1163.

MORTON, B. R. & IBBETSON, A. 1996 Jets deflected in a crossflow. *Exp. Thermal Fluid Sci.* **12**, 112–133.

MOUSSA, Z. M., TRISCHKA, J. W. & ESKINAZI, S. 1977 The near field in the mixing of a round jet with a cross-stream. *J. Fluid Mech.* **80**, 49–80.

MUNGAL, M. G. & LOZANO, A. 1996 Some observations of a large, burning jet in crossflow. *Exps. Fluids* **21**, 264–267.

MYDLARSKI, L. & WARHAFT, Z. 1998 Three-point statistics and the anisotropy of a turbulent passive scalar. *Phys. Fluids* **10**, 2885–2894.

NIEDERHAUS, C. E., CHAMPAGNE, F. H. & JACOBS, J. W. 1997 Scalar transport in a swirling transverse jet. *AIAA J.* **35**, 1697–1704.

OBOKHOV, A. M. 1949 Structure of the temperature field in turbulent flows. *Izv. Akad. Nauk SSSR Geogr. Geophys.* **13**, 58–69.

OULD-ROUIS, M., ANSELMET, F., LE GAL, P. & VAIENTI, S. 1995 Statistics of temperature increments in fully developed turbulence. Part II. Experiments. *Physica D* **85**, 405–424.

PATRICK, M. A. 1967 Experimental investigation of the mixing and penetration of a round turbulent jet injecting perpendicular into a transverse stream. *J. Hydronaut. Div. ASCE* **45**, 16–31.

PRATTE, B. D. & BAINES, M. 1967 Profiles of the round turbulent jet in a crossflow. *J. Hydronaut. Div. ASCE* **92**, 53–64.

PRINGSHEIM, P. 1949 *Fluorescence and Phosphorescence*. Interscience.

PUMIR, A. 1994 A numerical study of the mixing of a passive scalar in three dimensions in the presence of a mean gradient. *Phys. Fluids* **6**, 2118–2132.

REILLY, R. S. 1968 Investigation of the deformation and penetration of a turbulent subsonic jet issuing transversely into a uniform, subsonic main stream. PhD thesis, University of Maryland.

RICOU, F. P. & SPALDING, D. B. 1961 Measurements of entrainment by axisymmetrical turbulent jets. *J. Fluid Mech.* **11**, 21–32.

SHAN, J. W., LANG, D. B. & DIMOTAKIS, P. E. 2004 Scalar concentration measurements in liquid-phase flows with pulsed lasers. *Exps. Fluids* **36**, 268–273.

SHRAIMAN, B. & SIGGIA, E. 2000 Scalar turbulence. *Nature* **405**, 639–646.

SMITH, S. H. & MUNGAL, M. G. 1998 Mixing, structure and scaling of the jet in crossflow. *J. Fluid Mech.* **357**, 83–122.

SREENIVASAN, K. R. 1991 On local isotropy of passive scalars in turbulent shear flows. *Proc. R. Soc. Lond. A* **434**, 165–182.

SREENIVASAN, K. R. & ANTONIA, R. A. 1997 The phenomenology of small-scale turbulence. *Annu. Rev. Fluid Mech.* **29**, 435–472.

SREENIVASAN, K. R., ANTONIA, R. A. & BRITZ, D. 1979 Local isotropy and large structures in a heated turbulent jet. *J. Fluid Mech.* **94**, 745–775.

SU, L. & MUNGAL, M. G. 2004 Simultaneous measurements of scalar and velocity field evolution in turbulent crossflowing jets. *J. Fluid Mech.* **513**, 1–45.

SU, L. K., HAN, O., MIRAFOR, M., & MUNGAL, M. G. 2000 Measurements of scalar and velocity fields in turbulent crossflowing jets with low velocity ratio. *AIAA Paper 2000-0815*

TAVOURALIS, S. & CORRIHN, S. 1981 Experiments in nearly homogeneous turbulent shear flow with a uniform mean temperature gradient. Part 2. The fine structure. *J. Fluid Mech.* **104**, 349–367.

TENNEKES, H. & LUMLEY, J. L. 1972 *A First Course in Turbulence*. MIT Press.

THORODDSEN, S. T. & VAN ATTA, C. W. 1992 Exponential tails and skewness of density-gradient probability density functions in stably stratified turbulence. *J. Fluid Mech.* **244**, 547–566.

TONG, C. & WARHAFT, Z. 1994 On passive scalar derivative statistics in grid turbulence. *Phys. Fluids* **6**, 2165–2176.

UBEROI, M. S. & SINGH, P. I. 1975 Turbulent mixing in a two-dimensional jet. *Phys. Fluids* **18**, 764–769.

VANLERBERGHE, W., SANTIAGO, J., DUTTON, J. & LUCHT, R. 2000 Mixing of a sonic transverse jet injected into a supersonic flow. *AIAA J.* **38**, 470–479.

VILLERMAUX, E., INNOCENTI, C. & DUPLAT, J. 2001 Short circuits in the Corrsin–Obukhov cascade. *Phys. Fluids* **13**, 284–289.

WALKER, D. A. 1987 A fluorescence technique for measurement of concentration in mixing liquids. *J. Phys. E: Sci. Instrum.* **20**, 217–224.

WARHAFT, Z. 2000 Passive scalars in turbulent flows. *Annu. Rev. Fluid Mech.* **32**, 203–240.

XU, X.-H. & YEUNG, E. S. 1997 Direct measurement of single-molecule diffusion and photodecomposition in free solution. *Science* **275**, 1106–1109.

YODA, M., HESSELINK, L. & MUNGAL, M. G. 1992 The evolution and nature of large-scale structures in the turbulent jet. *Phys. Fluids* **4**, 803–811.

YUAN, L. L. & STREET, R. L. 1998 Trajectory and entrainment of a round jet in crossflow. *Phys. Fluids* **10**, 23231–2335.

YUAN, L. L., & STREET, R. L. & FERZIGER, J. H. 1999 Large-eddy simulations of a round jet in crossflow. *J. Fluid Mech.* **379**, 71–104.



## Premixed laminar C<sub>1</sub>–C<sub>2</sub> stagnation flames: Experiments and simulations with detailed thermochemistry models

Jeffrey M. Bergthorson <sup>\*</sup>, Paul E. Dimotakis

*Graduate Aeronautical Laboratories, California Institute of Technology, Pasadena, CA 91125, USA*

---

### Abstract

A generally accepted mechanism for the combustion of C<sub>1</sub> and C<sub>2</sub> hydrocarbons is still elusive. This paper discusses a technique that can further validate and constrain such mechanisms, towards the development of a comprehensive model for small hydrocarbon combustion. The approach relies on detailed measurements of strained premixed flames in a jet-wall stagnation flow. This geometry yields a flow with boundary conditions that can be reliably specified, facilitating simulation and detailed comparisons with experiment. The diagnostics are optimized for accuracy, minimal flame disturbance, and rapid simultaneous recording of velocity and CH radical profiles. Flame simulations rely on a one-dimensional hydrodynamic model, a multi-component transport formulation, and several detailed chemistry models. Direct comparisons between experiment and simulation allow for an assessment of the various models employed. Experimental data for methane, ethane, and ethylene flames are compared to numerical simulations using several thermochemistry models. GRI-Mech 3.0, a C<sub>3</sub> model by Davis et al. (DLW99), and two versions of the San Diego mechanism are utilized. While GRI-Mech 3.0 and the DLW99 models accurately predict experiment in some cases, the 2005/03/10 revision of the San Diego mechanism is found to give the best overall agreement with experiment for methane, ethane, and ethylene flames.

© 2006 The Combustion Institute. Published by Elsevier Inc. All rights reserved.

**Keywords:** CANTERA; Kinetic mechanisms; Stagnation flames; Particle streak velocimetry; Planar laser induced fluorescence

---

### 1. Introduction

The validation of combustion models against well-defined experimental data is essential to ensure that models accurately predict the phenomena of interest. Although significant effort has been expended in developing reliable models for small hydrocarbon combustion (e.g., the

GRI-Mech initiative [1]), such models have not been validated against sufficient numbers of kinetically independent experiments [2]. The approach here is to directly compare measurements of premixed stagnation-point flames to simulations, providing a validation target for each experiment.

The stagnation flame geometry yields a flow with boundary conditions that can be accurately and reliably specified, facilitating simulation and comparison with experiment. The diagnostics are optimized for accuracy, minimal flame disturbance, and rapid simultaneous recording of flow velocity and CH radical profiles. Particle streak

<sup>\*</sup> Corresponding author. Fax: +1 626 395 4447.  
E-mail address: [jeffb@tyrvos.caltech.edu](mailto:jeffb@tyrvos.caltech.edu) (J.M. Bergthorson).

velocimetry (PSV), complemented by simultaneous CH planar laser induced fluorescence (PLIF) imaging, allows accurate concurrent measurement of both the velocity and CH radical profiles [3]. Simultaneous measurements of air, fuel, and diluent mass fluxes, as well as of stagnation plate temperature, allow an accurate specification of boundary conditions for simulations.

Experimental velocity and CH profiles are compared to one-dimensional simulation predictions using the CANTERA software package [4]. The simulations utilize a multi-component transport formulation [5]. Various chemical-kinetic models are employed to assess their ability to predict the experimental results.

Relatively few comparisons of stagnation flame simulations and experimental data are available. Sung, Law, and coworkers studied profiles of velocity, temperature, and major-species concentrations in methane-air opposed-jet flames to quantify the effect of stretch on flame structure [6–9]. These authors find good agreement for temperature and major-species profiles, while predicted post-flame velocity profiles remain above the data when particle-inertia and thermophoretic effects are included.

The technique is applied to methane, ethane, and ethylene flames as a function of equivalence ratio,  $\Phi$ . These data are available for validation or optimization targets [10,11], following the collaborative-data approach [12]. The methodology and diagnostics permit an assessment of numerical simulation predictions of strained-flames for  $C_1$ – $C_2$  hydrocarbons.

## 2. Experiments

Experiments were performed using a co-flow nozzle system to generate a premixed central-jet,  $d = 9.9$  mm, that impinges on a temperature-controlled (water-cooled) stagnation plate at a separation distance of  $L = 8$  mm. The central-jet flow is supplied from premixed fuel, air, and, in some cases, diluent streams. Either nitrogen or helium is used as the co-flow gas to improve flame stability.

In this work, two simultaneous laser-diagnostic techniques are utilized to measure velocity fields and CH radical profiles. PSV is used to record axial velocity profiles, while PLIF is utilized to measure relative concentration profiles of the CH radical.

In this PSV implementation, a Coherent Ar<sup>+</sup> laser beam, chopped with a 50% duty cycle at frequencies in the range  $1 < v_c < 2.5$  kHz, provides the illumination source. Images are recorded using an in-house developed digital-imaging system that relies on a low-noise,  $1024^2$ -pixel CCD. Typical exposure times of 100 ms result in multiple streaks from particles that completely traverse the image

during the exposure. The resulting streak record is digitally processed to determine the locations of the start and end of each streak. The particle displacement divided by the chopping period yields the velocity estimate.

The narrow spatial profile of the CH radical is measured using PLIF, as it is well-correlated with flame location and reveals where the combustion chemistry is taking place [13]. In this work, CH PLIF relies on excitation to the  $B$  state and detecting the fluorescence from the  $A-X$  transition [14,15]. A tunable dye laser (Sirah PrecisionScan) is used for the excitation source and the measurements are performed in the saturated fluorescence regime. The two-dimensional CH concentration field is recorded using a lens-coupled intensifier with a cooled CCD binned to  $344 \times 260$  pixel<sup>2</sup>. Light is collected at magnifications near 1:1. A gate time of 70 ns rejects chemiluminescence while retaining fluorescence. The CH signal is obtained by measuring the fluorescence signal both on and off of the resonance line, and taking the difference of the two, as previously suggested [15]. This is important as broadband fluorescence from polycyclic-aromatic hydrocarbons can produce a signal that competes with CH fluorescence [16].

Fuel, air, and diluent flow rates are set using sonic metering valves and monitored concurrently (Omega FMA flow meters). The flow meters are calibrated using a Bios DryCal ML-500 dry piston calibrator, and the estimated uncertainty for each stream is 0.6%. Mass-flow and stagnation plate temperature data are acquired synchronously with the digital-image acquisition to allow accurate specification of simulation boundary conditions. The diagnostics employed here and some methane flame results were reported previously [3]. Further details on the experimental apparatus and laser diagnostics are also available [10].

## 3. Numerical method

Axisymmetric premixed flame simulations are performed using the CANTERA reacting-flow software package [4]. The simulations rely on a one-dimensional hydrodynamic model for axisymmetric stagnation flow [5,17]. Exploiting the nonreacting, inviscid solution to the stream-function model, a parabola is fit to the velocity data in the cold region upstream of the flame [3]. The inlet velocity,  $u_t$ , and velocity-gradient,  $u'_t$ , boundary conditions are taken from these parabolic fits and specified at  $x = \ell = 6$  mm, with the results not sensitive to this choice [10]. The velocity and velocity gradient are set to zero at the stagnation-wall,  $x = 0$  mm, to satisfy the no-penetration and no-slip conditions. The hydrodynamic model has been validated against nonreacting impinging-jet experiments and axisymmetric

two-dimensional direct numerical simulations [18]. The one-dimensional model is found to give good agreement with experiment and more detailed simulations if the inlet velocity boundary conditions are specified from fits to the data.

The energy and species equations are also solved with specification of inlet composition, inlet temperature, and stagnation-wall temperature [5]. Inlet composition boundary conditions are determined from measurements of individual mass-flow rates. The stagnation-wall temperature is specified from experimental measurements, and the inlet temperature is assumed to be equal to the measured room temperature. A no-flux (multi-component) boundary-condition for species is applied at the wall. The simulations use a multi-component transport model [5], and several chemical-kinetic mechanisms.

GRI-Mech 3.0 is a mechanism developed to model natural-gas combustion and contains 53 species and 325 reactions [1]. The C<sub>3</sub> mechanism of Davis et al. (DLW99) is developed to describe the combustion of C<sub>1</sub>–C<sub>3</sub> hydrocarbons and contains 71 species and 469 reactions [19]. The San Diego mechanism is also developed to model the combustion of C<sub>1</sub>–C<sub>3</sub> hydrocarbons. Two releases of the San Diego mechanism are utilized in this study, the 2003/08/30 version (SD2003) containing 39 species and 173 reactions, and the 2005/03/10 version (SD2005) containing 39 species and 175 reactions [20].

The virtual inlet velocity,  $u_\ell$ , was corrected for velocity lag of the tracer particles at the local velocity gradient,  $u'_\ell$  [10,21]. To account for the effects of particle-inertia and thermophoresis, the particle behavior in the simulated flow field is solved using a Lagrangian technique, similar to that employed by Sung et al. [7,8]. The resulting particle position-time record is post-processed to account for the finite chopping frequency employed, and results in a modeled-particle-tracking (modeled-PT) profile. The modeled-PT profile accounts for particle-inertia, thermophoretic, and finite particle-track interval effects and can be directly compared to experiment. Details on the methodology for estimating the modeled-PT profile are available elsewhere [10,21].

#### 4. Results and discussion

Of the models studied, the 2005 version of the San Diego mechanism yields the best agreement with our experimental results over the range of fuels and stoichiometries investigated [10]. Figure 1 shows a comparison of experimental PSV and CH PLIF profiles with numerical predictions, using SD2005, in a  $\Phi = 1.0$  methane-air flame. The simulated fluid velocity profile, the predicted particle trajectory, and the modeled-PT profile are all included. The PSV data were recorded

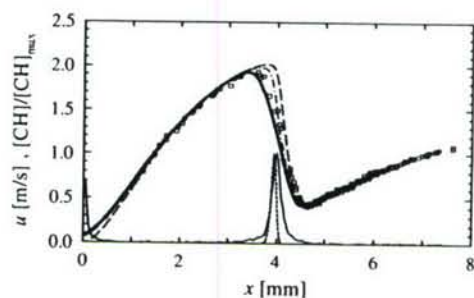


Fig. 1. Stoichiometric methane-air flame profiles simulated with SD2005. PSV data (squares), simulated fluid velocity (long-dash line), predicted particle profile (dot-dash line), modeled-PT profile (thick solid line), PLIF data (thin solid line), and simulated CH profile (short-dash line) are included. Position,  $x$ , is measured from the stagnation wall and  $-u$  is plotted in Figs. 1–6.

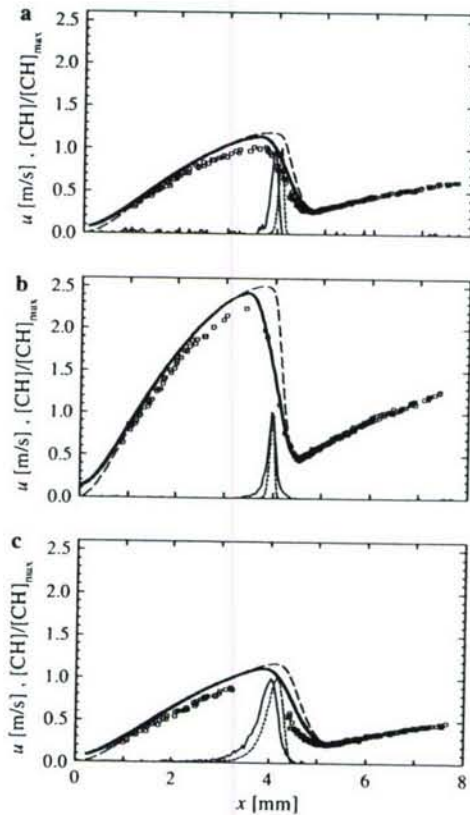


Fig. 2. Ethane-air flame profiles simulated with SD2005 mechanism. (a)  $\Phi = 0.7$ . (b)  $\Phi = 1.0$ . (c)  $\Phi = 1.5$ . Legend as in Fig. 1.

using 3  $\mu\text{m}$  ceramic microspheres (3 M Zeeospheres), and the chopping frequency was  $v_c = 2$  kHz. Modeling the particle motion and the experimental analysis technique brings the modeled-PT velocity profile into close agreement with experiment [21]. In Figs. 1–3 single-shot

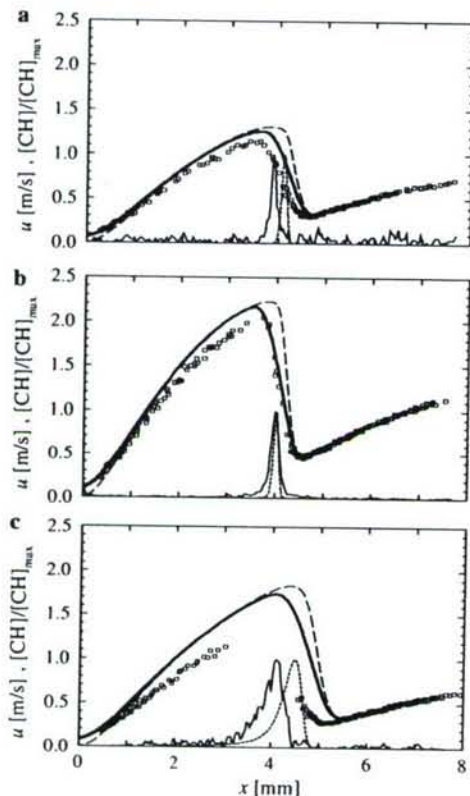


Fig. 3. Ethylene flame profiles simulated with SD2005 mechanism. (a)  $\phi = 0.6$ , 21%  $O_2:(O_2 + N_2)$ . (b)  $\phi = 1.0$ , 17%  $O_2:(O_2 + N_2)$ . (c)  $\phi = 1.8$ , 21%  $O_2:(O_2 + N_2)$ . Legend as in Fig. 1.

CH PLIF profiles, averaged over the central 50 columns about the jet axis (1.7 mm in the flow), are plotted to indicate the signal-to-noise ratio of the PLIF images [3]. The peak of the predicted CH profile lies slightly downstream of measurement for the stoichiometric methane-air flame.

In our studies, kinetic effects are found to be most sensitive to the fuel type and inlet composition [10]. In the current experimental setup, stable methane-air flames were established for equivalence ratios in the range  $0.7 \leq \phi \leq 1.3$ . Experimental and predicted velocity and CH profiles for a lean and rich methane flame were presented previously [3] and are not included here. In that work, GRI-Mech 3.0 yields good agreement with rich methane-air flame data, but predicts higher flame speeds than measured for lean flames, consistent with previous results [1,22,23].

Ethane-air flames were stabilized for equivalence ratios in the range  $0.7 \leq \phi \leq 1.5$  in our experiment. Profiles for a lean, stoichiometric, and rich ethane-air flame are presented in Fig. 2, simulated using the SD2005 mechanism. Particle velocity profiles are omitted for clarity.

PSV measurements are performed using 1  $\mu$ m alumina particles ( $\rho_p \approx 3830 \text{ kg/m}^3$ ), and the chopping frequencies are  $v_c = 1.6, 2.4$ , and  $1.6 \text{ kHz}$  for the lean, stoichiometric, and rich flames, respectively. The modeled-PT profiles capture the shape of the experimental profiles, illustrating the importance of accounting for particle-inertia, thermophoretic, and finite particle-track interval effects. For this mechanism, good agreement between predicted and measured profiles is seen for stoichiometric conditions, although the predicted velocity profile lies above the data in the post-flame region. The predicted velocity profiles for the lean and rich flame lie above the experimental data. The discrepancy is more evident in the post-flame region of the flow, as velocity differences upstream of the flame are amplified by the density drop through the reaction zone that results from the heat release [21]. The predicted CH profile also lies upstream of experiment for these cases. The CH and velocimetry results are self-consistent and indicate that the flame speed predicted by SD2005 for lean and rich conditions is slightly higher than observed experimentally. Velocity data were not measured through the reaction zone for rich ethane and ethylene flames due to increased  $C_2$  chemiluminescence noise in PSV images that passes the bandpass filter employed. Increasing CH-layer width and asymmetry with increasing  $\phi$  are evident.

Stable ethylene flames were established in our apparatus for equivalence ratios in the range  $0.6 \leq \phi \leq 1.8$ . Profiles for a lean, stoichiometric, and rich flame are presented in Fig. 3, also simulated using the SD2005 mechanism. The lean and rich flames are not diluted, while the stoichiometric flame was diluted such that the percentage of oxygen in the "air" was 17%  $O_2:(O_2 + N_2)$  [10]. PSV measurements are performed using 1  $\mu$ m alumina particles ( $\rho_p \approx 3830 \text{ kg/m}^3$ ) and chopping frequencies are  $v_c = 1.6, 2.4$ , and  $1.6 \text{ kHz}$  for the lean, stoichiometric, and rich flames, respectively. For the stoichiometric flame, good agreement is seen between experiment and prediction. The simulations, however, predict higher flame speeds than measured for lean and rich conditions, as for ethane flames. CH profile asymmetry is evident in the  $\phi = 1.8$  flame, for which the signal-to-noise ratio of single-shot profiles is relatively low because of the low CH concentration [10].

It is of interest to compare the predictions of multiple chemistry models to experiment to assess their relative performance. Flames for each fuel over a range of equivalence ratios were simulated using GRI-Mech 3.0, the DLW99 mechanism, and two releases of the San Diego mechanism, SD2003 and SD2005. Results for lean, stoichiometric, and rich methane-air flames are presented in Fig. 4. The modeled-PT profiles obtained from the simulated flow field for the experimental particle properties and tracking time are compared to

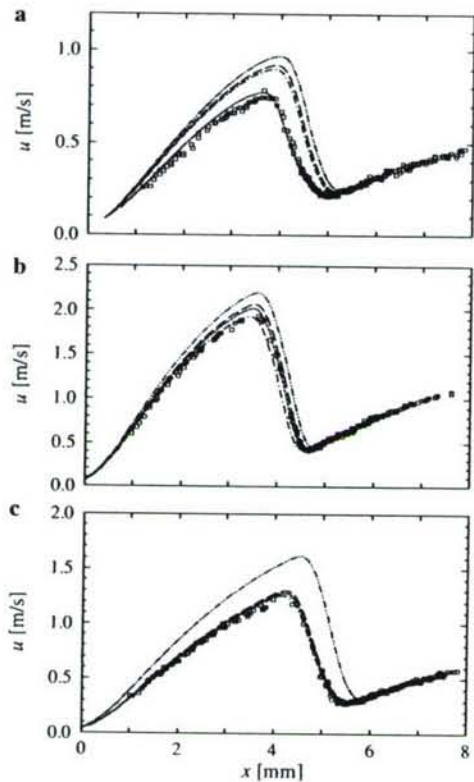


Fig. 4. Methane-air flames simulated with multiple mechanisms. (a)  $\phi = 0.7$ . (b)  $\phi = 1.0$ . (c)  $\phi = 1.3$ . PSV data (squares) and modeled-PT profiles are included with GRI-Mech 3.0 (long-dash line), DLW99 (short-dash line), SD2003 (dash-double-dot line), and SD2005 (dash-dot line) mechanisms.

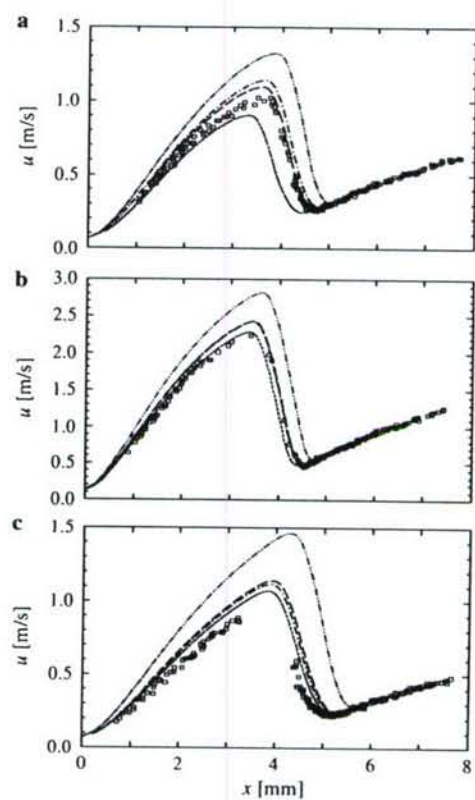


Fig. 5. Ethane-air flames simulated with multiple mechanisms. (a)  $\phi = 0.7$ . (b)  $\phi = 1.0$ . (c)  $\phi = 1.5$ . Legend as in Fig. 4.

the PSV data. For lean methane-air flames, the DLW99 mechanism gives the best prediction of the experimental data, while SD2005 is in close agreement with GRI-Mech 3.0. The SD2003 mechanism shows the largest variance with experiment. For stoichiometric methane-air flames, profiles from the different chemistry models almost collapse onto each other, exhibiting only slight differences in flame speed, and are in reasonable agreement with experiment. Good agreement is also seen for rich methane-air flames, except for SD2003, which predicts a higher flame speed than measured. The results indicate that the flame speed predicted by GRI-Mech 3.0 for lean to stoichiometric methane-air flame speeds is slightly higher than observed experimentally, as shown previously [1,3,22,23].

The lean, stoichiometric, and rich ethane-air flames presented in Fig. 2 are also simulated with the four mechanisms and the results are given in Fig. 5. For the lean flame, the DLW99 mechanism predicts a lower flame speed than measured, while

GRI-Mech 3.0 and the SD2005 mechanism are in close agreement and predict slightly higher flame speeds than measured. Good agreement with experiment is seen for the DLW99, GRI-Mech 3.0, and SD2005 mechanisms for the stoichiometric flame. For the rich flame, the DLW99, GRI-Mech 3.0, and SD2005 mechanisms give consistent predictions with each other and exhibit slightly higher flame speeds than observed in the experiment. The SD2003 mechanism overpredicts the flame speed for all ethane-air flames.

Figure 6 gives the profiles for a lean, stoichiometric, and rich ethylene flame. For the lean flame, the DLW99 and GRI-Mech 3.0 mechanisms predict lower and higher flame speeds than measured, respectively. The SD2003 model closely matches GRI-Mech 3.0, while the newer San Diego mechanism, SD2005, gives closer agreement with experiment. For the stoichiometric flame, the DLW99 and SD2005 models are close to each other and accurately predict the flame speed, while the SD2003 and GRI-Mech 3.0 mechanisms predict higher flame speeds than measured. Under rich conditions, all of these models predict higher flame speeds than measured. GRI-Mech 3.0 was

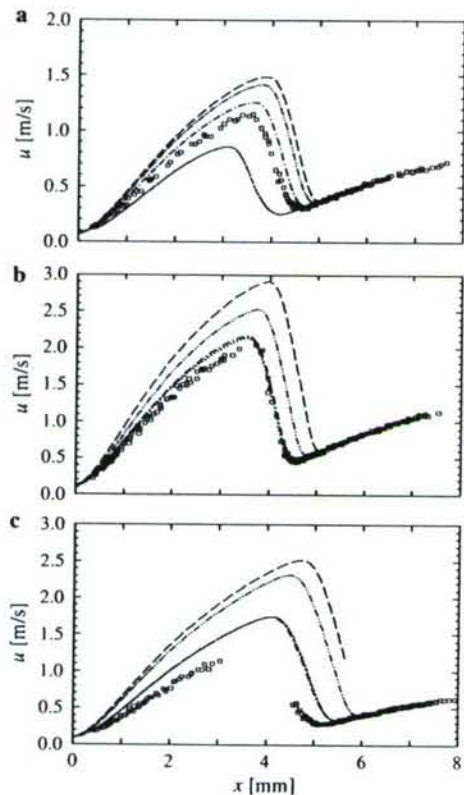


Fig. 6. Ethylene flames simulated with multiple mechanisms. (a)  $\phi = 0.6$ , 21%  $O_2/(O_2 + N_2)$ . (b)  $\phi = 1.0$ , 17%  $O_2/(O_2 + N_2)$ . (c)  $\phi = 1.8$ , 21%  $O_2/(O_2 + N_2)$ . Legend as in Fig. 4.

not optimized for ethylene flames and predicts higher flame speeds than measured for all stoichiometries, as shown previously [24].

To illustrate variations between experimental data at all equivalence ratios and different chemistry models, the difference between measured and predicted CH-layer locations is utilized [3]. The predicted location of the CH profile,  $x_{CH, sim}$ , is compared to the measured CH profile location,  $x_{CH}$ , and the difference between the two is normalized by the simulated CH-layer thickness,  $\delta_{CH}$ , calculated using the SD2005 model at stoichiometric conditions. The stoichiometric CH-layer thickness is an appropriate length scale for normalizing positional differences and different chemistry models predict similar CH-layer thicknesses [10]. To account for asymmetry of the CH profiles in rich  $C_2$  flames, “two-sided” Lorentzian fits were performed on single-image PLIF profiles, given by  $S_{CH}(x < x_{CH}) = S_{CH,max} w_1^2 / [(x - x_{CH})^2 + w_1^2]$ ,  $S_{CH}(x > x_{CH}) = S_{CH,max} w_2^2 / [(x - x_{CH})^2 + w_2^2]$ , where  $S_{CH,max}$  is the peak intensity,  $x_{CH}$  is the peak location, and  $w_1$  and  $w_2$  are the widths corre-

sponding to the half-maximum value on either side of  $x_{CH}$ . The experimental CH location,  $x_{CH}$ , is taken as the mean of the fit values from single-shot profiles, averaging typical records of 1000 PLIF images. The simulated CH location,  $x_{CH,sim}$ , is taken to be the location of the CH profile peak from simulations, and the locations of the half-max value on either side of the peak were interpolated from the simulated profiles. The difference in location of the two half-max values yields the CH-layer thickness,  $\delta_{CH}$ .

Figure 7 plots the difference between measured and predicted CH profile locations for methane, ethane, and ethylene flames at variable stoichiometry. Positive values of  $(x_{CH,sim} - x_{CH}) / \delta_{CH,SD2005,\phi=1}$  indicate that the simulated CH profile is *upstream* of the PLIF profile and that the predicted flame speed is *higher* than experiment. The uncertainty in the boundary-condition measurements corresponds to a total estimated uncertainty in the predicted flame location of  $\approx 0.5\delta_{CH}$  [10].

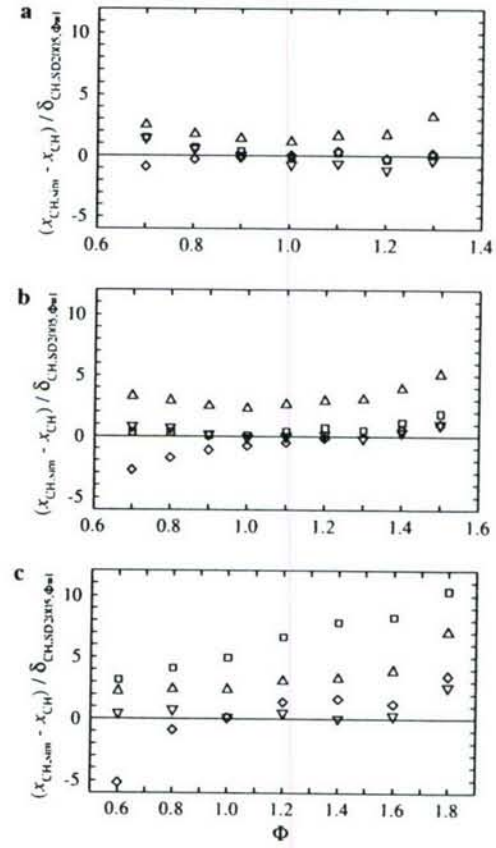


Fig. 7. Difference between simulated,  $x_{CH,sim}$ , and measured,  $x_{CH}$ , peak locations of CH scaled by the stoichiometric CH-layer thickness,  $\delta_{CH}$ . (a) Methane-air flames. (b) Ethane-air flames. (c) Ethylene flames. Simulations performed using GRI-Mech 3.0 (□), DLW99 (△), SD2003 (▽), and SD2005 (▽) mechanisms.

For methane flames (Fig. 7a), the mechanisms tend to agree within one CH-layer thickness near stoichiometry and for rich flames. For lean flames, GRI-Mech 3.0 and SD2005 both predict higher flame speeds than measured, while the DLW99 mechanism predicts slightly lower flame speeds than measured. The SD2003 mechanism predicts higher flame speeds than measured for all equivalence ratios. The performance of GRI-Mech 3.0 reported here is consistent with that found by other techniques [1,22,23].

For ethane flames (Fig. 7b), the GRI-Mech 3.0 and SD2005 mechanisms show the closest agreement with experiment, with GRI-Mech 3.0 showing better agreement for lean flames, while the SD2005 mechanism more closely matches experiment for rich conditions. The DLW99 mechanism predicts weaker flames than observed for lean conditions and predicts similar results to SD2005 for rich flames. The SD2003 mechanism again overpredicts the flame speed for all equivalence ratios. Dong et al. measured laminar flame speeds in lean ethane-air flames,  $0.6 \leq \phi \leq 0.8$ , and find that GRI-Mech 3.0 predicted flame speeds 2–4 cm/s higher than measured [22]. Data on the GRI-Mech 3.0 web page [1] show an underprediction of the flame speed for lean ethane-air flames and an overprediction for rich conditions. The results presented here show good agreement for lean to slightly rich conditions and a predicted flame speed that is higher than experiment for rich flames. The origin of these discrepancies in the reported performance of GRI-Mech 3.0 is unclear. For the other mechanisms, similar comparisons are not available.

For ethylene flames (Fig. 7c), the models exhibit the largest variance with each other and experiment. Flames were diluted with excess nitrogen to maintain similar flame speeds across different stoichiometries [10]. The compositions studied are  $\phi = 0.6$ , 21%  $O_2:(O_2 + N_2)$ ,  $\phi = 0.8$ , 19.5%  $O_2:(O_2 + N_2)$ ,  $\phi = 1.0$ , 17%  $O_2:(O_2 + N_2)$ ,  $\phi = 1.2$ , 16.5%  $O_2:(O_2 + N_2)$ ,  $\phi = 1.4$ , 18%  $O_2:(O_2 + N_2)$ ,  $\phi = 1.6$ , 21%  $O_2:(O_2 + N_2)$ , and  $\phi = 1.8$ , 21%  $O_2:(O_2 + N_2)$ . GRI-Mech 3.0 was not optimized for ethylene combustion and predicts much higher flame speeds than measured, in accord with previous findings [24]. The SD2003 mechanism predicts higher flame speeds than measured, as for methane- and ethane-air flames. The SD2005 model, however, shows the best agreement with experiment. A comparison of measured burning velocities for ethylene-air flames with this mechanism, available on the San Diego mechanism web site [20], shows good agreement between model and experiment with a slight overprediction for lean flames, consistent with the results presented here. The DLW99 mechanism is found to be in accord with experiment only for stoichiometric conditions. Ethylene-air laminar flame speed measurements were compared to predictions of a mechanism that

was composed of the DLW99 kinetics and additional butane reactions [25]. These authors report generally good agreement for all  $\phi$ , with measured flame speeds for lean flames falling above the predictions and predicted flame speeds for stoichiometric and rich flames falling above the data, consistent with results presented here.

## 5. Conclusions

The axisymmetric, stagnation-point flame environment is used to validate chemical-kinetic mechanisms, exploiting the sensitivity of flame location to predicted flame speed and the availability of a one-dimensional hydrodynamic description of the flow. Accounting for the effects of particle-inertia, thermophoresis, and finite particle-track interval brings measured and predicted velocity profiles closer together. The approach presented permits an assessment of the numerical simulation predictions of strained flames for  $C_1$ – $C_2$  hydrocarbons.

Of the three fuels investigated, the mechanisms studied here showed the largest variance with each other and experiment for ethylene flames. GRI-Mech 3.0 yields good agreement with experiment for methane- and ethane-air flames, predicting slightly higher flame speeds than measured, but is at variance with experiment for ethylene flames, for which it was not optimized. A  $C_3$  mechanism by Davis et al. yields reasonable agreement for stoichiometric and rich flames, but consistently predicts lower flame speeds than measured under lean conditions. For the San Diego mechanism, the 2003/08/30 version predicts higher flame speeds than measured for all cases studied, while the 2005/03/10 revision yields the best overall agreement with experiment for methane, ethane, and ethylene flames. The improved agreement with experiment of SD2005 compared to SD2003 is attributed to an increase in the rate of the  $H + OH + M \rightleftharpoons H_2O + M$  reaction, and a decrease in the rate of the  $HO_2 + H \rightleftharpoons 2OH$  reaction [20].

The technique presented here is sensitive to the residual between measured and predicted flame speed, and highlights variances in model predictions. The results are consistent with comparisons of the same models to data by other investigators. These results indicate that further kinetic model evaluation and optimization is needed to comprehensively describe the combustion of  $C_1$ – $C_2$  hydrocarbons. The experimental data are available to modelers for use as validation and optimization targets [11].

## Acknowledgments

We acknowledge discussions with K. Sone and L. Benzezech, as well as assistance by D. Lang with

digital-imaging, and D. Goodwin with the CAN-TERA software package. The work was funded by AFOSR Grant F49620-01-1-0006, whose support is gratefully acknowledged.

## References

- [1] G.P. Smith, D.M. Golden, M. Frenklach, et al., *GRI-Mech 3.0*, available at <[http://www.me.berkeley.edu/gri\\_mech/](http://www.me.berkeley.edu/gri_mech/)>.
- [2] M. Frenklach, H. Wang, M.J. Rabinowitz, *Prog. Energy Combust. Sci.* 18 (1992) 47–73.
- [3] J.M. Bergthorson, D.G. Goodwin, P.E. Dimotakis, *Proc. Combust. Inst.* 30 (2005) 1637–1644.
- [4] D.G. Goodwin, in: *Proc. of CVD XVI and EuroCVD Fourteen*, Electrochem. Soc., 2003, pp. 155–162.
- [5] R.J. Kee, M.E. Coltrin, P. Glarborg, *Chemically Reacting Flow—Theory and Practice*, John Wiley & Sons, Hoboken, NJ, 2003.
- [6] C.K. Law, C.J. Sung, G. Yu, R.L. Axelbaum, *Combust. Flame* 98 (1994) 139–154.
- [7] C.J. Sung, C.K. Law, R.L. Axelbaum, *Combust. Sci. Technol.* 99 (1994) 119–132.
- [8] C.J. Sung, J.S. Kistler, M. Nishioka, C.K. Law, *Combust. Flame* 105 (1996) 189–201.
- [9] C.J. Sung, J.B. Liu, C.K. Law, *Combust. Flame* 106 (1996) 168–183.
- [10] J.M. Bergthorson, *Experiments and Modeling of Impinging Jets and Premixed Hydrocarbon Stagnation Flames*, PhD thesis, California Institute of Technology, 2005, available at <<http://resolver.caltech.edu/CaltechETD:etd-05242005-165713/>>.
- [11] J.M. Bergthorson, PhD thesis Data Archive, 2005, available at <<http://resolver.caltech.edu/CaltechBLOB:ETD.ets-05242005-165713/>>.
- [12] M. Frenklach, A. Packard, P. Seiler, R. Feeley, *Int. J. Chem. Kinet.* 36 (2003) 57–66.
- [13] D.R. Crosley, *Combust. Flame* 78 (1989) 153–167.
- [14] C.D. Carter, J.M. Donbar, J.F. Driscoll, *Appl. Phys. B* 66 (1998) 129–132.
- [15] J.A. Sutton, J.F. Driscoll, *Appl. Opt.* 42 (2003) 2819–2828.
- [16] T.S. Norton, K.C. Smyth, *Combust. Sci. Technol.* 76 (1991) 1–20.
- [17] R.J. Kee, J.A. Miller, G.H. Evans, G. Dixon-Lewis, *Proc. Combust. Inst.* 22 (1988) 1479–1494.
- [18] J.M. Bergthorson, K. Sone, T.W. Mattner, P.E. Dimotakis, D.G. Goodwin, D.I. Meiron, *Phys. Rev. E* 72 (2005) 066307–1–12.
- [19] S.G. Davis, C.K. Law, H. Wang, *Combust. Flame* 119 (1999) 375–399.
- [20] *San Diego mechanism*, available at <<http://maeweb.ucsd.edu/combustion/cermech/>>.
- [21] J.M. Bergthorson, P.E. Dimotakis, *Exp. Fluids* 41 (2006) 255–263.
- [22] Y. Dong, C.M. Vagelopoulos, G.R. Spedding, F.N. Egolfopoulos, *Proc. Combust. Inst.* 29 (2002) 1419–1426.
- [23] K.J. Bosschaart, L.P.H. de Goey, *Combust. Flame* 136 (2004) 261–269.
- [24] F.N. Egolfopoulos, P.E. Dimotakis, *Combust. Sci. Technol.* 162 (2001) 19–35.
- [25] T. Hirasawa, C.J. Sung, A. Joshi, Z. Yang, H. Wang, C.K. Law, *Proc. Combust. Inst.* 29 (2002) 1427–1434.

## Comments

*Forman Williams, UCSD, USA.* It is good to see how sensitive your accurate experiments are to predictions of different reaction mechanisms. As improved elementary rate parameters are developed, agreements may improve. Studies may make use of your results to test hypotheses on important elementary reactions.

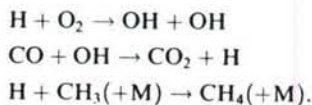
*Reply.* As you suggest, the purpose of the present experiments is to provide a technique and dataset that can be used to test future generations of kinetics mechanisms. Mechanism revisions should take into account new experimental measurements and theoretical predictions of individual reaction rates. Sensitivity analysis can be used to determine whether changes in a specific reaction rate will affect a specific comparison between simulation and experiment [1]. For methane-air flames, brute-force sensitivity analysis shows that the results are mostly sensitive to initiation by H radicals through the reaction  $\text{CH}_4 + \text{H} \rightarrow \text{CH}_3 + \text{H}_2$ , as observed for premixed laminar flames [1]. However, even a slight dependence could become significant when rates are adjusted by orders of magnitude. The appropriate measure of influence for a reaction is not the sensitivity coefficient alone, but the product of the sensitivity coefficient and the estimated uncertainty in the rate.

## Reference

- [1] C.K. Westbrook, F.L. Dryer, *Prog. Energy Combust. Sci.* 10 (1984) 1–57.

•

*David Smith, University of Leeds, UK.* Do you have an idea of which reactions in the model would need to change to improve experimental/simulation agreement? If flame speed is any guide, I suspect the most sensitive reactions will be:



The first two of these are very well characterized, through the third slightly less so. If the answer does not lie within this triumvirate, one is in the game of varying a large number of reactions, and mostly in the same direction.

*Reply.* As you suggest, comparisons between the simulations and experiments discussed in this paper are sensitive to the residual between the measured and predicted flame speed. Brute-force sensitivity analysis (see Williams' comment) can be used to identify the reactions that have the largest leverage on the experimental results. The results of the sensitivity analysis are not included here for brevity, but are available in ([10] in paper). The three reactions you mention have a large influence on the simulation predictions for all flames studied. However, there are several other reactions whose influence is comparable to those mentioned and that may be less well characterized. As an example, an increase in the rate of the  $H + OH + M \rightarrow H_2O + M$  reaction, and a decrease in the rate of the  $HO_2 + H \rightarrow 2OH$  reaction lead to the improved agreement with experiment seen for SD2005 as compared to SD2003. As discussed in ([2] in paper), an optimum set of rate constants can be identified by including experimental data such as these in large-scale mechanism optimizations. For such an optimization to be well posed, data must be obtained that are sensitive to all of the reactions included in the mechanism. Techniques such as those described in this paper allow new validation targets to be obtained for each experiment performed, reducing the experimental burden required to obtain the requisite dataset.

•

*Harsha Chelliah, University of Virginia, USA.* Did you measure the radial velocity component to verify that the differences in velocities between experiments and predictions are due to mass conservation effects? I believe this should be verified before validation of kinetic models.

*Reply.* Radial velocities were not measured in this study; however, the one-dimensional hydrodynamic model was previously validated against cold impinging-jet experiments and direct numerical simulations ([18] in paper). The one-dimensional model yields good agreement with both experiment and more detailed simulations if the boundary conditions are specified from fits to the data, indicating that the mass and momentum equations are accurately represented by this model and its associated approximations. The direct numerical simulations also show that radial velocities in this geometry vary linearly in the radial direction from the axis to approximately 60% of the nozzle radius, as assumed in the stream function model [1] ([10] in paper). Introduction of heat release will not affect the ability of the model to represent the hydrodynamics. In addition, the experimental flames are found to be planar over a large fraction of the radial domain, indicating one-dimensionality in the reacting flow ([3,10,21] in paper). Other investigators have measured the radial velocity profiles in non-reacting [2] and reacting ([22,25] in paper) stagnation flows, and found them to vary linearly in the radial direction near the jet axis, also consistent with the one-dimensional model employed here.

## References

- [1] J.M. Bergthorson, K. Sone, T.W. Mattner, P.E. Dimotakis, D.G. Goodwin, D.I. Meiron, *Experiments And Modeling Of Impinging Laminar Jets At Moderate Separation Distances*, Technical Report GALCITFM:2005:003, Caltech, <<http://resolver.caltech.edu/CaltechGALCITFM:2005.003>>.
- [2] J.C. Rolon, D. Veynante, J.P. Martin, F. Durst, *Exp. Fluids* 11 (1991) 313–324.